The Bounce, The Bang, and The Bounds: Models of Modified Gravity

By Richard Daniel

A thesis submitted for the degree of Doctor of Philosophy,

At the School of Mathematics and Statistics,

University of Sheffield

Supported by STFC CDT Studentship

December 20, 2023

Supervisor: Prof. Carsten van de Bruck

To my parents and Nana

In the beginning, the Universe was created.
This made a lot of people angry and is widely considered a bad move.
— *Douglas Adams*, The Hitchhiker's Guide to the Galaxy

Abstract

The current paradigm of cosmology lacks a fundamental and definitive description of the accelerated expansion in the early and late Universe. Moreover, the issue of the initial singularity is often overlooked in cosmology. Motivated by these phenomena, we investigate modified gravity models in three separate epochs.

We forecast how gravitational wave experiments will constrain dark energy models by producing mock data and predicting an improved accuracy for the model parameters. In the following chapter, we implement scale invariance into the theory of inflation, extending the work of Starobinsky's R^2 model, resulting in non-trivial features for the primordial power spectrum. Furthermore, we consider cosmology before inflation, replacing the initial singularity with a bounce. Creating a model based on Starobinsky's R^2 model, we successfully create a classical bounce which results in enhanced stability and a natural transition into slow-roll inflation. With studies conducted in these three epochs, we conclude that modified gravity in future research will lead to a greater insight into the fundamental phenomenology of gravity and cosmology.

Preface

This thesis is presented for the degree of Doctor of Philosophy in Mathematics. This project has been supervised by Prof. Carsten van de Bruck, and the contents within are predominantly the result of the author's original work, unless stated otherwise.

- Chapter 1 presents an introductory overview of general relativity and cosmology, providing the foundational knowledge necessary for the thesis.
- Chapter 2 is based on collaborative work with Elsa Teixeira, Noemi Frusciante, and Carsten van de Bruck, published in Physical Review D [1]. Elsa Teixeira is author to the table 2.1 and figs. 2.3a to 2.3d.
- Chapter 3 draws from published work in Physical Review D [2] in collaboration with Carsten van de Bruck. The chapter has been extended to include reheating, which remains currently unpublished.
- Chapter 4 is based on the collaborative work with Mariam Campbell, Carsten van de Bruck, and Peter Dunsby published in Journal of Cosmology and Astroparticle Physics [3].
- Chapter 5 provides a summary of the thesis, and a discussion on modified gravity highlighting the relevance of the research outlined in this thesis.

Acknowledgements

I am immensely grateful for the guidance and support of my supervisor, and friend, Carsten. Not only because without his invaluable assistance this thesis would not have come to fruition, but also because his enthusiasm and humour created a fun working environment. Thank you for the enjoyable (socially distant) walks in the park during the pandemic, the often amusing lunches, and the countless meetings, no matter how small or significant the topic. Consequently from his mentoring, I have become a capable and confident person.

I extend my gratitude to the entire CRAG research group, and I'd like to offer special recognition to a couple in G16 whose presence have truly, positively impacted my life: Alessandro, whose easy-going attitude is a constant source of positivity, and Lisa, whose unwavering support, both academically and personally, has added that extra spark to my PhD journey. And of course, a monumental thank you to my dear friend Elsa, who journeyed alongside me during her own PhD tucked away in "our little matchbox".

I also thank all of my loved ones outside academia for supporting me. To Amy and my friends, for their continued encouragement and motivation. And to my family, especially my Mum, who has been a consistent source of support, I am deeply grateful for helping me achieved this significant milestone in my academic journey.

Contents

1 An Introduction to Gravity and Cosmology **1**

1.1 General Relativity 6

1.2 Modified gravity 12

1.3 Modern cosmology 18

1.3.1 Cosmological perturbations 32

2 Gravitational Waves as Standard Sirens **39**

2.1 Forecast of gravitational wave data 42

2.1.1 Cosmology of gravitational waves 44

2.1.2 Probability distribution 45

2.1.3 Simulation of measurements and errors 46

2.2 Results and constraints 52

2.2.1 Results 54

2.3 Discussion of forecasted gravitational waves as standard sirens 59

3 The Theory of Inflation **61**

3.1 Successes of inflation 62

3.2 Slow-roll inflaton 67

3.3 Modified gravity during inflation 71

3.3.1 Starobinsky inflation 71

3.3.2 Scale invariant extension to Starobinsky inflation . . . 73

3.4 Cosmological perturbations during inflation 84

3.4.1 Single field perturbations 84

3.4.2 Two field perturbations 87

3.4.3 Three field perturbations 90

3.4.4 Summary of cosmological perturbations 99
3.5 Reheating 101
3.5.1 The three field model in the Jordan frame 102
3.6 Discussion on the theory of inflation 108

4 Bouncing Cosmology **110**
4.1 A classical bounce 111
4.2 False vacuum model 115
4.2.1 Bounce dynamics 117
4.2.2 Numerical analysis 120
4.2.3 Resulting inflation 124
4.2.4 Cosmological perturbations in the Jordan frame 126
4.3 Discussion on classical bouncing cosmology 134

5 Conclusion and Discussion **136**

A Derivation of Modified Einstein Equation **142**

B Conformal Transformation **145**

C Additional LISA constraints: varied fiducial and smearing **147**

1 | An Introduction to Gravity and Cosmology

Cosmology is the study of the physical universe encapsulated as a whole. It is one of the earliest notions humans have tried to understand: seeking answers to the beginning of the Universe, understanding how we as complex creatures came to be, and ultimately what the Universe's fate is. Initially a metaphysical study, cosmology is based on logical ideas to answer phenomena such as the initialisation and final fate of the Universe, the notion of space and time, and the cosmos above. As such, cosmology became a core concept in mythologies, religions, and philosophies, forming different cultures.

Over time and with the advancement of technology, cosmology has undergone several shifts throughout history. Like many other philosophical branches, observations of new phenomena backed by theoretical models, such as the orbital motion of planets, have provided a paradigm shift. The initial study of cosmology and astronomy was known as celestial mechanics to understand the behaviour of celestial bodies of the cosmos. As increasingly precise observations became available, the study became more rigorous, employing mathematics to describe theoretical models of the Universe. These advancements often gave rise to opposing philosophies and a conflict of ideas. In the mid 16th century, Copernicus published the heliocentric model placing the Sun at the centre of the solar system, contradictory to the belief that the Earth was the centre of the solar system. This was later famously observed and defended by Galilei and extended by Kepler to include a more mathematically accurate description. With the scientific method becoming increasingly established at the beginning of the 17th century, cosmology was upgraded from a meta-physical philosophy to a distinct branch

of physics using mathematical models backed by empirical observations to provide answers regarding the dynamics of the Universe. This framework shift is regarded mainly due to the publication of Newton's Law of Gravitation: a universal law that governs all massive bodies, including Earth, mediated by the force of gravity. Moreover, with the development of a concrete mathematical theory of gravity, a clear distinction between cosmology and astronomy is required: astronomy is the study of large-scale structures in the Universe identified before as celestial bodies, and cosmology remains the study of the Universe's history and consequent fate. Although, the two studies remain entangled.

Consequently, cosmology investigates extreme time and length scales to answer questions such as whether the Universe has a beginning or an end. With new precise measurements leading to new exotic models from a range of fields of study, there seems to be an apparent connection between the most miniature and largest scales[1]. Therefore modern cosmology encompasses two fundamental theories: General Relativity (GR) and the standard model of particle physics. GR, developed by Einstein at the beginning of the 20th century, describes gravity from a fundamental level, which presents a new insight into the interplay between matter and the geometry of space and time. The standard model of particle physics unifies fundamental particles and the other forces of nature. The synergy of these two theories would result in a fundamental theory of cosmology. Unfortunately, GR's description of gravity remains incompatible with the framework of the standard model of particle physics.

Moreover, we cannot reproduce and repeat the evolution of the Universe, posing a unique challenge. To understand the Universe's evolution, we rely on past events and local astrophysical observations, which we use to model the dynamic behaviour of the Universe using known physical laws. The combination of theoretical models, simulations, and data gathered from experiments allow us to construct a detailed timeline of the Universe. Therefore, cosmology can be considered an endeavour similar to archaeology. Provided we obtain a well-fitting model today, we can extrapolate backwards

[1]The apparent link between the largest and smallest scales are often depicted in philosophical studies as a cosmic ouroboros [4], where inverse length scales are coupled.

to construct a history of the Universe. Our current standard cosmological model is known as ΛCDM. ΛCDM describes the evolution of the Universe using GR by modelling the behaviour of its contents. These contents include standard matter, modelled by particle physics, plus two other "dark" species that only seem to interact gravitationally, dark matter and dark energy. ΛCDM relies on an initial Hot Big Bang (HBB)[2], where the Universe was originally in a hotter and denser state.

Including an additional epoch before the HBB, where the Universe underwent accelerated expansion, relieves the issues of HBB. This period is aptly named inflation. The theory of inflation resolved issues of the HBB and predicted relevant quantities of the CMB, establishing it as a well-founded paradigm. The HBB model alone has some serious shortcomings, most famously requiring extreme fine-tuning of initial conditions. Although, standard inflation also suffers from problems such as implying an initial spatial singularity. Several models have been proposed, such as extending inflation to resolve the singularity or introducing a new alternative early universe model that does not suffer the same shortcomings. However, the features and signatures these models propose are hard to confirm or deny through observations at the current level of technological advancement. As such, there is an extensive catalogue of early universe models with distinguishable observable features and predictions that can be probed with the development of future technologies.

Extending or dismissing models is a natural part of the scientific method. Recently, we have entered a golden age of cosmological observations. We can obtain higher precision measurements with each new generation of instruments using recent technological advancements. As a result, this has allowed us to detect phenomena such as gravitational waves, ripples in spacetime from the acceleration of massive objects predicted by GR, and direct observations of black holes. Furthermore, the increased precision of probes in both the early and late universe show a disagreement in estimating fundamental cosmological parameters due to increased stringency on model parameters. Specifically, this has caused issues for ΛCDM, with early and

[2]Historically, HBB was modelled before ΛCDM. As we will discuss later in the thesis, it is based on intuitive ideas from measurements that showed the Universe was not static.

late universe parameter measurements disagreeing. These tensions within the standard model highlight potentially new physics.

This thesis builds a history of the Universe. Starting with astrophysical observations in chapter 2, we discuss independent cosmological observations originating from the early and late universe, how they are constructed, and what we can infer from them. If ΛCDM is assumed, new precision technology reveals tensions between measured parameters between the early and late universe, notoriously the H_0 tension. Gravitational waves, a recent independent observable, can probe further than other late-time measurements. The importance of this new observation is substantial in light of the emergence of the H_0 tension, as it can provide an independent measurement that directly probes larger length scales. Moreover, we can use it to constrain alternative models to ΛCDM. Therefore we simulate new gravitational wave detectors to find the statistical importance of the mock data to forecast future constraints of alternative models to ΛCDM.

In the second half of the thesis, we study the early universe. In chapter 3, we discuss in detail some of the famous shortcomings of the standard HBB model motivating the work of inflation. We also introduce a widely studied mechanism, slow-rolling inflation. Using the motivation and machinery of slow-roll inflation, we extend the work to include a modification of gravity. We start with a simple and famous model, Starobinsky inflation, and increase the complexity to incorporate additional motivations. We analyse the interesting features of inflation within these models and the cosmological perturbations that give rise to unique signatures in the CMB. After examining successful periods of inflation, we establish a short regime of producing particles. We also study a common mechanisms in the immediate aftermath of inflation, reheating, analysing its effectiveness assuming the inflationary models studied.

Finally in chapter 4, we mention alternative inflation models that can be used to solve the issues of the HBB. We examine a specific alternative to inflation by replacing the spatial singularity with a past collapsing universe, creating a transition called a "bounce". We outline the motivation and the complexities of modelling a classical bounce, allowing us to propose new modified gravity models, which have been shown to have unique and ad-

vantageous mechanisms. However, with many classical bouncing models, extreme fine-tuning is required. For the specific model analysed in chapter 4, it is shown that the modification to gravity can alleviate this issue.

In chapter 5, we review the thesis findings before discussing and reviewing modified gravity throughout different epochs. We then conclude by highlighting the weaknesses and merits of modified gravity to affirm the necessity of studying extensions to GR with an outlook on future research.

Notation and convention

In this thesis, unless stated otherwise, we will use the convention of using Greek indices to indicate the running over the four-dimensional space-time coordinates, $\alpha = 0, 1, 2, 3$ with the metric signature $(-, +, +, +)$. Lowercase Latin indices will identify a running over a three-dimensional spatial coordinate system $i = 1, 2, 3$. Repeated indices in a single term signify a summation according to the standard Einstein summation convention.

We will utilise the shorthand notation where a subscript identifies the partial derivative, $f_x \equiv \frac{\partial f}{\partial x}$. Furthermore, the subscript on a partial derivative, ∂_μ indicates a partial derivative with respect to the coordinates used, $\partial_\mu \equiv \frac{\partial}{\partial x^\mu}$.

Different time coordinates will be used throughout this thesis. An overdot will be used to indicate the differentiation with respect to cosmic time, t, $\dot{f} \equiv \frac{\partial f}{\partial t}$. Differentiation with respect to other time coordinates will be represented by a prime.

We will also use reduced Planck units, where $\hbar = c = 8\pi G = 1$. This also means that the reduced Planck mass, $M_{\rm Pl} \equiv (8\pi G)^{-1}\hbar c$ is also set to unity, $M_{\rm Pl} = 1$. However, to help illustrate dimensionality, it may be included.

1.1 General Relativity

Before the 1900s, Newton's law of gravity was the paradigm used to understand the invisible attractive force between all massive bodies. This law was based on the discoveries of Kepler, who established three laws of planetary motion, including that they followed an elliptical orbit. Newton built upon Kepler's work and deduced that the force between two masses is proportional to the product of their masses and inversely proportional to the square of the distance between them [5]. This relationship can be mathematically expressed as $F = G(m_1 \cdot m_2)r^{-2}$, where F is the force of attraction, G is the gravitational constant, m_1 and m_2 are the masses of the two objects, r is the distance between them, and G is the gravitational constant balancing the proportionality. This can be compactly written using Poisson's equation, where a density of mass ρ_m sources a gravitational force via the scalar potential, Φ, known as the gravitational potential, that is related to the acceleration by $g = -\nabla\Phi$, and therefore the force from Newton's second law. The relation between the gravitational potential and the mass density is given by:

$$\nabla^2\Phi = 4\pi G\rho_m. \tag{1.1}$$

This theory had stood the test of time, as it accurately mapped out the orbits of planets and even predicted Uranus before its observation. However, even as stated by Newton, the theory was incomplete. An example of an issue with Newton's gravity was the discrepancy between the measurement and calculation of perihelion precession of Mercury's orbit: a difference of 38 arcseconds per century between measurements and calculations[6].

The shortcomings of Newton's Law of Gravitation were addressed when Einstein formulated his theory of general relativity (GR) [7–11]. GR was verified with three tests that were not predicted using Newtonian gravity: accounting for the precession of Mercury, correctly measuring the bending of light around the sun, and the gravitational redshift of light as it moves away from massive bodies [10, 12–15]. Still, the current paradigm of gravity not only solves issues known from Newton's theory but, as good theories do, predicts newly observed phenomena such as direct observation of black holes [16–18] and the detection and measurement of gravitational waves

[19, 20].

John Wheeler briefly encapsulated the idea of GR with the quote, "Spacetime tells matter how to move; matter tells spacetime how to curve" [21]. We dedicate the remainder of this section to understanding what this famous quote means by providing a summary of GR, details of which can be found in [13–15] and references within.

There are two main core principles of GR: the notion of universality, where gravity affects all matter and forms of energy equally, and Einstein's Equivalence principle, "in small enough regions of spacetime, the laws of physics reduce to those of special relativity; it is impossible to detect the existence of a gravitational field by means of local experiments" [10] [3]. More technically, GR describes the Universe as a connected four-dimensional spacetime manifold, where gravity is interpreted as the curvature of said spacetime. Mathematically GR is a geometric theory that models a Lorenzian manifold, encoded with the metric tensor $g_{\mu\nu}$, describing the distance between events. The coordinate invariant line element describes the proper distance between events,

$$ds^2 = g_{\mu\nu} dx^\mu dx^\nu, \tag{1.2}$$

where dx^μ is the coordinate displacement between the events, where $dx^0 = dt$ is the time coordinate and $dx^{1,2,3} = dx, dy, dz$ as the spatial coordinates. The metric $g_{\mu\nu}$, a four-dimensional symmetric tensor, describes the geometry of the spacetime. For instance, reducing the line element to describe a Minkowski geometry $g_{\mu\nu} \to \eta_{\mu\nu} = \text{diag}(-1, 1, 1, 1)$ yields the line-element of special relativity, $ds^2 = -dt^2 + dx^2 + dy^2 + dz^2$. This metric provides an understanding of spacetime as it recovers special relativity linking it back to the equivalence principle, with the spatial part resulting in a Euclidean (flat) geometry. Therefore, the shortest path between two points in spacetime depends on the metric tensor, and any equations describing spacetime must be tensorial to maintain coordinate-invariant equations. As partial derivatives

[3] In this thesis, we will not cover special relativity (SR) as it is not directly relevant to the scope of our study. However, for completeness, as a concise overview: SR encapsulates electromagnetism and Newtonian mechanics into a singular theory and is based on two postulates. The first is relativity, which states that the laws of physics are the same in all inertial reference frames. The other is the invariance of the speed of light in a vacuum, irrespective of the motion of the source. [22]

are not tensorial and coordinate dependent. Therefore they cannot be used to describe the properties of spacetime. It is then necessary to use more advanced mathematical tools such as covariant derivatives, ∇_μ, to describe the geometry of spacetime in a tensorial manner. The covariant derivative of a vector field, V^ν is defined as,

$$\nabla_\mu V^\nu = \partial_\mu V^\nu + \Gamma^\nu_{\mu\sigma} V^\sigma, \tag{1.3}$$

where ∂_ν is the partial derivative with respect to x^ν and Γ is the Christoffel symbol and encodes how the curvature of a manifold affects the vector field. Γ is formally related to the metric components as

$$\Gamma^\nu_{\mu\sigma} = \frac{1}{2} g^{\nu\lambda} \left(\partial_\mu g_{\sigma\lambda} + \partial_\sigma g_{\lambda\mu} - \partial_\lambda g_{\mu\sigma} \right). \tag{1.4}$$

The covariant derivative, therefore, accounts for the fact that vectors in curved spacetime may change direction as they are transported along a path, ensuring that our equations are coordinate-invariant and provide a correct description of the underlying geometry of the spacetime.

A useful and straightforward example to understand the formulations above is the case of an unaccelerated particle, or "free-falling" particle, on a curved background. We can describe this as,

$$\frac{d^2 x^\mu}{d\lambda^2} + \Gamma^\mu_{\rho\sigma} \frac{dx^\rho}{d\lambda} \frac{dx^\sigma}{d\lambda} = 0. \tag{1.5}$$

This is called the geodesic equation, where λ is the affine parameter that is related to a time coordinate, thus parameterising the particle's motion $x^\mu(\lambda)$. In the simple setup of Minkowski spacetime $\Gamma = 0$, and thus we will be left with the equation for a straight line as expected.

Next we investigate the curvature itself, a fundamental concept of GR which is sourced by matter, analogous to the Newtonian potential of a massive body. A useful concept to illustrate the effect of curvature is parallel transport: maintaining a constant vector along a given path, as depicted by the red arrows in fig. 1.1. Parallel transport of a vector provides a means of understanding the impact of curvature. In contrast to flat space, the outcome of parallel transporting a vector on a curved space relies on the path taken as illustrated by the change of the vector, δV^ρ, in fig. 1.1. Given a loop along vector A^μ and B^ν, the change of the vector's direction is $\delta V^\rho = V^\sigma R^\rho_{\sigma\mu\nu} A^\mu B^\nu$.

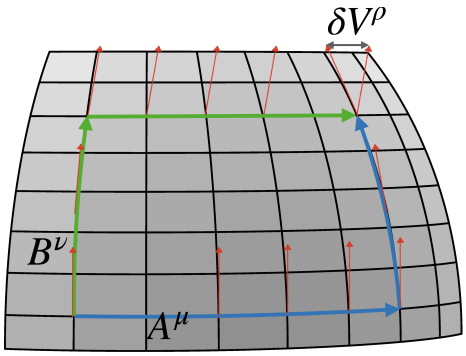

Figure 1.1: An illustration showing the change of a vector, V^σ (red), due to parallel transport along vectors, A^μ and B^ν, via two different paths (green and blue), on a curved background resulting in a small discrepancy, δV^ρ.

$R^\rho_{\sigma\mu\nu}$ is the Riemann tensor which measures the curvature and is defined as

$$R^\rho_{\sigma\mu\nu} = \partial_\mu \Gamma^\rho_{\nu\sigma} - \partial_\nu \Gamma^\rho_{\mu\sigma} + \Gamma^\rho_{\mu\lambda}\Gamma^\lambda_{\nu\sigma} - \Gamma^\rho_{\nu\lambda}\Gamma^\lambda_{\mu\sigma}. \tag{1.6}$$

If the metric has constant components, such as in a flat spacetime, the Riemann tensor vanishes, $R^\rho_{\sigma\mu\nu} = 0$. The contraction of the Riemann tensor results in the symmetric Ricci tensor,

$$R_{\mu\nu} = R^\rho_{\mu\rho\nu}. \tag{1.7}$$

With a further contraction, we can formulate the Ricci scalar

$$R = g^{\mu\nu} R_{\mu\nu}. \tag{1.8}$$

The Ricci tensor and scalar encode information regarding curvature, which can be neatly summarised as the Einstein tensor, a symmetric matrix of second derivatives of the metric,

$$G_{\mu\nu} = R_{\mu\nu} - \frac{1}{2} R g_{\mu\nu}, \tag{1.9}$$

that is covariantly conserved $\nabla_\mu G^\mu_\nu = 0$. Utilising our understanding of the concepts and interplay between geometry and curvature, we investigate the influence of matter. Drawing an analogy to Newton's law of gravitation, the matter density of (1.1) is generalised to a tensor that accounts for different forms of matter and energy, aptly labelled the energy-momentum tensor, $T_{\mu\nu}$. In the field of cosmology, we can make the approximation that we can treat all types of energy as a perfect fluid, this is due to the nature of the cosmological principle on large scales and is discussed later in section 1.3. This allows the

energy-momentum tensor to be characterised by two quantities: the energy density, ρ, and pressure, P, in the rest frame. Consequently, we define the energy-momentum tensor in cosmology as,

$$T_{\mu\nu} = \text{Diag}(\rho, P, P, P). \tag{1.10}$$

This tensor is covariantly conserved, $\nabla_\mu T^\mu_\nu = 0$, which is analogous to the conservation of energy and momentum in Newton's law. In order to relate the curvature and distribution of matter, we aim to combine our equations together. Utilising our analogy of Newton's Law of gravity, (1.1), and the two symmetric conserved tensors: the Einstein, (1.9), and energy-momentum tensor, (1.10), we conclude the combination that results in Einstein's field equations (EFEs) [8],

$$G_{\mu\nu} = R_{\mu\nu} - \frac{1}{2}Rg_{\mu\nu} = \kappa T_{\mu\nu}. \tag{1.11}$$

A proportionality constant, κ, has been included, and by taking the Newtonian limit, we set the proportionality constant to $\kappa = 8\pi G$. We can see that EFEs are symmetric and thus describe a matrix of 10 different second-order differential equations. The left-hand side contains second derivatives of the metric, encoded in the Einstein tensor, that characterises curvature of spacetime due to gravity. On the other hand, the right-hand side describes the matter content via the energy-momentum tensor. This equation maintains the analogy to the Poisson equation used in Newton's Law of Gravitation, (1.1). It also highlights the interconnection between spacetime and matter, bringing us back to Wheeler's famous quote, "Spacetime tells matter how to move; matter tells spacetime how to curve".

The EFEs are more commonly understood and derived through classical field theories. Following the work of David Hilbert, we choose a simple Lagrangian density that only depends on the Ricci scalar and the determinant of the metric [23],

$$\mathcal{S} = \frac{M_{\text{Pl}}^2}{2}\int d^4x\sqrt{-g}R + \mathcal{S}_M. \tag{1.12}$$

This is known as the Einstein-Hilbert action. M_{Pl} is a fundamental mass scale known as the reduced Planck mass and is related to the proportionality constant above, $\kappa = M_{\text{Pl}}^{-2}$. To account for the content of the Universe, a separate matter action, $\mathcal{S}_M$, is included. The matter content is related to the

energy-momentum tensor via a variational derivative with respect to the metric,

$$T_{\mu\nu} = -\frac{2}{\sqrt{-g}}\frac{\delta \mathcal{S}_M}{\delta g^{\mu\nu}}. \tag{1.13}$$

Computing the variation of the total action with respect to the metric, we derive the EFEs (1.11).

The Ricci scalar in eq. (1.12) is the simplest ansatz that results in the formulation of GR. A simple extension that Einstein originally considered was to include an arbitrary scalar quantity, Λ [11, 24]. The general action then becomes,

$$\mathcal{S} = \frac{M_{\rm Pl}^2}{2}\int d^4x\sqrt{-g}(R - 2\Lambda) + \mathcal{S}_M. \tag{1.14}$$

The negative sign is a choice based on classical field theory where $\mathcal{L} = T - V$ such that Λ acts as a potential, and the 2 is an aesthetic choice simplifying later results. The resulting EFEs with this minor modification are,

$$R_{\mu\nu} - \frac{1}{2}Rg_{\mu\nu} + \Lambda g_{\mu\nu} = \kappa T_{\mu\nu}. \tag{1.15}$$

This scalar quantity, Λ, remains a constant over all scales and is therefore aptly labelled a cosmological constant. Initially, Einstein included this constant to account for a static universe, which observations were suggesting at the time, with Λ counteracting the gravitational pull of standard matter. This is can be understood by moving $\Lambda g_{\mu\nu}$ to the right-hand side, explaining the choice for the negative sign. We can appreciate the physical intuition of this constant by examining the background scenario of flat space in a vacuum. We conclude that the only energy density remaining is this cosmological constant, $\Lambda g_{\mu\nu} = \kappa T_{\mu\nu}^{(\rm vacuum)}$. As such, the cosmological constant can be interpreted as the global vacuum energy that essentially shifts the minimum energy of the Universe by a factor of Λ. Of course, we are entirely free to set $\Lambda = 0$, which was the consensus until the turn of the century, until it was observed that the Universe was expanding at an accelerated rate [25–28]. Thus, the simplest extension, including a cosmological constant, remains unexplained from a fundamental point of view and continues to be a highly debated topic. As we will discuss in chapter 2, observational tensions have arisen assuming the simplest model utilising a cosmological constant.

Moreover, on more local scales, galaxy rotation curves highlight that stars and gas in galaxies do not follow the theoretical distribution expected

from GR. Thus to resolve these issues, a common approach is to include an additional type of matter that couples only to gravity [26–29]. Further details of this topic are discussed in section 1.3. Even if one is to accept an arbitrary cosmological constant or the inclusion of an additional unknown matter content, GR remains incomplete at extreme scales: it predicts the unphysical singularities [30–32]. The current theory of the beginning of the Universe, the Big Bang, initialises the Universe as a point source containing all the energy of the Universe. On more local scales, black holes, which have been directly detected and recently photographed [33, 34], are predicted by GR to contain a singularity at their centre. The predicted singularities are part of a more fundamental problem with GR: the division between GR and quantum mechanics. Unlike other classical field theories, such as electromagnetism, GR is nonrenormalisable: when building a quantum description of GR, the theory becomes divergent [35]. Although not a discussion of this thesis, many techniques and fields of study are motivated by this topic, such as extending quantum field theory to introduce curvature [36].

The shortcomings at high-energy scales highlight the possibility that a new, more complex theory is required that, in well-tested limits, reduces to GR. However, many of the issues that arise from GR are on the most extreme scales, cosmological and quantum, scales that are complex and hard to probe experimentally. Therefore theoretical modifications and extensions to the theory aim to explain the discrepancies and probe new insights into the fundamental nature of gravity.

1.2 Modified gravity

A theory is often preferred if it is simple, argued by the idea of Occam's razor[4] which favours theories with fewer free parameters and unnecessary

[4]The idea that a simpler theory with fewer free parameters is preferred due to a higher predictive power and being more testable. Therefore within the scientific method, Occam's razor highlights the power of logical reasoning that a theory that can be proven wrong is better than one that can predict anything.

complexities due to simpler theories having a higher predictive power. However, if a theory becomes incompatible with experimental observations, it may highlight the possibility of new physics, requiring modifications to the theory with new degrees of freedom or parameters. An example is the prediction of Neptune to account for the orbits in the solar system, as we have already discussed. Alternatively, one can employ a more radical approach: proposing a new theory that retains the successes of the old theory in certain limits whilst remaining compatible with observations. The severity and complexity of the problem determine whether the existing one can be modified to address the issue or if a new theory is required. Einstein's development of GR, challenging Newton's notion of gravity, is an example of the latter. Nevertheless, modifications should be considered when the theory breaks down and are often adequate solutions which can lead to new insights and mechanisms that more accurately represent nature. In the case of GR, around 50 years after its proposal, it was found to be incompatible with quantum effects, motivating extensions to GR.

Moreover, as technology advances, new features of the Universe are uncovered, requiring the current models and theories to be modified or dismissed. As mentioned above, recent observations show that the Universe is expanding at an accelerated rate, contrary to what GR intuitively describes (we will discuss the details of this expansion later in section 1.3). This incompatibility highlights that the simplest setup of GR is incomplete and motivates work to find modifications.

We have already discussed a simple extension to GR that Einstein introduced: the addition of a cosmological constant. However, this modification still exhibits tensions between theoretical and experimental physics. Another simple extension to GR is to include additional matter content. We introduce a scalar field, ϕ, that minimally couples to gravity [28, 37, 38], which means the field only interacts with the metric

$$\mathcal{S} = \int d^4x\sqrt{-g}\left[\frac{M_{\rm Pl}}{2}R - \frac{1}{2}g^{\mu\nu}\partial_\mu\phi\partial_\nu\phi - V(\phi)\right]. \tag{1.16}$$

Here $V(\phi)$ is the potential of the scalar field. Varying the action with respect to ϕ, we arrive at the Klein-Gordon equation, a second-order differential equation governing the dynamics of ϕ:

$$\Box\phi - V'(\phi) = 0. \tag{1.17}$$

The scalar field can serve as a model for various forms of energy and matter. It is included as the matter component of the action, $\mathcal{S}_m$, resulting in the stress-energy tensor given by (1.13),

$$T_{\mu\nu} = \partial_\mu\phi\partial_\nu\phi - g_{\mu\nu}\left[\frac{1}{2}g^{\rho\sigma}\partial_\rho\phi\partial_\sigma\phi + V(\phi)\right]. \tag{1.18}$$

Another possible extension is to generalise the Einstein-Hilbert action, depending on the Ricci scalar, as a function

$$\mathcal{S} = \int d^4x\sqrt{-g}f(R) + \mathcal{S}_M. \tag{1.19}$$

Many different functions of $f(R)$ have been studied (see [26, 39–43]), however, GR has been tested and confirmed on local scales. Therefore we know $f(R) \to R$ on local scales. This modification results in a change in the Einstein tensor when varying the action with respect to the metric,

$$FR_{\mu\nu} - \frac{1}{2}fg_{\mu\nu} - (\nabla_\mu\nabla_\nu - g_{\mu\nu}\Box)F = \kappa T_{\mu\nu}, \tag{1.20}$$

where $F = \partial f/\partial R \equiv f_R$. The modification results in an additional scalar degree of freedom, identified by F and labelled as a scalaron. In standard GR, $F \to 1$ and the additional degree of freedom vanishes. Taking the trace of (1.20) provides a useful alternative dynamical description of the modification,

$$\Box F = \frac{2f - FR}{3} + \frac{\kappa}{3}T. \tag{1.21}$$

This modification and the corresponding field equations belong to the Jordan frame formalism, where the modifications are in the gravitational sector. The dynamical system determines the additional propagating degree of freedom and is analogous to the Klein-Gordon equation of a scalar field.

In the case of standard GR, $F(R) = R$, we see that eq. (1.21) results in $R = -\kappa T$, which means that the Ricci scalar is determined by the trace of the stress-energy tensor. As such, the modification can be interpreted as including additional matter. It is possible to highlight this interpretation by transforming the action into a different frame, which can be beneficial in identifying any physical issues of the modification. Performing the transformation maps the gravitational modification to an additional component of the stress-energy tensor, that minimally couples to gravity resulting in the standard Einstein Hilbert action. To help illustrate the transformation, we

include an auxiliary field, χ, such that

$$\mathcal{S} = \int d^4x\sqrt{-g}\frac{M_{\rm Pl}^2}{2}\left[f(\chi) + f'(\chi)\left(R-\chi\right)\right], \tag{1.22}$$

where the prime indicates a derivative with respect to χ. When the action is varied with respect to χ we obtain the result $f''(\chi)(R-\chi) = 0$. Therefore provided $f''(\chi) \neq 0$, we recover our original action using the result that $R = \chi$. To make it explicit, we define the scalar degree of freedom,

$$\phi = f'(\chi),$$

which also implies that $\chi(\phi)$. Therefore that the action can be rewritten as,

$$\mathcal{S} = \int d^4x\sqrt{-g}\frac{M_{\rm Pl}^2}{2}\left[\frac{M_{\rm Pl}}{2}\phi R - V(\phi)\right], \tag{1.23}$$

where $V = M_{\rm Pl}^2(\phi\chi - f(\chi))/2$. The action has now been rewritten as a scalar-tensor theory[5] belonging to a class of theories known as Brans-Dicke (BD) [44, 45],

$$\mathcal{S} = \int d^4x\sqrt{-g}\left[\frac{M_{\rm Pl}}{2}F(\phi)R - \frac{\omega(\phi)}{2}g^{\mu\nu}\partial_\mu\phi\partial_\nu\phi - V(\phi)\right] + \mathcal{S}_M(g^{\mu\nu},\phi). \tag{1.24}$$

Brans-Dicke theories are a useful set of theories, as they can be transformed such that the scalaron is redefined so that it minimally couples to gravity, and we arrive back at the Einstein-Hilbert action plus a matter content. We will be considering the metric formalism within this thesis, which corresponds to $\omega = 0$ in the BD action above[6].

Since the Ricci scalar and scalaron are related to the metric, we consider a conformal re-scaling of the metric to remove the non-minimal coupling in eq. (1.24),

$$g_{\mu\nu} \to \tilde{g}_{\mu\nu} = F(\phi)g_{\mu\nu}, \tag{1.25}$$

where the tilde indicates the new re-scaled metric. We relabel our additional degree of motion as a field - the scalaron, $F(R) \to \psi$, such that

$$d\psi = M_{\rm Pl}\sqrt{\frac{3}{2}}\frac{dF}{F}. \tag{1.26}$$

[5]Scalar-tensor theories are a class of modifications where a scalar degree of freedom (in our case, known as ϕ) interacts with the metric and the curvature. Therefore ϕ is considered non-minimally coupled to gravity.

[6]For the metric formulation, which we are considering here, the metric encodes all the details and sets $\omega = 0$. Other formulations, such as metric-affine or the further reduced Palatini, where the connection is also viewed as a separate variable to the metric, sets $\omega = -3/2$ [41, 43, 46].

Therefore our scalar redefinition results in

$$F = e^{\sqrt{\frac{2}{3}}\frac{\psi}{M_{\rm Pl}}}. \tag{1.27}$$

Utilising the conformal transformation of the metric with its associated quantities such as the Ricci scalar and the field redefinition the action becomes,

$$\mathcal{S}_E = \int d^4x\sqrt{-\tilde{g}}\left[\frac{M_{\rm Pl}^2}{2}\tilde{R} - \frac{1}{2}\tilde{g}^{\mu\nu}\partial_\mu\psi\partial_\nu\psi - e^{-2\sqrt{\frac{2}{3}}\frac{\psi}{M_{\rm Pl}}}V(\psi)\right] + \mathcal{S}_M\left(e^{-\sqrt{\frac{2}{3}}\frac{\psi}{M_{\rm Pl}}}\tilde{g}^{\mu\nu}\right). \tag{1.28}$$

The action is now written with the scalaron non-minimally coupled to gravity, this is known as the Einstein frame, identified with the subscript E. The $f(R)$ action in the Einstein frame now resembles that of eq. (1.16). For more derivation details, see appendix B. To change from a non-minimally coupled field to a minimally coupled field we conformally transformed the metric.

The ψ–field, along with all other matter contained within the stress-energy tensor, follows the geodesics of our new metric, which depends on ψ.

This transformation results in the matter sector, being shifted by F^{-2}. To make this explicit we can analyse the transformation with respect to the stress-energy tensor. Using eq. (1.25) to provide the relation $\sqrt{-\tilde{g}} = F^2\sqrt{-g}$, we find that

$$\tilde{T}_{\mu\nu} = -F^{-1}T_{\mu\nu}, \tag{1.29}$$

where we have eq. (1.13). In a perfect fluid, eq. (1.10) changes as

$$\text{Diag}(\tilde{\rho}, \tilde{P}, \tilde{P}, \tilde{P}) = \text{Diag}(\rho, P, P, P)\, e^{-\sqrt{\frac{2}{3}}\frac{\psi}{M_{\rm Pl}}}. \tag{1.30}$$

Therefore if we are to include additional fields to eq. (1.19), they will experience a modification to their kinetic and potential terms. An example of this is given in section 4.2.3. Analysing the EFEs, we notice that we can now re-write eq. (1.20) as,

$$R_{\mu\nu} - \frac{1}{2}g_{\mu\nu}R = \frac{\kappa}{F}(T_{\mu\nu} + T^{(\rm mod)}_{\mu\nu}) \tag{1.31}$$

where,

$$\kappa T^{(\rm mod)}_{\mu\nu} = \frac{1}{2}g_{\mu\nu}\left(f - RF\right) + \left(\nabla_\mu\nabla_\nu - g_{\mu\nu}\Box\right)F \tag{1.32}$$

highlighting the interpretation of the scalaron as a new matter content and the effect it has on the stress-energy tensor. The action using the scalar

field written in this form is often refereed to as quintessence. To be more accurate we would state that this is an action of coupled quintessence, as the quintessence field now interacts matter due to the metric transformation, $\mathcal{S}_M\left(e^{-\sqrt{\frac{2}{3}}\frac{\psi}{M_{\rm Pl}}}\tilde{g}^{\mu\nu}\right)$.

There are many modified gravity theories, too many to be outlined in this thesis. However, in the last decade, a branch of modified gravity called Horndeski theories has become popular[47]. They include quintessence which has the form of eq. (1.16) and results in a dynamical cosmological constant[7] [28, 37, 38, 48], Brans-Dicke [44, 45], $f(R)$ [26, 39–43], and Galileon theories [49, 50] (a class of theories that utilise a scalar field that is constructed to have a shift symmetry such that $\phi \to \phi + b_\mu x^\mu + c$). They can all be conveniently combined in a single action to give what is known as the Horndeski Lagrangian,

$$\begin{aligned}\mathcal{L} &= G_2(\phi, X) + G_3(\phi, X)\Box\phi + G_4(\phi, X)R \\ &+ G_{4,X}(\phi, X)\left[(\Box\phi)^2 - (\nabla_\mu\nabla_\nu\phi)(\nabla^\mu\nabla^\nu\phi)\right] + G_5(\phi, X)G_{\mu\nu}\nabla^\mu\nabla^\nu\phi \\ &- \frac{1}{6}G_{5,X}(\phi, X)\left[(\Box\phi)^3 - 3(\Box\phi)(\nabla_\mu\nabla_\nu\phi)(\nabla^\mu\nabla^\nu\phi) + 2(\nabla^\mu\nabla_\rho)(\nabla^\rho\nabla_\sigma)(\nabla^\sigma\nabla_\mu\phi)\right].\end{aligned} \tag{1.33}$$

$G_{1\ldots5}$ are functions that depend on the scalar field, ϕ, and its kinetic term, $X = g^{\mu\nu}\partial_\mu\phi\partial_\nu\phi$. We can arrive at quintessence by setting $G_2 = X - V, G_4 = M_{\rm Pl}^2/2$, and $G_3 = G_5 = 0$. $f(R)$ can be recovered if we set $G_2 = -M_{\rm Pl}^2(RF - f)/2, G_4 = M_{\rm Pl}^2F/2$, and $G_3 = G_5 = 0$. Horndeski theories encapsulate modifications to GR while retaining second-order field equations and avoiding the introduction of instabilities and ghost fields. They are compatible with cosmological observations [51, 52], provided the fine-tuning of parameters, but are useful to present a general structure to study modified gravity.

[7] The keen reader will notice that a constant cannot be a dynamical, we discuss this later and label the vacuum energy as a dark energy.

1.3 Modern cosmology

A foundational principle of cosmology is the assumption of a spatially homogeneous and isotropic universe on large scales, meaning the Universe looks "the same everywhere" and "in all directions", respectively. Assuming both homogeneity and isotropy, we conclude that it should apply to all regions in space. Thus our assumption invokes the Copernican or cosmological principle stating, "we do not live in a special place in the Universe". Therefore our cosmological observations are generic, allowing us to make conclusions about the laws of nature governing the Universe as a whole. On small scales, details of different structures are clustered non-uniformly, thus breaking the cosmological principle. These inhomogeneities can be used as useful cosmological probes, as we will discuss in section 1.3

Many cosmological models will make this assumption on the basis that we are looking at a scale larger than 100 Mpc[8], therefore remaining within the validity of the cosmological principle. This assumption simplifies many equations to describe the Universe, allowing approximations to be used. For example, exact solutions to EFEs are difficult to find; however, a simple metric can be found that is a solution to the EFE, assuming the cosmological principle.

An evolving universe

The discovery that the Universe is not static but evolving is the core of modern cosmology and marked a significant paradigm shift. This conclusion was determined in the early 20th century by astrophysicists who measured the frequency of light emitted by galaxies. It was observed that galaxies exhibited a shift in the emitted wavelength. We quantify the change of wavelength by the redshift,

$$z \equiv \frac{\lambda_f - \lambda_i}{\lambda_i}, \tag{1.34}$$

where λ_i is the wavelength emitted by the source and λ_f is the wavelength observed. In a local region with non-relativistic sources, the redshift is

[8]This is a lower bound for cosmology, referring to the approximate scale of the largest known structures seen in the Universe: the length of super-clusters and voids [27].

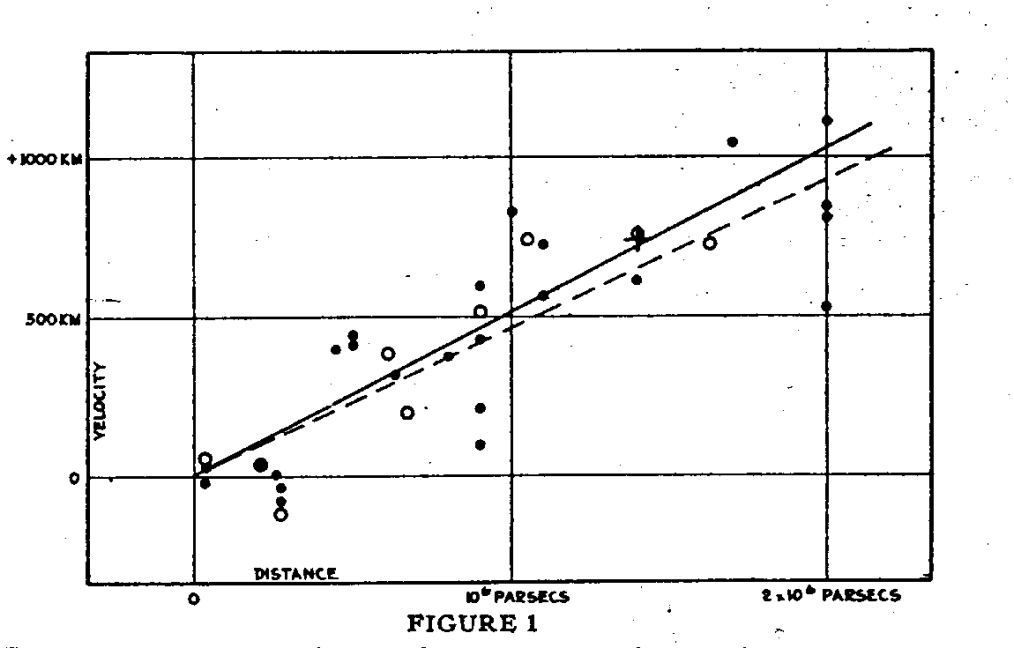

Figure 1.2: Hubble's original plot of redshift velocity and radial distance [53] with a line of best fit. The plot shown here and in Hubble's original paper has incorrect velocity units, with the correct units $Km\ s^{-1}$. The filled circles and solid line represent the solution for the individual motion of stars within the galaxy centres. The empty circles and broken line represent grouped stars.

equivalent to the Doppler shift: the change in frequency of a source due to its motion towards or away from the observer e.g. the change in the sound of a moving car. This provides us with a simple relation between the redshift and the velocity of the source, v relative to the speed of light, c, $z = v/c$. In 1929, enough data had been collected for Edwin Hubble and his colleagues to propose a linear relationship between the receding velocity, v and the distance, d, relative to Earth depicted in fig. 1.2 [53]. This relation is known as Hubble's Law [27, 53, 54],

$$v = H_0 d \tag{1.35}$$

where H_0 is a constant of proportionality known as Hubble's constant. An interesting conclusion from Hubble's Law is that the recessional velocity of galaxies increases with their distance from us. Assuming the cosmological principle, this suggests that, on average, all observers conclude the same law. Therefore, every galaxy is receding from each other. This led to the conclusion that the Universe is expanding and not static as previously

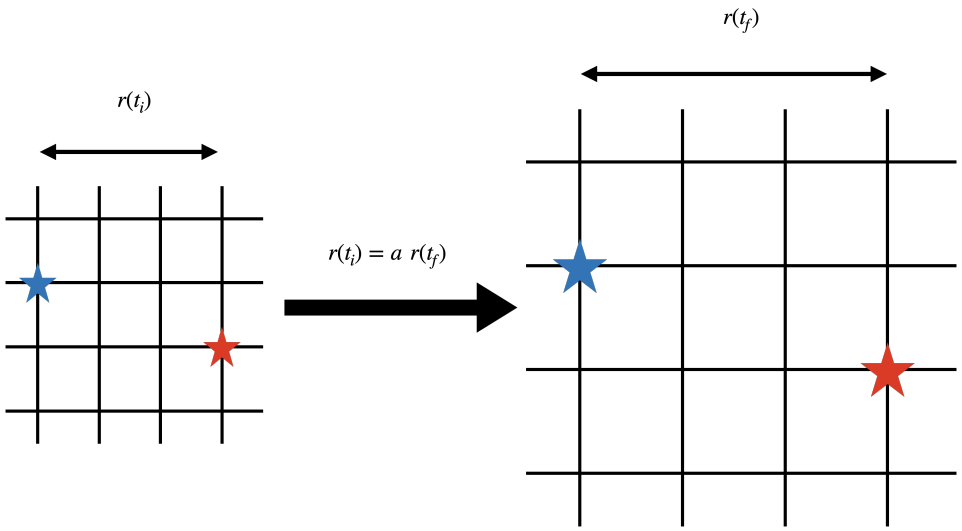

Figure 1.3: A visual representation describing the scale factor and comoving coordinates

thought.

Moreover, by extrapolating backwards in time, an expanding universe implies we previously lived in a hotter, denser universe. Therefore we conclude that the Universe started at a spatial singularity, where all the contents were contained in a single point in space. This is the basic premise for the Big Bang theory. Therefore Hubble's Law was the first evidence for the Big Bang theory. We can also use Hubble's Law to estimate the Universe's age, $t \sim H_0^{-1} \sim 13$ Gyrs.

The Friedmann, Lemaître, Robertson and Walker metric and the Friedmann equations

Thus far, we have largely ignored the notion of cosmological time. However, the fact that the Universe is expanding requires more careful consideration. Firstly, we define a dimensionless scale factor $a(t)$, illustrated in fig. 1.3, which represents the scale of space at a given time, t. It is defined as the ratio of distances, r, at t_f and an initial time t_i, i.e., $a(t) = r(t)/r(t_i)$. Therefore the scale factor represents the size of the Universe at a given time slice. As a function of time, it can be used to find the relative rate of expansion, defined as $\dot{a}/a$. We can then generalise the Hubble constant to the Hubble parameter, with the Hubble constant identifying the current expansion rate.

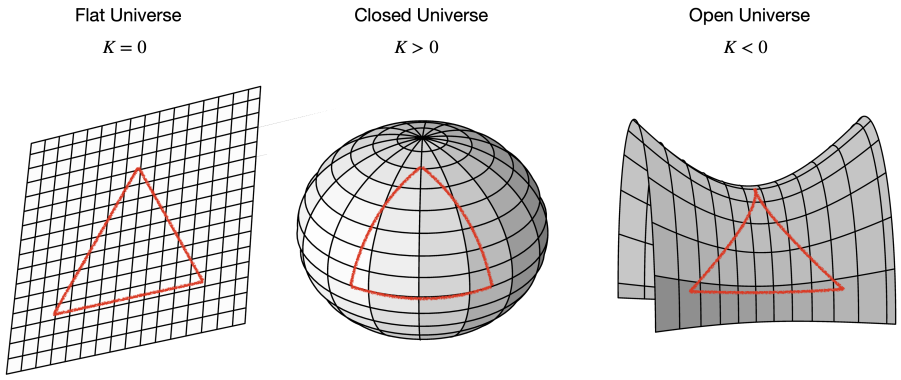

Figure 1.4: An illustration showing how a flat, closed and open universe can be related to the measurement of angles. Notice how initially parallel lines converge or diverge for closed and open universes respectively.

The Hubble parameter is defined as

$$H(t) = \frac{\dot{a}(t)}{a(t)}. \tag{1.36}$$

For convenience, the scale factor is generally normalised such that $a_0 = 1$ today.

Implementing the scale factor to encode the evolution of the Universe into GR, Friedmann, Lemaître, Robertson, and Walker developed the most general metric dubbed the FLRW metric using the assumption of homogeneity and isotropy [55–58],

$$ds^2 = -dt^2 + a(t)^2 \left(\frac{dr^2}{1 - Kr^2} + r^2 d\Omega \right). \tag{1.37}$$

Here $d\Omega = d\theta + \sin^2\theta d\phi$ for standard spherical coordinates; K is a purely geometric quantity known as spatial curvature at constant slices of time, it encodes the geometry of the Universe as shown by fig. 1.4. The coordinates of the metric (r, θ, ϕ) are comoving coordinates, which means that they remain at a constant with the expansion of the Universe. On the other hand, physical scales are re-scaled by the expansion so that $r^{(\text{physical})} = a(t)r$. On local scales, we can approximate $K \to 0$ and $a \to 1$; the FLRW metric then reduces to Minkowski.

An often useful time coordinate is conformal time, $d\tau = a^{-1}dt$, which re-scales the time coordinate such that the FRLW metric becomes,

$$ds^2 = a(\tau)^2 \left(-d\tau^2 + \frac{dr^2}{1 - Kr^2} + r^2 d\Omega \right). \tag{1.38}$$

Furthermore, conformal time can provide a more constructive evaluation of quantities in cosmology. For example, calculating redshift: if we assume a flat universe and consider a single event of light emission with a $\delta\tau$ duration, the scale factor remains a constant in conformal time. However, the physical time interval of emission δt_i and detection δt_f will be different due to the expansion of the Universe. The ratio of these intervals gives a relation between the wavelength of the emitted signal and the scale factor,

$$\frac{\lambda_i}{\lambda_f} = \frac{a(t_i)}{a(t_f)}. \tag{1.39}$$

Using this relation with our definition of redshift eq. (1.34), we find a useful way to describe the time of an astrophysical event,

$$1 + z = \frac{1}{a(t_i)}, \tag{1.40}$$

using the fact that detection is today at $a(t_f) = 1$.

Equipped with a metric that encodes the expansion of the Universe and curvature whilst assuming homogeneity and isotropy, we investigate the evolution of the Universe, particularly the behaviour of the scale factor. We start by determining the curvature terms from the metric eq. (1.37),

$$\begin{aligned} R_{00} &= -3\frac{\ddot{a}}{a} \\ R_{ij} &= a^2\delta_{ij}\left(\frac{\ddot{a}}{a} + 2\frac{\dot{a}^2}{a^2} + 2\frac{K}{a^2}\right) \\ R &= 6\left(\frac{\ddot{a}}{a} + \frac{\dot{a}^2}{a^2} + \frac{K}{a^2}\right) \end{aligned} \tag{1.41}$$

Next, we determine the form of our stress-energy tensor, which encodes the matter of the Universe. We assume that the content of the Universe behaves as a perfect fluid and the stress-energy tensor takes the form eq. (1.42):

$$T_{\mu\nu} = \begin{pmatrix} \rho & 0 & 0 & 0 \\ 0 & P & 0 & 0 \\ 0 & 0 & P & 0 \\ 0 & 0 & 0 & P \end{pmatrix} - \frac{\Lambda}{8\pi G}\begin{pmatrix} -1 & 0 & 0 & 0 \\ 0 & a & 0 & 0 \\ 0 & 0 & a & 0 \\ 0 & 0 & 0 & a \end{pmatrix}, \tag{1.42}$$

where ρ and P are the energy density and pressure of the cosmological matter, respectively, and we have included the cosmological constant. By solving the Einstein field equations with the FLRW metric and given stress-energy tensor, we arrive at the Friedmann equations, which describe the

evolution of the scale factor. The first Friedmann equation, obtained from the temporal component of the field equations, $G_{00} = \kappa T_{00}$, relates the expansion of the Universe with the energy content

$$\frac{\dot{a}^2}{a^2} \equiv H^2 = \frac{8\pi G}{3}\rho - \frac{K}{a^2} - \frac{\Lambda}{3}. \tag{1.43}$$

The second Friedmann equation relates the acceleration of the scale factor to the energy density and pressure. The spatial component, $G_{ii} = \kappa T_{ii}$, gives the second Friedmann equation

$$\frac{\ddot{a}}{a} + \frac{1}{2}\frac{\dot{a}^2}{a^2} + \frac{1}{2}\frac{K}{a^2} = -\frac{4\pi G}{2}P. \tag{1.44}$$

This can be used in combination with eq. (1.43) to provide the rate of change of the Hubble parameter,

$$\dot{H} = -4\pi G(\rho + P) + \frac{K}{a^2}. \tag{1.45}$$

It is also useful to independently understand the scale factor's behaviour relative to the Universe's content. Using the Friedmann equations, we find the second derivative of the scale factor, indicating the acceleration of the Universe at a given time,

$$\frac{\ddot{a}}{a} = -\frac{4\pi G}{3}(\rho + 3p) + \frac{\Lambda}{3}. \tag{1.46}$$

If we assume $(\rho + 3P) > 0$ it is clear that without the cosmological constant, the Universe does indeed decelerate and eventually collapse as initially thought. Therefore it is useful to define a deceleration parameter,

$$q \equiv -\frac{\ddot{a}a}{\dot{a}^2} = -\frac{\dot{H}}{H^2} - 1$$

In the Jordan frame, $f(R)$ theories will alter the Friedmann equations, as they modify the EFEs (eq. (1.20)) as discussed in section 1.2. This results in the modified Friedmann equations,

$$H^2 + \frac{K}{a^2} = \frac{FR - f}{6F} - H\frac{\dot{F}}{F} + \kappa\rho \tag{1.47}$$

$$\dot{H} - \frac{K}{a^2} = H\frac{\dot{F}}{2F} + \kappa\frac{\rho + P}{2F} - \frac{\ddot{F}}{2F} \tag{1.48}$$

The Friedmann equations determine the evolution of the scale factor given the total energy density and pressure of the Universe. These equations

allow us to study the past and future evolution of the Universe and make predictions about its fate. By measuring the Universe's expansion history through experiments, we can constrain the parameters in the Friedmann equations and infer the composition and history of the Universe.

To study different matter content of the universe, such as radiation or baryonic matter, and their effect on the Universe's history, we define the critical energy density,

$$\rho_c = \frac{3H^2}{8\pi G}. \tag{1.49}$$

This parameter describes the total energy density of a flat Universe (with $K = \Lambda = 0$). From this, we define the dimensionless density parameter,

$$\Omega_i = \frac{\rho_i}{\rho_c} \tag{1.50}$$

where the subscript i refers to the species contributing to the energy density e.g. radiation. Therefore if the sum of energy densities is unity, $\Omega_{tot} = 1$, the Universe remains flat. However, including curvature, an open universe results in $\Omega_{tot} > 1$ and a closed universe in $\Omega_{tot} < 1$.

Earlier, we discussed the assumption of a perfect fluid. Within the fluid approximation, it is assumed that the pressure within the fluid is assumed to be linearly related to the energy density,

$$P(t) = w\rho(t), \tag{1.51}$$

where w is the equation of state parameter. This assumption is based on the idea that the fluid can be considered a collection of particles interacting through collisions. Their macroscopic behaviour can be described through variables such as pressure, energy density, and velocity. The parameter w is a constant and allows us to characterise the content contained in the Universe.

Another important aspect implemented in GR, and discussed in section 1.1, is energy conservation, which is given by,

$$\nabla_\mu T^{\mu\nu} = 0. \tag{1.52}$$

For our perfect fluid described by eq. (1.42), we obtain an energy conservation equation known as the fluid equation,

$$\dot{\rho} + 3H(\rho + P) = 0. \tag{1.53}$$

Using the equation of state to remove P and assuming that w is a constant, we find that the energy density can be calculated from the scale factor

$$\rho = \rho_0 a^{-3\int(1+w)}. \tag{1.54}$$

Using (1.43) we find a solution for the scale factor,

$$a = \left(\frac{t}{t_0}\right)^{\frac{2}{3(1+w)}}, \tag{1.55}$$

where we have assumed that $a_0 = 1$ and w is a constant.

Components of the Universe

Next, we discuss the contents of the Universe. We begin by analysing the Universe with well-established content: non-relativistic matter and radiation. To study the behaviour of each species, we initially consider a universe that is only filled by the species in question. Non-relativistic matter exerts a negligible pressure ($w_m \approx 0$) and its energy density will decrease at a rate proportional to the expansion of the Universe, $\rho_m \propto a^{-3}$. Using eq. (1.55) we obtain that the Universe with only matter scales as $a \propto t^{2/3}$. On the other hand, radiation has an associated temperature and thus a non-zero pressure ($w_r = 1/3$). Its energy density also decreases at a rate of the expansion of the Universe, with an additional decrease as the wavelength is stretched leading to $\rho_r \propto a^{-4}$. Therefore a universe containing only radiation will scale as $a \propto t^{1/2}$.

With both radiation and matter present in the Universe, the expansion is no longer uniform as both species evolve at different rates so one will come to dominate the total energy density. Therefore, the Universe's expansion will be separated into two distinct epochs. In a hotter and more dense universe, a will be smaller such that ρ_r initially dominates the energy density, then as the Universe expands and cools with a larger a the energy density will become matter-dominated. We identify the transition between the two as matter-radiation equality. Next, we investigate the inclusion of spatial curvature ($K \neq 0$) in the evolution of the Universe. If we assume that the Universe will continue to expand the curvature will dominate over matter and radiation epochs due to the scaling of its energy density $\rho_k \propto a^{-2}$, where $\rho_k = Ka^{-2}$. If it is an open universe, then the spatial curvature will act as a source term

in the Friedmann equations, resulting in an indefinite expansion. However, if the spatial curvature is positive, such that it is a closed universe, then the spatial curvature acts against the expansion in the Friedman equations. This results in the Universe eventually beginning to contract, ending in the "Big Crunch" when eq. (1.43) vanishes and the Universe ends in a singular point. These two outcomes can be identified from eq. (1.45).

Finally, we consider the inclusion of a cosmological constant, which does not evolve in time by definition and has no dependence on the scale factor. Therefore if the cosmological constant is non-zero, it will at some point dominate over all other terms in the Friedman equation resulting in $H^2 \propto \Lambda = \text{const}$. Solving for the scale factor

$$a \propto e^{Ht}. \tag{1.56}$$

In this scenario, the Universe will begin to expand exponentially with Λ dominating over all other terms indefinitely, this is referred to as a de-Sitter universe.

With multiple different components, each potentially dominating the Friedmann equation, it is often helpful to break down the energy densities further, such that the eq. (1.43) becomes,

$$3H^2 = \rho_r + \rho_m + \rho_k + \rho_\Lambda, \tag{1.57}$$

where $\rho_\Lambda = \Lambda$. As discussed above, we also know the solution to each of these components in terms of the scale factor. Therefore we can rewrite this in a compact form,

$$H^2 = H_0[\Omega_{r,0}a^{-4} + \Omega_{m,0}a^{-3} + \Omega_{k,0}a^{-2} + \Omega_{\Lambda,0}], \tag{1.58}$$

where the subscript 0 indicates the measured value today. This equation illustrates how each term has the potential to dominate a specific epoch in the evolution of the Universe. Working with density parameters is often more convenient as they are bounded between 0 and 1 and naturally normalises the Hubble parameter to the Hubble constant. In addition, eq. (1.58) is helpful to bridge the gap between the theoretical and experimental side of cosmology as experimental cosmologists often work with redshift as a time coordinate, which can be easily implemented into eq. (1.58) using (1.34). This allows for the measurement of the Hubble parameter at different redshifts,

enabling reconstruction of the history of the Universe through the Hubble parameter and determination of its content.

Cosmological observations are currently experiencing a golden age of new and advanced technologies. These observations are revealing new features, motivating extensions and modifications to current theoretical paradigms. For instance, astrophysical measurements of galaxies and galaxy clusters have observed an intriguing feature: there seems to be the presence of an invisible mass halo surrounding them. This mysterious mass has been aptly named dark matter (DM), due to its non-existent interaction with the electromagnetic spectrum. An early method for measuring the fraction of dark matter utilises the rotation curves of galaxies: by plotting the speed of rotation relative to the centre of mass, and comparing it to the theoretical relation due to observed mass (standard baryonic matter such as stars and dust), a significant discrepancy is identified [59, 60]. This reveals that the Universe contains around $\Omega_M \approx 0.3$ non-relativistic matter, of which a small fraction $\Omega_b \approx 0.05$ is standard baryonic matter. Therefore, the Universe comprises of $\Omega_{DM} \approx 0.25$, some dark matter that does not interact with EM radiation. Moreover, DM not only accounts for the additional mass discrepancy within galaxy rotation curves, which multiple different observations have verified [61–63]. It also has been verified by simulations of galaxy clusters and structure formation, which rely on the current ratio of dark matter to baryonic matter, [64].

Type 1a supernovae (SN1a) provides a means to measure luminosity distance versus redshift, known as standard candles[9], allowing astronomers to map out the relation between the two. Starting with closer sources to accurately and precisely measure H_0, astronomers have slowly built up a catalogue of sources, calibrating standard candles to build a cosmic distance ladder of luminosity distances vs redshift. Just before the turn of the millen-

[9]Type 1a supernovae are the process of a white dwarf obtaining additional mass from a neighbouring star or gas cloud. This results in the dwarf star crossing the Chandrasekhar limit and exploding. This event produces a luminosity strongly related to the properties of the white dwarf. This relation allows the luminosity to be compared against the observed magnitude of the source allows us to determine the distance or redshift to the source. Therefore, sources such as SN1a provide a standardised measurement of distance related to observed luminosity, and have been 'standard candles' [65].

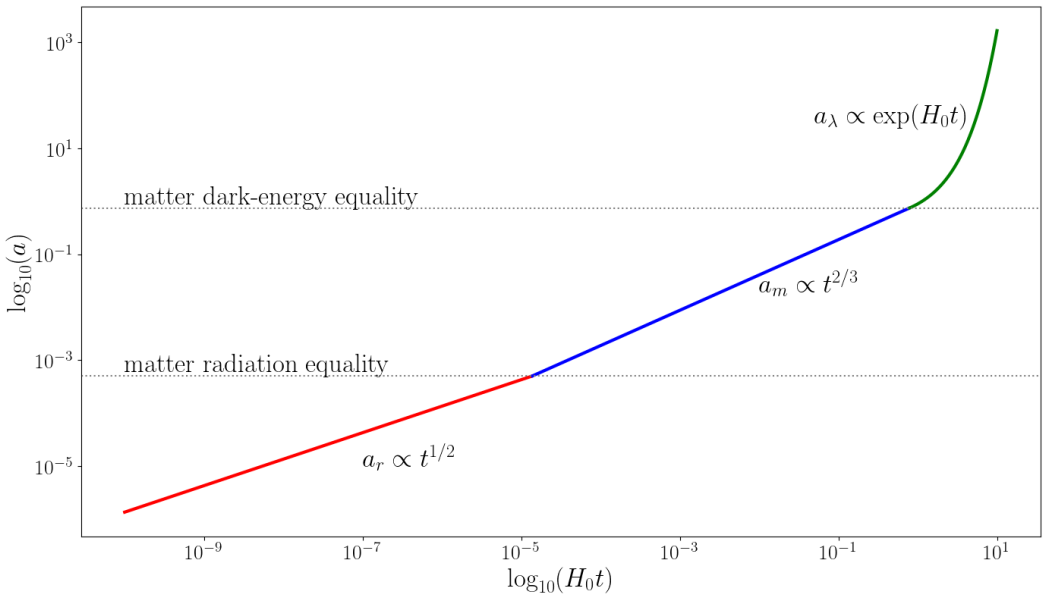

Figure 1.5: Each fluid will dominate the evolution of the Universe at different times depending on the relevant proportionality. The scale factor and time scale have been normalised relative to values measured today.

nia, two independent teams, [66, 67], mapped out the distance ladder from SN1ae. They discovered that the Universe was expanding at an accelerated rate, concluding that the energy density of the Universe was dominated by repulsive dark energy. This was confirmed and verified by different cosmological observations and led to the conclusion that the contents of the Universe are $\Omega_{M,0} \simeq 0.3$ and $\Omega_{\Lambda,0} \simeq 0.7$ [68].

Dark energy is estimated to make up approximately 70% of the current energy density of the Universe, with a corresponding equation of state parameter of $w_0 \approx -1$. Within the structure of eq. (1.58), a non-diluting cosmological constant is a good candidate that fits the observations well. If this is the case, the other Universe components will eventually be diluted away.

From current observations, assuming ΛCDM, the parameters of eq. (1.58) are [27, 68],

$$H_0 \approx 70 \text{kms}^{-1}\text{Mpc}^{-1}, \quad \Omega_{r,0} \approx 10^{-4}, \quad \Omega_{m,0} \approx 0.3, \quad \Omega_{k,0} \approx 0, \quad \Omega_{\Lambda,0} \approx 0.7. \tag{1.59}$$

Using these measured values, we can determine the evolution of the Universe using the scale factor as depicted in fig. 1.5.

The nature of dark energy and its non-zero value remain highly debated

and an active area of research. The current paradigm is ΛCDM, which includes a non-zero cosmological constant and non-relativistic (cold) dark matter. This model is the simplest model of the Universe, requiring six parameters to be fitted to current observations. As discussed, including a cosmological constant from the foundation of GR is well established; however, the physical interpretation remains to be answered. Quantum field theory states a uniform field throughout the Universe with a non-zero minimum energy. This is calculated to give a uniform energy density $\rho_\Lambda^{(the)}$. We assume the minimum vacuum energy density is of the order of the cutoff scale of the theory, the Planck mass. Compared with the observed cosmological constant energy density, $\rho_\Lambda^{(obs)}$, we find a discrepancy $\rho_\Lambda^{(the)} \approx 10^{120}\rho_\Lambda^{(obs)}$ [69]. Although the number is quoted due to be provocative, a more realistic approach is to use the energy scale of known particles. Setting the energy scale to that of the strong force used in particle physics or the energy scale of quantum chromodynamics, the discrepancy reduces to $O(10^{60})$ [70]. This remains one of the biggest discrepancies between theorised and observed parameters in physics.

There are many different candidates to explain dark energy, such as modified gravity, which provides a dynamical element to the cosmological constant. For instance, we can investigate how a quintessence model outlined in section 1.2, can justify the measured value. Assuming the presence of a homogeneous scalar field in an FLRW universe, the energy density and pressure calculated from eq. (1.18) are given by,

$$\rho = \frac{1}{2}\dot{\phi}^2 + Ve^{-2\sqrt{\frac{2}{3}}\frac{\phi}{M_{\rm Pl}}}, \quad P = \frac{1}{2}\dot{\phi}^2 - Ve^{-2\sqrt{\frac{2}{3}}\frac{\phi}{M_{\rm Pl}}}. \tag{1.60}$$

with the corresponding Klein-Gordon equation,

$$\ddot{\phi} + 3H\dot{\phi} + V_\phi = 0.$$

The acceleration equation eq. (1.46) becomes,

$$\frac{\ddot{a}}{a} = -\frac{4\pi G}{3}(\dot{\phi}^2 - e^{-2\sqrt{\frac{2}{3}}\frac{\phi}{M_{\rm Pl}}}V). \tag{1.61}$$

Provided the potential is always positive, we can expect the field to settle in a minimum or slowly roll down the exponential tail due to the damping effect from the expansion of the Universe. This can be seen from the KG equation, where the $3H\dot{\phi}$ will act as a damping term. Therefore, the second term will

dominate the acceleration equation, accelerating expansion. The behaviour and value of the vacuum energy density are given by the details of effective potential energy, which can match observed values depending on the given field values. The dynamical interpretation of dark energy from the potential is known as quintessence and has many interesting features [71, 48]. While this brief quintessence illustration was motivated by modified gravity, many different models have been investigated with varying potentials to give rise to DE.

The hot big bang

Given the framework of cosmology discussed, we can reconstruct details of the early universe. As the Universe expanded and the distance between particles increased, the temperature decreased due to the redshifting of photons, resulting in a cooling effect. Consequently, the early universe is characterised by a much hotter and denser region of space than today. Extrapolating, we conclude that matter would have existed in a relativistic state, contributing to the radiation density. In this regime, photons and neutrinos would have been trapped via interactions in the thermal plasma bath of relativistic matter. This initial radiation-dominated setup is called the Hot Big Bang (HBB).

Equilibrium is an essential aspect in the dynamics of the HBB. If the particle interacts at a rate greater than the expansion of the Universe, then the particle remains in equilibrium with the thermal bath. As the expansion of the Universe increases, the interaction rate drops below the expansion. Therefore, the relativistic particles will decouple from the thermal bath and essentially be frozen. With further cooling, the photons will eventually decouple from the plasma. At this point, the Universe becomes illuminated, as the photons free-streaming away and are observed today as a cosmic microwave background (CMB). Thus the CMB encodes information about recombination and the dynamics of the early universe [72–76].

Moreover, we can also infer details about the expansion of the Universe, as these photons have been free-streaming to us since decoupling. Therefore it also includes the nature of expansion through the Universe's history. The CMB was first measured in a fortunate accident by Arno Penzias and

Robert Wilson [77] using a radio antenna first mistaken as noise from nearby pigeons. This measurement was later confirmed and identified as the CMB, a background of primordial photons. The Planck team undertook the latest measurement of the CMB [68].

The CMB is a crucial tool for understanding the early universe, providing information about its isotropy. Small perturbations in the gravitational potential felt by the photons at decoupling produce very small temperature anisotropies, denoted δT. According to the latest measurements from Planck, the level of anisotropies is constrained to

$$|\frac{\delta T}{\bar{T}}| \lesssim 10^{-5}, \tag{1.62}$$

where the bar represents the average temperature of the CMB, $\bar{T} = 2.728 \pm 0.004$. These findings support the assumption that the Universe is homogeneous and isotropic on large scales.

These anisotropies are decomposed into spherical harmonics, Y_{lm}, with the amplitude, a_{lm}, parametrised by the positive integers l and m. This allows us to determine the corresponding angular power spectrum of temperature fluctuations, C_l^{TT},

$$\frac{\delta T}{T} = \sum_{l,m} a_{lm} Y_{lm}(\theta, \varphi), \quad C_l^{TT} = \langle |a_{lm}|^2 \rangle. \tag{1.63}$$

These small fluctuations in temperature identify the gravitational fluctuations in the early universe. Therefore they encode the initial conditions that eventually give rise to inhomogeneities, the seeds of large-scale structures we observe at the local scale. The shape of the power spectrum will depend on the details of the expansion of the Universe, leaving signatures about the Universe's history and allowing us to constrain different cosmological models. A model must be fitted to the data to describe the Universe's history accurately. In the case of ΛCDM, the best-fit parameters are listed in eq. (1.59), and the resulting normalised angular power power spectrum, $\mathcal{D}_l^{TT} = l(l+1)\bar{T}^2 \mathcal{C}_l^{TT}/2\pi$, is shown in fig. 1.6.

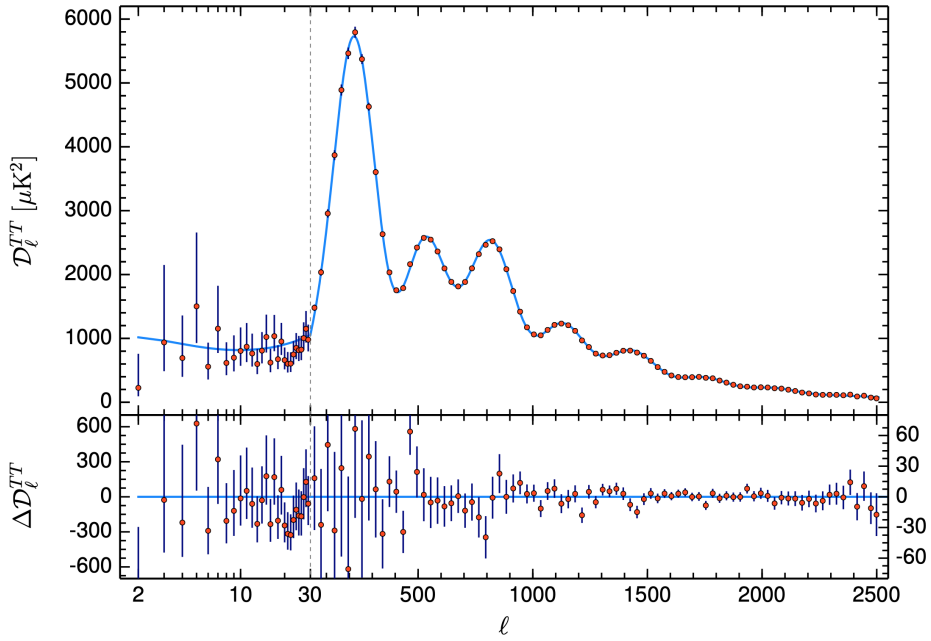

Figure 1.6: CMB angular power spectrum of the temperature-temperature (TT) correlations, taken from Planck 18's mission [68] and the blue curve represents the best-fit data of ΛCDM. The panel below identifies the residual of the fitting between the two.

1.3.1 Cosmological perturbations

Therefore if we are interested in the small spatial fluctuations of the temperature, we analyse the small spatial variation of gravity. Due to the nature of gravity, small fluctuations will demonstrate unstable growth. These fluctuations are studied in the theory of linearised gravitational perturbations in a non-static universe. This theory of cosmology has been successful, being used to predict the CMB fluctuations and the growth of structures, and used to detect gravitational waves. The necessary cosmological perturbations depend on the context and epoch or model. Thus, we briefly outline the theory of cosmological perturbations in a generic FLRW universe, detailed in [73, 74, 76, 78, 79], and analyse the perturbations for different epochs in the relevant chapters of the thesis.

We assume, as we have discussed, that the Universe is homogeneous and isotropic at large scales, we define this idea of large scales to be the background. However, we know the Universe deviates from the perfect and ideal background model discussed above. Therefore a secondary small part is added to model the deviations from the background allowing us to rewrite

quantities decoupled into background and perturbations. For instance, the metric now becomes,

$$g_{\mu\nu} = \bar{g}_{\mu\nu}(t) + \delta g_{\mu\nu}(t, \mathbf{x}) \tag{1.64}$$

where we identify the background quantity with a bar and the perturbation by δ, and we assume $\bar{g}_{\mu\mu} \gg \delta g_{\mu\mu}$. We have discussed how the metric affects matter and matter affects the metric. Thereby logically, we know that our perturbation should lead to perturbations in other quantities that are coupled to gravity e.g. matter.

A tensor can in general be decomposed into scalar, vector and tensorial parts. A FLRW metric can be written as,

$$g_{\mu\nu} = \begin{pmatrix} -(1+2\Phi) & a(B_i) \\ a(B_i) & a^2\left[(\gamma_{ij} + E_{ij}\right] \end{pmatrix} \tag{1.65}$$

Here γ_{ij} represents a general background spatial metric on constant time hypersurfaces (in a flat space $\gamma_{ij} = \delta_{ij}$).

The decomposition means we split our vectors into the gradient of the scalar and a divergence-free vector,

$$B_i = \partial_i B + S_i$$

, where B is the scalar quantity and $\partial^i S_i = 0$. The same can then be done with the tensor modes,

$$E_{ij} = -2\Psi\gamma_{ij} + 2\partial_i\partial_j E + \partial_j F_i + h_{ij}$$

. The first two terms contain the scalar quantities of tensor, Ψ and E. The first term encodes the trace of of the spatial perturbations, leaving the remaining terms traceless. The remaining vector F_i and h_{ij} are divergence-free and correspond to transverse perturbations.

Therefore our resulting metric to linear order becomes,

$$g_{\mu\nu} = \begin{pmatrix} 1+2\Phi & a(B_{,i} + S_i) \\ a(B_{,i} + S_i) & a^2\left[(1-2\Psi)\gamma_{ij} + 2E_{,ij} + 2F_{(i,j)} + h_{ij}\right] \end{pmatrix} \tag{1.66}$$

We can see that the metric has been broken down into 4 scalar perturbations, Φ, B, Ψ, E; 2 vector divergence-free perturbations, S_i, F_i, which then corresponding to two components each; and a single traceless transverse tensorial part, h_{ij}, which contains two independent components. We now see that

we have 10 independent metric quantities as expected from a symmetric tensor in 4 dimensions. However, we note that after choosing a gauge, we are left we remove two scalar and two vector degrees of freedom, while the tensors remain untouched, as they are already gauge-invariant. Therefore, after gauge fixing, we have a total of 6 degrees of freedom.

Depending on the regime and problem in question, only certain perturbations must be considered. For instance: in section 3.4, we focus on the scalar perturbations that give rise to the CMB, and in section 4.2.4, we analyse how each mode of the perturbations are affected through a bouncing universe.

Scalar modes

For this thesis, we will discuss scalar perturbations in the early universe, focusing on inflation and their impact on detectable cosmological observables arising from the power spectrum of the CMB. As stated before, perturbing gravity via the metric coincides with the perturbation of matter fields. However, there is some ambiguity about the interaction between the perturbed and non-perturbed quantities. Therefore we make a gauge choice to work in the Newtonian/Longitudinal gauge for the scalar perturbations which sets $B = E = 0$. Our scalar perturbed line element now simplifies to,

$$ds^2 = -(1+2\Phi)dt^2 + a^2(1-2\Psi)\delta_{ij}dx^i dx^j \tag{1.67}$$

We now consider the perturbed EFEs of the form eq. (1.11), $\delta G^\mu_\nu = 8\pi G \delta T^\mu_\nu$:

$$\delta G^0_0 = 2\nabla^2\Psi - 6H\left(\dot{\Psi} + H\Phi\right) = 8\pi G\delta\rho \tag{1.68}$$

$$\delta G^0_i = -2\left(\dot{\Psi} + H\Phi\right)_i = 8\pi G\delta q_i \tag{1.69}$$

$$\delta G^i_i = \left(\dot{\Psi} + H\Phi\right)_0 + 3H\left(\dot{\Psi} + H\Phi\right) + \dot{H}\Phi + \nabla^2(\Phi - \Psi) = 8\pi G\delta P \tag{1.70}$$

$$\delta G^i_{j\neq i} = (\Psi - \Phi) = 8\pi G\delta\Pi. \tag{1.71}$$

Where δq_i is the scalar part of the three momenta, it can be best understood by its coordinate transform $\delta q_i \to \delta q_i + (\rho + P)\delta t$, and $\delta\Pi$ is the anisotropic stress which encodes the off-diagonal terms. In this thesis, we will consider the matter content as perfect fluids on large scales with negligible anisotropic

stress. This allows us to make the relation

$$\Psi = \Phi. \tag{1.72}$$

We will expand the perturbations in Fourier space,

$$\Psi(\mathbf{x}, t) = \int \frac{d^3\mathbf{k}}{(2\pi)^{3/2}} e^{i\mathbf{k}\cdot\mathbf{x}} \Psi_{\mathbf{k}}(t). \tag{1.73}$$

We will drop the subscript $\mathbf{k}$ to shorten the expressions and utilise the eigenvectors of the spatial Laplacian, $\nabla^2\Psi = -k^2\Psi$. Here k is the comoving wavenumber of the perturbations, assuming flat space, related to the physical wavelength of the perturbation, $\lambda = 2\pi a/k$.

Observations are made from gauge-invariant properties. There are two commonly used curvature perturbations, we will use the comoving curvature perturbation,

$$\mathcal{R} \equiv \Psi - \frac{H}{\rho + P}\delta q. \tag{1.74}$$

We also will work with isocurvature modes or also known as entropy modes,

$$\mathcal{S} = H\left(\frac{\delta P}{\dot{P}} - \frac{\delta\rho}{\dot{\rho}}\right) \tag{1.75}$$

As we will discuss later, these identify the perturbations arising from more than a single degree of freedom.

From our curvature perturbations, we are able to define the primordial power spectrum of scalar fluctuations at any given scale,

$$\mathcal{P}_{\mathcal{R}} = \frac{k^3}{2\pi^2}|\mathcal{R}|^2. \tag{1.76}$$

We also define the corresponding isocurvature power spectrum,

$$\mathcal{P}_{\mathcal{S}} = \frac{k^3}{2\pi^2}|\mathcal{S}|^2. \tag{1.77}$$

The primordial power spectrum is then used as an experimental tool that allows us to constrain early universe physics and, thus, different models of inflation. A small range of wavenumbers corresponds to the CMB measurements. The observed primordial power spectrum can be classified by its small-scale dependence at the horizon crossing ($k = aH$). This is known as the spectral index or tilt,

$$n_s - 1 \equiv \left.\frac{d\ln\mathcal{P}_{\mathcal{R}}}{dk}\right|_{k=aH}. \tag{1.78}$$

If we had $n_s = 1$ this would indicate a flat spectrum at the horizon crossing telling us there is no scale dependence at that point. However, we currently measure from the CMB $n_s \simeq 0.965$, a very slight drop in power around the horizon crossing. We can then further examine the running, α_s, and the running, β_s, which indicate further deviations from a flat or even constant power spectrum. Given these CMB parameters, the power spectrum can be approximated to

$$\mathcal{P}_{\mathcal{R}} \propto \left(\frac{k}{k_0}\right)^{n_s - 1 + \frac{1}{2}\alpha_s \ln(k/k_0) + \frac{1}{6}\beta_s (\ln(k/k_0))^2}, \tag{1.79}$$

where both α_s and β_s are evaluated at the reference point k_0.

Vector modes

Isolating the vector perturbations from eq. (1.66), the line element is,

$$ds^2 = -dt^2 + 2aS_i dt dx^i + a^2 \left[\gamma_{ij} + 2F_{(i,j)}\right] dx^i dx^j. \tag{1.80}$$

The two vector perturbations are divergence-free, $\partial^i S_i = \partial^i F_i = 0$. A gauge invariant quantity can be constructed from the vector perturbations $\sigma_i = \dot{F}_i + S_i/a$ which is also related to the divergence-free 3 momentum,

$$16\pi G \delta q_i = -\nabla^2 \sigma_i \tag{1.81}$$

However, δq_i obeys the momentum conservation,

$$\delta \dot{q}_i + 3H\delta q_i = -\nabla^2 \delta \Pi_i. \tag{1.82}$$

Therefore it is clear that if we assume anisotropic stress is negligible, the 3-momentum will be redshift away with the expansion of the Universe.

Tensor modes

The remaining tensor perturbations can be written in the line element as,

$$ds^2 = -dt^2 + a^2 \left[\gamma_{ij} + h_{ij}\right] dx^i dx^j. \tag{1.83}$$

The spatial tensor perturbation, h_{ij}, is already symmetric and gauge invariant and therefore is a real physical quantity, they are more commonly known as gravitational waves (GW). Moreover, the tensor perturbation is transverse, $\partial_i h_{ij} = 0$, and traceless, $h_{ii} = 0$[10].

[10]Due to the set-up of our metric, this result is natural. A corresponding calculation can be computed to find the same outcome starting from a Minkowski background plus a gravitational wave source, $g_{\mu\nu} = \eta_{\mu\nu} + h_{\mu\nu}$

We can then find the solution to the linearised EFEs to determine an equation governing the tensor perturbation:

$$\Box h_{ij} = -16\pi G\delta\bar{\Pi}_{ij}, \tag{1.84}$$

where $\bar{\Pi}_{ij}$ is the transverse traceless part of the anisotropic stress, which we assume to vanish. Therefore the perturbations result in a wave equation as expected

$$\Box h_{ij} = 0 \quad \Rightarrow \quad h_{ij} = A_{ij}e^{ik_m x^m}, \tag{1.85}$$

where A_{ij} is a constant, symmetric, rank-2 tensor encoding the polarisation of the wave, and k_l is the momentum of the gravitational wave. Due to our tensor being transverse and traceless this then implies the conditions respectively:

$$k_m A^{mi} = 0, \quad A^m_m = 0. \tag{1.86}$$

Therefore if a wave travels in the z-direction ($k^m = (0, 0, k)$) our conditions set

$$A_{ij} = \begin{pmatrix} A_{xx} & A_{xy} & 0 \\ A_{xy} & -A_{xx} & 0 \\ 0 & 0 & 0 \end{pmatrix} \tag{1.87}$$

along with $A_{xy} = A_{yx}$ and $A_{xx} = -A_{yy}$. From this we can then see that there are two obvious polarisations of gravitational waves: $A_{xy} = 0$ which leaves the wave to displace in the vertical and horizontal lines, labelled as $+$ polarisation. The other polarisation, set by $A_{xx} = 0$, stretches and squishes along diagonal lines denoted as $\times$ polarisation. Therefore the tensor perturbation is often written as

$$h_{ij} = h_+ \begin{pmatrix} 1 & 0 & 0 \\ 0 & -1 & 0 \\ 0 & 0 & 0 \end{pmatrix} + h_\times \begin{pmatrix} 0 & 1 & 0 \\ 1 & 0 & 0 \\ 0 & 0 & 0 \end{pmatrix} \tag{1.88}$$

where $h_{+,\times}$ are the mode functions of the perturbation in the given polarisation. The tensorial power spectrum can be calculated from eq. (1.85). However, it is often more useful to rewrite the equations of motion for the tensor perturbations by defining a new variable, $v = ah$, and rewriting eq. (1.85) as,

$$v'' + (k^2 - \frac{a''}{a})v = 0 \tag{1.89}$$

where the prime donates conformal time $d\tau = a^{-1}dt$. This equation is often much easier to solve in terms in the context of inflation due to the change of time coordinate. The primordial tensor power spectrum is then computed in a similar way to the scalar,

$$\mathcal{P}_{\mathcal{T}} = \frac{4k^3}{\pi^2}|h|^2 = \frac{4k^3}{\pi^2}\left|\frac{v}{a}\right|^2 . \tag{1.90}$$

The problem with tensor fluctuations is that they are currently still undetectable given CMB experiments. However, we are able to determine the magnitude of the perturbations through the scalar-to-tensor ratio, r, a cosmological observable parameter at the horizon crossing,

$$r \equiv \frac{\mathcal{P}_{\mathcal{T}}}{\mathcal{P}_{\mathcal{R}}}. \tag{1.91}$$

The latest CMB data have constrained this to $r \lesssim 0.035$ [80] at the horizon crossing. We will see later, during examples of inflation in section 4.2.3, measuring the amplitude of a gravitational wave background is vital to our understanding of inflation, as it sets the energy scale of inflation.

2 | Gravitational Waves as Standard Sirens

Everything reviewed thus far describes how the Universe is evolving: Is it expanding or contracting, accelerating or decelerating? As we have discussed, this depends on the Universe's contents. Thus we make approximations, modelling the contents as different fluids with specific properties. In section 1.3, we have briefly referred to using cosmological observations to refine or modify cosmological paradigms. However, recently a plethora of modified gravity models have emerged, primarily motivated by the unknown nature of the dark sector [26, 28, 37, 38, 48] and the particular mechanics of inflation [42, 74, 81]. Therefore cosmological observations are a valuable tool to constrain the parameters of new models and sometimes dismiss them.

In this thesis, we will focus on observations in two epochs: the late universe, limited to only a few redshifts, measuring properties of large-scale structures, and early universe measurements, specifically the CMB, an imprint of inflation and the Big Bang. Utilising independent observations from both the early and late universe, we can begin to constrain cosmological parameters while minimising any bias. However, these two measurements are not in total agreement. With the increased precision of local measurements from Cepheids, [82] identified a 4.4σ discrepancy in H_0 compared to the late universe measurements of Planck, [68]. This discrepancy is reviewed with additional measurements in [83, 84] identifying a $4.4 - 6.3\ \sigma$ difference in the measurement of H_0 between the CMB and local measurements.

As we have discussed, the measurements of the CMB heavily rely on the model being used. The current best-fitting model with the CMB is ΛCDM and an inflationary model. Using measurements from the CMB, we can indirectly infer the best-fit value of H_0 using measurements that rely on

the assumption of ΛCDM. The commonly cited figure for early universe measurement of H_0 is taken from [68] Planck 2018 + CMB lensing finding $H0 = 67.36 \pm 0.54 \text{kms}^{-1}\text{Mpc}^{-1}$ at 68% confidence level. It is important to note that other early universe measurements, such as baryon oscillation spectroscopic surveys, also agree with CMB H_0 measurements [85]. In contrast, H_0 is directly measured from our local (late) universe, using a distance-redshift relation. An example is using SN1a to measure luminosity distances using a calibrated cosmic distance ladder. For instance, the S$H0$ES Team, which uses a distance ladder calibrated with techniques requiring Cepheids, measured $H_0 = 73.2 \pm 1.3 \text{kms}^{-1}\text{Mpc}^{-1}$ at 68% confidence level [86], this result is confirmed with other local sources[1].

This tension can result from systematic errors in local or early universe measurements, or more interestingly, these tensions highlight the breakdown of the ΛCDM model. This motivates research into new, more exotic models of the Universe's expansion in the latter's case.

Gravitational waves

To address the cosmological tensions that have arisen in the last decade, GWs offer a promising aid to resolve the observed tensions. GWs are emitted by massive objects that undergo acceleration, and lack spherical symmetry, such as a binary system. This is analogous to the electromagnetic radiation which is sourced from an accelerating charged object. GWs are a prediction of GR[2], representing a fundamental aspect of the Universe and offering new insight into cosmology. They are a relatively new and unique cosmological probe because they are weakly interacting with matter, making them difficult to detect. Nonetheless, the first directly detected GW was measured in 2016 by the Laser interferometer gravitational-wave observatory (LIGO) and Virgo collaboration using ground-based detectors [20].

GW detectors utilise laser interferometers to measure the small change in displacement as GWs interact with the equipment. Detectable GWs, from

[1] All local measurements are based on a cosmic distance ladder, but the calibration and events differ to reduce any bias. Some of the commonly used sources are Cepheids [87, 86] and the evolution of red giants [88].

[2] A derivation of the GWs arising from a perturbative analysis of GR can be found in section 1.3.1.

ground-based detectors, can be generated through the merger of binary black holes (BHs), binary neutron stars (NSs), or a BH-NS system. The characteristics of the merger can be determined by analysing the evolution of the GW signal. Unlike electromagnetic radiation, GWs weakly interact with matter, enabling the accurate determination of redshift distance with minimal interference. The confirmation of this observation provides a window to study the Universe's extreme events and fundamental cosmological concepts.

However, GWs are insufficient to provide a luminosity-redshift distance alone; specific mergers can also include an electromagnetic (EM) counterpart. The first observation of a binary neutron star merger (GW170817) with a gamma-ray burst counterpart has led to identifying various interesting phenomena about the Universe. The speed of GWs, represented by v_{GW}, is estimated to be constrained between [89]

$$-3 \times 10^{-15} \leq \frac{v_{GW} - c}{c} \leq 7 \times 10^{-16}.$$

This simple result identifies the speed of GWs as the speed of light. Therefore, the result strongly constrains cosmological models, with many dismissed [90, 52].

GWs can be considered a new independent standard candle, discussed in section 1.3. Although, due to the displacement nature of GW rather than an optical observation, it is referred to as a "standard siren". An accurate and comical term coined by [91] – allowing for an intuitive picture of cosmological speakers calling out. Moreover, the GWs can probe larger redshifts than their optical counterparts. Probing larger redshifts means the measurement becomes more model dependent, with dark energy becoming a significant factor. These standard sirens can serve as a complementary observation technique to the cosmic microwave background and supernoave, aiding in the identification of systematic errors in local measurements and the accuracy of calculating H_0, constraining cosmological models.

Furthermore, GWs can be used as a new independent measurement to constrain late universe cosmological models that propose explanations for the dark sector of the Universe. As discussed in section 1.2 and section 1.3, possible alternatives to the contested ΛCDM model lie in adding new degrees of freedom, either in the gravitational sector resulting in modified

gravity models or generalising the cosmological constant to a dynamical DE by introducing a scalar field controlled by its potential. Utilising more generalised models allows for not only an explanation of the nature of DE and DM, and if there is any non-minimal interaction between them, but also the possibility of addressing the cosmological tensions. Modifications to the gravitational sector or including a dynamical DE content will produce specific and measurable features in astrophysical and cosmological measurements. Therefore, these alternative models have a limited parameter space for modifications that are potentially testable with GWs.

2.1 Forecast of gravitational wave data

Current first GW detectors, advanced Virgo [92] and advanced LIGO [93] collaborations, are ground-based detectors: LIGO collaboration currently consists of two detectors in the United States, both constructed with a Michelson interferometer with 4km arms and oriented in the same direction, to confirm detection. Virgo is also a Michelson interferometer based in Italy, with an arm length of 3km. Together LIGO and Virgo can survey the entire sky for GWs and have agreed to jointly analyse data to ensure confirmation of detection and catalogue of data. Since the first detection, both observatories have been upgraded to enhance sensitivity. Along with the upgrade, another GW observatory in Japan, KAGRA, came online in 2020 [94], totalling four independent detectors.

However, these first and second-generation GW detectors are limited in their sensitivity and precision, and detectable GWs with EM counterparts are rare, with only a single detection so far. Nonetheless, the single measurement of the speed of gravitational waves already has ruled out many modified gravity models which predicted the speed of gravity out of the allowed bounds [90, 95, 96]. The next generation of GW detectors is designed to become more sensitive and precise and detect over a larger range of frequencies. In this chapter, we simulate a range of mergers with an EM counterpart, and create mock data from the detection of proposed

third-generation observatories, the ground-based Einstein Telescope (ET) [97] and the space-based Laser Interferometer Space Antenna (LISA) [98]. This allows us to forecast the parameter space for modified gravity models.

The ET builds upon the success of second-generation detectors. The interferometer will be built in an underground structure to help eliminate noise. It will consist of three 10km arms in an equilateral triangle formation with two interferometers at each vertex. The two interferometers will be set up to measure different frequencies to ensure a larger range of detectable frequencies. The ET is proposed to be operational in 2034. LISA is based on a similar design to ET, with three spacecraft in a formation of an equilateral triangle, with each spacecraft armed with an interferometer and detector. The arms of the interferometer will be 2.5×10^9m long to maximise sensitivity and allow for a lower frequency range. LISA will orbit the sun, trailing Earth's orbit by $20°$. Due to the setup, it is estimated LISA will be able to detect GW beyond $z = 20$. LISA is expected to launch sometime in the 2030s.

The script used to create the mock data can be found in GWSS [99], standing for gravitational wave standard sirens. The details of the process are described in more detail in the following sections, but it follows the general procedure:

- Choose background cosmology:

Simulate a range of merging events at given redshifts and the corresponding Hubble parameter, luminosity distance, and time taken from event to observation based on background cosmology.

- Specify details about merger:

Assign details of each merger, e.g. orientation, mass, and position in the sky. Redistribute the redshift of the mergers based on the probability distribution of observed events.

- Simulate observed error:

Compute the signal-to-noise ratio and implement the error associated with the observatory used. Remove any mergers with errors or signal-to-noise ratios that are too high for confirmed mergers.

- Artificially spread mergers from background:

Redistribute the luminosity distance of the merges based on a Gaussian distribution around the background cosmology to artificially create ran-

domness, utilising the calculated errors as the standard deviation.

2.1.1 Cosmology of gravitational waves

To simulate gravitational waves data from future probes of black hole mergers, we require some cosmological quantities: the redshift of the merger, z, the value of the Hubble rate at merger, H, its comoving and luminosity distance, d_c and d_l respectively, and the time difference of the merger to measurement, t. For this purpose, we resorted to the public Einstein-Boltzmann code `CLASS` code [100, 101], which is adapted to accommodate general models of interacting dark energy[3].

Therefore the required cosmological parameters were generated and extracted from the code's output, from which different models can be chosen, given an accurate sample of the data. This work opted to simulate the data with the fiducial model ΛCDM, according to the best-fit cosmological parameters from Planck likelihood [68] with:

$$H_0 = 67.32\,\mathrm{km\,s^{-1}\,Mpc^{-1}},\ \Omega_b h^2 = 0.022383,\ \Omega_c h^2 = 0.12011,$$

where $h = H_0/100$ and $\Omega_b,\ \Omega_c$ is the density of baryons and cold dark matter, respectively. This results in the derived quantity $\Omega_m^0 = \Omega_b + \Omega_c = 0.3144$. This will allow us to assess how the simulated GW data compares with current observational data such as SNIa, BAO, and CC. However, it is important to note that using Planck likelihood, which assumes ΛCDM, will create a strong bias towards ΛCDM cosmology. Thus we interpret the produced GW mock data as a prediction of measurements in a ΛCDM Universe.

From here, it is also possible to test the constraining power of the forecast sample on the coupling parameter of the interacting dark energy (IDE) models, β, as discussed in section 1.2. Since the observational measurements are based on frequency evolution, we opt to convert all of the output parameters from `CLASS` into units of seconds.

[3]The `CLASS` code is just one of many Einstein-Boltzmann solvers. The code numerically solves the background and linear perturbations of the EFEs and the interaction between the species identified by Boltzmann's equations. After solving the equations numerically, the code outputs the predicted measured quantities, such as background quantities like H_0 and the CMB anisotropy spectra. For this thesis, we are only concerned with the background quantities for a ΛCDM model.

2.1.2 Probability distribution

The Einstein telescope is designed to probe a range of frequencies, f, similar to that of LIGO, detecting merger events of nearby compact objects such as binary neutron stars (BNS), in the range $[1,2][1,2]\mathrm{M}_{\odot}$, and black hole neutron star binaries (BHNS), including $[3,10][1,2]\mathrm{M}_{\odot}$, respectively, with the $[\cdot,\cdot]$ notation indicating the respective range of masses considered, according to a uniform distribution. Advanced LIGO claims a measured BHNS to BNS merger events ratio of ~ 0.03 [102]. The redshift probability distribution of these events is proportional to

$$P \propto \frac{4\pi d_c(z) R(z)}{(1+z)H(z)}, \tag{2.1}$$

where d_c and H are the comoving distance and the Hubble parameter, respectively, both are taken at various redshifts determined by CLASS. $R(z)$ stands for the merger rate, which, at a linear approximation, is [103]

$$R = \begin{cases} 1+2z & \text{if } z < 1 \\ \frac{3}{4}(5-z) & \text{if } 1 \leq z < 5 \\ 0 & \text{otherwise.} \end{cases} \tag{2.2}$$

On the other hand, LISA will target lower frequencies when compared with other proposed third-generation GW detectors. This implies that LISA will be sensitive to events from larger mass binary systems since $f \propto M^{-1}$. Therefore we will focus on simulating the detection of events from extreme mass ratio inspiral (EMRI), $[1-30][10^4-10^8]\mathrm{M}_{\odot}$ [104] and binary massive black holes (BMBH), $[10^4-10^8][10^4-10^8]\mathrm{M}_{\odot}$ [105]. We estimate the proportion of BMBH to EMRI events according to the mission proposal [106], which consists of a $2:1$ ratio.

While the individual masses of the objects are not directly accessible, LISA is sensitive to the chirp mass, a collective mass quantity related to the frequency evolution of the signal emitted before the merger, during the inspiral phase of the binary [107], defined as

$$M_c = (1+z)\left(\frac{(m_1\, m_2)^3}{m_1+m_2}\right)^{1/5}, \tag{2.3}$$

where $(1+z)$ is a conversion factor from the physical to the observational chirp mass and m_1 and m_2 are the two masses of the binary.

Although LISA will also be able to probe mergers of binary intermediate-mass black holes, IMBH, and binary compact objects, we have opted to discard these from the simulations. This is due to no definitive observational proof of IMBH, and expected events from binary compact objects will only be observed at redshifts $z \approx 3$ [108]. These events will be insignificant since we are interested in the higher range of redshifts for our cosmology.

Considering events involving BMBH only, the redshift probability distributions are based on the histogram for the mission[4] of L6A2M5N2 [105] and shown in fig. 2.1. As there is no widely accepted model for the formation of BMBH, we consider three separate models: The light seed model (pop III) describes a formation of BMBH from the remnants of population III stars around $z = 15 - 20$; heavy seed models represent an already formed black hole of 10^5 $M_\odot$ at $z = 15 - 20$. Heavy seed models are further split, into delay or no-delay models, which describe if their is a delay in the binary forming since the formation of the black hole. More details on the model can be found in Refs. [109]. This allows us to simulate any number of events over a continuous distribution in the range $0 < z \lesssim 10$ and interpolate the remainder of our cosmological parameters, again to allow us to simulate any number of events.

2.1.3 Simulation of measurements and errors

To simulate the errors associated with GWs we follow the methodology of [110–112]. Inferometers are sensitive to the strain $h(t)$ from a GW event, which in the transverse-traceless gauge is described as

$$h(t) = F_\times(\theta_0, \phi_0, \psi)h_\times(t) + F_+(\theta_0, \phi_0, \psi)h_+(t), \tag{2.4}$$

where θ_0 and ϕ_0 define the initial location of the event relative to the detector in polar coordinates, and ψ is the polarisation of the GW event. We adopt a random sampling method, setting θ_0, ϕ_0 and ψ to be in the range of the uniform distributions $[0 - 2\pi], [0 - \pi], [0 - \pi]$, respectively. The factor $F_{\times,+}$

[4]Here mission refers to the specific configuration of LISA, as outlined in section 2.1.3, and the models of BMBH models resulting in fig. 2.1

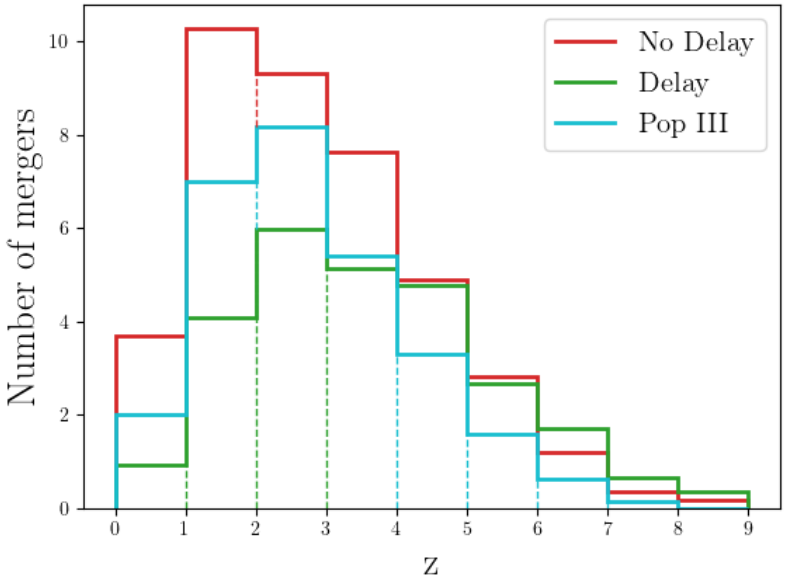

Figure 2.1: A histogram of the number of expected BMBH mergers over 10 years for the relevant BMBH merger models, according to the mission L6A2M5N2

describes the antenna beam pattern function,

$$F_{\times}^{(1)} = \frac{\sqrt{3}}{2}\left[\frac{1}{2}(1+\cos^2(\theta))\cos(2\phi)\cos(2\psi) + \cos(\theta)\sin(2\phi)\cos(2\psi)\right],$$
$$F_{+}^{(1)} = \frac{\sqrt{3}}{2}\left[\frac{1}{2}(1+\cos^2(\theta))\cos(2\phi)\cos(2\psi) - \cos(\theta)\sin(2\phi)\cos(2\psi)\right]. \tag{2.5}$$

The superscript number indicates which interferometer we are looking at. Since the detectors are spatially distributed in an equilateral triangle formation, the other two antenna pattern functions are simply

$$F_{\times,+}^{(1)}(\theta,\phi,\psi) = F_{\times,+}^{(2)}(\theta,\phi+\frac{2\pi}{3},\psi) = F_{\times,+}^{(3)}(\theta,\phi+\frac{4\pi}{3},\psi). \tag{2.6}$$

LISA has an additional complication to consider: Being sensitive to larger masses and equivalently lower frequencies, LISA can detect GW events of inspiral mergers lasting over several months, during which LISA's position will change relative to the event. The timescale of the event is described as,

$$t = t_c - 5(8\pi f)^{-8/3}M_c^{-5/3}. \tag{2.7}$$

Here t_c is the time of the merger and t indicates the time at which LISA begins to detect the merger. This relation is used to update the location

angles relative to an orbit of one year, T:

$$\theta = \cos^{-1}\left[\frac{1}{2}\cos(\theta_0) - \frac{\sqrt{3}}{2}\sin(\theta_0)\cos\left(\frac{2\pi t}{T} - \phi_0\right)\right], \tag{2.8}$$

$$\phi = \frac{2\pi t}{T} - \tan\left[\frac{\sqrt{3}\cos(\theta_0) + \sin(\theta_0)\cos\left(\frac{2\pi t}{T} - \phi_0\right)}{2\sin(\theta_0)\cos\left(\frac{2\pi t}{T} - \phi_0\right)}\right]. \tag{2.9}$$

These updated positions are implemented into the beam pattern functions.

The confirmed detection of a GW event is assessed by evaluating the signal-to-noise ratio (SNR) and is only confirmed if SNR > 8. The SNR is defined as,

$$\rho^2_{1,2,3} = 4\int_{f_{min}}^{f_{max}} df \frac{|\mathcal{H}|^2}{S_h}, \tag{2.10}$$

$_{1,2,3}$ indicates which interferometer we are currently describing and f_{min} and f_{max} are frequency limitations specific for each detector. $\mathcal{H}$ is the Fourier transform of the strain, and S_h is the noise power spectral density, an SNR weighting function that accounts for the particular properties of the instruments used. Therefore, the ET and LISA will have different S_h, corresponding to ET and LISA being sensitive to different frequencies.

The Einstein telescope's specific S_h is designed to follow [111]

$$S_h^{(\mathrm{ET})} = S_0\left(x^{p_1} + a_1 x^{p_2} + a_2\frac{1 + \sum_{n=1}^{n=6} b_n x^n}{1 + \sum_{n=4}^{n=4} c_n x^n}\right), \tag{2.11}$$

where

$$\begin{aligned}
&x = \frac{f}{200\mathrm{Hz}}, \quad S_0 = 1.449 \times 10^{-52}\mathrm{Hz},\\
&p_1 = -4.05, \quad p_2 = -0.69, \quad a_1 = 185.62, \quad a_2 = 232.56,\\
&b_n = 31.18, \quad -64.72, \ 52.24, \quad -42.16, \ 10.17, \ 11.53,\\
&c_n = 13.58, \quad -36.46, \ 18.56, \ 27.43,
\end{aligned}$$

with an assumed lower cutoff at $f = 1$ Hz. On the other hand, for LISA, this depends on the instrumental (or short) noise, S_{inst}, noise from low-level acceleration, S_{acc}, and confusion background noise, S_{conf} [109]:

$$S_h^{(\mathrm{LISA})} = \frac{20}{3}\frac{4S_{acc} + S_{insta} + S_{conf}}{L^2}\left[1 + \left(\frac{fL}{0.81c}\right)\right], \tag{2.12}$$

where L is the arm length and

$$\begin{aligned}
S_{acc} &= \frac{9 \times 10^{-30}}{(2\pi f)^4}\left(1 + \frac{10^{-4}}{f}\right),\\
S_{inst} &= 2.22 \times 10^{-23},\\
S_{conf} &= 2.65 \times 10^{-23}.
\end{aligned} \tag{2.13}$$

Once again, we follow the work in Ref. [110] and compute the Fourier transform of the strain using the stationary phase approximation [113]:

$$\mathcal{H} = \mathcal{A} f^{-7/6} e^{i\Psi(f)}, \tag{2.14}$$

where $\Psi(f)$ is the phase of the waveform. Notice that when $\mathcal{H}$ is substituted into (2.10), the exponential term disappears, meaning that the $\Psi(f)$ factor can be discarded for our purposes. $\mathcal{A}$ is the Fourier amplitude of the waveform,

$$\mathcal{A} = \frac{M_c^{5/6}}{d_l} \pi^{-2/3} \sqrt{\frac{5}{96}} \sqrt{[F_+(1+\cos^2(l))]^2 + (2F_\times \cos(l))^2},$$

where d_l is the luminosity distance obtained from the background code and l is the inclination angle, which we have sampled randomly between $[0°, 20°]$, as that is the maximum detection inclination range [113].

LISA has been designed to effectively measure frequencies as low as $f_{min} = 10^{-4} Hz$, which is why it is a promising probe of BMBH and EMRI mergers. For the simulations, the upper bound frequency of LISA is determined by two quantities: the structure of LISA itself and the last stable orbit of the merging system. LISA can detect frequencies up to $f_{max} = c\,(2\pi L)^{-1}$, where L is the length of LISA's interferometer arm, taken to be 2.5 Gm. Moreover, the total mass of an orbiting system is inversely proportional to the measured frequency. This means that even though massive mergers give rise to large detection amplitudes, their frequency will fall below f_{min}. Therefore if the last stable orbit frequency, $f_{LSO} = (6^{3/2} 2\pi M_{obs})^{-1}$, with M_{obs} being the observed total mass, is found to be lower than f_{min}, we disregard that simulated event. If it is between f_{min} and f_{max} then f_{LSO} becomes the new maximum frequency for that event. This constrains the bounds for the integral in Eq. (2.10), which can be solved to determine $\rho^2_{1,2,3}$ for each detector by replacing (2.14) with either Eq. (2.11) or Eq. (2.12) for the ET and LISA, respectively. The total SNR is then given by

$$\rho_{tot} = \sqrt{\rho_1^2 + \rho_2^2 + \rho_3^2}. \tag{2.15}$$

The luminosity distance error from the instruments used is determined *via* the Fisher Matrix,

$$\sigma^{inst}_{d_l} \approx \langle \frac{\partial \mathcal{H}}{\partial d_l}, \frac{\partial \mathcal{H}}{\partial d_l} \rangle^{-\frac{1}{2}}. \tag{2.16}$$

Since $\mathcal{H} \propto d_l^{-1}$ this becomes simply

$$\sigma^{inst}_{d_l} \approx \frac{2 d_l}{\rho}. \tag{2.17}$$

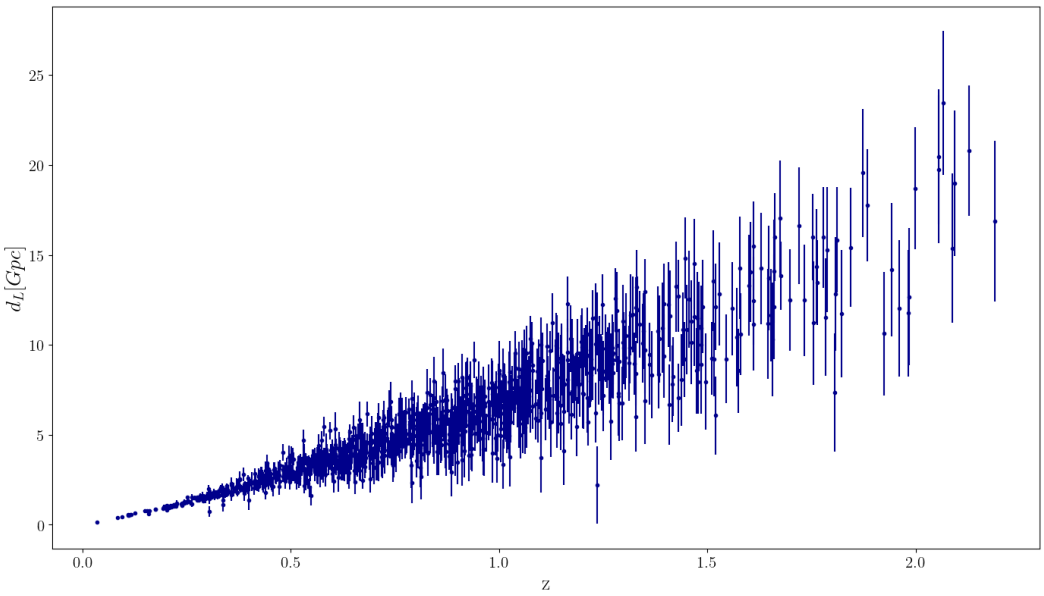

(a) Einstein Telescope

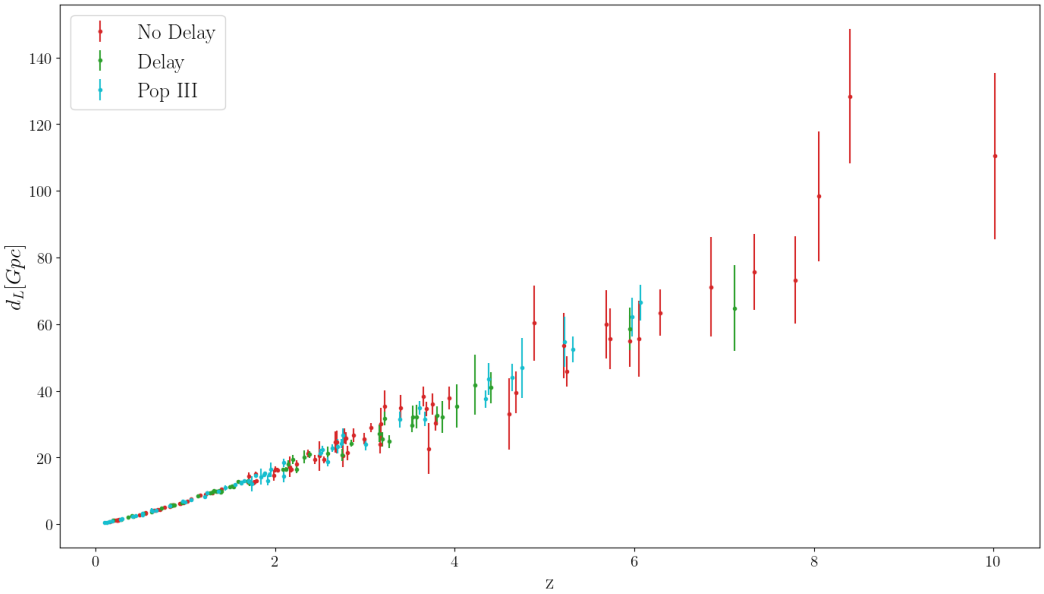

(b) LISA

Figure 2.2: An example of the results, simulating GWSS for both ET and LISA. Within LISA's results, we also included each model that was simulated, No delay, Delay and Pop III. Note that ET and LISA are limited to $z = 2.5$ and $z = 11$, respectively, due to the large associated errors, and therefore signal-to-noise ratio, that grow with the redshift.

The additional factor of 2 accounts for the symmetry in the inclination angle, which ranges from $-20°$ to $20°$. The error due to gravitational lensing is [103],

$$\sigma_{d_l}^{len} = \frac{d_l}{2} \times 0.066 \left[4(1-(1+z)^{1/4})\right]^{1.8}, \tag{2.18}$$

reduced by a half to account for the merger and ringdown of the event. For

LISA, there is also an error associated with the peculiar velocities of GW sources [114]:

$$\sigma_{d_l}^{pec} = d_l \frac{\sqrt{\langle v^2 \rangle}}{c} \left[1 + \frac{c(1+z)}{H d_l} \right], \tag{2.19}$$

with an estimate of the peculiar velocity of the host galaxy with respect to the Hubble flow as $\sqrt{\langle v^2 \rangle} = 500 kms^{-1}$. The total luminosity error is calculated simply as a combination of the errors in Eqs. (2.17)-(2.19):

$$\sigma_{d_l} = \sqrt{(\sigma_{d_l}^{inst})^2 + (\sigma_{d_l}^{len})^2 + (\sigma_{d_l}^{pec})^2}. \tag{2.20}$$

The number of mergers detected by the ET will depend on factors such as running costs and the corresponding detection with other detectors [111]. Moreover, ET is expected to detect more than 10^4 mergers yearly. However, due to the rarity of an EM counterpart, the predicted number of detectable mergers, in 10 years, with an EM counterpart is approximately 200 [115] From [105], we see that LISA's number of detected mergers is more model dependent. For a 10-year mission proposal, we expect 56 for Pop III, 52 for the delay, and 80 for the no-delay models. The process described above is encoded in the script, `GWSS`. An example of the mock data that can be collected is illustrated in fig. 2.2.

2.2 Results and constraints

This chapter aims to constrain a modified gravity model often considered to modify late-time dynamical behaviour. As we have seen in section 1.2, mapping from the Jordan frame to the Einstein frame changes the action. The additional degree of freedom initially non-minimally coupled to gravity in the Jordan frame transforms such that a new field is coupled to all matter and non-minimally coupled to gravity.

We are interested in the coupling effect of our scalar field to other matter, such as dark matter, rather than the exact form of the modified gravitational sector. Therefore we parameterise the additional degree of freedom in eq. (1.25) with $F(\phi) = e^{2\beta\phi}$ and the specified potential $V(\phi) = V_0 e^{-\kappa\lambda\phi}$.

Bayesian analysis

Next, we want to use our mock data to forecast what constraining power GW data will have on our specified modified gravity model and specifically if there is a preference for modified gravity over ΛCDM. In our analysis, we constrain the relative parameters against the mock GW data produced in a ΛCDM modelled Universe and other observational data sets. Therefore our analysis forecasts the expected constraints on the model parameters assuming that we are in a ΛCDM Universe. Thus, we do not focus on the resulting best-fit parameter values but rather on the forecasted constraining power of GWs.

The idea applied to cosmology is that our knowledge of a parameter or particular condition is updated, resulting in a convergence towards the "true" result. The computation of updating the system is known as Bayes' theorem: the posterior, a probability density function (PDF) that encodes the degree of belief in a parameter X given the data D, $P(X|D)$, is proportional to the likelihood, that D can be explained by X, $P(D|X)$, multiplied prior belief of the parameters true value, $P(X)$. The proportionality is resolved by normalising against the evidence the total sum of likelihoods multiplied by the probability of all parameters [116, 117]. This can be compactly written as

$$P(X|D) = \frac{P(D|X)P(X)}{\sum_n P(D|X_n)P(X_n)}. \tag{2.21}$$

With the given posterior PDF, we implement a sampling algorithm, specifically in this work, a Markov Chain Monte Carlo (MCMC) algorithm, utilising a Nested Sampling procedure implemented in the `MultiNest` [118, 119] and `PyMultiNest` [120] packages. The MCMC generates a random walk, starting from a initial condition given by the priors: the relative baryon density parameter, $\Omega_b h^2 = [0.018, 0.03]$, relative cold dark matter density, $\Omega_c h^2 = [0.1, 0.2]$, relative Hubble parameter, $h = [0.6, 0.8]$, the potential parameter, $\lambda = [0, 2]$, and the coupling parameter, $\beta = [0, 2]$. The walk then moves forwards dependent on the PDF function given. For our work we use flat priors. Therefore, the random walks will make a chain and eventually converge towards the "true" parameter.

We can determine the marginalised constraint for each parameter by integrating all the other parameters, which then provides a marginalised distribution of likelihood for the given parameter[116, 117, 121]. The likelihood function for the simulated dataset of standard sirens GW events is constructed using an effective Gaussian distribution.

The MCMC chains are then analyzed, and the results are presented in fig. 2.3 and table 2.1[5] using the `GetDist` package [122]. The constraint is calculated as the mean value of the distribution, such that the area on either side of the mean value is equal, as can be seen in table 2.1. If the distributions were symmetrical, the mean would indicate the best fit. However, as seen from fig. 2.3, many distributions are highly non-symmetrical. We assume that the mean value best indicates the "true" value. However, we can state how confident we are that the true value is within a given range. This confidence then indicates the error we associate with the measurement. For instance, to be 98% confident, we ensure that 49% on either side of the mean value is encoded. However, to account for this, the error associated with the constraint is the value variation from the mean to account for the 49%. For this work, we take our mean value with a 68% confidence, as given in table 2.1

To assess the constraining power of standard siren data from ET and LISA on coupled quintessence models, we compare the independent and

[5]The table and figures presented here were created by Elsa Teixeira for the purposes of this collaborative work

combined constraints with current background data. This comparison allows us to determine whether GW catalogues can improve the constraints on parameters such as Ω_m^0, H_0 and model-specific parameters that affect the background evolution.

Our analysis includes baryonic acoustic oscillations (BAO) data from the Sloan Digital Sky Survey (SDSS) DR7 Main Galaxy Sample [123], SDSS DR12 consensus release [124] and the 6dF Galaxy Survey [125], in combination with distance *moduli* measurements of 1048 type Ia Supernova (SNIa) data from Pantheon [126]. This combined data set is referred to as "SNIa+BAO".

2.2.1 Results

Conformal Coupled Quintessence				
Data sets	Ω_m^0	H_0	β	λ
BAO+SNIa	$0.3019^{+0.0088}_{-0.0059}$	$73.2^{+4.7}_{-3.5}$	$0.085^{+0.055}_{-0.043}$	$0.42^{+0.20}_{-0.36}$
ET	$0.307^{+0.011}_{-0.0050}$	$67.49^{+0.39}_{-0.34}$	$0.115^{+0.060}_{-0.079}$	$0.50^{+0.26}_{-0.38}$
ET+BAO+SNIa	$0.3046^{+0.0099}_{-0.0051}$	67.37 ± 0.36	$0.063^{+0.033}_{-0.045}$	$0.49^{+0.26}_{-0.35}$
LISA delay	$0.281^{+0.031}_{-0.013}$	$66.2^{+1.4}_{-0.67}$	$0.105^{+0.043}_{-0.084}$	$0.77^{+0.43}_{-0.66}$
LISA delay+BAO+SNIa	$0.3004^{+0.0085}_{-0.0044}$	67.34 ± 0.51	$0.046^{+0.023}_{-0.037}$	$0.39^{+0.19}_{-0.34}$
LISA no-delay	$0.278^{+0.027}_{-0.016}$	$66.1^{+1.0}_{-0.62}$	$0.091^{+0.046}_{-0.067}$	$0.87^{+0.60}_{-0.53}$
LISA no-delay+BAO+SNIa	$0.2979^{+0.0092}_{-0.0041}$	$66.95^{+0.42}_{-0.35}$	$0.041^{+0.020}_{-0.034}$	$0.43^{+0.21}_{-0.36}$
LISA pop3	$0.3039^{+0.0093}_{-0.0049}$	$67.50^{+0.50}_{-0.44}$	$0.167^{+0.085}_{-0.11}$	$0.33^{+0.15}_{-0.32}$
LISA pop3+BAO+SNIa	$0.3028^{+0.0065}_{-0.0036}$	67.52 ± 0.37	$0.048^{+0.025}_{-0.037}$	$0.33^{+0.15}_{-0.29}$

Table 2.1: Marginalized constraints on cosmological and model parameters for coupled quintessence at 68% C.L.

To analyse the results, we use the notation

$$\mathcal{F}_i^j[a] = \frac{\sigma_j}{\sigma_i}, \tag{2.22}$$

which describes the fractional increase ($\mathcal{F} > 1$) or decrease ($\mathcal{F} < 1$) of the 1σ error calculated as the mean error given in table 2.1 of the parameter represented by a. i, j indicates the data sets being analysed, such that data set j is compared to the data set i.

Based on the analysis presented in fig. 2.3 and table 2.1, we notice that there is a discrepancy in the forecasted cosmological parameters, Ω_m^0 and H_0, between the data sets. ET and LISA pop3 exhibit a narrower distribution

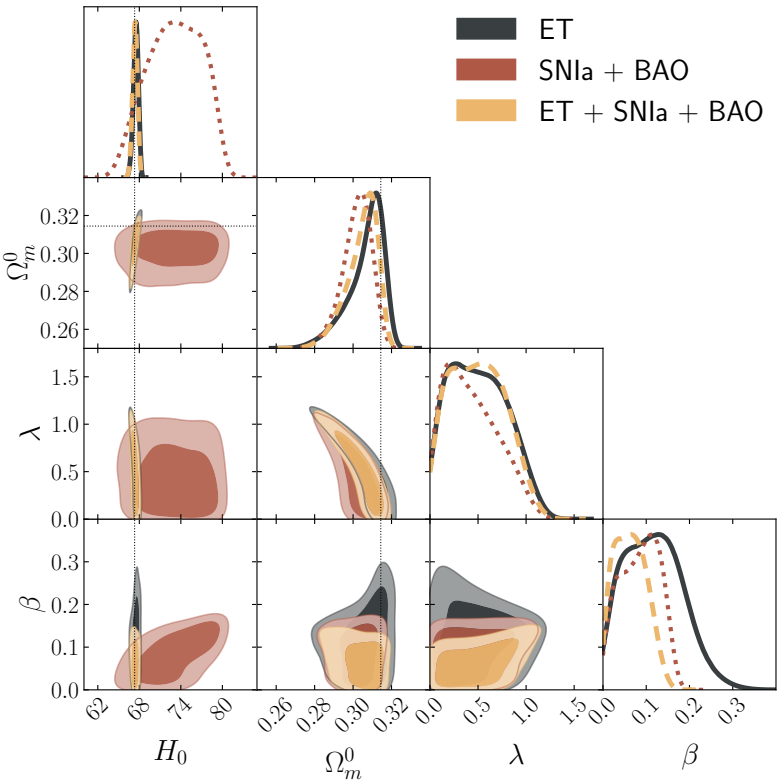

(a) Einstein Telescope

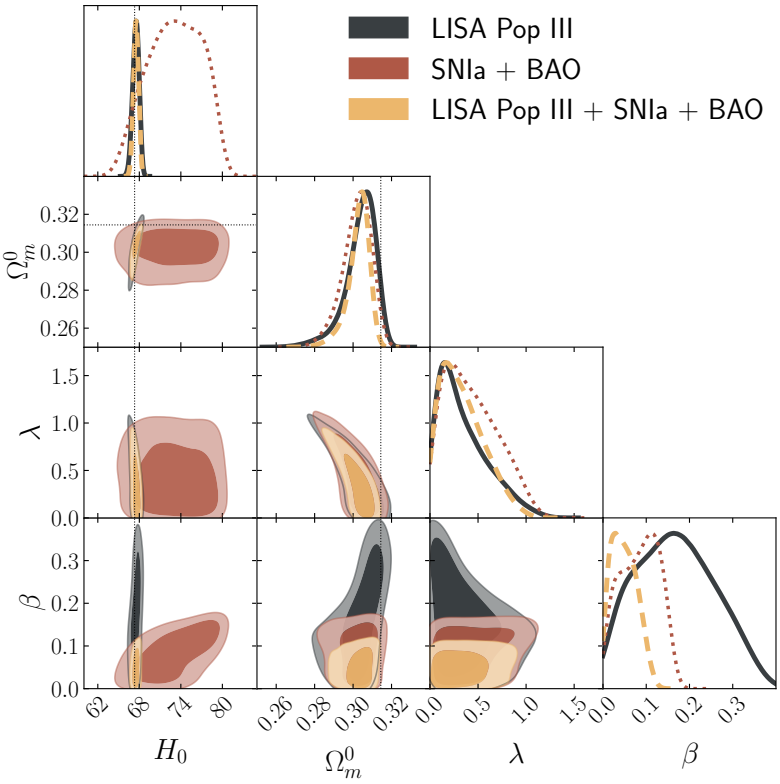

(b) LISA pop3

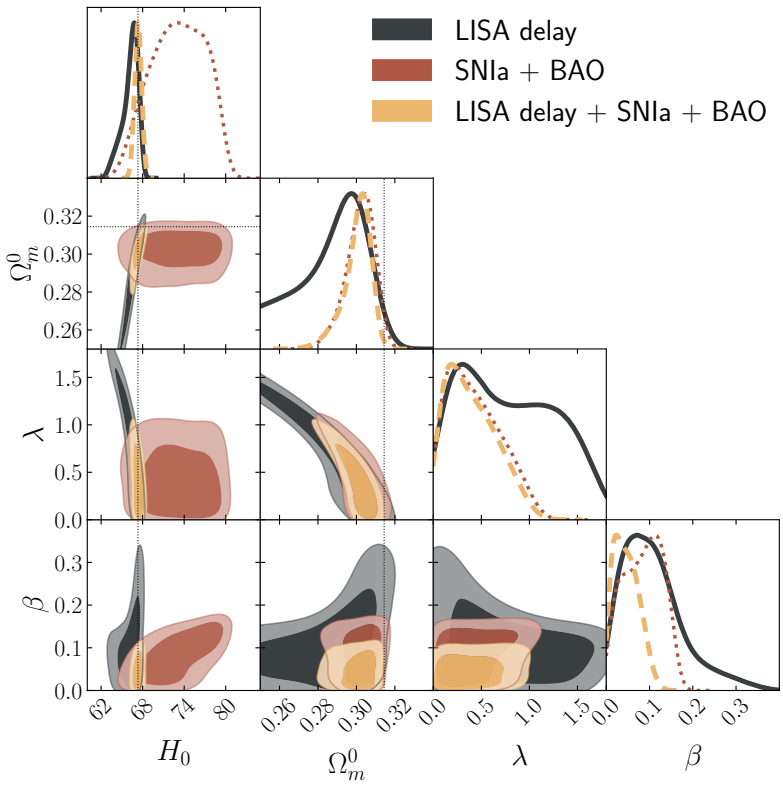

(c) LISA delay

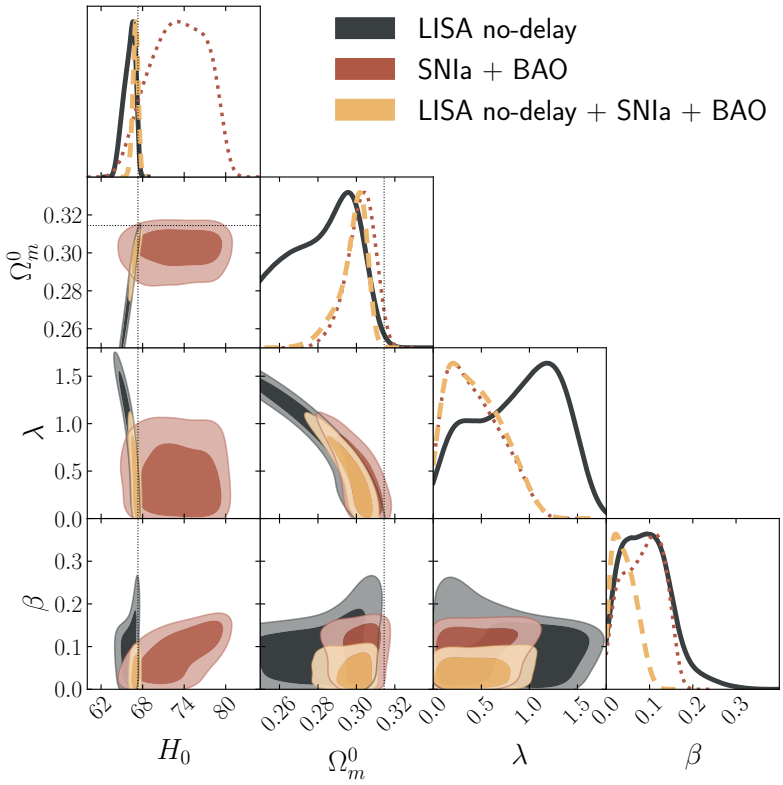

(d) LISA no-delay

Figure 2.3: Constraints for Conformal Coupled Quintessence. The darker contour identifies the 1σ region, and the lighter 2σ. The fiducial cosmological parameters are identified on the graph by the dotted back line.

seen in figs. 2.3a and 2.3b for Ω_m^0 and H_0 compared to the other LISA data sets, figs. 2.3c and 2.3d. The difference can be attributed to the specifics of the simulation: ET can probe many mergers, providing a more precise reading on its given cosmological parameters. Moreover, ET is limited to $z < 5$, which minimises the smearing effect of the input values given from `CLASS`. Similarly, for LISA pop3 data set, the redshift distribution of the pop3 model is shifted towards lower redshifts. This can be seen in section 2.1.3, where the cyan (pop3) model dominates the number of sources in the lower range, $0 < z < 5$. Therefore the smearing effect, which is more prevalent at higher redshifts, is reduced, resulting in a strong bias to the fiducial Planck likelihood input values. In contrast, the other two data sets of LISA, delay and no-delay, have a much broader redshift distribution probing higher redshifts. This has resulted in a larger deviation from the input values and the local data sets of BAO+SN1a, as seen in table 2.1, with a broader parameter distribution seen in figs. 2.3c and 2.3d.

Moreover, we notice that the accuracy, as measured by the average error, for Ω_m^0 is worse or comparable in GWs data sets compared to the local data sets of BAO+SNIa, with $\mathcal{F}^{\text{ET}}_{\text{BAO+SNIa}}[\Omega_m^0] = 1.1$, $\mathcal{F}^{\text{Delay}}_{\text{BAO+SNIa}}[\Omega_m^0] = 3.0$, $\mathcal{F}^{\text{No Delay}}_{\text{BAO+SNIa}}[\Omega_m^0] = 2.9$, $\mathcal{F}^{\text{Pop III}}_{\text{BAO+SNIa}}[\Omega_m^0] = 0.97$. Therefore, GWs alone are unlikely to significantly enhance the confidence in constraining Ω_m^0.

However, the GW data sets alone are much more precise in constraining H_0 than BAO+SNIa, where $\mathcal{F}^{\text{ET}}_{\text{BAO+SNIa}}[H_0] = 0.089$, $\mathcal{F}^{\text{Delay}}_{\text{BAO+SNIa}}[H_0] = 0.25$, $\mathcal{F}^{\text{No Delay}}_{\text{BAO+SNIa}}[H_0] = 0.20$, $\mathcal{F}^{\text{Pop III}}_{\text{BAO+SNIa}}[H_0] = 0.11$. Hence, we predict that 3G detectors will be crucial in resolving the tension regarding the H_0 parameter. Although we note that the estimated parameter values given in table 2.1, are subject to change as there is a bias to the fiducial values. In appendix C, changing the fiducial value of H_0 is explored.

Unlike H_0, the model parameters β and λ are better constrained utilising BAO+SNIa data compared to GW data sets alone (excluding LISA pop3 for λ) shown by $\mathcal{F}^{\text{ET}}_{\text{BAO+SNIa}}[\beta, \lambda] = \{1.4, 1.1\}$, $\mathcal{F}^{\text{LISA delay}}_{\text{BAO+SNIa}}[\beta, \lambda] = \{1.3, 1.9\}$, $\mathcal{F}^{\text{No Delay}}_{\text{BAO+SNIa}}[\beta, \lambda] = \{1.2, 2.0\}$, $\mathcal{F}^{\text{Pop III}}_{\text{BAO+SNIa}}[\beta, \lambda] = \{2.0, 0.84\}$. Therefore, to increase the constraining power, future GW data sets must be combined with local data such as BAO+SNIa to increase the overall accuracy of the parameter estimation.

When combined with the data sets, we see that β is vastly improved, whereas for λ, there is only an increase in accuracy for delay and no-delay: $\mathcal{F}^{\text{ET+BAO+SNIa}}_{\text{BAO+SNIa}}[\beta,\lambda] = \{0.80, 1.1\}$, $\mathcal{F}^{\text{LISA delay+BAO+SNIa}}_{\text{BAO+SNIa}}[\beta,\lambda] = \{0.61, 0.9\}$, $\mathcal{F}^{\text{No Delay+BAO+SNIa}}_{\text{BAO+SNIa}}[\beta,\lambda] = \{0.55, 1.0\}$, $\mathcal{F}^{\text{Pop III+BAO+SNIa}}_{\text{BAO+SNIa}}[\beta,\lambda] = \{0.63, 0.79\}$. The increased constraints can be further identified in the more localised peaks in figs. 2.3a and 2.3b, compared to figs. 2.3c and 2.3d. The narrower distribution in λ, results in an increased accuracy compared to the other two LISA data sets. On the other hand, the distribution for β is broader and thus less accurate as identified in table 2.1.

It is important to highlight that the values of $\beta = 0$ and $\lambda = 0$, which indicate λCDM, are no longer within the 1σ error, shown in table 2.1 and fig. 2.3, for all data sets analysed.

We see that the combined data set for Ω^0_m results in improved accuracy, $\mathcal{F}^{\text{ET+BAO+SNIa}}_{\text{BAO+SNIa}}[\Omega^0_m] = 1.0$, $\mathcal{F}^{\text{Delay+BAO+SNIa}}_{\text{BAO+SNIa}}[\Omega^0_m] = 0.88$, $\mathcal{F}^{\text{No Delay+BAO+SNIa}}_{\text{BAO+SNIa}}[\Omega^0_m] = 0.90$, $\mathcal{F}^{\text{Pop III+BAO+SNIa}}_{\text{BAO+SNIa}}[\Omega^0_m] = 0.69$. The trend continues for H_0, with better constraints with the combined data sets, $\mathcal{F}^{\text{ET+BAO+SNIa}}_{\text{BAO+SNIa}}[H_0] = 0.088$, $\mathcal{F}^{\text{Delay+BAO+SNIa}}_{\text{BAO+SNIa}}[H_0] = 0.0.12$, $\mathcal{F}^{\text{No Delay+BAO+SNIa}}_{\text{BAO+SNIa}}[H_0] = 0.094$, $\mathcal{F}^{\text{Pop III+BAO+SNIa}}_{\text{BAO+SNIa}}[H_0] = 0.09$.

2.3 Discussion of forecasted gravitational waves as standard sirens

With the launch of new third generation (3G) GW detectors, we are expected to be able to detect many events that produce both a GW and an EM counterpart that will allow for accurate distance measurement; these are known as standard sirens. Thus, GW act as a useful probe of gravitational effects that can constrain cosmological models.

We have outlined the procedure for simulating gravitational waves that can be used as standard sirens, a useful probe of gravitational effects and cosmological parameters. We simulated the expected measurement and errors from two 3G observatories: Einstein telescope, a ground-based detector measuring low mass and low redshift events, and LISA, a space-based detector probing MBHB of redshifts potentially as large as $z = 20$. The procedure outlined in this chapter resulted in the script, `GWSS`, that utilises the background output from a Boltzmann solver such as `CLASS`. Therefore, the script can be used for any given model, provided the modifications to `CLASS`, to produce simulated mock data. For the work studied in this chapter, a fiducial model of ΛCDM was given, creating a bias encoded in the resulting simulation.

Using our simulated results, based on ΛCDM, we then utilised this to constrain the conformal coupling of a scalar field to matter for a given scalar field potential. We then compared our simulated mock data with local measurements of SNIa and BAO. We noticed from the analysis that the range of redshift plays a critical role in the data's ability to constrain the cosmological parameters, with the lower redshift GW models of ET and LISA pop3, forcing much tighter constraints on H_0 and Ω_m^0, due to limited deviation from the fiducial values of ΛCDM. Interestingly these lower redshift models also exhibited a tightly constrained value of λ but not the parameter β. However, the larger redshift sources, LISA delay and no-delay, display much larger freedom in the parameter space due to the larger errors and greater deviation from the fiducial model associated with greater distances.

We found that the accuracy for GWs in constraining the model's parame-

ters, β and λ, is worse than BAO+SNIa, apart from LISA pop3 for λ. However, combining the two measurements results in improved accuracy, with a reduction in the value of the estimated parameters. Thus we can conclude that future GW measurements will play a crucial role in constraining modified gravity models. Moreover, we noticed that the mock GW measurements are more accurate in constraining H_0 than BAO+SNIa alone. Although the fiducial model was ΛCDM taken from Planck, and as a result the average H_0 measurement for GW is 67 [km s^{-1} Mpc^{-1}]. Therefore we do not conclude that the forecasted value of H_0 is the "true" value. Rather the accuracy of the new 3G detectors will be critical in resolving the H_0 tension.

Although simulated GW data has not identified any tensions between any of the parameters, we can see that it has further constrained the model's parameters, particularly with LISA's data sets, as they can probe larger redshifts. As we have seen from our simulation, larger redshift events lead to a broader distribution. Thus, we expect a slight difference between the cosmological parameter measurements between ET and LISA.

3 | The Theory of Inflation

In Section 1.3, we discussed the HBB model, specifically, the initial conditions of a radiation-dominated universe with fluctuations that lead to the CMB. Although, as discussed in the previous chapter, chapter 2, tensions have arisen between the CMB and local measurements. Moreover, the HBB model encounters significant challenges, such as the horizon and flatness problems [127]. The theory of inflation was proposed in 1981 [128, 129] as a solution to address these issues, and it has now become the prevailing paradigm describing the early universe. According to this theory, the Universe experienced a period of near-exponential expansion, $a \simeq \exp(Ht)$, shortly after the spatial singularity. This behaviour is described as a quasi-de Sitter expansion, similar to the dynamics of a cosmological constant, which results in a homogeneous and smooth Universe. Alan Guth succinctly describes the essence of this behaviour as "The inflationary universe is a theory of the 'bang' of the big bang" [130]. Furthermore, inflation naturally explains the primordial density perturbations that ultimately result in the formation of large-scale structures and the CMB.

Despite its successes, inflation still suffers from conceptual challenges, such as an initial singularity and the dependence on arbitrary initial conditions. Assuming that inflation is described by the simplest de Sitter behaviour leads to past-incompleteness, attributed to its exponential phase. Many inflationary singularity theorems have shown that the universe had must of had a beginning, assuming a classical theory. [30, 31, 128, 131, 132]. These singularity theorems are dependent on adhering to the weak energy condition. Addressing the singularity concern necessitates an additional phase where this condition is violated, potentially in a quantum gravity era, the singularity issue is explored further in chapter 4.

These limitations have motivated researchers to explore extensions and

modifications to the inflationary framework, leading to new phenomenological predictions like primordial black holes [133]. In this chapter, we first summarise the work outlined in [73–76, 79, 134] relevant to this thesis by providing a brief review of the achievements of inflation and its underlying mechanism. Subsequently, we delve into the motivations for, and the study of, specific modifications to address the conceptual shortcomings of inflation and explore potential future observational prospects.

3.1 Successes of inflation

Horizon problem

Due to the vast size of the Universe and assuming the HBB model, we observe patches in the sky that have never been in causal contact with each other. Therefore no information has been passed between them. However, as discussed in section 1.3, the Universe is homogeneous and isotropic on cosmological scales. This is supported by the observation that, on average, patches of the CMB appear to be in thermal equilibrium. How can this be the case, given different regions of space that cannot interact? This question can be further examined by considering the distance light has travelled since some time, t_i, which is given by the comoving horizon $d_h = \tau$, which for light is equal to conformal time[1],

$$\tau = \int_{t_i}^{t} \frac{d\tilde{t}}{a} = \int_{a_i}^{a} \frac{d\ln a}{aH}. \tag{3.1}$$

The a_i indicates the initial value of the scale factor. We have also introduced an important length scale $(aH)^{-1}$, known as the comoving Hubble radius, that characterises the Hubble sphere. Everything within the Hubble sphere

[1]Massless particles such as photons, travel along the light curve and are referred to as null paths. Null paths then have $ds^2 = 0$, from eq. (1.38), we see that $d_h \equiv dr = d\tau$.

has the potential to interact [2]. If we assume a universe filled with only radiation or matter, denoted by the subscript r, m, respectively, the comoving Hubble radius and comoving horizon behave as

$$\begin{aligned} (aH)_r^{-1} &\propto t^{1/2} \qquad & \tau_r &\propto a, \\ (aH)_m^{-1} &\propto t^{2/3} \qquad & \tau_m &\propto a^{1/2}. \end{aligned} \tag{3.2}$$

Thus, assuming only matter or radiation, the comoving Hubble radius and horizon increase monotonically. Therefore the furthest events entering the horizon today have been outside the comoving Hubble radius since the HBB, hence causally disconnected. Unless additional ingredients are used, we identify this as an initial condition problem: the Universe at its creation was almost perfectly uniform and in thermal equilibrium.

If we include an epoch of inflation, we assume $a \simeq \exp Ht$ and consequently $H \simeq const.$ Then the comoving Hubble sphere will effectively shrink,

$$\frac{d}{dt}(aH)^{-1} < 0, \tag{3.3}$$

More formally, the integration for the comoving horizon will become,

$$d_h = H^{-1} \int_{a_i}^{a} \frac{d \ln a}{a} \simeq (aH)^{-1} - (a_i H)^{-1} \tag{3.4}$$

the subscript i indicates the initial scale factor at the beginning of inflation. Assuming that the beginning of inflation is given as $a_i \to 0$, we see that conformal time is extended. Hence, the beginning of inflation becomes $\tau_i \to -\infty$ and the end of inflation, and the start of the former HBB, is at $\tau = 0$. This is shown in fig. 3.1a, where the light cones effectively become stretched by the extension of $\tau_i \to -\infty$. This extension of conformal time and stretching of light cones then allows causal contact between the regions of space that would have otherwise been disconnected in the HBB model.

Flatness problem

Many cosmological models assume a spatially flat universe, a well-justified approximation with the spatial curvature experimentally constrained to

[2] We characterise this with the concept of a cosmological horizon, taking ourselves to be at the centre of the Hubble sphere. Events that we can observe are considered subhorizon, analogous to ships in the ocean, which we can then pass information to. However, any events outside our Hubble sphere are past the horizon known as superhorizon. The notion of sub/superhorizon is further illustrated in fig. 3.1

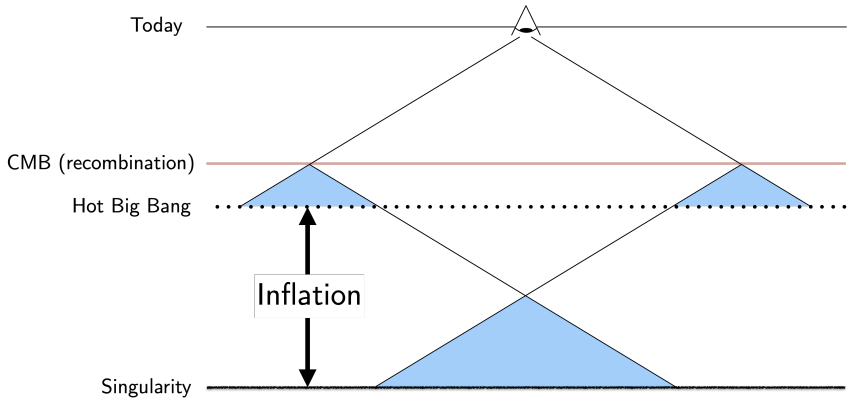

(a) Horizon Problem

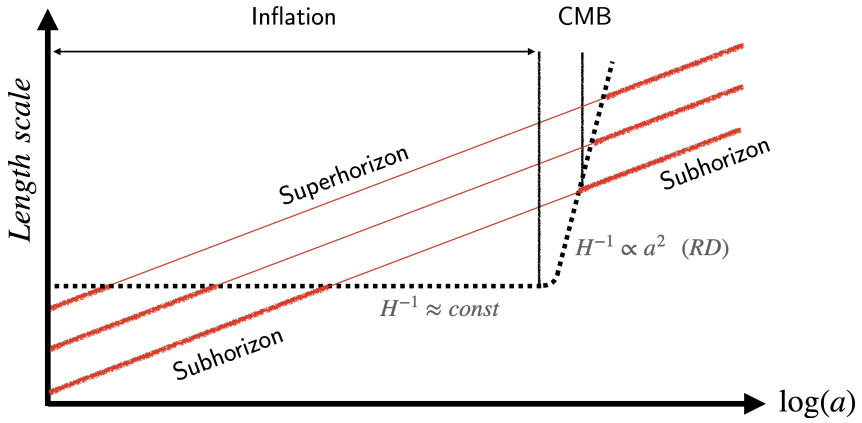

(b) Correlation Problem

Figure 3.1: An illustrative sketch showing how inflation solves the horizon problem, fig.(a), by extending the conformal time to allow for the light curves to coincide and therefore interact (Indicated by the light blue area). Without inflation, it is clear that the two regions are never in causal contact. Although given fine-tuned initial conditions, the regions could appear to be in causal contact. Inflation also resolves the correlation problem, fig.(b), by effectively shrinking the Hubble horizon, allowing fluctuations to be subhorizon before entering superhorizon modes and becoming frozen during inflation and imprinting on the CMB.

$\Omega_k(t_0) \approx 10^{-3}$ [80]. However, a much lower value would be expected if the universe is flat, $K = 0$. Here we have parameterised the spatial curvature, assuming a homogeneous and isotropic Universe, by finding the deviation from a flat universe,

$$\Omega_k(t) = \frac{\rho_c - \rho}{\rho_c} = \frac{K}{(aH)^2}. \tag{3.5}$$

The dependence on the Hubble radius causes an issue for the HBB model. We have studied the effect matter and radiation have on the Hubble radius, $(aH)^{-1}$, resulting in a growth, illustrated by eq. (3.2). Therefore Ω_k will grow and deviate towards ± 1 with time, showing that $\Omega_K = 0$ is an unstable fixed point. As a result, either $K = 0$ such that the Universe was always and will continue to be spatially flat or the Universe had to be extremely fine-tuned: extrapolating backwards through matter and radiation-dominated epochs, we find the approximate value of Ω_k at the time of nucleosynthesis[3] ($t_{nuc} \simeq 1$s after the HBB) to be

$$|\Omega_k(t_{nuc})| = \Omega_k(t_0) \cdot \frac{(aH)_0^2}{(aH)_{eq}^2} \cdot \frac{(aH)_{eq}^2}{(aH)_{nuc}^2} \approx 10^{-16}. \tag{3.6}$$

Here the subscript eq represents the matter-radiation equality. Each ratio is calculated from eq. (3.2), depending on whether they are in a matter or radiation-dominated epoch.

We now study how inflation can resolve the flatness problem. As discussed, during inflation, the comoving Hubble radius shrinks, $(a\dot{H})^{-1} < 0$. Therefore, $\Omega_K = 0$ becomes a stable fixed point as the spatial curvature is diluted away. Extending the calculation above to include inflation, we can identify the effect an exponential expansion has on Ω_K. Assuming inflation ends around $t_f \approx 10^{-34}s$ [74] with the Universe entering a radiation-dominated epoch,

$$|\Omega_k(t_i)| = \Omega_K(t_0) \cdot \frac{(aH)_0^2}{(aH)_{eq}^2} \cdot \frac{(aH)_{eq}^2}{(aH)_f^2} \cdot \frac{(aH)_f^2}{(aH)_i^2}. \tag{3.7}$$

Utilising the assumption of a quasi de-Sitter epoch, $H \approx const$, and setting $|\Omega_k(t_i)| = 1$ to represent a maximal spatially curved initial state, we find that the scale factor would need to increase by $a_f = 10^{26} a_i$, to allow for $\Omega_k(t_0) \approx 10^{-3}$.

As the Universe is required to grow drastically quickly, that cosmic time is almost unchanged and is generally not considered a good time coordinate for this extreme epoch. When studying inflation, a more intuitive time coordinate is the growth of the size of the Universe given in terms of the dimensionless e-fold number, defined as $N \equiv \ln(a/a_i)$[4] . Therefore, assuming

[3]Here we are only concerned with an approximate time scale that is within a radiation dominated epoch, to highlight the fine-tuning effect.

[4]The formal definition is $dN \equiv d\ln a$. However, during inflation we approximate $H \approx const$, such that $N \propto a$, which can be normalised with a_i.

the basic setup of our calculation above, inflation must last $N \gtrsim 60$ to resolve the flatness problem[5]. A subtlety often overlooked when studying inflation is that both the horizon and flatness problems, the commonly cited successes of inflation introduced by [127], are initial condition problems arising from the singularity. Moreover, dependent on the model of the early Universe before inflation, the horizon and flatness problem may not be a significant issue to be avoided. For instance, by replacing the singularity with a past universe, as discussed in chapter 4, the flatness and horizon problems can be resolved.

Origin of inhomogeneities and large scale structures

As stated in section 1.3, we know large-scale structures observed in the Universe result from gravitational fluctuations in the early universe. Therefore, by measuring the temperature anisotropies in the CMB and calculating the corresponding power spectrum, we quantify the deviation away from homogeneity on cosmological scales to infer the details of these fluctuations. However, the wavelengths of the fluctuations evolve as $\lambda \propto a$, stretching with the Universe's expansion. The correlation between temperature anisotropies from the CMB indicates a small amplitude and near-scale-invariant behaviour on large scales. Therefore assuming an FRLW metric and the HBB model, these fluctuations could not have formed via causal processes generating the near scale-invariance we see in the power spectrum as depicted in fig. 3.1. This is similar to the horizon problem and is often titled a re-imagined horizon problem [75]. As we have seen, the Hubble radius increases in a matter and radiation-dominated epoch. Therefore we can conclude that correlated fluctuations entering the horizon today, $k < aH$ (subhorizon), have always been outside the Hubble radius before, $k > aH$, (superhorizon), assuming a matter and radiation-filled Universe.

If we include an inflationary epoch, we assume the Universe was much smaller, with a gradually shrinking Hubble sphere. Thus, the gravitational perturbations arising from quantum fluctuations are free to interact on sub-

[5]The precise number of e-folds required to solve the flatness problem is dependent on the mechanics of the model used, nevertheless for most models, a lower bound is set $N \geq 50$.

horizon scales, $k < aH$, as depicted in fig. 3.1b. Once inflation starts, these fluctuations exit the horizon and become superhorizon, where they are causally disconnected and remain frozen for the duration of inflation. Thereby imprinting the characteristic signature of the fluctuations before inflation. Once inflation ends, the wavelengths of these fluctuations become subhorizon again, allowing them to interact freely. Therefore the initial perturbations before inflation influence the subsequent dynamics of the perturbations after and are encoded into the CMB.

3.2 Slow-roll inflaton

We require a period where the Hubble radius is shrinking to resolve the horizon, flatness and origin of inhomogeneities problems above. To study this effect, we expand eq. (3.3), taking the time derivative of the comoving Hubble radius,

$$\frac{d}{dt}\left(aH\right)^{-1} = -\frac{1}{a}(1-\epsilon). \tag{3.8}$$

Here we have defined the slow-roll parameter

$$\epsilon \equiv -\frac{\dot{H}}{H^2}. \tag{3.9}$$

Provided $\epsilon < 1$, the Hubble radius is shrinking. We can also relate the derivative of the Hubble radius with the acceleration of the scale factor,

$$\frac{d}{dt}\left(aH\right)^{-1} = -\frac{\ddot{a}}{(aH)^2}. \tag{3.10}$$

Therefore, we can conclude that if we have a shrinking Hubble radius, we must have an accelerated expansion.

Disregarding perturbations, the Hubble parameter H is a constant when $\epsilon = 0$, leading to a perfect de-Sitter universe with exponential expansion as given in (1.56). Therefore, we identify similarities between the nature of dark energy and inflation. However, we cannot utilise a cosmological constant to source the acceleration, as this would provide an indefinite expansion, with the cosmological constant continuing to dominate the energy density. Instead, we impose that the energy density is initially similar to

a cosmological constant but is dynamical, eventually breaking the de-Sitter epoch. Thus, we require the start of inflation to have the equation of state $w \approx -1$, before evolving to $w \to 1/3$ for a radiation-dominated Universe as deceleration occurs. Thus, we require $\dot{H}$ to be non-zero, which imposes a lower bound constraint, $0 < \epsilon < 1$, during inflation. This identifies inflation as a quasi-de-Sitter epoch. As described above for the flatness problem, inflation is required to persist for a sufficiently long duration. Hence the evolution of ϵ is also constrained by a second slow-roll parameter,

$$|\eta| = |\epsilon - \frac{\dot{\epsilon}}{2\epsilon H}| \ll 1. \tag{3.11}$$

Exploiting the similarities between inflation and dynamical dark energy, we model the driving force of this accelerated expansion to be determined by scalar field dynamics. Assuming the FRLW metric, we know from eq. (1.46) we require that $\rho + 3p < 0$ for the Universe to accelerate. This implies the condition, $\dot{\phi}^2 \ll 2V$, such that the energy density during this epoch is dominated by the field's potential energy with only a minor contribution from the kinetic energy. This scalar field behaviour is called slow-roll inflation and was first utilised by [127, 135]. We find, assuming ρ and P from eq. (1.18), that this provides us with the initial de-Sitter universe we are after as

$$w = \frac{\frac{1}{2}\dot{\phi}^2 - V}{\frac{1}{2}\dot{\phi}^2 + V} \to -1. \tag{3.12}$$

Using the other Friedmann equations, we further illustrate the effect of the slow-roll behaviour,

$$H^2 = \frac{\dot{\phi}^2 + 2V}{6M_{\text{Pl}}^2} \to \frac{V}{3M_{\text{Pl}}^2} \tag{3.13}$$

$$\dot{H} = -\frac{\dot{\phi}^2}{2M_{\text{Pl}}^2}. \tag{3.14}$$

In the first equation, the slow-roll condition sets the expansion rate to be determined by the scalar field's potential. Moreover, for the kinetic energy to not dominate, the potential's gradient must be small, resulting in an almost constant H and a quasi-de-Sitter state. The second equation identifies $|\dot{H}| < H^2$, such that our slow-roll parameter is

$$\epsilon = \frac{3\dot{\phi}^2}{\dot{\phi}^2 + 2V} \tag{3.15}$$

and is much less than unity while the field is slowly rolling.

Therefore we have identified a successful dynamical candidate that exhibits a quasi-de-Sitter behaviour. The field governing inflation is aptly dubbed the "inflaton". To further understand the dynamics of this field, we examine the equation of motion governing them: the Klein-Gordon equation,

$$\ddot{\phi} + 3H\dot{\phi} + V_\phi = 0. \tag{3.16}$$

In an expanding Universe, the scalar field experiences a damping effect due to the $H\dot{\phi}$ term. Moreover, we identify that the smallness of the potential's gradient is relative to the Hubble damping term. The scalar field will remain slowly rolling while the damping term dominates the dynamics of the field. By determining

$$\dot{\epsilon} = \frac{\dot{\phi}^2}{M_{\rm Pl}^2 H}\left(\frac{\ddot{\phi}}{\dot{\phi}H} + \epsilon\right) \tag{3.17}$$

we can then rewrite the second slow-roll parameter,

$$\eta = -\frac{\ddot{\phi}}{\dot{\phi}H}. \tag{3.18}$$

Therefore we can see that for $|\eta| \ll 1$, we have the constraint $\ddot{\phi} \ll H\dot{\phi}, V_\phi$, which enforces inflation to last sufficiently long.

Consequently, we conclude that slow-roll inflation is governed by the shape of the scalar field's potential. The approximation that the kinetic term is negligible and the acceleration vanishes in the Klein-Gordon equation, we can state

$$H^2 \simeq \frac{V}{3M_{\rm Pl}}, \qquad 3H\dot{\phi} \simeq -V_\phi. \tag{3.19}$$

This allows us to define the slow-roll parameter via the potential,

$$\epsilon \approx \epsilon_v \equiv \frac{M_{\rm Pl}^2}{2}\left(\frac{V_\phi}{V}\right)^2. \tag{3.20}$$

The subscript v identifies the slow-roll parameters defined by the potential. Using this result and substituting $\dot{\epsilon} = M_{\rm Pl}^2\dot{\phi}(V_\phi/V)(V_{\phi\phi} - (V_\phi/V)^2)$ into eq. (3.11), we find

$$\eta \approx \eta_v \equiv M_{\rm Pl}^2\frac{V_{,\phi\phi}}{V}. \tag{3.21}$$

We can further utilise the slow-roll approximation to determine the duration of inflation through the e-fold number. We characterise the end of

inflation when $\epsilon = 1$, so the field no longer exhibits a slow roll behaviour. We can determine the final field value at the end of inflation, subject to the potential, and integrate backwards to find the initial conditions required to produce a sufficient epoch,

$$N = \int_{a_i}^{a_f} d\ln(a) = \int_{t_i}^{t_f} H dt = \int_{\phi_f}^{\phi_i} \frac{d\phi}{\sqrt{2\epsilon_v} M_{\rm Pl}}. \tag{3.22}$$

Moreover, during a single field slow-roll epoch, we can also determine the cosmological parameters: the scalar tilt, n_s, and scalar-tensor ratio, r. We will discuss details of these parameters and cosmological perturbations during inflation in section 3.4, but summarise the findings of [74, 75] for slow-roll inflation. We utilise a spatially flat gauge for this example for an analytical expression [73]. In this gauge, we can directly relate the curvature perturbation to the field perturbation, $\mathcal{R} = \delta\phi H/\dot{\phi}$. By specifying the spectrum at the horizon crossing $k = aH$, the scalar and tensor power spectrum from eqs. (1.76) and (1.90) can be written as,

$$\mathcal{P}_{\mathcal{R}} = \frac{1}{8\pi^2 M_{\rm Pl}^2} \frac{H^2}{\epsilon} \qquad \mathcal{P}_{\mathcal{T}} = \frac{2}{\pi^2} \frac{H^2}{M_{\rm Pl}^2}.$$

Using the definition of eq. (1.78) and eq. (1.91) we find at the horizon crossing

$$n_s - 1 = 2\eta - 2\epsilon, \qquad r = 16\epsilon. \tag{3.23}$$

3.3 Modified gravity during inflation

Although inflation remains the current paradigm for the early universe, largely due to its simplicity, embedding inflation into a fundamental theory is still an ongoing challenge. We have discussed how inflation is driven by the matter sector, utilising a scalar field. However, benefiting from the slow-roll mechanism requires a careful choice of potential such that there is a sufficient shallow plateau region with the correct energy scale. This has resulted in numerous inflation models with distinct potentials and mechanisms.

To embed inflation into a more fundamental theory, we can declare the source of inflation is due to modifications of the gravitational sector [136]. In section 1.2, we identified how $f(R)$ could be interpreted as a new matter source. Analogous to the dynamical dark energy, we can utilise the modification to drive inflation with the slow-roll mechanism described above; thus, the scalaron becomes the inflaton. This assumes that modifications to GR appear naturally in fundamental theories at the given energy scale of inflation. However, many observational constraints have limited the allowed modified gravity models used [137, 138], therefore, the resulting scalaron potentials. For this chapter, we limit our study to $f(R)$ models, specifically extensions to Starobinsky's R^2 model, which we will examine below. For further details on the plethora of other models, see the reviews [42, 73–75, 139] and references within.

3.3.1 Starobinsky inflation

One of the earliest modified gravity inflationary models is Starobinsky's $f(R)$ model, developed in 1981, based on a higher-order R^2–term in the gravitational sector [128]. Despite its age, it has proven to be one of the most robust models of inflation, remaining consistent with advanced observations when other simple models have been ruled out [80]. Due to its simplicity and robustness, Starobinsky inflation provides an interesting phenomenological insight into the behaviour of modified gravity in the early universe. Consequently, there have been many works studying the R^2–model and its extensions, [41, 140–150].

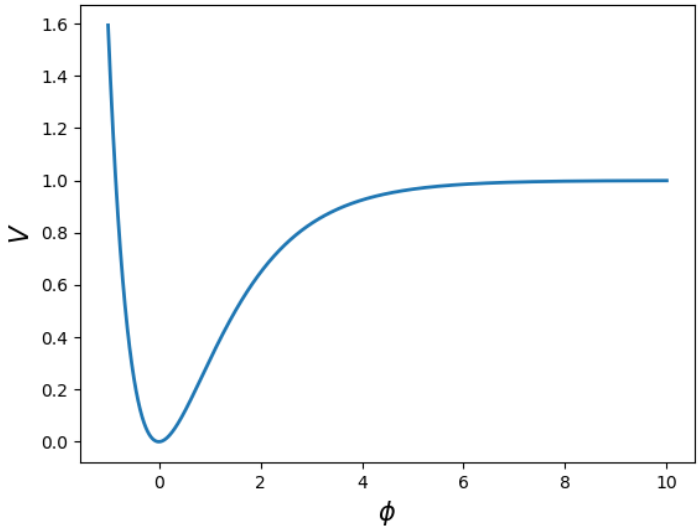

Figure 3.2: An illustration of the R^2 plateau given in eq. (3.25) with $M_{\rm Pl} = 1$ and $\mu = 2$.

Starobinsky's inflation is described by the $f(R)$ action,

$$\mathcal{S} = \frac{M_{\rm Pl}^2}{2} \int d^4x\sqrt{-g}\left[R + \frac{1}{\mu^2}R^2\right], \tag{3.24}$$

where μ is a model parameter and has dimensions of mass[6]. The higher-order correction remains subdominant during low curvatures and therefore hidden at the local scales. This is easily seen by mapping to the Einstein frame, where the additional scalar degree of freedom from the R^2 term, is re-defined as a scalar field, ϕ. Following the procedure outlined in section 1.2, the action becomes,

$$\mathcal{S} = \int d^4x\sqrt{-g}\left[\frac{M_{\rm Pl}^2}{2}R - \frac{1}{2}g^{\mu\nu}\partial_\mu\phi\partial_\nu\phi - \frac{M_{\rm Pl}^2\mu^2}{4}\left(1 - e^{-\sqrt{\frac{2}{3}}\frac{\phi}{M_{\rm Pl}}}\right)^2\right]. \tag{3.25}$$

We can now see that the field is determined by the given potential

$$V = \frac{M_{\rm Pl}^2\mu^2}{4}\left(1 - e^{-\sqrt{\frac{2}{3}}\frac{\phi}{M_{\rm Pl}}}\right)^2, \tag{3.26}$$

often known as an R^2 plateau due to its shape illustrated in fig. 3.2. Provided large field values, so the field sits along the plateau, it will experience the slow-roll behaviour described in section 3.2. Therefore we can estimate

[6]Provided that our action can be rewritten as eq. (3.25) our action is required to have dimensions of $[M]^4$. Therefore the additional degree of freedom, R^2,is set by μ. Interestingly, this sets the mass scale of the scalaron, as seen by eq. (3.26)

the end of inflation, using our slow-roll parameter, eq. (3.20), to find that inflation ends when $\phi \approx M_{\rm Pl}$. We find the duration of inflation is encoded into the initial conditions of the field ϕ. This can be shown by using eq. (3.22) to find

$$N \approx \frac{3}{4} e^{\sqrt{\frac{2}{3}} \frac{\phi_i}{M_{\rm Pl}}}, \tag{3.27}$$

where ϕ_i is the initial field value, and we have assumed that $\phi_i / M_{\rm Pl} \gg 1$. Using this relation, we can approximate the slow-roll parameters as a function of e-folds,

$$\epsilon_v \approx \frac{3}{4N^2}, \quad \eta_v \approx \frac{1}{N}. \tag{3.28}$$

Using the results found in eq. (3.23), the cosmological parameters, n_s and r can be written as

$$n_s - 1 = -\frac{2}{N}, \quad r = \frac{12}{N^2}. \tag{3.29}$$

This simple result is strongly supported by cosmological constraints from CMB measurements [41, 80], allowing Starobinsky to remain a valid inflation model with increasingly precise measurements, motivating further extensions of the work.

3.3.2 Scale invariant extension to Starobinsky inflation

We have studied single-field inflation models with an example of Starobinsky inflation that remains compatible with CMB observations. As discussed, this depends on certain conditions, such as the field's initial behaviour and the shape of the potential. Although modified gravity models can provide a more fundamental starting point by utilising the action, these conditions can limit the range of possible inflationary models and limit the range of phenomenology to be explored. Moreover, in recent years the parameter space from cosmological observations has forced many single-field models to be dismissed as incompatible [80]. On the other hand, multifield inflation allows for more diverse inflationary dynamics due to additional interaction between fields that can cause non-trivial behaviour. This can lead to different observable signatures in the CMB [151].

Multifield inflation can also be motivated by other high-energy theories. Many theories, such as string theory, predict multiple light scalar fields [152]. Including multiple fields can lead to distinguishable features in the CMB

that are observed by a non-standard potential, such as features in the power spectrum. In addition, multiple fields source non-adiabatic perturbations and deviations in the tensor perturbations in the early universe [153–155]. With advancing technology, signatures of these perturbations are expected to be detectable, thus, constraining theories beyond the standard model.

Multifield inflation provides a rich and diverse framework for studying the early universe and its properties, with new potential insights into fundamental physics beyond inflation. Therefore exploring beyond the most straightforward scenario can result in productive phenomenology. However, the field(s) governing the role of inflation remains to be discovered. As discussed later in section 3.5.1, the inflaton is heavy and assumed to decay away after inflation and unlikely to be detected with particle accelerators. Since the discovery of the Higgs field, a lot of literature has been dedicated to embedding the Higgs field, the only detected scalar field in the SM, as the inflaton [156, 157].

Scale-invariance is a fundamental principle in physics that states that the laws of nature remain unchanged when a variable is multiplied by a given constant parameter. This symmetry was first studied in the context of gravity by Weyl [158] with the original motivation to unify physics through geometry. With a new resurgent in interest [159, 150], scale-invariant GR provides a potential link to particle physics, such as being an important principle within the Higgs mechanism. Thus it is hoped that the study of scale symmetries in gravity may provide clues towards fundamental scalar fields and symmetries [160–162].

Scale-invariant GR requires modifications as the standard EH action will not inherently exhibit an invariant nature. If used in conjunction with multiple fields, a scale-invariant action can dynamically generate mass scales providing a structure for embedding the modifications into a more fundamental theory. Moreover, the modification introduces an interesting feature for multifield scale invariance, such as producing generic hierarchal vacuum expectation values for the fields. This feature suggests a potential explanation for the hierarchical nature between the energy scale of particle physics and gravity by assuming the Higgs field to be present during inflation and non-minimally coupled to gravity [163]. Therefore the theory of inflation

can be embedded into a larger fundamental framework of classical physics using a modified gravity that utilises the scale invariance.

In the remainder of this section, we consider extending Starobinsky inflation to implement the features of scale invariance. Thus, the action omits an intrinsic mass scale. Instead, the mass scale, identified as the Planck mass, is dynamically sourced by the interaction of the fields considered during inflation.

A two-field scale invariant model

We first briefly highlight the mechanisms utilised in scale-invariant inflation similar to models studied in [142, 143, 150, 159, 164–166]. We include an additional scalar field χ in the R^2 model, which couples to the Ricci-scalar to generate scale invariant action. The action in the Jordan frame is specified by,

$$\mathcal{S} = \int d^4x\sqrt{-\tilde{g}}\left(f(\tilde{R},\chi) - \frac{1}{2}\tilde{g}^{\mu\nu}\partial_\mu\chi\partial_\nu\chi - U(\chi)\right), \tag{3.30}$$

with

$$f(\tilde{R},\chi) = \frac{1}{2}A\chi^2\tilde{R} + \frac{B^2}{2}\tilde{R}^2, \tag{3.31}$$

$$U(\chi) = \frac{\lambda}{4}\chi^4. \tag{3.32}$$

Here, A, B and λ are constant parameters of the model. The action above, eqs. (3.30) to (3.32) is invariant under the global Weyl transformation

$$\begin{aligned} g_{\mu\nu} &\to e^{2\alpha}g_{\mu\nu}, \\ \chi &\to e^{-\alpha}\chi \end{aligned} \tag{3.33}$$

where α is a constant. We study the model in the Einstein frame following convention to analyse the predictions from inflation. We bring the action into the Einstein–frame via a conformal transformation of the metric following the procedure outlined in section 1.2. Defining the auxiliary field

$$\psi = \frac{\ln\left(2\kappa^2 f_{,\tilde{R}}\right)}{\beta\kappa}, \tag{3.34}$$

where κ is a generic mass scale and $\beta = \sqrt{2/3}$ to ensure a canonical kinetic term in the scalaron. We use the conformal transformation $\tilde{g}_{\mu\nu} = \exp(-2\beta\kappa\psi)g_{\mu\nu}$, to rewrite the action in the Einstein frame,

$$\mathcal{S} = \int dx^4\sqrt{-g}\left[\frac{R}{2\kappa^2} - \frac{1}{2}g^{\mu\nu}\partial_\mu\psi\partial_\nu\psi - \frac{1}{2}e^{-\beta\kappa\psi}\partial_\mu\chi\partial_\nu\chi - V(\psi,\chi)\right]. \tag{3.35}$$

Here we have identified $\kappa = M_{\rm Pl}^{-1}$. Therefore the additional degree of freedom in the Jordan frame, identified with $f_{,\tilde{R}}$, encodes the mass scale of the model, which we have identified with the Planck mass in the Einstein frame.

As discussed in section 1.2, the potential now characterises the system's dynamics. Our original potential, in the Jordan frame, is modified and now takes the form of,

$$4\kappa^4 V(\psi,\chi) = \frac{1}{2B^2}\left(1 - A\kappa^2\chi^2 e^{-\beta\kappa\psi}\right)^2 + \lambda\chi^4 e^{-2\beta\kappa\psi}. \tag{3.36}$$

At the minimum of the potential, specified by $V_\psi = V_\chi = 0$, we find

$$M_{\rm Pl}^2 = \frac{2B^2}{A}\left(\lambda + \frac{A^2}{2B^2}\right)\chi_{\rm min}^2 e^{-\beta\kappa\psi_{\rm min}} \tag{3.37}$$

where the subscript $\rm min$ identifies the fields at the global minimum, i.e. their vacuum expectation values (VEVs). We notice now that the Planck mass is determined by the parameters of the model and the ratio between the VEVs of the two fields. Analysing the potential further, we find the minimum is given by

$$V_{\rm T,min} = \frac{M_{\rm Pl}^4}{4}\frac{\lambda}{2B^2\lambda + A^2}. \tag{3.38}$$

Thus as long as λ does not vanish, a cosmological constant is generated[7]. Furthermore, we can calculate the mass of the scalaron, $m_\psi^2 = V_{\psi\psi}$, at the minimum

$$\frac{m_\psi^2}{M_{\rm Pl}^2} = \frac{1}{6B^2}\frac{A^2}{2B^2\lambda + A^2}. \tag{3.39}$$

Therefore, in this model, the cosmological constant and the scalaron mass are linked via

$$V_{\rm T,min} = \frac{3}{2}\frac{\lambda B^2}{A^2} m_\psi^2 M_{\rm Pl}^2. \tag{3.40}$$

The corresponding global symmetry found in the Jordan frame, eq. (3.33), also exists in the Einstein frame for the action given by (3.35) and the potential energy given by (3.36) with the field transformations,

$$\begin{aligned} \chi &\to e^\alpha \chi \\ \psi &\to \psi + \frac{\sqrt{6}}{\kappa^2}\alpha, \end{aligned} \tag{3.41}$$

[7] In the Jordan–frame, after inflation, the vacuum expectation value of χ does not vanish. The potential energy will not vanish if λ is non-zero, resulting in a positive cosmological constant.

leaving the Einstein–frame action invariant. Therefore using Noether's theorem which states, a symmetry in system will result in a conserved current or qunatity [167, 168]. In classical field theory the conserved current associated with the fields is given by,

$$j_\mu = \frac{\partial \mathcal{L}}{\partial^\mu(\phi^{(I)})}\delta\phi^{(I)} = c \tag{3.42}$$

where $\delta\phi$ is the transform associated with the symmetry, (I) identifies the scalar field, and c is a constant. Given that our Lagraingan is invariant about the Weyl transformation and omitting the associated constant α, our system results in the current

$$j_\mu = \sqrt{-g}\partial_\mu\left(3e^{\beta\kappa\psi} + \frac{1}{2}\chi^2\right) = c. \tag{3.43}$$

As we are considering a flat Robertson–Walker metric with

$$ds^2 = -dt^2 + a^2(t)\delta_{ij}dx^i dx^j,$$

our current becomes,

$$a^3\frac{d}{dt}\left(3e^{\beta\kappa\psi} + \frac{1}{2}\chi^2\right) = c. \tag{3.44}$$

Therefore, during inflation in which the scale factor grows quasi–exponentially, we quickly approach a regime where

$$3e^{\beta\kappa\psi} + \frac{1}{2}\chi^2 = \text{constant} \equiv 3\tilde{c}, \tag{3.45}$$

and the two–field model quickly becomes effectively a one–field system during slow-roll inflation. This allows us to rewrite eq. (3.36) as

$$\kappa^4 V_T = 9\left(1 - \tilde{c}e^{-\beta\kappa\psi}\right)^2\left(\frac{A^2}{2B^2} + \lambda\right). \tag{3.46}$$

As expected the effective potential is similar to standard Starobinsky, eq. (3.26).

We now turn to find the constraints on the parameter of the model. Apart from constraints coming from the spectral index, the tensor-to-scalar ratio and the amplitude of scalar perturbations generated during inflation, we will also discuss the implications of the non-vanishing vacuum energy density in the model.

The slow-roll parameters of our model are,

$$\epsilon_v = \frac{1}{2\kappa^2}\left(\frac{V_{T,\psi\psi}}{V}\right)^2 = \frac{4}{3}\frac{\tilde{c}^2}{(e^{\beta\kappa\psi} - \tilde{c})^2}, \tag{3.47}$$

$$\eta_v = \frac{1}{\kappa^2}\frac{V_{T,\psi\psi}}{V} = -\frac{4}{3}\tilde{c}\frac{e^{\beta\kappa\psi} - 2\tilde{c}}{\left(e^{\beta\kappa\psi} - \tilde{c}\right)^2}. \tag{3.48}$$

We have a successful slow-roll inflationary period while $\epsilon < 1$, which sets the field value at the end of inflation to be

$$\exp(\beta\kappa\psi_{\text{end}}) = (\tilde{c} + \tilde{c}\sqrt{3})/\sqrt{3}.$$

From the slow roll parameters, we determine the inflationary observables, eq. (3.23) ,the scalar spectral index, n_s and the tensor-to-scalar ratio, r, from the background fields,

$$n_s \simeq 1 - \frac{2}{N}, \qquad r \simeq \frac{12}{N^2}. \tag{3.49}$$

Here we have written n_s and r in terms of the number of e-folds, N, to highlight the fact that the prediction for these observables are the same as in Starobinsky inflation, eq. (3.29).

Finally, we constrain the model parameters. From CMB measurements, the energy scale of inflation is $V \approx 10^{-12} M_{\text{Pl}}^4$ [73, 74]. In our model, we use the form of (3.46) at the top of the plateau to constrain our parameters,

$$V \simeq \left(\frac{A^2}{2B^2} + \lambda\right) = 10^{-12} M_{\text{Pl}}^4 \tag{3.50}$$

Other than measurements from the CMB, constraints on modified gravity models have been introduced at local scales. For instance, from Casimir experiments, the scalaron's interaction range is constrained to be less than a millimetre, implying that $m_\psi^{-2} < 1\text{mm}^2$ [169]. This allows us to further constrain our model via (3.39) to give

$$\frac{B^4}{A^2} \lesssim 10^{77}. \tag{3.51}$$

Finally, we demand that the energy density at the minimum drives the cosmological expansion today, i.e. we set $V_T = 10^{-122} M_{\text{Pl}}$ at the minimum to be the observed dark energy density [80]. This gives the result

$$A \simeq 10^{-6} B, \qquad B \lesssim 10^{33} \quad \text{and} \quad \lambda < 10^{-65}. \tag{3.52}$$

This result implies that λ has to be unnaturally small, coming from the demand that the cosmological constant is small. Of course, in theory, dark energy might originate from a different sector, and we could demand that $\lambda = 0$. On the other hand, rather than relying on the self–interactions to

vanish or to be unnaturally small, it would be more satisfying if the resulting dark energy, interpreted as a cosmological constant, arising in this model is dynamically driven to zero during inflation.

A three–field scale invariant model

In light of the unnatural fine-tuning result of a generic two-field scale-invariant model, we extend it by modifying the potential by including an additional scalar field, to eliminate the cosmological constant and allow for more larger parameter ranges. The action we consider is a variant of the action (3.30), with the addition of a second field σ:

$$\mathcal{S} = \int d^4x\sqrt{-\tilde{g}}\left(f(\tilde{R},\chi) - \frac{1}{2}\tilde{g}^{\mu\nu}\partial_\mu\chi\partial_\nu\chi - \frac{1}{2}\tilde{g}^{\mu\nu}\partial_\mu\sigma\partial_\nu\sigma - U(\chi,\sigma)\right), \quad (3.53)$$

with

$$f(\tilde{R},\chi) = \frac{1}{2}A\chi^2\tilde{R} + \frac{B^2}{2}\tilde{R}^2 \quad (3.54)$$

$$U(\chi,\sigma) = \frac{\lambda}{4}(\chi^2-\sigma^2)^2. \quad (3.55)$$

Here we couple only χ to the Ricci–scalar and only χ determines the value of the Planck mass. An extension of the model in which also the σ–field couples to the Ricci–scalar is possible, but that would introduce additional parameters and results in σ mimicking the role of χ[8] . The role of the field σ is to drive the cosmological constant in the Einstein–frame to zero. It is possible to fix σ to a constant, but this would break the scale-invariant setup.

In the Einstein frame the action becomes a three-field system and reads

$$\mathcal{S} = \int d^4x\sqrt{-g}\left\{\frac{R}{2\kappa^2} - \frac{1}{2}g^{\mu\nu}\left[\partial_\mu\psi\partial_\nu\psi + e^{-\beta\kappa\psi}\left(\partial_\mu\chi\partial_\nu\chi + \partial_\mu\sigma\partial_\nu\sigma\right)\right] - V(\psi,\chi,\sigma)\right\}, \quad (3.56)$$

with the potential

$$V(\psi,\chi,\sigma) = \frac{1}{8B\kappa^4}\left(1 - A\kappa^2\chi^2e^{-\beta\kappa\psi}\right)^2 + \frac{\lambda}{4}\left(\chi^2-\sigma^2\right)^2e^{-2\beta\kappa\psi}. \quad (3.57)$$

With the addition of the new field, the potential has now a global minimum at which $V=0$. This is similar to a dynamical Higgs VEV model shown in [161]. At the minimum we have

$$\chi^2_{\rm min} = \sigma^2_{\rm min}, \qquad e^{\beta\kappa\psi_{\rm min}} = \kappa^2A\sigma^2_{\rm min}. \quad (3.58)$$

[8]This would allow us to redefine the field σ as a linear function of χ. This would not provide any new phenomenology.

The equations of motion for the fields in our model are given by:

$$\Box\psi = \frac{\partial V}{\partial \psi} - \frac{\beta\kappa}{2} e^{-\beta\kappa\psi} g^{\mu\nu} \left(\partial_\mu \chi \partial_\nu \chi + \partial_\mu \sigma \partial_\nu \sigma\right), \tag{3.59}$$

$$\Box\chi = \beta\kappa g^{\mu\nu} \partial_\mu \psi \partial_\nu \chi + \frac{\partial V}{\partial \chi} e^{-\beta\kappa\psi}, \tag{3.60}$$

$$\Box\sigma = \beta\kappa g^{\mu\nu} \partial_\mu \psi \partial_\nu \sigma + \frac{\partial V}{\partial \sigma} e^{-\beta\kappa\psi}. \tag{3.61}$$

In an expanding homogeneous and isotropic universe, the Friedmann equation reads

$$H^2 = \frac{\kappa^2}{3}\left[\frac{1}{2}\dot{\psi}^2 + \frac{1}{2} e^{-\beta\kappa\psi}\left(\dot{\chi}^2 + \dot{\sigma}^2\right) + V(\psi, \chi, \sigma)\right]. \tag{3.62}$$

The action is invariant under the following transformations of the fields

$$\sigma \to e^{\alpha}\sigma,$$

$$\chi \to e^{\alpha}\chi,$$

$$\psi \to \psi + \frac{\sqrt{6}}{\kappa^2}\alpha,$$

and as before there is a conserved current, which allows us to reduce our system to an effective two field case at late times during inflation. Repeating the procedure of the two-field case, we find that the conserved current results in, at late times,

$$\chi^2 + \sigma^2 = \mathcal{C} - \frac{6}{\kappa^2} e^{\beta\kappa\psi}, \tag{3.63}$$

where $\mathcal{C}$ is a constant of integration specified by initial conditions for the fields that arise under the assumption that the fields exhibit a slow-roll behaviour. This has been confirmed numerically with various initial conditions and parameters. We will use this result in the next section to simplify and understand the results of our model.

Background evolution

Since the three-field system is too complicated to find useful analytical solutions, we study the inflationary dynamics and the evolution of perturbations numerically. The following set of background equations governs the evolution of the fields:

$$\ddot{\psi} + 3H\dot{\psi} + V_\psi = -\frac{\beta\kappa}{2} e^{-\beta\kappa\psi}\left(\dot{\chi}^2 + \dot{\sigma}^2\right), \tag{3.64}$$

$$\ddot{\chi} + (3H - \beta\kappa\dot{\psi})\dot{\chi} + V_\chi e^{-\beta\kappa\psi} = 0, \tag{3.65}$$

$$\ddot{\sigma} + (3H - \beta\kappa\dot{\psi})\dot{\sigma} + V_\sigma e^{-\beta\kappa\psi} = 0. \tag{3.66}$$

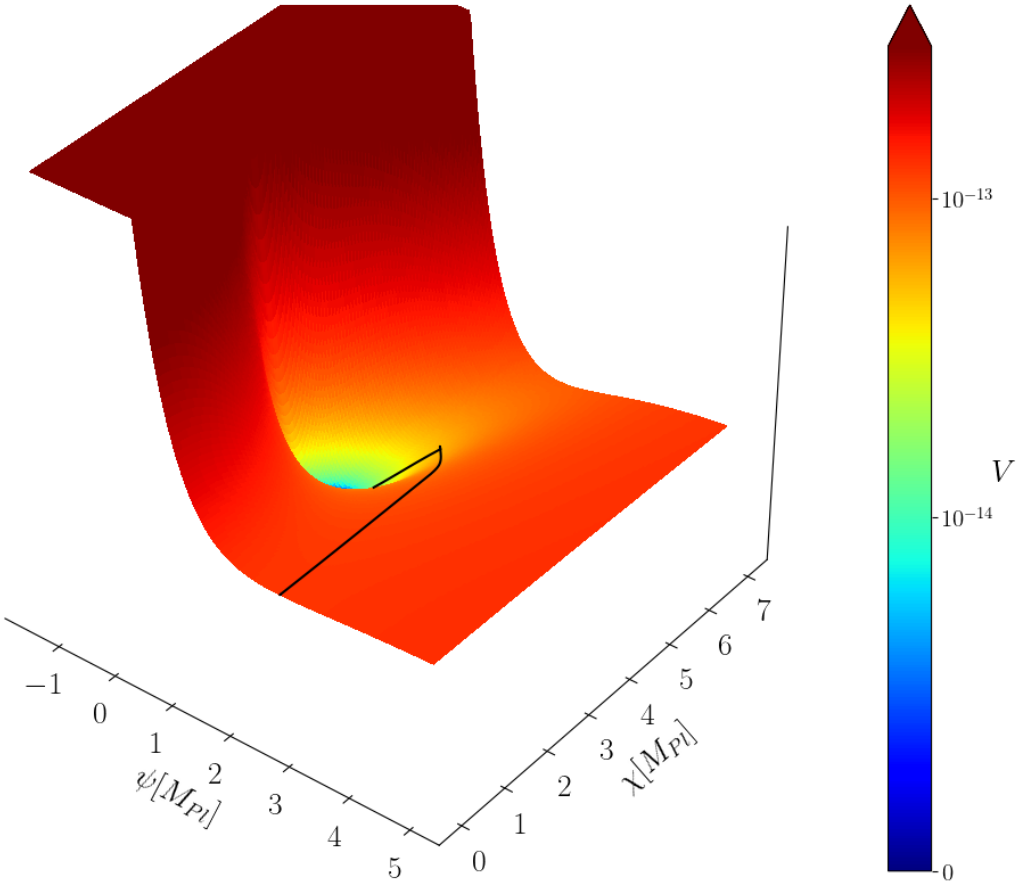

Figure 3.3: A 3D surface plot above its contour of the three field potential (3.57). Here we have used the surface plot to illustrate the two slow-roll regimes, with the trajectory plotted on top in blue. We have set, $A = 0.05$, $B = 10^6$, $\lambda = 10^{-15}$ and used eq. (3.63) to trade σ in favour of χ and ψ with $\mathcal{C} = 7.7$, to match the used initial conditions of fig. 3.4. The colour bar indicates the value of the potential in Planck units.

For the Noether current to remain a constant such that eq. (3.63) is fulfilled, we require the scale factor to increase exponentially and the Universe to undergo a quasi-de-Sitter expansion. This can be seen in eq. (3.44). The current becomes a constant after the first few e-folds. Using this equation to relate σ to χ and ψ and plugging this into the potential, V, we obtain an effective two–field potential. The precise form of this effective two-field potential depends on the initial conditions for the fields, encoded in the constant $\mathcal{C}$ in eq. (3.63), but there are some general features, as seen in fig. 3.3: in the ψ–direction we have plateau-like potential with a barrier near $\psi = 0$, which is typical for R^2 theories. However, the addition of σ creates a well in the potential. At the bottom of the well, the potential energy vanishes.

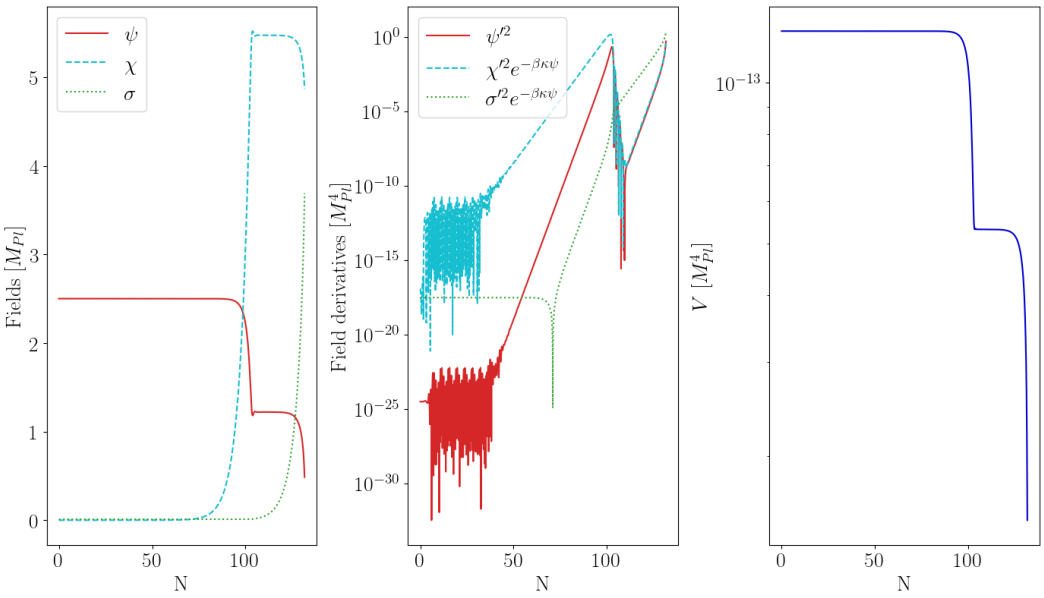

(a) Background quantities: ψ, χ, σ, their respective velocities, and V.

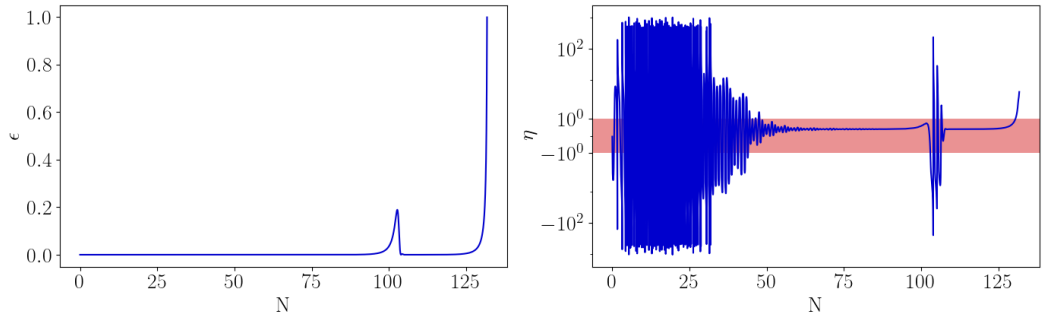

(b) Slowroll parameters ϵ and η with the bounds of $|\eta| < 1$ shown in red.

Figure 3.4: fig. 3.4a illustrates the background evolution of the fields. The left plot shows the field evolution, the middle plot is the effective velocity of the fields with respect to e-folds, and the right is the value of the potential. Note ψ and χ have two periods of slow-roll, $N = 0 - 100,\ 100 - 125$. fig. 3.4b depicts the slow roll parameters. The left plots shows ϵ, identifying the end of inflation with $\epsilon = 1$. The right plot shows η, where the red band highlights the bounds $|\eta| < 1$. We can identify the separation of the two periods of inflation around $N \approx 100$ by the increase in value of the two parameters. The parameters and initial conditions are $A = 0.05$, $B^2 = 2 \times 10^{12}$, $\lambda = 10^{-15}$, $\psi = 2.5$, $\chi = 10^{-8}$, and $\sigma = 10^{-2}$.

The dynamics of the fields depend on the initial conditions. Here, we focus on the case where $\sigma_{\text{ini}} \approx 0$ and $\chi, \psi > 0$. In the first part of inflation, $\sigma \approx 0$ is effectively frozen, whereas ψ and χ are rolling down the potential. Eventually, the two fields roll off the plateau, at which point the slow–roll

conditions are briefly violated, as seen from the evolution of the slow-roll parameter in fig. 3.4. The condition $\eta \ll 1$ is severely violated at this point, creating additional features in the power spectrum, as we will see later. Afterwards, ψ and χ–fields settle in a local valley (shown in fig. 3.3). This marks the end of the first period of inflation. The two fields, ψ and χ are effectively frozen compared to the σ–field. The σ field continues to roll, minimising the coupling to the χ field. After $N \approx 25$, ψ and χ begin to steadily roll faster, while σ remains frozen, this allows η to settle. Around $N \approx 70$ σ begins to roll such that $\sigma \to \chi$. This forces all of the fields to fall into the global minimum, driving the potential to zero and ending inflation. We conclude from this model that the initial conditions dictate the final values of χ, σ and ψ and the e-folds of each period of inflation.

Summary of scale invariant inflation

We have studied the scale-invariant two-field and three-field model as an extension of Starobinksy's R^2 inflation, introduced in [143, 150]. For the two-field case, we have identified that while it is a successful inflationary model, a non-zero cosmological constant is generated due to the self-coupling of the scalar field χ, whose VEV generates the Planck mass. To remove the potentially large cosmological constant at the end of inflation, we extend the model and add another scalar field σ, interacting with χ in a scale-invariant way, forcing the vacuum energy to vanish at the global minimum. Thus, we have used the three-field scenario to probe for new insights into scale-invariant inflation.

Our results in this three-field example of inflation demonstrate several non-trivial features that can occur during inflation. The model can exhibit two periods of inflation. The two periods are separated by a brief (and mild) violation of the smallness of the ϵ slow roll parameter and a noticeable drop in potential energy. The first period of inflation exhibits similar dynamics to that of the two-field case as the additional field σ is effectively frozen at $\sigma = 0$. The only noticeable difference in behaviour is the severe violation of the slow-roll parameter, η, initially within this model due to the locally bound χ and σ field. Although not majorly affecting the model dynamics, this feature essentially traps the χ–field, thus prolonging this period of

inflation.

The transition between the two periods of inflation marks a shift in the hierarchy of the fields dominating the slow-roll behaviour, with the kinetic term of σ dominating over the other fields. As this second period of inflation is short and within approximately 20 e-folds of the end of inflation, it is expected to have significant consequences for the resulting power spectrum. Therefore the addition of a third field, initially with the motivation to remove the cosmological constant, has the potential to induce non-trivial features due to only interacting within the final e-folds of inflation.

3.4 Cosmological perturbations during inflation

3.4.1 Single field perturbations

We now build upon our discussion of cosmological perturbations in section 1.3.1 in the Newtonian gauge, following the work of [75, 73, 76, 170] and extend it to model inflationary perturbations. Until now, we have described the background dynamics of inflation using homogeneous scalar fields. We extend the work to include, to first order, inhomogeneous perturbations,

$$\psi(t) \to \psi(t) + \delta\psi(t, x). \tag{3.67}$$

As a starting example, we will assume a standard quintessence Lagrangian of eq. (1.16), with an FRLW metric, resulting in the equation of motion,

$$\Box\psi - V_\psi = 0,$$

and the stress-energy tensor of the form eq. (1.18). To linear order for a single field the perturbed energy density, pressure, and scalar momentum (eqs. (1.68) to (1.70)) read, respectively:

$$\delta\rho = \dot{\psi}\delta\dot{\psi} - \dot{\psi}^2\Phi + V_\psi\delta\psi, \tag{3.68}$$

$$\delta P = \dot{\psi}\delta\dot{\psi} - \dot{\psi}^2\Phi - V_\psi\delta\psi, \tag{3.69}$$

$$\delta q = -\dot{\psi}\delta\psi. \tag{3.70}$$

In Fourier space, the scalar field perturbation is governed by a perturbed KG equation,

$$\delta\ddot{\psi} + 3H\delta\dot{\psi} + \frac{k^2}{a^2}\delta\psi + V_{\psi\psi}\delta\psi = -2V_\psi\Phi + 4\dot{\psi}\dot{\Phi}, \tag{3.71}$$

where k is the wavenumber. It will be useful to define the gauge invariant Mukhanov-Sasaki (MS) variable [171]

$$Q = \delta\psi + \frac{\dot{\psi}}{H}\Phi. \tag{3.72}$$

This is related to the comoving curvature perturbation,

$$\mathcal{R} = -\frac{H}{\dot{\psi}}Q. \tag{3.73}$$

Therefore if we can find approximate solutions to MS variable, we can understand the behaviour of the curvature perturbation at different scales. Using the MS variable we can remove the metric perturbation to obtain an equivalent equation of motion to eq. (3.71),

$$\ddot{Q} + 3H\delta\dot{Q} + \left[\frac{k^2}{a^2}\delta\psi + V_{\psi\psi} - \frac{1}{M_{\rm Pl}^2 a^3}\left(\frac{a^3\dot{\psi}^2}{H}\right)\right]Q = 0. \tag{3.74}$$

This equation can be simplified even further by introducing new variables, $u = aQ$ and $z = a\dot{\psi}/H$. Switching to conformal time, τ, where the prime indicates the derivative with respect to τ, this results in

$$u'' + (k^2 - \frac{z''}{z})u = 0. \tag{3.75}$$

This is known as the Mukhanov-Sasaki equation [171] and is also the equation for a harmonic oscillator with a frequency given by,

$$\omega^2 = k^2 - \frac{z''}{z}. \tag{3.76}$$

In the context of slow-roll inflation, where $H \approx const$ and $\ddot{\psi}$ is negligible, we see that $z''/z \to a''/a \approx 2(aH)^2$, where we have used the definition of conformal time, $dt = ad\tau$. This means that the term z''/z is proportional to the inverse of the comoving Hubble radius. We can now analyse the behaviour of u and, correspondingly, the curvature perturbation in different regimes. In the subhorizon scale at early times, when the Hubble radius is much larger than the physical wavelength of fluctuations, we have the limit $k^2 \gg z''/z$. This means that $\omega \approx k$, and our MS equation becomes

$$u'' = -k^2 u, \tag{3.77}$$

exhibiting an oscillating behaviour with the solution $u \propto e^{\pm ik\tau}$. This will correspond to an oscillating curvature perturbation decaying as the Universe expands. If we assume at the beginning of inflation, $\tau \to -\infty$, all fluctuations were at subhorizon scales, the MS equation has the approximate solution [9]

$$u = \frac{1}{\sqrt{2k}} e^{-ik\tau}. \tag{3.78}$$

This is known as the Bunch-Davis vacuum (BD) solution [172].

Eventually, as required the comoving Hubble radius will shrink as inflation progresses until the modes are larger than the Hubble radius [10] and they exit the horizon. This results in $k^2 \ll z''/z$ and $\omega \approx -z''/z$. The MS equation now becomes,

$$u'' = \frac{z''}{z} u, \tag{3.79}$$

which results in two solutions $u \propto z$ and $u \propto z^{-2}$. Analysing the curvature perturbation $\mathcal{R} = -\frac{u}{z}$, we can see that the growing solution, $u \propto z$, results in a constant curvature perturbation, $\mathcal{R} \to const$, effectively freezing the perturbation in superhorizon scales. The decaying solution $u \propto z^{-2}$ results in a negligible contribution to $\mathcal{R}$ in an expanding Universe.

The power spectrum from the definition, eq. (1.76), becomes

$$\mathcal{P}_{\mathcal{R}} = \frac{k^3}{2\pi^2} \left| \frac{u}{z} \right|^2. \tag{3.80}$$

The entropy from eq. (1.77), becomes

$$\mathcal{S} = 2\frac{HV_\psi}{\dot{\rho}\dot{P}} \left(\ddot{\psi}\delta\psi - \dot{\psi}\delta\dot{\psi} - \dot{\psi}\dot{\Phi} \right). \tag{3.81}$$

However, we notice the term inside the brackets is equivalent to $-\delta\rho + 3H\delta q$. Therefore rewriting this in terms of the metric perturbation, using eqs. (1.68) and (1.69),

$$\mathcal{S} \propto -\frac{k^2}{a^2}\Phi. \tag{3.82}$$

Therefore entropy perturbations quickly drop with the expansion of the Universe and are negligible for single-field inflation.

[9] The proportionality of the solution is found through the quantisation of u, where we assume we are in a sufficiently flat spacetime due to de-Sitter expansion. This means that the FLRW metric can be approximated to a Minkowski spacetime [73].

[10] Another interpretation, dependent on the frame, is the fluctuations are stretched beyond the Hubble radius, as depicted in fig. 3.1

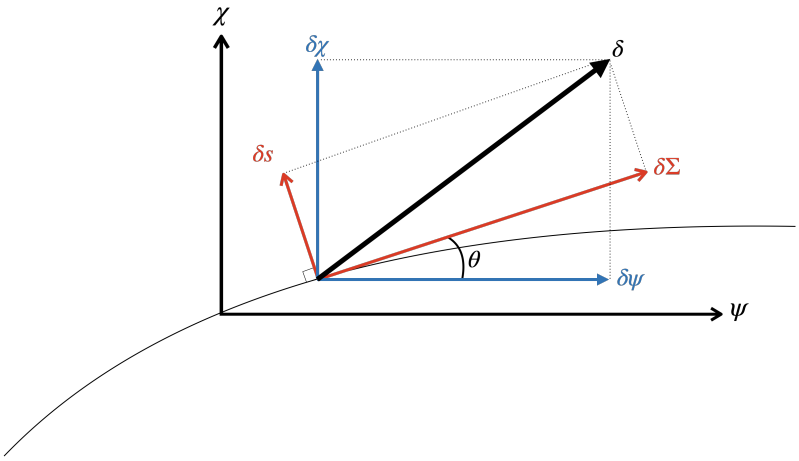

Figure 3.5: A diagram, adapted from [75], depicting the adiabatic, $\delta\Sigma$, and entropy, δs, perturbations, related to the original field perturbations, $\delta\psi$ and $\delta\chi$ by eqs. (3.92) and (3.93), utilising the defined angle, θ, and the resulting perturbation given by δ. The diagram is given on an axis of the background fields, and the solid line gives the background field trajectory.

3.4.2 Two field perturbations

As discussed in section 3.3.2, a natural extension to the theory of inflation is to include additional degrees of freedom. In the remainder of this section, we consider how the perturbations change in multi-field inflation. Thus, we include an additional background field χ. The fields are chosen to resemble the fields in the model of section 3.3.2. We will assume that both fields follow the equations of motion arising from a modified gravity model mapped into the Einstein frame detailed in sections 1.2 and 3.3.2,

$$\ddot{\psi} + 3H\dot{\psi} - b_\psi e^{2b}\dot{\chi}^2 + V_\psi = 0, \tag{3.83}$$

$$\ddot{\chi} + (3H + 2b_\psi\dot{\psi})\dot{\chi} + e^{-2b}V_\chi = 0, \tag{3.84}$$

with

$$\rho = \frac{\dot{\psi}^2 + e^{2b}\dot{\chi}^2}{2} + V, \qquad P = \frac{\dot{\psi}^2 + e^{2b}\dot{\chi}^2}{2} - V. \tag{3.85}$$

To keep the formulation general, b is an arbitrary linear function of ψ. This can be specified to the section 3.3.2 by setting $b = -\beta\kappa\psi$. This gives rise to the perturbed KG equations,

$$\delta\ddot{\psi} + 3H\delta\dot{\psi} + \left(\frac{k^2}{a^2} + V_{\psi\psi} - b_\psi^2 e^{2b}\dot{\chi}^2\right)\delta\psi - 2b_\psi e^{2b}\dot{\chi}\delta\dot{\chi} + V_{\psi\chi}\delta\chi = 4\dot{\psi}\dot{\Phi} - 2V_\psi\Phi, \tag{3.86}$$

$$\delta\ddot{\chi} + (3H + 2b_\psi\dot{\psi})\delta\dot{\chi} + \left(\frac{k^2}{a^2} + e^{-2b}V_{\chi\chi}\right)\delta\chi + 2b_\psi\dot{\chi}\delta\dot{\psi} + e^{-2b}\left(V_{\chi\psi} - 2b_\psi V_\chi\right)\delta\psi = 4\dot{\chi}\dot{\Phi} - 2e^{-2b}V_\chi\Phi. \tag{3.87}$$

The perturbed energy density and momentum read

$$\delta\rho = \dot{\psi}\delta\dot{\psi} + e^{2b}\dot{\chi}\delta\dot{\chi} - (\dot{\psi}^2 + e^{2b}\dot{\chi}^2)\Phi + b_\psi e^{2b}\dot{\chi}^2\delta\psi + V_\psi\delta\psi + V_\chi\delta\chi, \tag{3.88}$$

$$\delta q = -\dot{\psi}\delta\psi - e^{2b}\dot{\chi}\delta\chi. \tag{3.89}$$

In single field inflation, the comoving curvature perturbation is defined in the direction of the inflaton. However, the inclusion of additional fields requires the identification of the overall background trajectory of the fields. As such, the two fields, ψ and χ can be redefined into the adiabatic field[11] Σ, representing the path of the background fields, and the entropy field s, representing the movement orthogonal to the background trajectory. This formalism was introduced in [75, 79], which we summarise below.

We define the directional velocity of the adiabatic field by Pythagoras' theorem according to the background fields,

$$\dot{\Sigma}^2 = \dot{\psi}^2 + e^{2b}\dot{\chi}^2. \tag{3.90}$$

Therefore, we can determine the relative angle of the field to the background trajectory,

$$\cos(\theta) = \dot{\psi}/\dot{\Sigma}, \qquad \sin(\theta) = e^b\dot{\chi}/\dot{\Sigma} \tag{3.91}$$

Utilising the relative angles, we can then formulate the adiabatic field as linear combinations of the field perturbations as illustrated in fig. 3.5,

$$\delta\Sigma = \cos(\theta)\delta\psi + \sin(\theta)e^b\delta\chi, \tag{3.92}$$

and the orthogonal entropy field,

$$\delta s = \cos(\theta)e^b\delta\chi - \sin(\theta)\delta\psi. \tag{3.93}$$

The KG equation neatly governs the adiabatic field,

$$\ddot{\Sigma} + 3H\dot{\Sigma} + V_\Sigma = 0, \tag{3.94}$$

[11] The two new fields, Σ and s, are not physical fields; they are defined to encode the dynamical behaviour of the model's scalar fields, simplifying the calculations.

where $V_\Sigma = \cos(\theta)V_\psi + \sin(\theta)e^{-b}V_\chi$. With the new redefinition of adiabatic and entropy fields, we can repeat the procedure outline for the single field case, section 3.4.1, to find the comoving curvature perturbation. In the same way as before, we define the MS variable for our adiabatic field,

$$Q_\Sigma = \delta\Sigma + \frac{\dot{\Sigma}}{H}\Phi. \tag{3.95}$$

This MS quantity is related to the standard field MS variables by the defined rotation given in the definition of Σ, eq. (3.92)

$$Q_\Sigma = \cos^2(\theta)Q_\psi + \sin^2(\theta)e^b Q_\chi. \tag{3.96}$$

Therefore we see that Q_Σ identifies the perturbation that is parallel to the background directional velocity. As such, the total comoving curvature perturbation, eq. (3.73), which is defined to be in the direction of the background trajectory, becomes

$$\mathcal{R} = \frac{H}{\dot{\Sigma}}Q_\Sigma = \cos(\theta)\mathcal{R}_\psi + \sin(\theta)e^b\mathcal{R}_\chi, \tag{3.97}$$

where $\mathcal{R}_\psi$ and $\mathcal{R}_\chi$ are the curvature perturbations for the fields, ψ and χ, respectively. We also define the entropy perturbation, which can be expressed in terms of our entropy field

$$\mathcal{S} = \frac{H}{\dot{\Sigma}}\delta s. \tag{3.98}$$

With additional interactions in our system, the entropy perturbations are more important than in the single field case, as they do not vanish on large scales. Moreover, by taking the derivative of the comoving curvature perturbation, we find that the entropy perturbations source the curvature perturbation

$$\dot{\mathcal{R}} = \frac{H}{\dot{H}}\frac{k^2}{a^2}\Phi - \frac{2H}{\dot{\Sigma}^2}V_s\delta s, \tag{3.99}$$

where $V_s = \cos(\theta)e^{-b}V_\chi - \sin(\theta)V_\psi$. This quantity describes how the fields will change depending on each field's effective potential. In the literature, it is common to use the turning rate, $\dot{\theta}$, to illustrate the sourcing effect of the comoving curvature, defined as

$$\dot{\theta} = -V_s/\dot{\Sigma} - b_\psi\dot{\Sigma}\sin(\theta),$$

which encodes how the background field trajectory changes and therefore Q_Σ. Provided $\dot{\theta} \neq 0$, which identifies different regimes of fields dominating

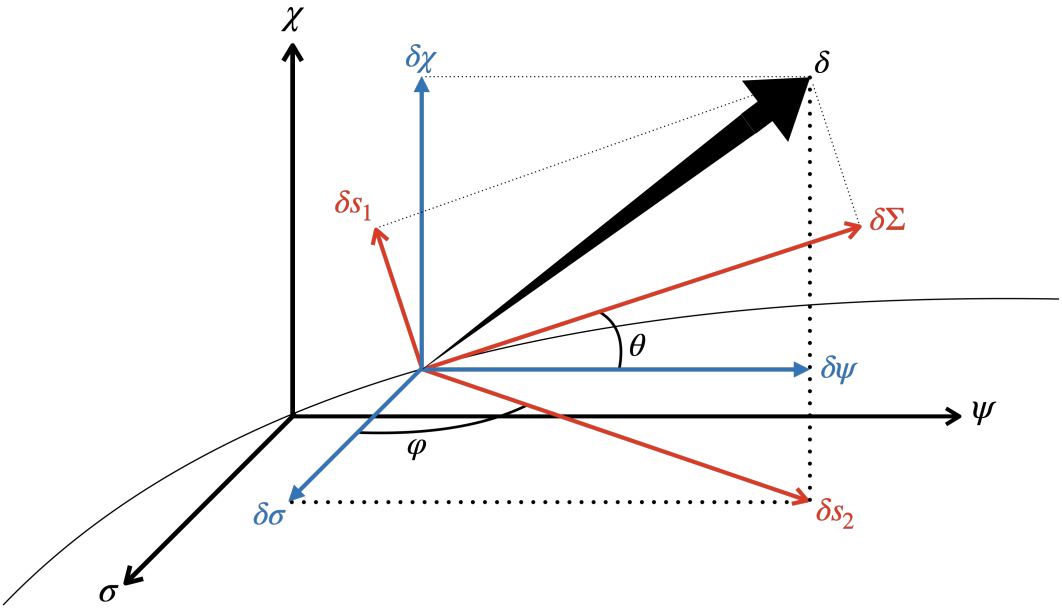

Figure 3.6: An extension of the diagram fig. 3.5, to include an additional field, $\delta\sigma$, with an additional angle, φ fixed in the $\sigma - \psi$ plane, while θ remains fixed to the $\chi - \psi$ plane. Due to the additional dimension in field space, an additional entropy is required, which can be identified with the subscript 2 and the subscript 1 indicates the entropy perturbation in fig. 3.5. To illustrate the 3D nature of the perturbations, the perturbation arrow δ is shown coming out of the page.

the perturbations, non-trivial features arise due to the sourcing effect of $\mathcal{R}$. This will then affect the resulting power spectrum resulting in potentially detectable signatures.

3.4.3 Three field perturbations

In the scale-invariant model studied in section 3.3.2, we determined that three fields were required. Thus, we extend the formalism above to include three fields, allowing us to calculate the power spectrum for our three-field model in section 3.3.2. We maintain the procedure of decomposing the field perturbations into tangential and orthogonal components with respect to the trajectory of the background fields. Again, the tangential perturbation equates to the curvature or adiabatic component, while we identify the orthogonal perturbations as entropy components. As described in [173] we have one curvature component and $D - 1$ entropy components, where D is the number of fields. In the two-field case, we redefined the fields using

a 2D circular coordinate system. Therefore, given an additional degree of freedom, we utilise, in this section, a 3D spherical coordinate system to redefine the field perturbations.

We will assume the equations of motion for three fields are determined from a modified gravity action mapped into the Einstein frame, as done in section 3.3.2. To make the link to the model studied in section 3.3.2 explicit we identify the fields (ψ, χ, σ) such that the KG equations read,

$$\ddot{\psi} + 3H\dot{\psi} - b_\psi e^{2b}\dot{\chi}^2 + V_\psi = 0, \tag{3.100}$$

$$\ddot{\chi} + (3H + 2b_\psi\dot{\psi})\dot{\chi} + e^{-2b}V_\chi = 0, \tag{3.101}$$

$$\ddot{\sigma} + (3H + 2b_\psi\dot{\psi})\dot{\sigma} + e^{-2b}V_\sigma = 0, \tag{3.102}$$

with

$$\rho = \frac{\dot{\psi}^2 + e^{2b}\left(\dot{\chi}^2 + \dot{\sigma}^2\right)}{2} + V, \qquad P = \frac{\dot{\psi}^2 + e^{2b}\left(\dot{\chi}^2 + \dot{\sigma}^2\right)}{2} - V, \tag{3.103}$$

and b is a linear function of ψ, to allow further generalisation of the formalism used. This will result in the corresponding perturbed KG equations and energy and momentum constraints from the perturbed EFEs:

$$\begin{aligned}\delta\ddot{\psi} + 3H\delta\dot{\psi} + \left[\frac{k^2}{a^2} + V_{\psi\psi} - 2b_\psi^2(\dot{\chi}^2 + \dot{\sigma}^2)e^{2b}\right]\delta\psi \\ + V_{\psi\chi}\delta\chi + V_{\psi\sigma}\delta\sigma - 2b_\psi e^{2b}(\dot{\chi}\delta\dot{\chi} + \dot{\sigma}\delta\dot{\sigma}) = 4\dot{\Phi}\dot{\psi} - 2V_\psi\Phi,\end{aligned} \tag{3.104}$$

$$\begin{aligned}\delta\ddot{\chi} + 3H\delta\dot{\chi} + \left[\frac{k^2}{a^2} + V_{\chi\chi}e^{-2b}\right]\delta\chi - 2b_\psi(\dot{\chi}\delta\dot{\psi} + \dot{\psi}\delta\dot{\chi}) \\ + \left(V_{\chi\psi} - 2b_\psi V_\chi\right)e^{-2b}\delta\psi + V_{\chi\sigma}e^{-2b}\delta\sigma = 4\dot{\Phi}\dot{\chi} - 2V_\chi e^{-2b}\Phi,\end{aligned} \tag{3.105}$$

$$\begin{aligned}\delta\ddot{\sigma} + 3H\delta\dot{\sigma} + \left[\frac{k^2}{a^2} + V_{\sigma\sigma}e^{-2b}\right]\delta\sigma - 2b_\psi(\dot{\sigma}\delta\dot{\psi} + \dot{\psi}\delta\dot{\sigma}) \\ + \left(V_{\sigma\psi} - 2b_\psi V_\sigma\right)e^{-2b}\delta\psi + V_{\sigma\chi}e^{-2b}\delta\chi = 4\dot{\Phi}\dot{\sigma} - 2V_\sigma e^{-2b}\Phi,\end{aligned} \tag{3.106}$$

$$\begin{aligned}\delta\rho = \dot{\psi}\delta\dot{\psi} + e^{2b}\left[\dot{\chi}\delta\dot{\chi} + \dot{\sigma}\delta\dot{\sigma} + b_\psi\delta\psi(\dot{\chi}^2 + \dot{\sigma}^2)\right] \\ - \left[\dot{\psi}^2 + e^{2b}(\dot{\chi}^2 + \dot{\sigma}^2)\right]\Phi + V_\psi\delta\psi + V_\chi\delta\chi + V_\sigma\delta\sigma,\end{aligned} \tag{3.107}$$

$$\delta q = -\dot{\psi}\delta\psi - e^{2b}\left(\dot{\chi}\delta\chi + \dot{\sigma}\delta\sigma\right). \tag{3.108}$$

To ensure the curvature perturbation is in the direction of the background trajectory, we assume the fields can be redefined into a new adiabatic field Σ (not to be confused with the additional classical field σ introduced in section 3.3.2). This allows the curvature perturbation to be written in terms of the field perturbations. As before in section 3.3.2 we require the perturbations to be decomposed into tangential and orthogonal perturbations, with respect to the background trajectory. Using the definition of the curvature perturbation, eq. (3.73), that depicts the tangential perturbation, we define an analogous result to eq. (3.97),

$$\mathcal{R} = H\frac{Q_\Sigma}{\dot{\Sigma}} = H\frac{\dot{\psi}Q_\psi + e^b\dot{\chi}(e^bQ_\chi) + e^b\dot{\sigma}(e^bQ_\sigma)}{\dot{\Sigma}^2}. \tag{3.109}$$

Here we have used the standard MS variables,

$$Q_\psi = \delta\psi + \frac{\dot{\psi}}{H}\Phi, \quad Q_\chi = \delta\chi + \frac{\dot{\chi}}{H}\Phi, \quad Q_\sigma = \delta\sigma + \frac{\dot{\sigma}}{H}\Phi, \tag{3.110}$$

and,

$$\dot{\Sigma}^2 = \dot{\psi}^2 + e^{2b}\left(\dot{\chi}^2 + \dot{\sigma}^2\right) \tag{3.111}$$

is the three-field adiabatic component, representing the velocity parallel to the trajectory. This allows us to define Q_Σ as the instantaneous curvature Mukhanov-Sasaki variable corresponding to the perturbations parallel to the trajectory of $Q_\psi, e^bQ_\chi, e^bQ_\sigma$, defined in the same way as [79]. Following the methodology laid out in [174], we set up our three-field model by extending the 2D circular coordinate system to a 3D spherical system. Using the $Q_\psi, e^bQ_\chi, e^bQ_\sigma$, as a coordinate basis we define

$$Q_\Sigma \equiv \sin(\varphi)\left(\cos(\theta)Q_\psi + \sin(\theta)e^bQ_\chi\right) + \cos(\varphi)e^bQ_\sigma. \tag{3.112}$$

Substituting the ansatz into the defined $\mathcal{R}$ for three-fields in eq. (3.109), we determine the corresponding angles:

$$\begin{aligned} \cos(\varphi) &= \frac{e^b\dot{\sigma}}{\dot{\Sigma}}, & \sin(\varphi) &= \frac{\sqrt{\dot{\psi}^2 + e^{2b}\dot{\chi}^2}}{\dot{\Sigma}}, \\ \cos(\theta) &= \frac{\dot{\psi}}{\sqrt{\dot{\psi}^2 + e^{2b}\dot{\chi}^2}}, & \sin(\theta) &= \frac{e^b\dot{\chi}}{\sqrt{\dot{\psi}^2 + e^{2b}\dot{\chi}^2}}. \end{aligned} \tag{3.113}$$

In this notation the explicit form of the orthogonal perturbation is

$$\delta\Sigma = \sin(\varphi)\left(\cos(\theta)\delta\psi + \sin(\theta)e^b\delta\chi\right) + \cos(\varphi)e^b\delta\sigma. \tag{3.114}$$

We will use the MS form of the orthonormal perturbation for ease. With the angles established, we can calculate the entropy perturbations, δs_1 and δs_2, which are defined to be orthogonal to the trajectory, eq. (3.112):

$$\delta s_1 = \cos(\varphi)\left[\cos(\theta)Q_\psi + \sin(\theta)(e^b Q_\chi)\right] - \sin(\varphi)(e^b Q_\sigma), \tag{3.115}$$

$$\delta s_2 = -\sin(\theta)Q_\psi + \cos(\theta)(e^b Q_\chi). \tag{3.116}$$

Using (3.113) we can rewrite this in terms of the fields,

$$\delta s_1 = \frac{e^b\dot\sigma}{\dot\Sigma\sqrt{\dot\psi^2+e^{2b}\dot\chi^2}}\left[\dot\psi Q_\psi + e^b\dot\chi(e^bQ_\chi)\right] - \frac{\sqrt{\dot\psi^2+e^{2b}\dot\chi^2}}{\dot\Sigma}(e^bQ_\sigma), \tag{3.117}$$

$$\delta s_2 = \frac{-e^b\dot\chi Q_\psi + \dot\psi(e^bQ_\chi)}{\sqrt{\dot\psi^2+e^{2b}\dot\chi^2}}. \tag{3.118}$$

We can then calculate the entropy component,

$$\mathcal{S}_i = \delta s_i H/\dot\Sigma. \tag{3.119}$$

More importantly, we now have a complete system for our three field system that allows us to relate our field perturbations into tangential and normal components via the rotational matrix,

$$\begin{pmatrix} Q_\Sigma \\ \delta s_1 \\ \delta s_2 \end{pmatrix} = \begin{pmatrix} \sin(\varphi)\cos(\theta) & \sin(\varphi)\sin(\theta) & \cos(\varphi) \\ \cos(\varphi)\cos(\theta) & \cos(\varphi)\sin(\theta) & -\sin(\varphi) \\ -\sin(\theta) & \cos(\theta) & 0 \end{pmatrix} \begin{pmatrix} Q_\psi \\ e^bQ_\chi \\ e^bQ_\sigma \end{pmatrix}. \tag{3.120}$$

As seen in eq. (3.99), we predict that $\mathcal{R}$ has a non-negligable sourcing term arising from the entropy components. To do this, and for completion, we find the Klein-Gordon equation for our adiabatic field,

$$\ddot\Sigma + 3H\dot\Sigma + V_\Sigma = 0, \tag{3.121}$$

and the turning rates,

$$\dot\varphi = -\frac{V_{s_1}}{\dot\Sigma} + b_\psi\dot\Sigma\cos\theta\cos\varphi, \qquad \dot\theta = -\frac{V_{s_2}}{\sqrt{\dot\psi^2+e^{2b}\dot\chi^2}} - \frac{\dot\Sigma}{\sqrt{\dot\psi^2+e^{2b}\dot\chi^2}}b_\psi\dot\Sigma\sin\theta. \tag{3.122}$$

The adiabatic and entropy potentials follow the same rotation as (3.120),

$$\begin{pmatrix} V_\Sigma \\ V_{s_1} \\ V_{s_2} \end{pmatrix} = \begin{pmatrix} \sin(\varphi)\cos(\theta) & \sin(\varphi)\sin(\theta) & \cos(\varphi) \\ \cos(\varphi)\cos(\theta) & \cos(\varphi)\sin(\theta) & -\sin(\varphi) \\ -\sin(\theta) & \cos(\theta) & 0 \end{pmatrix} \begin{pmatrix} V_\psi \\ e^{-b}V_\chi \\ e^{-b}V_\sigma \end{pmatrix}. \tag{3.123}$$

Taking the derivative of $\mathcal{R}$, with respect to time, we find a similar compact version to [79, 175, 176] and eq. (3.99)

$$\dot{\mathcal{R}} = \frac{H}{\dot{H}}\frac{k^2}{a^2}\Phi - 2\frac{H}{\dot{\Sigma}^2}(V_{s_1}\delta s_1 + V_{s_2}\delta s_2). \tag{3.124}$$

We see that the additional entropy term, $V_{s_1}\delta s_1$, provides an additional contribution to the source term. Finally, using (3.107) and (3.108), this allows us to rewrite our perturbed Klein-Gordon equations (3.104) - (3.106) as

$$\begin{aligned}\ddot{Q}_\psi + 3H(\dot{Q}_\psi) - 2b_\psi e^{2b\psi}\left(\dot{\chi}\dot{Q}_\chi + \dot{\sigma}\dot{Q}_\sigma\right) \\ + \left(\frac{k^2}{a^2} + C_{\psi\psi}\right)Q_\psi + C_{\psi\chi}Q_\chi + C_{\psi\sigma}Q_\sigma = 0,\end{aligned} \tag{3.125}$$

$$\ddot{Q}_\chi + 3H\dot{Q}_\psi + 2b_\psi\dot{\chi}\dot{Q}_\chi + 2b_\psi\dot{\psi}\dot{Q}_\chi + \left(\frac{k^2}{a^2} + C_{\chi\chi}\right)Q_\chi + C_{\chi\psi}Q_\psi + C_{\chi\sigma}Q_\sigma = 0, \tag{3.126}$$

$$\ddot{Q}_\sigma + 3H\dot{Q}_\sigma + 2b_\psi\dot{\sigma}\dot{Q}_\psi + 2b_\psi\dot{\psi}\dot{Q}_\sigma + \left(\frac{k^2}{a^2} + C_{\sigma\sigma}\right)Q_\sigma + C_{\sigma\psi}Q_\psi + C_{\sigma\chi}Q_\chi = 0, \tag{3.127}$$

with the coefficients

$$\begin{aligned}
C_{\psi\psi} &= V_{\psi\psi} + \frac{2\kappa^2}{H}V_\psi\dot{\psi} + 3\kappa^2\dot{\psi}^2 - 2b_\psi^2\kappa^2(\dot{\chi}^2 + \dot{\sigma}^2)e^{2b} - \frac{\kappa^4\dot{\psi}^2}{2H^2}\dot{\Sigma}^2, \\
C_{\psi x} &= V_{\psi x} + \frac{\kappa^2}{H}V_\psi\dot{x}e^{2b} + \frac{\kappa^2}{H}V_x\dot{\psi} + 3\kappa^2e^{2b}\dot{\psi}\dot{x} - \frac{\kappa^4\dot{\psi}\dot{x}e^{2b}}{2H^2}\dot{\Sigma}^2, \\
C_{xx} &= V_{xx}e^{-2b} + \frac{2\kappa^2}{H}V_x\dot{x} + 3\kappa^2\dot{x}^2e^{2b} - \frac{\kappa^4\dot{x}e^{2b}}{2H^2}\dot{\Sigma}^2, \\
C_{x\psi} &= V_{x\psi}e^{-2b} + \frac{\kappa^2}{H}V_\psi\dot{x} + \frac{\kappa^2}{H}V_x\dot{\psi}e^{-2b} - 2b_\psi V_x e^{-2b} + 3\kappa^2\dot{\psi}\dot{x} - \frac{\kappa^4\dot{\psi}\dot{x}}{2H^2}\dot{\Sigma}^2, \\
C_{x\tilde{x}} &= V_{x\tilde{x}}e^{-2b} + \frac{\kappa^2}{H}V_{\tilde{x}}\dot{x} + \frac{\kappa^2}{H}V_x\dot{\tilde{x}} + 3\dot{x}\dot{\tilde{x}}\kappa^2e^{2b} - \frac{\kappa^4\dot{x}\dot{\tilde{x}}e^{2b}}{2H^2}\dot{\Sigma}^2.
\end{aligned}$$

The perturbed KG equations, eqs. (3.125) to (3.127), are invariant in the exchange of χ and σ, as expected from the symmetry seen in eq. (3.63). Thus for brevity, we implement the notation where $x = \chi$ or σ and $\tilde{x} = \sigma$ or χ represents the other field. Using eqs. (3.125) to (3.127), we can compute $\mathcal{R}$, $\mathcal{S}_1$ $\mathcal{S}_2$ for our three-field system.

Three field scale invariant example

To calculate the resulting power spectra and determine constraints on the three-field model considered in section 3.3.2, we utilised the derived formulation of section 3.4.3. Here we present the numerical procedure of

determining the primordial power spectrum for a three-field system and the resulting predicted angular power spectrum, n_s and r for the system studied in section 3.3.2.

We numerically integrate eqs. (3.125) to (3.127), using the results of section 3.3.2. We assume that the fields start deep inside the Hubble radius. Therefore we impose BD initial conditions eq. (3.78) for our tangential and normal perturbations $(Q_\Sigma, \delta s_1, \delta s_2)$ at $k = 50aH$. Assuming initially slow-rolling light fields, the eqs. (3.125) to (3.127) become uncouple in the limit $k \gg aH$. This results in independent adiabatic and entropy fluctuations deep inside the Hubble radius [75, 174, 177]. This can be further highlighted by eq. (3.124), where $\mathcal{R}$ is only effectively sourced by the metric perturbations, akin to single-field inflation.

Therefore, to ensure no correlation between the curvature and entropy modes deep inside the Hubble radius, we integrate the perturbation equations three times with different initial conditions. In the first run, we choose Q_Σ to have BD initial conditions and $\delta s_1 = \delta s_2 = 0$; then we permute these initial conditions on each component. We indicate the run by Roman numerals so that the results of each run are $\mathcal{R}_{\rm I}$, $\mathcal{R}_{\rm II}$ and $\mathcal{R}_{\rm III}$ and correspondingly for $\mathcal{S}_{1,(I,II,III)}$ and $\mathcal{S}_{2,(I,II,III)}$. Then we compute the curvature and isocurvature power spectrum from our three runs and obtain the prediction for the power spectra as follows:

$$\mathcal{P}_{\mathcal{R}}(k) = \frac{k^3}{2\pi^2}\left(|\mathcal{R}_{\rm I}|^2 + |\mathcal{R}_{\rm II}|^2 + |\mathcal{R}_{\rm III}|^2\right), \tag{3.128}$$

$$\mathcal{P}_{\mathcal{S}_1}(k) = \frac{k^3}{2\pi^2}\left(|\mathcal{S}_{1,\rm I}|^2 + |\mathcal{S}_{1,\rm II}|^2 + |\mathcal{S}_{1,\rm III}|^2\right), \tag{3.129}$$

$$\mathcal{P}_{\mathcal{S}_2}(k) = \frac{k^3}{2\pi^2}\left(|\mathcal{S}_{2,\rm I}|^2 + |\mathcal{S}_{2,\rm II}|^2 + |\mathcal{S}_{2,\rm III}|^2\right), \tag{3.130}$$

with the tensor modes computed using eq. (1.90). To compute cosmological observables, we set a reference scale of $k_0 = 0.05$ Mpc^{-1} to leave the Hubble radius 50 e-folds before the end of inflation, allowing for a comparison to literature.

Our results shown in fig. 3.7, show an interesting feature, an initial drop in power before exhibiting the expected near-scale invariance. This is the result of the initial violation of the slow-roll condition $\eta \gg 1$ shown in fig. 3.4. As discussed in section 3.3.2, is due to the initial set-up of the fields:

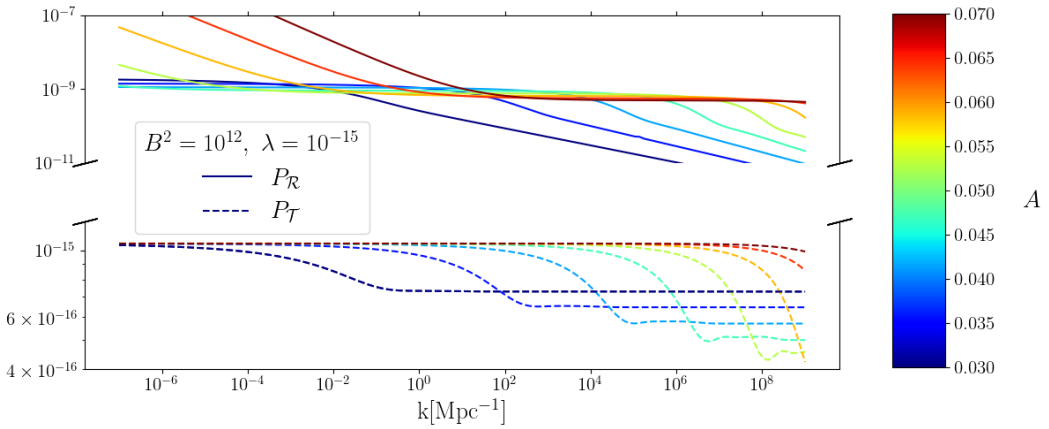

(a) Variation of A on $\mathcal{P}_\mathcal{R}$ and $\mathcal{P}_\mathcal{T}$

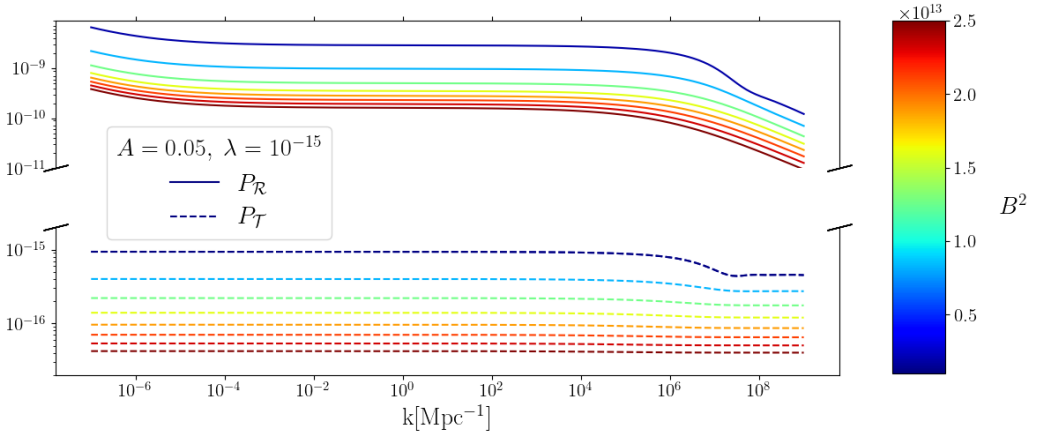

(b) Variation of B on $\mathcal{P}_\mathcal{R}$ and $\mathcal{P}_\mathcal{T}$

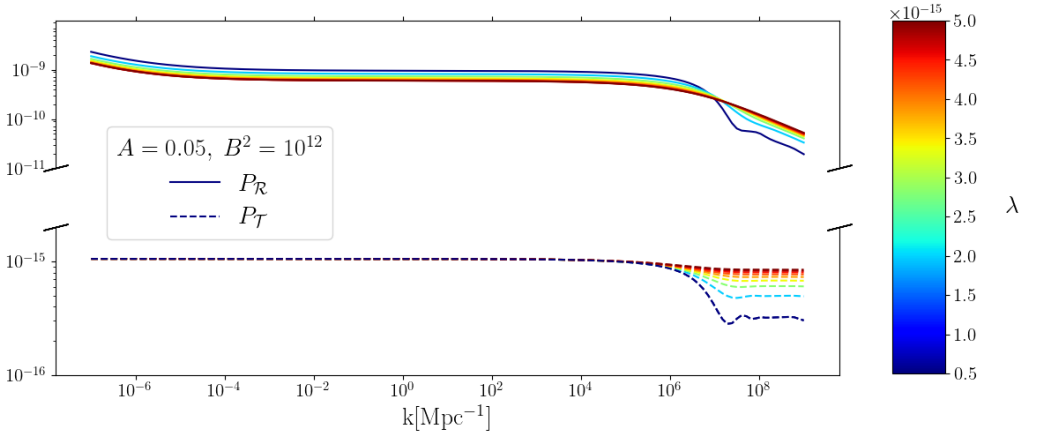

(c) Variation of λ on $\mathcal{P}_\mathcal{R}$ and $\mathcal{P}_\mathcal{T}$

Figure 3.7: The curvature (solid) and tensor (dashed) power spectrum, evaluated at the end of inflation. We have varied parameters, A fig. 3.7a, B fig. 3.7b and λ fig. 3.7c and used the same initial conditions to compute fig. 3.4.

Considering the initial conditions used to produce fig. 3.7, the initial value of σ is small but larger than χ. However, the potential's gradient in the σ–direction is smaller than in the χ–direction, the value of χ will eventually become larger than σ, creating a brief period of strong interactions between the two fields at that time. This causes χ to oscillate as it rolls, which can be seen from the evolution of $\dot{\chi}$ in fig. 3.4. This results in ϵ remaining small, but causes η to osciallate with a large amplitude, as shown in fig. 3.4. The drop in amplitude in fig. 3.7 at large scales, which we observe in some runs for some choice of parameter, is because those scales cross the Hubble radius during this initial period in which η becomes large.

An alternative set-up of initial conditions where $\sigma_{\text{ini}} < \chi_{\text{ini}}$ was also studied: the violation of the slow–roll condition $\eta \ll 1$ does not occur, and there is no drop in amplitude of power at small k–values. A change in parameter choice is required in this scenario to ensure that the spectrum has an amplitude $O(10^{-9})$.

Length scales that cross the Hubble radius during the first period of inflation produced a near-scale invariant power spectrum. This is to be expected as our fields behave similarly to standard Starobinsky inflation, slowly rolling on the plateau, as shown fig. 3.4. In our numerical runs, we have chosen the parameter such that the amplitude of the scalar perturbations matches data from the CMB. For large k–values, we see a drop in the power spectrum caused by the end of the second period of inflation as the fields fall into the global minimum of the potential. The σ–field is evolving considerably during the second period of inflation. This, in turn, forces the fields into a steep potential, increasing the velocity of the fields. This drop of power at small scales in fig. 3.7 means our model does not predict the formation of primordial black holes from a spike in the power spectrum [133, 178]. Unlike similar models to ours, our potential does not create large entropy perturbations; we see the opposite effect due to the evolution of σ from zero (this effect has been studied in similar models to ours in [179] and [180]).

We also individually vary each of the parameters A, B and λ in fig. 3.7 while keeping the initial conditions for the fields fixed, to analyse the effect the parameter choice has on the results.

We also analyse the effect of changing the parameters on the resulting power spectrum. From fig. 3.7a, we see that A determines the range of k–values for which the power spectrum of scalar perturbations is nearly scale–independent. This is because A determines the width of the valley region in the potential, as seen from eq. (3.57). A smaller parameter A results in an earlier start of the second period of inflation (for a given set of initial conditions). Thus this alters the time at which the term corresponding to k^2/a^2 becomes subdominant in eqs. (3.125) to (3.127) compared to the second derivative of the gradient, which creates a peaked damping term. This increased damping term reduces the entropic sourced term in eq. (3.124), thus setting $\mathcal{R} = const.$

On the other hand, B determines the steepness of the potential into the valley region and the overall energy scale of the plateau, with smaller B decreasing the gradient and λ determines the valley's potential energy, as seen from eq. (3.57). The parameter B and λ affect the ψ and χ-field's speed during the transition to the second period of inflation. Therefore affecting the spike in the evolution of epsilon seen in fig. 3.4. As such, they have a large effect on the amplitude of the power spectrum, depicted in figs. 3.7b and 3.7c for wave numbers which leave the horizon around the transition from the first to the second period of inflation as illustrated in figs. 3.7b and 3.7c.

Consequently, the standard power law of eq. (1.79) does not describe the resulting predicted power spectra well for any of the runs in fig. 3.7. From our numerical simulations, we find that the predicted tensor-to-scalar ratio $r(k_0)$ is of order 10^{-6}, substantially reduced from the two field case described in section 3.3.2 and similar models [150, 159]. Other R^2 scale-invariant models find a similar reduction in r, such as [145, 181]. For the parameters values $A = 0.055$, $B = 10^6$, and $\lambda = 10^{-15}$, we find that the spectral index is consistent with current CMB observations, $n_s(k_0 = 0.05) \simeq 0.97$, and has a substantial running ($\alpha_s \approx 10^{-2}$) at large scales but varies widely and becomes negative at large wavenumbers. However the running of α_s, $\beta_s(k_0) \approx -10^{-3}$, remains approximately of a similar order of magnitude, but negative, to α_s for all values of k. The model is an example in which isocurvature modes can cause the running of the spectral index and the running of the running

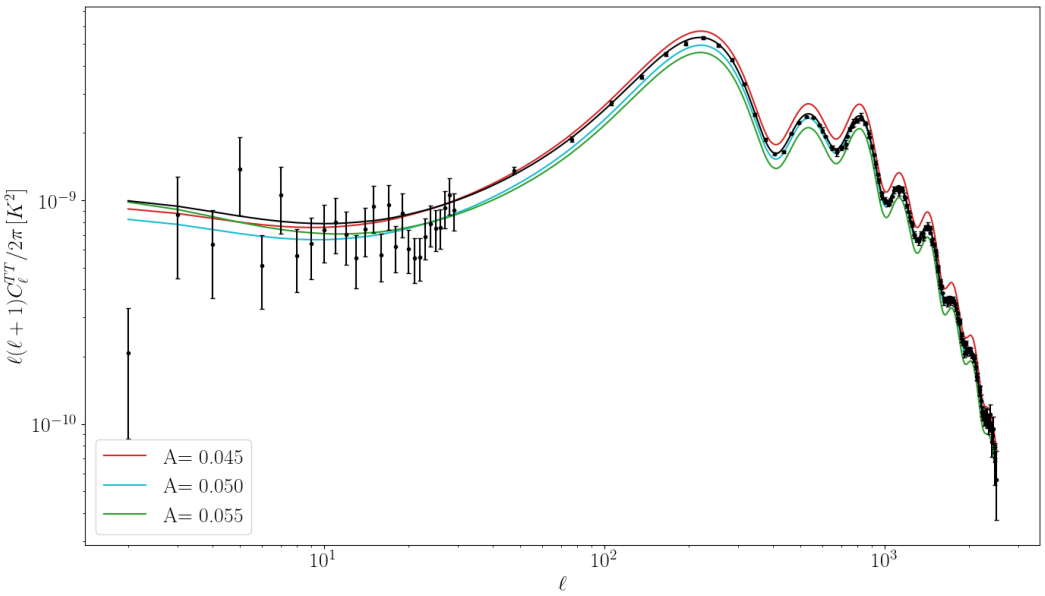

Figure 3.8: The CMB temperature lensed angular spectra based off our model with $B^2 = 5 \times 10^{11}$ and $\lambda = 10^{-15}$, and initial conditions used in fig. 3.4. The solid black is calculated from the standard power-law with $P_{\mathcal{R}}(k = 10^{-2}) = 2 \times 10^{-9}$ and $n_s = 0.965$ with data points from [68] for reference.

to be of a similar order of magnitude [182].

Finally, we investigate how the introduced features impact the predictions of the CMB angular spectra. As shown in Figure 3.7, it is clear that modifying B or λ corresponds to a change power spectrum's amplitude. As such, we constrain the value of B and λ such that $P_{\mathcal{R}}(k_0) \simeq 2 \times 10^{-9}$ with $A = 0.05$. We then compute the CMB temperature angular spectra, using CAMB [183], while varying A fig. 3.8. We see that the features naturally manifest themselves at lower multipoles. However, even a small change in the parameter A causes a shift in the amplitude of the power spectrum.

3.4.4 Summary of cosmological perturbations

We have extended the perturbation formalism used for two–field of [79] and [174] to three fields. Using a similar methodology, we created three orthogonal components in field space, one of which was tangential to the resulting direction. This then allowed us to compute the scalar primordial power spectrum. This formalism was then used to continue the analyses of the three-field system in the Einstein frame, in which inflation is driven by

three scalar fields (χ, σ and the scalaron ψ).

As discussed, our results show that the model can exhibit two periods of inflation, separated by a brief violation of the smallness of the ϵ slow roll parameter. We have numerically solved the perturbation equations and determined the power spectrum for different parameter values. From the amplitude of CMB anisotropies, we find that small values for the parameter A are preferred ($A \approx 10^{-2}$). We identify three regimes in the predicted scalar power spectrum: at large scales, where the scales cross the horizon before all three fields begin to slow roll, the power decreases due to violation of the smallness of the η parameter; at intermediate scales, the power spectrum is flat and can match the CMB data; and at large wavenumbers, we find a further decrease in the amplitude for very large k–values (the scales leave the horizon in the second period of inflation, at the time when σ rolls significantly and is driving the potential to zero, eventually ending inflation).

We also discussed the predictions for the spectral index n_s, its running α_s, the running of the running β_s and the tensor–to–scalar ratio r. We see a substantial reduction in r compared to ordinary R^2–inflation and its scale–invariant version [143, 150]. We find that our model can potentially break the usual hierarchy $n_s > |\alpha_s| > |\beta_s|$, due to entropy perturbations produced by the σ field, making the model testable with current and future cosmological data.

3.5 Reheating

As we have discussed, one of the major successes of inflation is the effectiveness of homogenising the Universe by evolving with a quasi-de-Sitter behaviour. However, we know that the expansion also affects the temperature of the Universe. A rapid expansion means the Universe falls out of thermal equilibrium and enters a cold non-thermal state [184]. However, after inflation we know that the Universe will slowly begin to cool due to its decelerated expansionas seen in fig. 1.5, until our measured value today of $T \approx 3K$ [80]. The temperature of the Universe at the end of inflation has a lower bound $T \gg 1MeV$ for nucleosynthesis to be compatible with cosmological observations [75, 185, 186] and an upper bound $T < 10^{14}$GeV set from the energy scale of inflation [75, 187, 188]. Thus, a model of the transition between the two epochs, inflation and a radiation-dominated HBB, is required. Moreover, we are left with an empty universe and fast-rolling scalar field(s) after inflation. In contrast, we require a hot thermal bath of plasma that will cool, decouple and form the elementary particles of the standard model of particle physics.

Reheating describes a mechanism that transfers the energy density initially dominated by the inflaton's potential into the production of particles. This is through an oscillatory decay of the inflaton. As we will discuss, the decay rate is proportional to the mass of the inflaton. Therefore, the effectiveness of reheating is determined by the model's potential. The process of heating the Universe after inflation is often considered part of the theory of inflation, as the potential highly determines the model's validity during the expansion phase and the phase transition into a hot plasma.

We outline the mathematical process of the reheating mechanism from [75, 189, 149] before utilising the three-field scale-invariant inflation, section 3.3.2, as an example. Whilst we will only cover the notion of reheating in this thesis, many other mechanisms can create a hot thermal plasma of the HBB. A commonly studied mechanism, through a non-perturbative production, of inducing an increase in temperature and starting particle production is preheating. This is achieved through parametric resonance and exciting field fluctuations. Many models have used preheating as an efficient mecha-

nism to produce particles and it is often used in combination with reheating [190, 191]

3.5.1 The three field model in the Jordan frame

We present the mechanism of reheating in the context of the example model studied above in section 3.3.2. We choose to keep the resulting energy density of the scalaron non-minimally coupled to gravity and, unless specified, not coupled to SM particles. Therefore, we study reheating in the Jordan frame allowing an explicit choice of interaction between the fields and the SM particles. We begin by summarising the dynamics in the Jordan frame.

The action is the same used in section 3.3.2, eq. (3.53), rewritten here for brevity,

$$\mathcal{S} = \int d^4x\sqrt{-g}\left(f(R,\chi) - \frac{1}{2}g^{\mu\nu}\left(\partial_\mu\chi\partial_\nu\chi + \partial_\mu\sigma\partial_\nu\sigma\right) - V(\chi,\sigma)\right) + \mathcal{S}_m, \tag{3.131}$$

with

$$f(R,\chi) = \frac{1}{2}A\chi^2 R + \frac{B^2}{2}R^2, \qquad V(\chi) = \frac{\lambda}{4}(\chi^2 - \sigma^2). \tag{3.132}$$

We find the equations of motion in the Jordan frame for the scalaron using the procedure shown in section 1.2,

$$3\Box F + FR - 2f = T. \tag{3.133}$$

Explicitly defining the scalaron as a field, $F = \phi$, we conclude the curvature can be written as

$$R = \frac{\phi - \frac{1}{2}A\chi^2}{B^2}. \tag{3.134}$$

This allows us to determine the equations of motion for the scalaron in terms of the other fields. Assuming that matter and radiation are negligible in the early universe, $\rho^{(m)} = \rho^{(r)} = 0$, the only contribution to the stress-energy tensor is the other inflationary fields,

$$\Box\phi = V_\phi + \frac{1}{3}T^{(\chi,\sigma)}, \tag{3.135}$$

where the potential is given by eq. (1.21),

$$V_\phi = \frac{1}{3}(2f - \phi R) = \frac{A\chi^2}{6B^2}(\phi - \frac{1}{2}A\chi^2).$$

Here we have marked the stress-energy tensor and subsequently the corresponding energy density and pressure with a superscript in brackets as a bookkeeping term to indicate the field dynamics. We will assume, as we did for inflation, that the metric is of the form of the FLRW metric, eq. (1.37). The resulting equations of motion for the fields are,

$$\begin{aligned}\ddot{\phi} + 3H\dot{\phi} &= -V_\phi + \frac{1}{3}\left(\rho^{(\chi,\sigma)} - 3P^{(\chi,\sigma)}\right), \\ \ddot{\chi} + 3H\dot{\chi} &= -V_\chi + A\chi R, \\ \ddot{\sigma} + 3H\dot{\sigma} &= -V_\sigma.\end{aligned} \tag{3.136}$$

We complete our equations of motion with the field equations in a flat FLRW metric as given by eqs. (1.47) and (1.48),

$$\begin{aligned}H^2 &= \frac{\phi R - f}{6\phi} - H\frac{\dot{\phi}}{\phi} + \frac{\rho^{(\chi,\sigma)}}{3\phi}, \\ \dot{H} &= \frac{R}{6} - 2H^2.\end{aligned} \tag{3.137}$$

The corresponding energy density and pressure is given by

$$\begin{aligned}\rho^{(\chi,\sigma)} &= \frac{1}{2}(\dot{\chi}^2 + \dot{\sigma}^2) + V(\chi,\sigma), \\ P^{(\chi,\sigma)} &= \frac{1}{2}(\dot{\chi}^2 + \dot{\sigma}^2) - V(\chi,\sigma).\end{aligned} \tag{3.138}$$

A detailed study of the inflationary dynamics for his model has been completed in the Einstein frame in section 3.3.2. To illustrate the physical equivalence, the background dynamics of the fields are shown in fig. 4.5 to be compared to fig. 3.4. We know that $\chi = \sigma$ at the minimum of the potential by design, and consequently $\phi = A\chi^2/2$. Therefore we determine the masses of the fields ($m_x^2 = V_{xx}$) at the end of inflation in terms of the VEV of χ_{min},

$$\begin{aligned}m_\phi^2 &= \frac{A\chi_{\text{min}}^2}{6B^2}, \\ m_\chi^2 = m_\sigma^2 &= 2\lambda\chi_{\text{min}}^2.\end{aligned} \tag{3.139}$$

As described in section 3.3.2, the Planck mass is dynamically given by eq. (3.58), which sets $A\chi_{\text{min}}^2 = M_{\text{Pl}}^2\phi_{\text{min}}$. Moreover, we discussed for the model to be compatible with current cosmological data, we found $A \simeq 0.05$, $B \simeq 10^6$, $\lambda \simeq 10^{-15}$. Given these parameters, at the end of inflation, we find that each of the masses of the fields given eq. (3.139) is similar. Therefore, we analyse the decay for each of the fields.

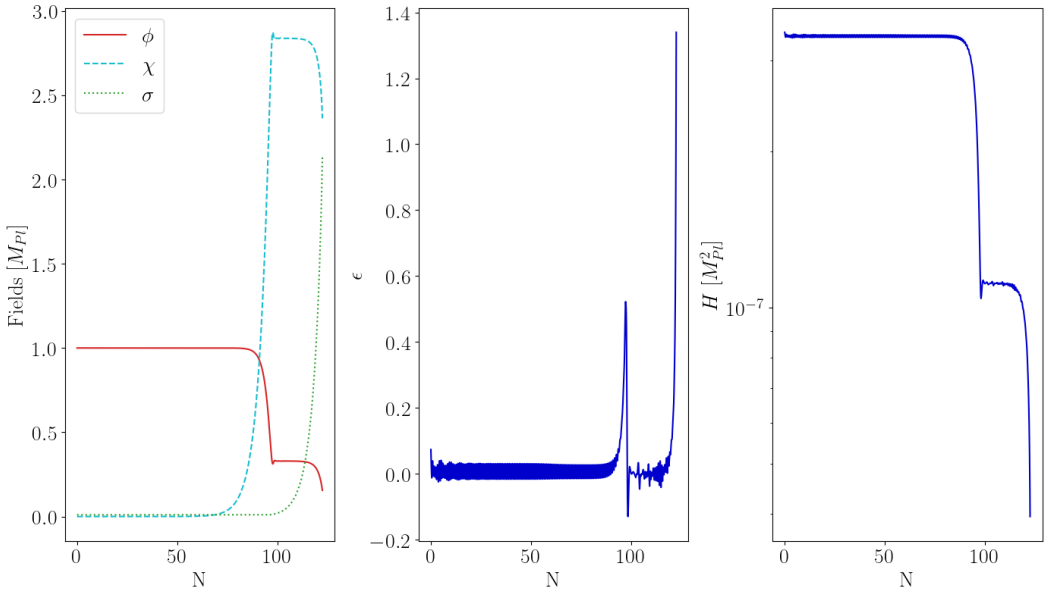

Figure 3.9: Inflationary dynamics of the model, with initial conditions, $\phi = 1, \chi = 10^{-8}, \sigma = 10^{-2}$ and parameter choice, $A = 0.054, B = 10^6, \lambda = 10^{-15}$. $\phi = 1$ is approximately equivalent to the field ψ in section 3.3.2. The left plot shows the field dynamics, the middle is the slow roll parameter, ϵ and the right plot is the Hubble parameter during inflation. We see that the overall dynamics and values are the same as fig. 3.4

Reheating

We now study a simplistic model of reheating for our three-field model to illustrate reheating and to ensure compatibility. The reheating process describes a mechanism where the inflationary scalar fields decay, creating relativistic particles. When the inflationary scalar fields begin to oscillate around their VEVs after inflation, we treat them as a particle with a finite probability of decaying into another given particle. This is modelled by introducing by hand additional couplings to the scalar fields such that

$$\mathcal{S}_m = \int d^4x\sqrt{-g}\left(-\frac{1}{2}\bar{g}^2\varphi^2\Phi_I^2 - \bar{h}\bar{\vartheta}\vartheta\Phi_I\right). \tag{3.140}$$

Here Φ_I indicates any or all species of inflationary scalar fields decaying. The decaying fields are then coupled to a bosonic field, φ, and a fermionic field, ϑ, with the dimensionless coupling constants $\bar{g}$ and $\bar{h}$. The additional matter term only grows once the fields begin oscillating around their VEVs.

We describe the decay rates of a fields as [75, 192, 188],

$$\Gamma_{\Phi_I\to\varphi\varphi} = \frac{\bar{g}^4\Phi^2_{I,\min}}{8\pi m_{\Phi_I}} \qquad \Gamma_{\Phi_I\to\vartheta\bar{\vartheta}} = \frac{\bar{h}^2 m_{\Phi_I}}{8\pi}. \tag{3.141}$$

We interpret these decay rates as an energy transfer, in the same way as the energy of inflation is converted into the expansion of the Universe. Therefore, we rewrite the equations of motion for Φ_I, eq. (3.136), to include the decay into relativistic particles,

$$\begin{aligned}
&\ddot{\phi} + (3H + \Gamma_\phi)\dot{\phi} = -V_\phi + \frac{1}{3}\left(\rho^{(\chi,\sigma)} - 3P^{(\chi,\sigma)}\right), \\
&\ddot{\chi} + (3H + \Gamma_\chi)\dot{\chi} = -V_\chi + A\chi R, \\
&\ddot{\sigma} + (3H + \Gamma_\sigma)\dot{\sigma} = -V_\sigma.
\end{aligned} \tag{3.142}$$

Here we can see that if the expansion of the Universe ($3H$) dominates the equations of motion, then very few particles will be produced. Once the expansion slows down after inflation and $\Gamma > 3H$, the energy density of the fields is sunk into the production of new particles. This then results in an exponential decay of the field. We assume that all particles produced will be relativistic and contribute towards the energy density of radiation. Therefore, the decay rate becomes a source term for the energy density of radiation,

$$\dot{\rho}_r = -4H\rho_r + \Gamma_\phi\dot{\phi}^2 + \Gamma_\chi\dot{\chi}^2 + \Gamma_\sigma\dot{\sigma}^2. \tag{3.143}$$

If we assume at the end of reheating, all of the energy density of the Universe is contained within ρ_γ, and the particles are briefly in thermal equilibrium the energy density is proportional to the quartic of the temperature,

$$\rho_r = CT^4. \tag{3.144}$$

The constant of proportionality is given by Bose–Einstein statistics, with $C = C_*\pi^2/30$, where C_* is the number of relativistic degrees of freedom and is approximated to $C_* = 100$ [192, 188, 189]. We can then use the decay rate to estimate the expected reheating temperature, given the maximum temperature will be reached when $\sum_I \Gamma_{\Phi_I} = H$. Therefore, subsituting eq. (3.144) for H, we obtain $T_{re} \approx \sqrt{M_{\rm Pl}\sum_I \Gamma_{\Phi_I}}$.

We aim to analyse the efficiency of reheating in our model, determined by the number of e-folds for the universe to be dominated by radiation, whilst checking that the reheating temperature remains within the cosmological

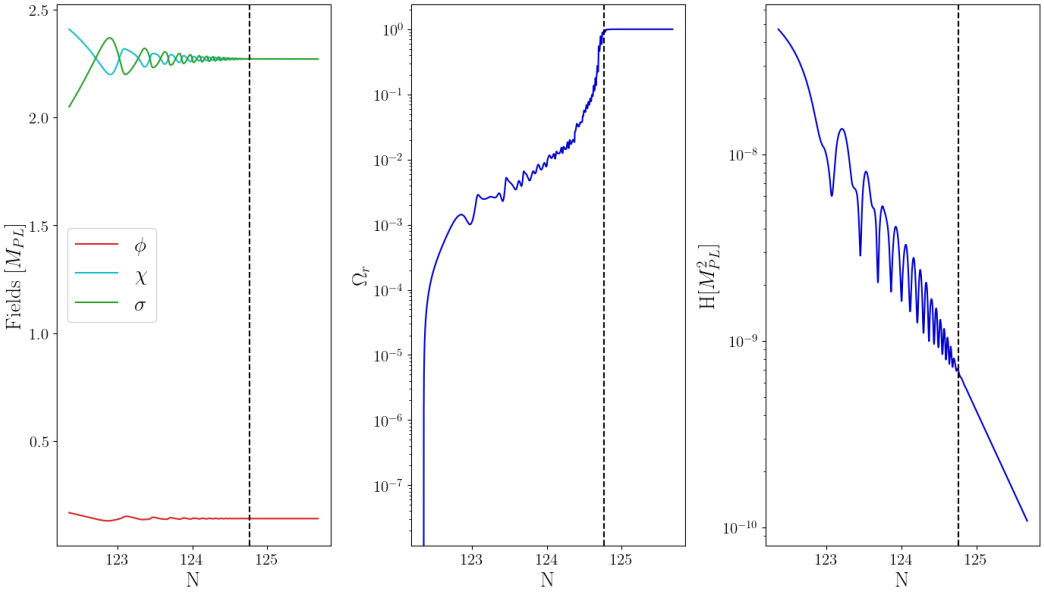

Figure 3.10: Numerical plot demonstrating the effect of reheating with the given parameters $\Gamma_\phi = \Gamma_\chi = \Gamma_\sigma = 10^{-10} M_{\rm Pl}^2$. The left plots show the field dynamics; the middle shows the density parameter of radiation in the Universe; and the right shows the Hubble parameter, which follows an $H \propto t^{-1}$ after reheating as expected for a radiation-dominated Universe. The plots immediately continue from fig. 4.5, and the black dotted line indicates the end of reheating with $\Omega_r = 0.95$.

bounds discussed earlier. Thus, to analyse the effects of reheating, we numerically integrate our equations of motion and vary the value of $\Gamma_{\phi,\chi,\sigma}$ as the masses of the fields have been set by the model parameters. This is equivalent to varying the dimensionless couplings in eq. (3.141). We set these to be the same as fig. 4.5 to ensure that the parameters used are consistent with current cosmological data. Our results determined the end of reheating when $\rho_r/\rho_{total} = 0.95$. The results are compiled in table 3.1 along with the corresponding figures in fig. 3.10.

The reheating process for our model is very effective compared to standard single-field [193] and other extensions of Starobinsky [149], illustrated by the short reheating duration ($\Delta N \simeq 2 - 2.7$). The addition of the Higgs-like potential creates a steep and deep well within the potential, creating rapid oscillations and enhancing the decay into relativistic particles. We also notice that increasing one of the decay rates rapidly increases the effectiveness of reheating. We understand this as forcing one of the fields to

	Case							
	1	2	3	4	5	6	7	8
$\Gamma_\phi\ [M_{\rm Pl}^2]$	10^{-10}	10^{-6}	10^{-10}	10^{-10}	10^{-6}	10^{-10}	0	0
$\Gamma_\chi\ [M_{\rm Pl}^2]$	10^{-10}	10^{-10}	10^{-6}	10^{-10}	10^{-6}	0	10^{-10}	0
$\Gamma_\sigma\ [M_{\rm Pl}^2]$	10^{-10}	10^{-10}	10^{-10}	10^{-6}	10^{-6}	0	0	10^{-10}
$T_{re}\ [10^{12}\text{GeV}]$	9.85	2.00	42.2	33.0	25.3	2.76	7.01	8.98
ΔN	2.41	1.63	1.65	1.92	4.28	2.52	2.98	2.41

Table 3.1: The numerical results for various cases, with the reheating temperature, T_{re}, described by eq. (3.144) and ΔN is the duration of reheating.

have a large decay rate and then indirectly forcing the other fields to settle quicker.

We can see that the decay of χ and σ has a greater effect on the reheating temperature than ϕ. This is because given the parameters used $m_\chi^2 > m_\phi^2$, and therefore has a faster decay, producing more relativistic particles before the ϕ–field decays away. Moreover, we see that our model produces a much larger reheating temperature than the estimate given by $T_{re} \approx \sqrt{M_{\rm Pl} \sum_I \Gamma_{\Phi_I}}$. This is due to the rapid decay of the fields in a very short duration, such that the decay terms dominate eq. (3.143).

3.6 Discussion on the theory of inflation

We have studied the effect of embedding inflation into modified gravity. Specifically, adding a higher-order term R^2 to the Einstein Hilbert action results in an interesting and unique potential ideal for a slow-rolling mechanism. Extending Starobinksy's inflation to generate a Planck mass dynamically required adding multiple fields to the model. This allows for greater phenomenological insight into inflation, with many interesting features and predictions, such as a drop in the power spectrum at small wavelengths. Moreover, including an additional field allowed the model to become compatible with a vanishing cosmological constant whilst remaining within current cosmological bounds on n_s and r. However, if the aim is to fit the theory to data, an arbitrary number of fields can be introduced to make the theory compatible. Therefore multi-field, if required, should be utilised delicately and implemented into a more fundamental theory.

While models of inflation and the early universe are studied in depth, the importance of reheating and particle production can sometimes be overlooked. We analysed the effect of reheating within our model to determine the effectiveness of creating a hot thermal plasma as required for the HBB model. Like inflation, the dynamics of reheating are determined by the shape of the potential's minimum. Therefore new models with exotic potentials must be analysed through to completion when the fields decay. We found that the three-field model was very effective at reheating and producing particles due to the shape of the effective potential and interaction between the fields. The reheating mechanism illustrated in section 3.5.1 further illustrated the model's validity given the parameter constraints of sections 3.3.2 and 3.4. However, it was found that the decays of certain fields were more effective than others at reheating the universe.

The theory of inflation is a powerful tool, explaining phenomena such as primordial perturbations that are observationally consistent with the CMB. Although inflation can be recreated with minimal extensions to standard GR, there remain conceptual problems with the theory. For instance, the initial successes of inflation, namely the horizon and flatness problem, can be resolved by fine-tuning initial conditions, is inflation required? If slow-

roll is the mechanism used to drive inflation, what determines the field's initial conditions? Are the perturbations that produce a near-flat power spectrum unique to inflation? Many of these issues are problems of setting initial conditions in the early universe. We have studied how inflation reformulates the initial conditions and pushes them back to an earlier time, albeit with a much larger degree of freedom. Therefore the theory of inflation is better thought of as a mechanism that rapidly expands the Universe before reheating and entering a hot radiation-dominated universe. This pushes back many conceptual problems to a smaller and earlier universe. Leading to the most disturbing problem, a spatial singularity, which inflation does not address.

Thus there has been a range of alternative models to inflation that are motivated by the conceptual problems of inflation. Some of these models stem from more fundamental theories of gravity, such as quantum gravity [194, 195]. While these theories are beyond the scope of this thesis, it is essential to note that any alternative to inflation must still account for the successes of inflation, including the generation of the primordial power spectrum and the production of particles during reheating, even if it is not necessary to resolve the horizon and flatness problems. A more effective procedure is to incorporate the successes of modified gravity during the early universe as EFTs, embedding the success and range of unique mechanisms of inflation into a more fundamental theory of gravity.

4 | Bouncing Cosmology

Although inflation has significantly contributed to our understanding of the early universe, it still depicts a universe originating from a singular point [30, 31]. This issue can be addressed by assuming the Universe is eternal and undergoing its evolution cycles. In this scenario, the Universe is separated into two eras: a contracting and expanding era separated by a non-singular turnaround transition called a bounce. The idea of replacing the Big Bang singularity with a non-singular transition, a bounce, has been considered in past literature, and reviews on this topic have been published [42, 81, 196, 197]. Another criticism of inflation is the arbitrary initial conditions required to initiate it [198, 199]. In contrast, a bounce transition before inflation would lead to predetermined initial conditions based on the bounce dynamics. Therefore a bouncing Universe followed by an epoch of inflation is an attractive model.

However, bouncing scenarios are also considered as an alternative to inflation. As discussed in section 3.4, initial perturbations become frozen during inflation and leave signatures in the CMB afterwards, resulting in a scale-invariant primordial power spectrum. Many bouncing models can also produce a scale-invariant spectrum, similar to what is seen in the CMB, without relying on the inflationary paradigm [200–202], however both scenarios are sensitive to initial perturbations. Moreover, bouncing scenarios can avoid the horizon and flatness problem without requiring an inflationary epoch [203–206]. Therefore, bouncing models can provide a more natural explanation for the problems that establish inflation as the current early universe paradigm.

Although a unique bouncing solution will provide a useful phenomenological insight to the early universe, a single bouncing model may not necessarily solve the initial condition or singularity problem. Instead, a unique

solution would push the problem back to an earlier state, albeit with considerably more freedom of parameter space, similar to inflation in regards to the HBB model.

4.1 A classical bounce

Depending on one's philosophical stance, the Universe's overall dynamics should remain describable within the classical framework with extensions motivated by higher energy theories, similar to that of reheating with the inclusion of decay rates in the Friedmann equations. Moreover, the classical picture should also remain physically sensible and singularity free. Identifying a singularity highlights the breakdown of the current theory and motivates the need for modified gravity. At the extremes of the Universe, we expect high-energy corrections from theories such as quantum gravity to become more important. We assume that these effects can be captured in a classical theory by utilising modified gravity as an effective field theory, providing new phenomenological insight into the fundamental behaviour around the bounce.

In the following, we investigate whether the transition between a collapsing and expanding phase and *vice versa* is achievable within the framework of GR while assuming an FLRW metric. As stated above, these transitions must be non-singular to resolve the issues of the early universe.

We identify a contracting universe by $\dot{a} < 0$ and in the same way for an expanding universe $\dot{a} > 0$, with the turnaround transition at $\dot{a} = 0$[1]. We refer to the transition from an expanding to a collapsing Universe as a halt, where the Universe reaches a maximum size, a_{max}. The bounce is the transition from a contracting universe to an expanding one, such that the universe reaches a minimum and finite size, $a_{\text{min}} > 0$. We depict the general behaviour of a bounce assuming an FLRW metric in fig. 4.1. For the

[1]It is worth noting that a universe maintaining $\dot{a} = 0$ is a static state universe. This was Einstein's initial motivation to include a cosmological constant. However, it has been shown that these steady-state universes are inherently unstable [207].

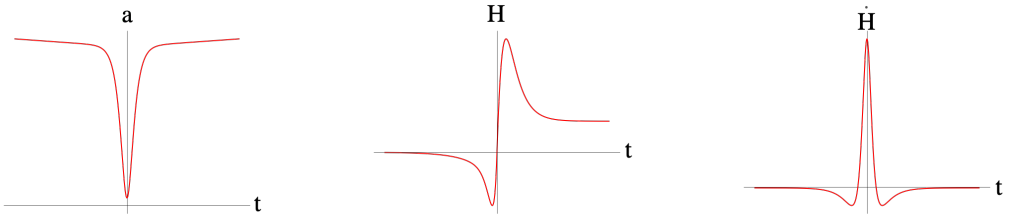

Figure 4.1: A schematic representation illustrating the evolution of the Universe through a bounce assuming an FLRW metric. Notably, both the initial and final phases exhibit resemblances to a de-Sitter universe. The occurrence of a non-singular bounce is characterized by specific conditions: when the scale factor a reaches a minimum, the Hubble parameter H equals zero, and the time derivative of the Hubble parameter $\dot{H}$ attains a maximum value. Consequently, instances immediately preceding and following the bounce correspond to the extrema of the Hubble parameter, given by $\dot{H} = 0$.

remainder of the chapter, we will denote the moment of the bounce with a subscript b such that $a_{\text{min}} \equiv a(t_b) = a_b,\ \dot{a}_b = 0$.

A common problem when considering classical bouncing cosmologies is driving $H \to 0$ in a collapsing era without breaking the weak energy condition[2], $\rho \geq 0$ and $\rho + P \geq 0$.

A resolution to this issue, utilising the cosmological framework, is to include a positive spatial curvature. In this scenario, the Friedmann equations, given here for brevity,

$$H^2 + \frac{K}{a^2} = \frac{\dot{\phi}^2 + 2V}{6M_{\text{Pl}}}, \tag{4.1}$$

$$\dot{H} - \frac{K}{a^2} = -\frac{\dot{\phi}^2}{2M_{\text{Pl}}} \tag{4.2}$$

can reach the bounce conditions $H_b = 0,\ \ \dot{H} > 0$ without breaking the weak energy conditions or setting $\rho = 0$. Assuming a zero cosmological constant, the inclusion of a positive curvature in an expanding era can results in the Universe transitioning into a collapsing era, as studied in section 1.3. If in the late universe $\dot{\phi} \to 0$ as the universe expands, we can see from eq. (4.2) $\dot{H}$ will become positive, dominated by the spatial curvature. This then allows K/a^2 to dominate the potential energy and setting $H = 0$.

[2]The energy conditions are used to indicate real physical solutions and are often used to dismiss solutions on the basis they are unphysical [25, 81].

However, bouncing cosmologies also exhibit a diverging behaviour due to the Universe's collapse: given a toy universe in a collapsing era containing only a scalar field, the Klein-Gordon equation, given here for brevity,

$$\ddot{\phi} = -3H\dot{\phi} - V_\phi, \tag{4.3}$$

depicts a growing solution of ϕ and therefore ρ. In previous chapters, the $3H\dot{\phi}$ acts as a damping term as the Universe expands, generating a decaying solution. However, in a collapsing scenario, the opposite is true. The $3H\dot{\phi}$ amplifies the field's growth during the collapse as $H \to -|H|$. Therefore during the collapse,both ϕ and $\dot{\phi}$ will slowly grow due to the amplification term, unless $\dot{\phi} = 0$. Eventually the field will become fast rolling with the $3H\dot{\phi}$ term dominating V_ϕ. At which point the solution to the equation becomes $\dot{\phi} \propto e^{|H|t}$.

Considering the back reaction to this effect, the problem is much worse than switching a damping term to an amplification term, as it causes a feedback loop: assuming a collapsing era, the source term quickly dominates. The solution to the KG equation, in this case, is an exponential growth. The exponentially growing field results in $\dot{\phi}$ dominating the Friedmann equation eq. (4.2), further enhancing the collapse rate and acceleration. Therefore, H becomes more negative, enhancing the already exponential growth of the scalar field andϕ and H, sourcing each others growth further. This leads to a divergent solution with $\phi \to \pm\infty$, $H \to -\infty$, resulting in $a \to 0$ which is identified as the spatial singularity.

Therefore, although the curvature can offset the positive nature of the perfect fluid considered in eq. (4.2), it is not guaranteed to grow sufficiently and dominate the energy density. We have already identified that a closed universe will eventually lead to a collapse. In the collapsing epoch, as a gets smaller, the matter and radiation content will begin to dominate (analogous to a time reversal in fig. 1.5). If we simplify the issue and assume only a simple scalar field, the spatial curvature component cannot dominate unless the field remains stuck around $\dot{\phi} = 0$ to remove the Hubble source term in eq. (4.3). Hence we enter a fine-tuning problem: We have to balance the ingredients in the Universe such that the Universe collapses slowly enough to allow the spatial curvature to dominate the equations of motion, allowing for a bounce. This issue has already been investigated by [81, 208], illustrating

the fine-tuning required of a simple, classical, scalar field bounce.

Moreover, the bouncing model is required to achieve the same success as inflation or be embedded into inflation as a prerequisite. Therefore a natural starting point is a modification of GR, which has produced many successful models within inflation [42].

We have already studied the success of modified gravity within the context of the early universe, particularly Starobinsky's inflation. Focusing on an $f(R)$ modification, in section 1.2, we reviewed how the modification can be interpreted as an additional matter content, namely the scalaron, F. Moreover, it also modifies the Friedmann equations to eqs. (1.47) and (1.48), written below for ease,

$$H^2 + \frac{K}{a^2} = \frac{FR - f}{6F} - H\frac{\dot{F}}{F} + \frac{\rho}{3FM_{\rm Pl}}, \tag{4.4}$$

$$\dot{H} - \frac{K}{a^2} = H\frac{\dot{F}}{2F} + \frac{\rho + P}{2FM_{\rm Pl}} - \frac{\ddot{F}}{2F}. \tag{4.5}$$

This modification of the Friedmann equations permits new freedom of mechanisms for $H \to 0$ without violating the weak energy condition. The scalaron will still experience the same growing behaviour due to the collapse. However, the feedback loop where the Hubble parameter is driven to more negative values can be potentially neglected or reduced with the inclusion of the scalaron as all terms are divided by F.

4.2 False vacuum model

We study a model based on the assumption that the Universe is spatially closed[3] and extend the work of [211], by inducing an epoch of finite inflation after the bounce. It relies on a modified gravity theory with a non–minimally coupled scalar field. The scalar field is assumed to initially sit in a false vacuum in a local minimum of its effective potential in a slow-contracting Universe. Inflation after the bounce is driven by corrections to the Einstein–Hilbert action, which we assume to be of the form of $R+R^2$ gravity[4] resulting in Starobinsky inflation studied in section 3.3.1. We find that for an extensive range of parameter values, the scalar field rolls down towards the global minimum, triggering a bounce. At the same time, the scalaron is driven up its potential energy, resulting in a period of Starobinsky–inflation. The main result is that inflation, driven by the R^2–term, happens naturally in such a setup. Moreover, it is found to be stable for a large region of parameter space.

We assume a closed, isotropic and homogeneous background described by the Friedmann–Robertson–Lemaître–Walker (FRLW) metric

$$ds^2 = -dt^2 + a(t)^2 \left[\frac{dr^2}{1 - Kr^2} + r^2 \left(d\theta^2 + \sin^2 \theta d\phi^2 \right) \right] , \tag{4.6}$$

with $K > 0$. Our theory is an extension of Starobinsky's R^2 model [128] with an additional scalar field non-minimally coupled to gravity,

$$\mathcal{S} = \int d^4x\sqrt{-g} \left[\frac{1}{2} \left(M_{\rm Pl}^2 - \alpha\phi^2 \right) R + \frac{1}{2} AR^2 - \frac{1}{2}(\nabla\phi)^2 - V(\phi) \right] . \tag{4.7}$$

Here α and A are constants parameterising the coupling of the scalar field to GR and the modification of Starobinsky's term, respectively. We follow [211] and choose the potential to be of the form

$$V = \frac{m^2}{2}\phi^2 + \frac{\beta}{3}\phi^3 + \frac{\lambda}{4}\phi^4, \tag{4.8}$$

where m and β are constants with dimensions of mass, and λ is dimensionless constant. As we are interested in the potential that has a false vacuum,

[3] Recent analyses of Planck data are consistent with a small positive curvature [68, 209, 210]. In our model, the spatial curvature at present can indeed be very close to zero.

[4] Bouncing cosmologies in these type of modified gravity theories have been discussed in [212, 213].

we set $\beta < 0$. This results in a local minimum and maximum., further details are given in section 4.2.1. We map the action (4.7) to a scalar–tensor theory by defining $f(\phi, R) = \frac{1}{2}\left(M_{\rm Pl}^2 - \alpha\phi^2\right) R + \frac{1}{2}AR^2$. Our additional scalar degree of freedom is then defined in the standard way, following the procedure in section 1.2, setting $\psi = f_{,R}$. This allows us to write the Ricci scalar and the function $f(R, \phi)$ in terms of the two fields as

$$R = \frac{1}{A}\left(\psi - \frac{M_{\rm Pl}^2 - \alpha\phi^2}{2}\right), \quad f = \psi R - \frac{\left[\psi - \frac{1}{2}(M_{\rm Pl}^2 - \alpha\phi^2)\right]^2}{2A}. \tag{4.9}$$

Following the procedure outlined in section 1.2, the field equations are obtained from the action by taking the variation with respect to the metric and are the same as eq. (1.20), rewritten here

$$\psi R_{\mu\nu} - \frac{f g_{\mu\nu}}{2} - (\nabla_\mu\nabla_\nu - g_{\mu\nu}\Box)\psi = T_{\mu\nu}^{(\phi)}\,. \tag{4.10}$$

Taking the trace of the last equation and making use of equations (4.9) we determine the evolution equation for ψ,

$$\Box\psi = \frac{1}{3}\left[\frac{M_{\rm Pl}^2 - \alpha\phi^2}{2A}\left(\psi - \frac{1}{2}(M_{\rm Pl}^2 - \alpha\phi^2)\right) + T\right], \tag{4.11}$$

where T is the trace of the energy-momentum tensor of the ϕ field. In a closed FRLW spacetime, the equations of motions for the fields ψ and ϕ read

$$\ddot{\psi} + 3H\dot{\psi} = \frac{1}{3}\left[\frac{M_{\rm Pl}^2 - \alpha\phi^2}{2A}\left(\frac{1}{2}(M_{\rm Pl}^2 - \alpha\phi^2) - \psi\right) + (\rho - 3P)\right], \tag{4.12}$$

$$\ddot{\phi} + 3H\dot{\phi} = -V_{,\phi} - \alpha\phi R. \tag{4.13}$$

The Friedmann equations are given by, eqs. (1.47) and (1.48),

$$H^2 + \frac{K}{a^2} = \frac{\psi R - f}{6\psi} + \frac{\rho}{3\psi} - H\frac{\dot{\psi}}{\psi}, \tag{4.14}$$

$$\dot{H} - \frac{K}{a^2} = \frac{H\dot{\psi}}{2\psi} - \frac{\ddot{\psi}}{2\psi} - \frac{(\rho + P)}{2\psi}, \tag{4.15}$$

with the standard relation,

$$\frac{R}{6} = \dot{H} + 2H^2 + \frac{K}{a^2}. \tag{4.16}$$

We aim to use the bounce to set the initial conditions for a subsequent inflationary epoch driven by the R^2 term.

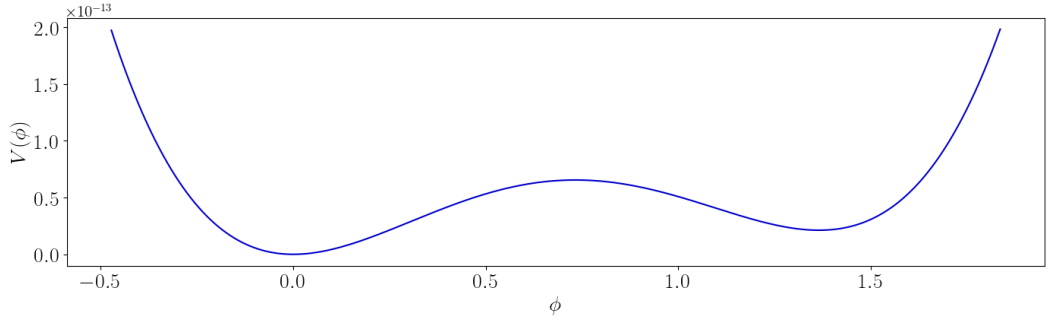

Figure 4.2: The potential eq. (4.8) for ϕ, as studied in [211]. The initial conditions of our scalar field will be determined by the location of the local minimum given by the choice of parameters of the potential. The parameters for this potential are $m = 10^{-6} M_{\rm Pl}$, $\beta = -\sqrt{4.4\lambda} m$ and $\lambda = 10^{-12}$.

4.2.1 Bounce dynamics

We continue to work in the Jordan frame to analyse the cosmological dynamics as it is easier to spot potential instabilities in the equations, such as ghosts, and the resulting equations of motion to be integrated are more numerically stable. However, an analysis of the Einstein frame is also possible, as the condition $F_R > 0$ is maintained, allowing a mapping between the frames. Still, we will refrain from analysing the dynamics in that frame. Given the potential (4.8), we utilise the picture set forth by [211]: pre–bounce, we assume a slowly contracting universe dominated by dark energy. During this time, ϕ has settled in the false vacuum, providing initial conditions for our fields. The effective potential gives the location of the false vacuum for ϕ. From (4.13) we find extrema located at $\phi = 0$ (the true vacuum) and at

$$\phi_\pm = \frac{-\beta \pm \sqrt{\beta^2 - 4\lambda(m^2 + \alpha R)}}{2\lambda}. \tag{4.17}$$

The negative solution corresponds to the local maximum shown in fig. 4.2, and the positive solution is the semi-stable local minimum. To ensure that we have a local minimum, we require $\beta^2 > 4\lambda m^2$. Furthermore, we assume that the potential is positive at ϕ_-, such that $\phi = 0$ remains the global minimum, which constrains $\beta^2 < 4.5\lambda m^2$. It is worth noting that a deeper local minimum corresponds to a larger β^2.

Before the bounce, the field has settled at the initial value $\phi_i = \phi_+$. For $t \to -\infty$, we assume we are far away from the bounce so in a slowly

contracting Universe H and $\dot{H}$ are small and from eq. (4.16). We infer R will also be very small compared to the mass of the field, m., allowing us to disregard R in (4.17). To guarantee that the value of R is initially negligible, we set the parameter A to be large[5] compared to the fields, as seen in eqn. (4.9). Setting A to be large, forcing R to be initially negligible, we place ϕ at the local minimum ϕ_i. We further assume that the scalaron is initially at rest, thus allowing us to obtain the vacuum expectation value of the scalaron, $\psi_{\rm min}$, as a function of ϕ_i from eq. (4.12)

$$\psi_{\rm min}(\phi_i) = \frac{8AV(\phi_i)}{M_{\rm Pl}^2 - \alpha\phi_i^2} + \frac{1}{2}(M_{\rm Pl}^2 - \alpha\phi_i^2), \tag{4.18}$$

where we will set the initial value of the scalaron such that $\psi_i = \psi_{\rm min}(\phi_i)$.

Provided ϕ evolves slowly, the relation above shows that ψ will track ϕ. It is also clear that we cannot allow $\alpha\phi^2 = M_{\rm Pl}^2$, otherwise, the scalaron will be unbounded in eq. (4.18). This identifies a constraint on our model. Without loss of generality, we assume a natural range for ϕ up to $O(10\ M_{\rm Pl})$. Therefore we set $\alpha = 10^{-3}$ throughout this section unless stated otherwise.

Using the initial conditions provided above, we find from eq. (4.14) - (4.16) and (4.18)

$$V(\phi_i) \approx O(m^4), \tag{4.19}$$

$$R(\phi_i) \approx \frac{8V(\phi_i)}{M_{\rm Pl}^2 - \alpha\phi_i^2} \approx O\left(\frac{m^4}{M_{\rm Pl}^2}\right), \tag{4.20}$$

$$H(\phi_i)^2 \approx \frac{V(\phi_i)}{3(M_{\rm Pl}^2 - \alpha\phi_i^2)} \approx O\left(\frac{m^4}{M_{\rm Pl}^2}\right), \tag{4.21}$$

$$\dot{H} \approx 0, \tag{4.22}$$

assuming that R is negligible in eq. (4.17).

Appraching the bounce

In [211], it was argued that the field ϕ does not need to be fine-tuned to allow a stable solution in the past, provided the field has settled in the false vacuum.

[5]It is worth noting A has units of $[\text{mass}]^{-1/2}$, and in standard Starobinsky inflation, $M_{\rm Pl}^2 \gg A^{-1}$.

The assumption is that $\phi \to \phi_i$ as $t \to -\infty$. However, we also understand that small perturbations around the minimum become important, as the anti-Hubble damping term amplifies the growth of these perturbations, and is dependent on $H(\phi_i)$, given by the model's parameters. This hints that ϕ determines the bounce dynamics irrespective of ψ, assuming R is set to be negligible at times well before the bounce. We can show this more explicitly by considering the dynamics around the bounce: Consider the period between the extrema of H, when $\dot{H} = 0$ as illustrated in fig. 4.1. During which the Universe switches from a contraction to an expansion. In our set up the start and the end of this period is given by eq. (4.15),

$$\frac{K}{a^2} = -\frac{H\dot{\psi}}{2\psi} + \frac{\ddot{\psi}}{2\psi} + \frac{(\rho + P)}{2\psi}. \tag{4.23}$$

This corresponds to H reaching its extreme value $H_{\min/\max}$,

$$H^2_{\min/\max} = \frac{\psi R - f}{6\psi} - \frac{(\rho + 3P)}{6\psi} + \frac{|H|\dot{\psi}}{2\psi} + \frac{\ddot{\psi}}{2\psi}. \tag{4.24}$$

Although the equation governing $H_{\min}$ and $H_{\max}$ are the same, the values of ϕ and $\dot{\phi}$, thereby ρ, and ψ and $\dot{\psi}$ will differ at the two extema. If we assume that the fields are well-behaved, which is verified later numerically, and they do not rapidly diverge in the collapsing epoch to avoid the singularity ($\ddot{\psi},\ \ddot{\phi} < H\dot{\psi},\ H\dot{\phi}$), we can assume the scalaron will trace ϕ according to (4.18). This allows us to determine the Hubble parameter at the beginning of the bouncing epoch,

$$H^2_{\min} \approx \frac{2V}{3M^2_{\rm Pl}} + \frac{V - \dot{\phi}^2}{3\psi(\phi)} + \frac{\dot{\phi}^2}{54\psi(\phi)}. \tag{4.25}$$

Here we have made use of the assumed hierarchy $\psi_i > M^2_{\rm Pl} \gg \alpha\phi_i^2$ justified from eq. (4.18), to allow for inflation, explained in section 4.2.3. It is clear from (4.25) that the initial dynamics before the bounce is determined by ϕ.

The scalar field ϕ will be displaced from the local minimum during the collapsing phase, e.g. because of the presence of (small) perturbations. Perturbations will force the field value to grow; however, in most cases this happens slowly and leads to two scenarios: either the fields remain trapped in their local minima, expressed in fig. 4.3, or the fields escape their minima, a scenario that can be seen in fig. 4.4. In the latter case, the coupling of ϕ to the Ricci scalar introduces a time-varying effective potential, which can be

controlled by α, and leads to the local minimum vanishing. The ϕ–field will roll towards the global minimum at $\phi = 0$. This is the scenario discussed in [211]. Including an additional degree of freedom here (the scalaron) allows R to grow sufficiently but not to the extent that the local minimum vanishes. Further below, we discuss the different outcomes, the trapped ϕ–field and the scenario where the potential is shallower, allowing the ϕ–field to roll to the origin.

4.2.2 Numerical analysis

We perform a numerical analysis to determine the evolution of the fields and the evolution of the Universe. To this end, we integrate the field equations eqs. (4.12) to (4.14) and (4.16), with initial conditions given by eqs. (4.17) and (4.18) and with both fields starting at rest. Due to a long time of integration, the time has been re-scaled by $m/M_{\rm Pl}$. For ease, we plot the e-fold, defined as $N = \log(a)$, to illustrate the transition.

We have checked the validity of the numerical results by utilising the necessary conditions for a bounce set by [214]: given the bounce conditions

$$H(t_b) = 0, \qquad\qquad \dot{H}(t_b) > 0.$$

If we assume a barotropic fluid of the form $P = w\rho$, avoiding violating the strong energy condition constrains the equation of state to $w_b < -1/3$. An obvious quantity we can check at the bounce by imposing the first two bounce conditions above is (using eq. (4.16))

$$\psi_b + \frac{\alpha}{2}\phi_b^2 > \frac{6AK}{a_b^2} + \frac{M_{\rm Pl}^2}{2}. \tag{4.26}$$

This equation is fulfilled around the bounce using the values in fig. 4.3. We can also utilise the slow-roll parameter $\epsilon = -\dot{H}/H^2$. The condition on ϵ at the bounce is $\epsilon_b < 0$.

Using eqs. (4.14) and (4.16) and the bounce conditions above, we find the expression for ϵ_b:

$$\epsilon_b = \frac{3A(4K\psi_b - a_b^2\ddot{\psi}_b - a_b^2 R_b\psi_b)}{2AK\psi_b + \frac{1}{6}a_b^2\left[\frac{1}{2}(M_{\rm Pl}^2 - \alpha\phi_b^2) - \psi_b\right]^2} < 0 \tag{4.27}$$

confirming that the conditions for a bounce have been met.

Moreover the Ricci scalar

$$R = 6\left(\dot{H} + 2H^2 + \frac{K}{a^2}\right)$$

agrees, numerically, with eq. (4.9). Our analysis establishes three possible outcomes on how the Universe can evolve in this scenario. These outcomes are controlled by the choice of parameters, $A,\ \alpha,\ m,\ \beta,\ \lambda$, that determine the evolution of ϕ and, correspondingly, the Ricci scalar at the bounce.

- $\phi \approx 0$ at or near the bounce. The field ϕ can escape the false vacuum before the bounce and rolls towards the true minimum. This scenario can be obtained by forcing the evolution of R such that $R \geq R_{crit}$, at which point the local minimum ceases to exist, and the field ϕ starts to evolve. This was explored by [211] for a single field, where they were able to avoid the singularity by forcing the local minimum to be very close to the global minimum. Another way to allow the scalar field to oscillate freely is to construct the potential to have a very shallow and small barrier. This allows for the anti-friction term in (4.13) to be the initial dominating term removing any oscillations. Unless severely fine-tuned, the fields in this scenario will exhibit the standard divergent nature of bouncing mechanisms, quickly leading to a singularity [215, 216]. Therefore, we do not explore this scenario further.

- $\phi \approx \phi_i$ at bounce: The field ϕ is never significantly displaced from ϕ_i, therefore, the fields will remain trapped in their false vacuum state. This means R never reaches R_{crit} and does not evolve sufficiently to alter the potential. Consequently, after the bounce ϕ, ψ, and R will settle back in their initial conditions. This scenario is depicted in fig. 4.3 with the corresponding parameter choice, clearly showing a return to initial conditions after the bounce. This leads to an eternal inflation scenario with the dark energy of the previous universe continuing to dominate. This can be due to either a parameter choice creating a very steep and deep false vacuum, such as decreasing m, trapping the field through the bouncing epoch, or the chosen parameters do not allow R to vary. R can be set to have a minimal evolution through a parameter choice, such as setting the scalaron mass very high or reducing the

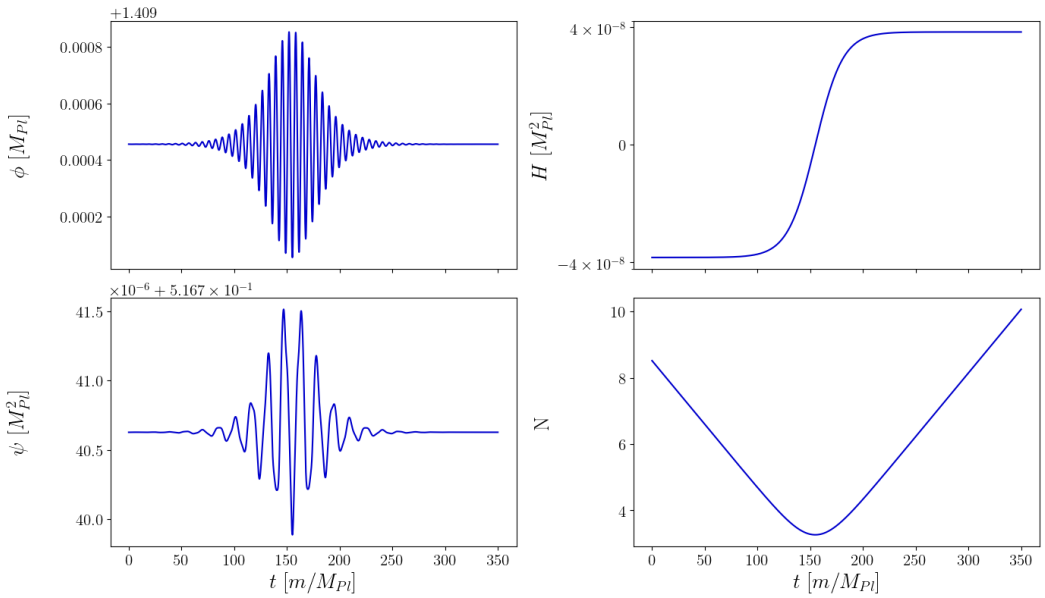

Figure 4.3: On the left plots we can see the dynamics of the fields, trapped in the false vacuum. In the top right plot, we see the change of sign in H, corresponding with the bottom right plot showing the e-folds of the universe initially decreasing and then growing after the bounce. The fields behave initially as expected in a collapsing universe, oscillating around their local minimum and growing in amplitude. The bounce is then caused when the spatial curvature dominates, switching to an expanding universe, and the fields become damped. The parameters used are $m = 10^{-6}\mathrm{M_{Pl}}$, $\beta = -\sqrt{4.49\lambda}m$, $\lambda = 10^{-12}$, $\alpha = 10^{-3}$, $V_0 = 0$, $A = 10^{12}$, $a = 10^2, K = m^2$ which in turn determine the initial conditions, ϕ_i and ψ_i.

coupling between ϕ and gravity. In both cases, the field only undergoes minor oscillations as the spatial curvature dominates. This means that the effective potential remains unchanged ($V_{,\phi} \gg \alpha\phi R$). The velocity term never dominates the right-hand side of (4.12), hence $\psi \approx \psi_{min}$, tracing the ϕ field. This creates a symmetric bounce as illustrated in fig. 4.3 as the scalaron is determined completely by the evolution of ϕ.

- $0 < \phi \lesssim \phi_-$ at the bounce: In the final scenario, the Ricci scalar can evolve sufficiently such that ϕ is displaced. Still, the false vacuum is not removed (i.e. the value of the Ricci scalar remains below R_{crit}). In this case, ϕ exhibits growing oscillations since the effective potential changes its form, eventually allowing the field to leave the local minimum before or as the bounce occurs but remaining displaced

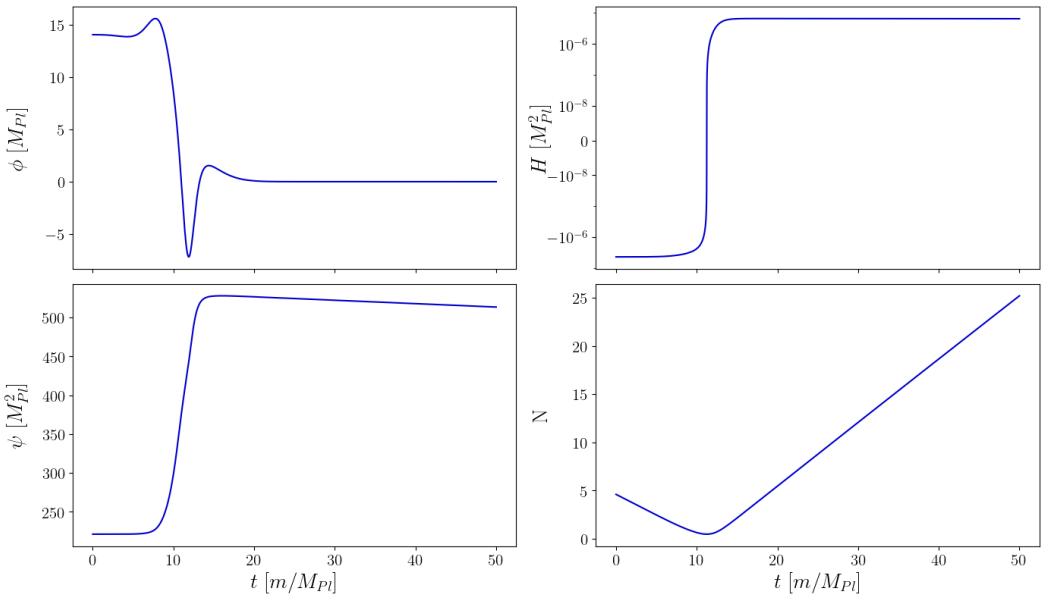

Figure 4.4: The same plot of fig. 4.3, with the parameters $m = 10^{-5}\mathrm{M_{Pl}}$, $\beta = -\sqrt{4.49\lambda}m$, $\lambda = 10^{-12}$, $\alpha = 10^{-3}$, $V_0 = 0$, $A = 10^{12}$, and $K = m^2$ which determine the initial conditions, ϕ_i and ψ_i, allowing the fields to leave the local minimum. As the bounce occurs and ϕ escapes the local minimum, ψ is driven up its potential.

from the global minimum at the time of the bounce, shown in fig. 4.4. The change of the potential provides ϕ with enough kinetic energy to overcome the barrier ($|H|\dot{\phi}^2 > V(\phi_-)$). In this scenario, the period of inflation following the bounce is initially driven by both fields. The field ϕ will always settle at the origin before ψ resulting in a period of standard single field inflation driven by ψ, the behaviour of which can be seen in fig. 4.4. This epoch of inflation can then be constructed to last much longer than 60 e-folds. Our choice of parameters forces the ϕ-field to settle immediately, resulting in approximately a single-field, Starobinsky inflation. We present more details in section 4.2.3.

4.2.3 Resulting inflation

As eternal inflation is incompatible with current observations, we focus on the scenario with a bounce resulting in standard inflation. We assume the fields to be in a slow rolling regime ($\ddot{\phi}, \ddot{\psi} \ll H\dot{\phi}, H\dot{\psi}$) corresponding to the fields evolving slowly and ϕ gradually escaping the false vacuum. We can then approximate, using Eq.(4.12),

$$3H\dot{\psi} \simeq \frac{M_{\rm Pl}^2(\frac{1}{2}M_{\rm Pl}^2 - \psi)}{6A} - \frac{\dot{\phi}^2 + 4V}{3}. \tag{4.28}$$

Given that we are motivated to find inflation after the bounce, we set the parameters such that $\psi_i \gg 2M_{\rm Pl}^2$. Therefore in a collapsing universe, we see that ψ is driven up its effective potential to larger values because its time–derivative at the local maximum, identified with the subscript c, is given by

$$\dot{\psi}_c \simeq \frac{\frac{M_{\rm Pl}^2\psi}{A} + 2\dot{\phi}^2 + 8V}{18|H_c|} > 0, \tag{4.29}$$

due to the fact the right-hand side will remain positive. Therefore, while ϕ is driven towards zero, the potential energy of ψ will become more relevant as time progresses. Hence, we arrive at a situation in which the bounce naturally produces the initial conditions for inflation, driven by the ψ–field. This period of inflation begins when H reaches its maximum value. We can use (4.25) to determine the value of ψ when inflation begins. For simplicity, we assume that $H_{\rm min}$ is reached when the ϕ–field escapes the local minimum, $\phi = \phi_-$, and the potential is dominating (4.25). Therefore, we can equate $H_{\rm min}^2 = H_{\rm max}^2$,

$$\frac{2V(\phi_-)}{3M_{\rm Pl}^2} = \frac{\psi R - f}{6\psi} - \frac{H\dot{\psi}}{\psi} \tag{4.30}$$

using (4.12) and the definition of f this results in

$$\psi_{\rm inf} = \frac{4AV(\phi_-)}{3M_{\rm Pl}^2} - \frac{M_{\rm Pl}^2}{18}, \tag{4.31}$$

where the subscript *inf* denotes the start of inflation. This calculation relies on the assumption of a symmetrical bounce. Due to the presence of the coupling of ϕ to the Ricci scalar as well as the scalaron, the bounce will not be symmetrical. However, given our choice of parameters, we have numerically verified that the scalaron plays a minor role during the bounce. Therefore, the approximation $H_{\rm min}^2 \approx H_{\rm max}^2$ is reasonable to find an approximation for

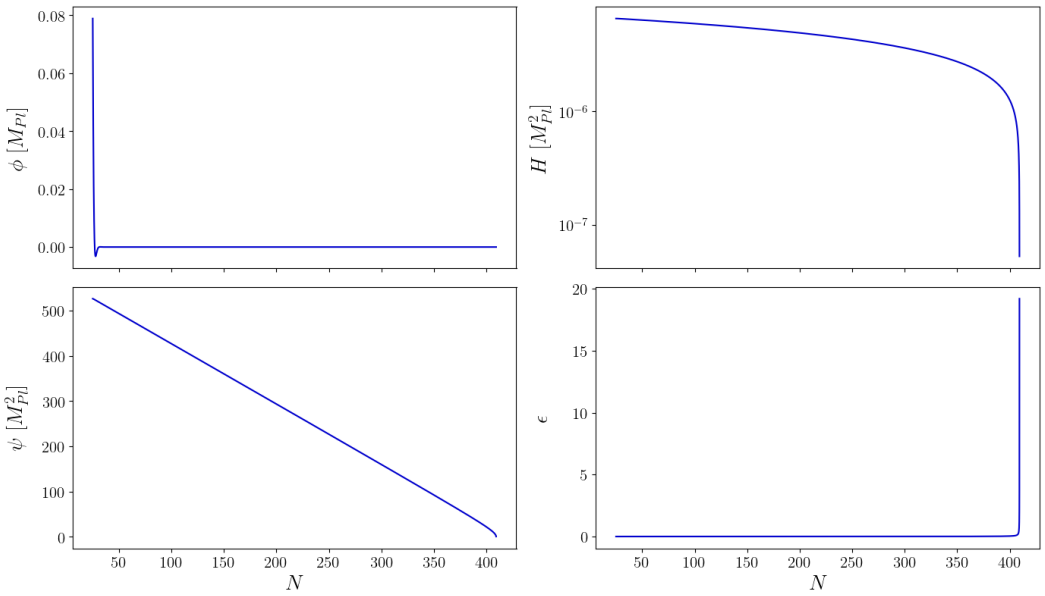

Figure 4.5: The evolution of the fields during inflation is shown in the left plots, using the same parameters as in fig. 4.4. Notice ϕ settles to the origin almost immediately. In the right plots, we show H and the slow roll parameter ϵ. We are using the e-fold number (measured after the bounce) as a time variable in these figures.

$\psi_{\rm inf}$. Nevertheless, the scenario in which $H^2_{\rm max} > H^2_{\rm min}$ is more realistic. In this case, the $\psi_{\rm inf}$ will be smaller, resulting in a shorter period of inflation. If $H^2_{\rm min} > H^2_{\rm max}$, $\psi_{\rm inf}$ is larger, resulting in a longer period of inflation.

As stated before, ϕ will settle at the origin after the bounce for the finite inflation case. Therefore we assume that inflation is predominantly driven by the scalaron, with initial conditions provided at the end of the bouncing epoch, $\psi_{\rm inf}$. The slow-roll parameter, eq. (3.20) becomes

$$\epsilon_v = \frac{4M_{\rm Pl}^4}{\psi^2}\left(\frac{\frac{M_{\rm Pl}^2}{2}-\psi}{M_{\rm Pl}^2-\psi}\right)^2. \tag{4.32}$$

Setting $\epsilon_v = 1$ we can determine the end of inflation occurs when $\psi \approx 2M_{\rm Pl}^2$. Therefore we require $\psi_i > 2M_{\rm Pl}^2$ at the beginning of that period. Integrating our slow roll parameter allows us to determine the initial conditions of inflation for ψ to achieve at least 60 e-folds of inflation.

$$N = \int_{2M_{\rm Pl}^2}^{\psi} \sqrt{\frac{2}{M_{\rm Pl}\epsilon_v}}. \tag{4.33}$$

Using the same parameters as in fig. 4.4, we find that $\psi_{inf} > 16M_{\rm Pl}^2$ to provide at least 60 e-folds of inflation driven by ψ. We can then use this value and

Eq. (4.31) to constrain the potential and the initial conditions of ϕ. We leave the detailed analysis for future work. In fig. 4.5, we show the evolution of the fields during inflation.

4.2.4 Cosmological perturbations in the Jordan frame

We evaluate the cosmological perturbations to ensure our model does not exhibit instabilities. Similar to the background quantities, the collapsing era will turn the Hubble parameter into a source term. In this section, we check that the perturbations remain small compared to their background quantities. As outlined in section 1.3.1, we consider the evolution of cosmological perturbations at linear order, decomposing them into scalar, vector and tensor perturbations with the metric given in eq. (1.66). In this section, we set $M_{\rm Pl} = 1$, unless stated otherwise.

Scalar perturbations

Firstly we focus on the scalar branch and working in the longitudinal gauge-section 1.3.1. The metric at first order scalar perturbation is given by the eq. (1.67) and written below for ease,

$$ds^2_{(s)} = -(1+2\Phi)dt^2 + a^2(1-2\Psi)\delta_{ij}dx^i dx^j, \tag{4.34}$$

where Φ and Ψ are metric perturbations. The gauge-invariant formalism for modified gravity is detailed in e.g. [217–219] and references therein. The perturbed Einstein equations reads[6] [220]

$$3H\left(\dot{\Psi} + H\Phi\right) + \frac{k^2 - 3K}{a^2}\Psi = -\delta\rho, \tag{4.35}$$

$$\dot{\Psi} + H\Phi = -\delta q, \tag{4.36}$$

$$3\left(\ddot{\Psi} + \dot{H}\Phi - H\dot{\Phi}\right) + 6H\left(\dot{\Psi} + H\Phi\right) + \Phi\left(3\dot{H} - \frac{k^2}{a^2}\right) = -\delta X, \tag{4.37}$$

$$\Psi - \Phi = \frac{\delta\psi}{\psi}, \tag{4.38}$$

[6] Often in the literature in modified gravity the above equations will have a replacement of $\psi \to F$ [220].

where k is the wavenumber, K is the spatial curvature and we have defined

$$\delta\rho = \frac{1}{2\psi}\left[3\dot{\psi}\left(\dot{\Psi}+H\Phi\right)-\left(\dot{\phi}^2+3V\right)\Phi \right. \\ \left. -3H\dot{\delta\psi}+\dot{\delta\phi}\dot{\phi}+\delta\psi\left(3\dot{H}-\frac{k^2}{a^2}+3H^2\right)+\delta\phi\left(V_\phi-\frac{f_\phi}{2}\right)\right], \tag{4.39}$$

$$\delta q = \frac{\dot{\delta\psi}+\delta\phi\dot{\phi}-H\delta\psi-\dot{\psi}\Phi}{2\psi}, \tag{4.40}$$

$$\delta X = \frac{1}{2\psi}\left[3\dot{\psi}\dot{\Phi}+3\left(\dot{\Psi}+H\Phi\right)\dot{\psi}+\Phi\left(6\ddot{\psi}+3H\dot{\psi}+4\dot{\phi}^2\right)\right. \\ \left. +\delta\psi\left(\frac{6K-k^2}{a^2}+6H\right)-\delta\phi\left(f_\phi-2V_\phi\right)-3H\dot{\delta\psi}-3\ddot{\delta\psi}-4\dot{\delta\phi}\dot{\phi}\right]. \tag{4.41}$$

The perturbed Klein-Gordon equations read,

$$\ddot{\delta\psi}+3H\dot{\delta\psi}-\left(\frac{R}{3}-\frac{k^2}{a^2}\right)\delta\psi+\frac{1}{3}\left(2f_\phi-4V_\phi\right)\delta\phi+\frac{1}{3}\psi\delta R+\frac{2}{3}\dot{\delta\phi}\dot{\phi} \\ =\dot{\psi}\left(\dot{\Phi}+3H\Phi+3\dot{\Psi}\right)+\Phi\left(2\ddot{\psi}+3H\dot{\psi}+\frac{2}{3}\dot{\phi}^2\right), \tag{4.42}$$

$$\ddot{\delta\phi}+3H\dot{\delta\phi}+\left(\frac{k^2}{a^2}-f_{\phi\phi}+2V_{\phi\phi}\right)\delta\phi-\frac{1}{2}\delta R\psi_\phi \\ =\dot{\Phi}\dot{\phi}+\Phi\left(3H\dot{\phi}+2\ddot{\phi}\right)+3\left(H\Phi+\dot{\Psi}\right)\dot{\phi}, \tag{4.43}$$

where δR is the perturbation of (4.9),

$$\delta R = \frac{\delta\psi+\alpha\phi\delta\phi}{A}. \tag{4.44}$$

We now define the comoving curvature perturbation, which is calculated in the longitudinal gauge as eq. (1.74),

$$\mathcal{R} = \Psi - \frac{H}{\rho+P}\delta q, \tag{4.45}$$

where δq is the field momentum perturbation. Given our model with eq. (4.40), the comoving curvature perturbation becomes

$$\mathcal{R} = \Psi - \frac{H}{\dot{H}}\left(\dot{\Psi}+H\Phi\right) = \Psi + \frac{H}{\dot{H}}\left(\frac{\dot{\delta\psi}+\delta\phi\dot{\phi}-H\delta\psi-\dot{\psi}\Phi}{2\psi}\right). \tag{4.46}$$

To further analyse the evolution of the perturbations we can combine the perturbed Einstein equations and the equations of motion eqs. (4.35) and (4.43) into two second-order differential equations. This is achieved by using the relation eqs. (4.38) to (4.41) to remove Φ, $\dot{\Phi}$, $\dot{\delta\phi}$ and $\delta\phi$ respectively. Assuming that $f_{RR} \neq 0$, this results in two coupled second order equations,

$$\begin{aligned}
&\delta\ddot{\psi} + \left[5H + \frac{\dot{\psi}}{\psi} + \frac{(2V_\phi - f_\phi)}{\dot{\phi}}\right]\delta\dot{\psi} \\
&\quad - \left[2(2\dot{H} + H^2) + \frac{(3\psi H - \dot{\psi})(2V_\phi - f_\phi)}{\psi\dot{\phi}} - \frac{10H\dot{\psi}}{\psi} - \frac{2\ddot{\psi}}{\psi} + \frac{\dot{\psi}^2}{\psi^2} + \frac{1}{3}\frac{k^2}{a^2}\right]\delta\psi \\
&\quad = \psi\left[4H - 6\frac{(2V_\phi - f_\phi)}{\dot{\phi}} + 6\frac{\dot{\psi}}{\psi}\right]\dot{\Psi} \\
&\qquad + 2\psi\left[H^2 + \left(\frac{\dot{\psi}}{6\psi} - H\right)\frac{(2V_\phi - f_\phi)}{\dot{\phi}} + \frac{2}{3}\frac{(k^2 - 3K)}{a^2} + 5H\frac{\dot{\psi}}{\psi} + \frac{\ddot{\psi}}{\psi}\right]\Psi,
\end{aligned} \tag{4.47}$$

$$\begin{aligned}
&\ddot{\Psi} + 5H\dot{\Psi} + \left[2(2\dot{H} + H^2) + \frac{1}{3}\frac{k^2 - 2K}{a^2}\right]\Psi \\
&\qquad = \frac{H}{\psi}\delta\dot{\psi} + \frac{2(2H' + H^2) - H\frac{\dot{\psi}}{\psi} + \frac{1}{3}\frac{(2k^2 - 3K)}{a^2}}{\psi}\delta\psi.
\end{aligned} \tag{4.48}$$

We find that the scalaron aids in the stability of Ψ: re-writing eq. (4.48) and grouping common terms

$$\begin{aligned}
\ddot{\Psi} = &-\left(\frac{\delta\dot{\psi}}{\psi} - \frac{\dot{\psi}}{\psi}\frac{\delta\psi}{\psi} - 5\dot{\Psi}\right)|H| - 2\left(2\dot{H} + H^2\right)\left(\Psi - \frac{\delta\psi}{\psi}\right) \\
&- \frac{K}{3a^2}\left[\left(n(n+2) - 2\right)\Psi - \left(2n(n+2) - 3\right)\frac{\delta\psi}{\psi}\right].
\end{aligned} \tag{4.49}$$

Here we have utilised the fact we are in a closed universe so the wavenumber will correspond to the eigenfunctions of the Laplacian operator [221, 222], resulting in the relation $k^2 = n(n+2)K$, where $n > 2$ is an integer eigenvalue[7]. We note that smallest wavenumber, depict very little change, as such the red curve is mostly hidden. From eq. (4.38), we expect the two perturbations $\delta\psi/\psi$ and Ψ to have similar magnitudes, which is also supported by our numerical results shown in figs. 4.6 and 4.7. In the last equation, eq. (4.49), terms containing $\delta\psi/\psi$ and Ψ have opposite signs, which implies a counteracting effect, reducing possible divergent behaviour during a collapse in this specific R^2 theory.

As discussed further below, for small values of n, our numerical calculations show that the last two terms in eq. (4.49) will remain negative during the collapse and bouncing epoch. However, the bracket in the first term will remain overall positive during the collapse and bounce, acting as a

[7] $n = 0$ is the homogeneous background and $n = 1$ is a gauge choice, so we limit ourselves to $n \geq 2$ [223]

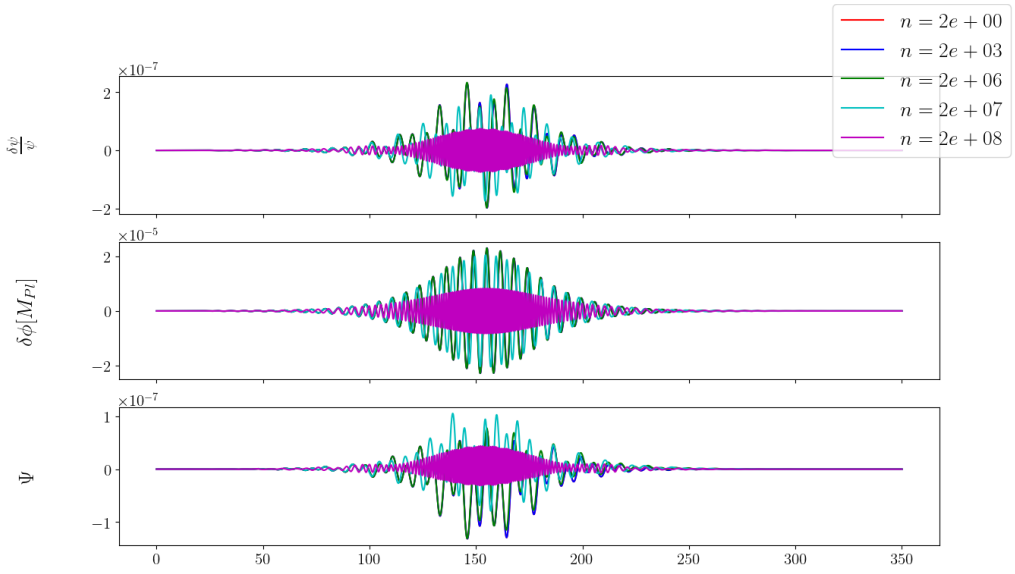

Figure 4.6: A plot demonstrating the effects of varying the wavenumber for the scario that results in eternal inflation. We see that the perturbations stabilise at and tend towards zero as the fields return to their initial values. We see larger wavelengths (smaller n) have an increased amplitude and decreased frequency compared to smaller wavelengths. These plots used the same parameter and initial conditions for the background fields as fig. 4.3.

source term which can lead to an instability. This instability is absent in our simulations since $\delta\dot{\psi}$ increases slower than $\delta\psi$.

Numerical analysis of scalar perturbations

The equations presented above are difficult to solve analytically, so we resort to numerical analysis. We numerically integrate eqs. (4.36), (4.40), (4.42) and (4.43), together with (4.38) to remove Φ and $\dot{\Phi}$. This also allows us to calculate $\mathcal{R}$ from (4.46). We use the following initial conditions, unless stated otherwise: $\delta\phi_i = H/(2\pi)$, $\delta\dot{\phi}_i = \dot{H}/(2\pi)$, $\delta\psi_i = \alpha(8AV(\phi_i) - 1)\phi_i\delta\phi_i$, $\delta\dot{\psi}_i = \alpha(8AV(\phi_i) - 1)\phi_i\delta\dot{\phi}_i$ from (4.18), and set $\dot{\Psi} = 0$. The metric perturbation Ψ is then given by (4.36)[8]. We explore a range of wave-numbers by varying n by orders of magnitude shown in fig. 4.6 and fig. 4.7. It is clear that the perturbations increase in amplitude towards the bounce, as expected, but always

[8]If we were to set the initial time derivatives to zero, this would result in slower growth of the perturbations, resulting in a more stable solution. However, to show the maximum growth, we take the time derivative of initial values.

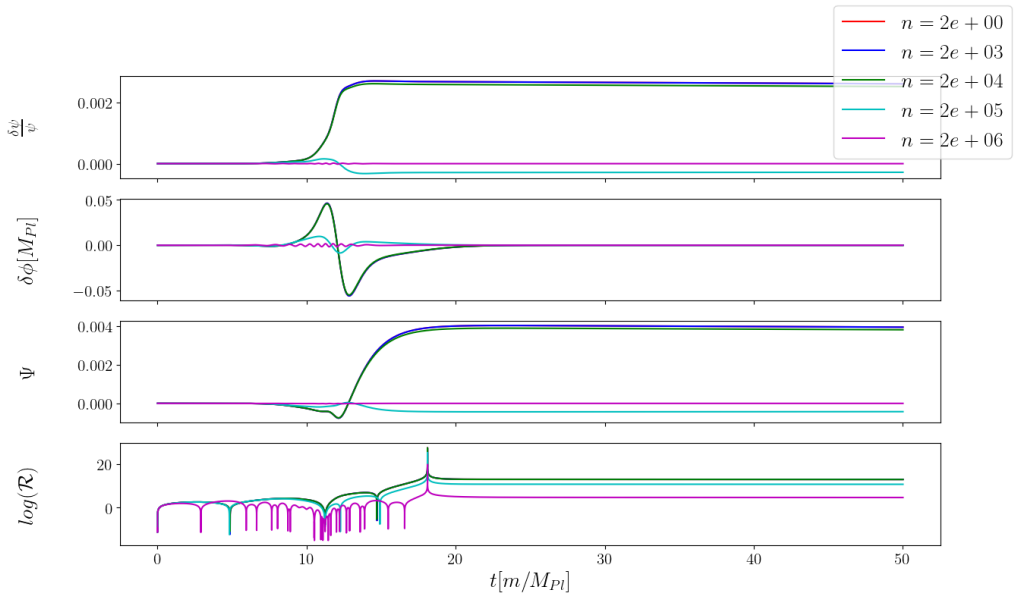

Figure 4.7: A plot demonstrating the effects of varying k. We see that as $\delta\phi \to 0$ and $\delta\psi$ stabilise at some constant non-zero value. Similar to fig. 4.6, we see larger wavelengths (smaller n) have a larger amplitude and decreased frequency compared to smaller wavelengths. For $\delta\psi$ and ψ we notice that the perturbations freeze in after the bounce. These plots used the same parameter and initial conditions for the background fields as fig. 4.4.

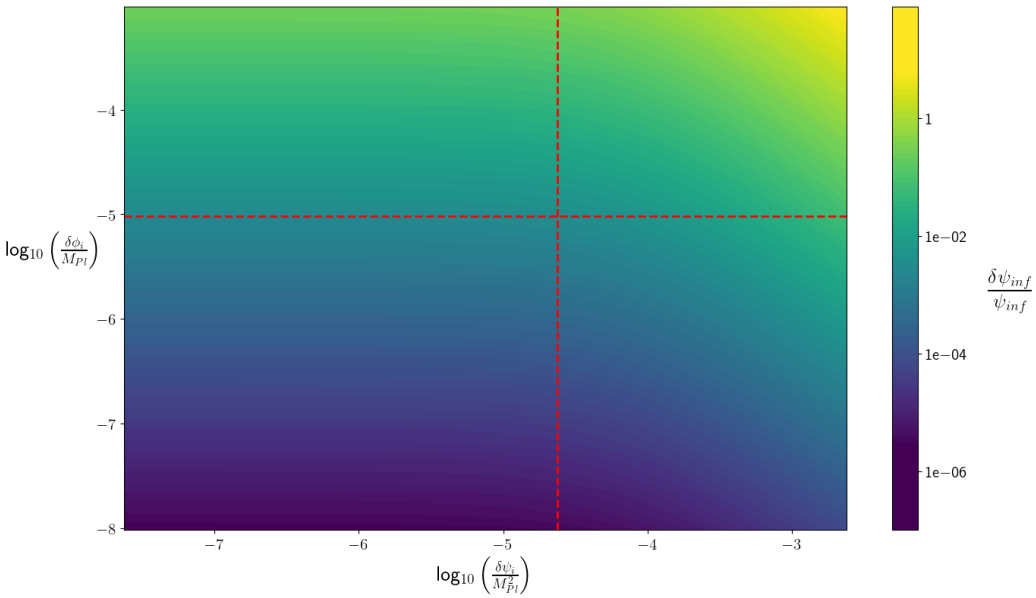

Figure 4.8: A contour plot illustrating the effect of initial conditions on the perturbations. It is clear there is a large range of initial conditions that result in $\delta\psi_{\text{inf}} \ll \psi_{\text{inf}}$. The red line indicates the de-Sitter initial value, $\delta\phi_i = (H/2\pi)$, corresponding to a given $\delta\psi_i$ via eq. (4.18).

remain finite. Furthermore, the perturbations behave as expected once the inflation regime begins; they settle to a constant value while stretched to superhorizon scales. We analyse the following two scenarios:

- $\phi \approx \phi_i$ at the bounce: This is the case resulting in eternal inflation after the bounce. As expected, the perturbations remain very well behaved, with a slight growth similar to the background field values during the bounce, but ultimately stabilising to zero. A noticeable feature is that a much larger wave-number is required to deviate from the behaviour of small wave-numbers compared fig. 4.4. This is because the ϕ-field, dominating the dynamics around the bounce, has been set to have a lower mass than in the finite inflation case.

- $0 < \phi \lesssim \phi_-$ at the bounce: For the scenario which results in finite inflation after the bounce, we notice from fig. 4.7 that perturbations on smaller wave-numbers exhibit a larger growth than perturbations on smaller wavelengths, highlighted between the difference between the green and cyan curves.

The initial conditions determine the evolution of the perturbations and whether instabilities are present. Therefore, we study the model's stability by changing the initial conditions of the perturbations. The stability of the perturbations has been verified and is clear from fig. 4.7. Since the ϕ-field in the finite inflation scenario will always tend towards zero, we concentrate our analysis on the behaviour of the scalaron since if an instability is present, it will manifest growth in $\delta\psi$. The results are shown in fig. 4.8, where we see that the system demonstrates stability in the perturbations. Interestingly, we see a stronger effect on the final perturbations of $\delta\psi_{\text{inf}}$ in fig. 4.8 varying the initial condition of $\delta\psi$. Similar to the background, we see that $\delta\phi$ sources the growth of $\delta\psi$, arising from the $\dot{\delta\phi}$ term in eq. (4.42). Therefore increasing the initial perturbation of $\delta\phi$ increases the growth of $\delta\psi$. Therefore varying $\delta\phi_i$ results in a larger effect in fig. 4.8 than varying $\delta\psi_i$.

Vector and tensor perturbations

Next, we briefly study the vector perturbations introduced in section 1.3.1 and [224, 225] for our bouncing model. Using the decomposed metric given

in eq. (1.80):

$$ds^2_{(v)} = -dt^2 + 2aS_i dt dx^i + a^2\left(\delta_{ij} + 2\partial_j F_i\right) dx^i dx^j \,. \tag{4.50}$$

We define the gauge independent vector shear $\sigma_i = \dot{F}_i + S_i/a$. The field equations for the vector degrees of freedom read

$$\delta\dot{q}_i + 3H\delta q_i = \frac{k^2 - 2K}{a^2}\delta\Pi_i \tag{4.51}$$

$$\frac{k^2 - 2K}{2a^2}\sigma_i = \frac{\delta q_i}{\psi}\,, \tag{4.52}$$

where, $\delta\Pi_i$ is the vector decomposition of the anisotropic stress [226] and δq_i is the momentum density perturbation. Interestingly only one equation is modified by the additional degree of freedom [220]. Assuming that the anisotropic stress vanishes, we can solve the first equation above to give

$$\delta q_i = \delta q_i^{(\mathrm{ini})}\left(\frac{a_{\mathrm{ini}}}{a}\right)^3,$$

where the script 'ini' denotes the initial values for the scale factor and δq_i. The second equation above then leads then to

$$\left(k^2 - 2K\right)\sigma_i = \delta q_i^{(\mathrm{ini})}\frac{a_{\mathrm{ini}}^3}{a}\frac{2}{\psi}. \tag{4.53}$$

As seen from these solutions, the vector perturbations remain finite (with a) growing before the collapse before diluting away with the universe's expansion. The scalaron ψ shows an almost exponential behaviour, while a behaves closer to a quadratic centred around the bounce, fig. 4.4. Thus, we expect the quantity $(a\psi)^{-1}$ to peak around the bounce. Numerically we see a growth of two orders of magnitude. After the bounce, the universe's expansion will cause the vector perturbations to become subdominant, decaying with the universe's expansion. Therefore we conclude that, given a reasonable assumption that the initial vector perturbations are less than two orders of magnitude compared to $\delta q_i^{(\mathrm{ini})}$, the vector modes are stable within this model.

Finally we examine the evolution of tensor perturbations outlined in section 1.3.1, with the line element, eq. (1.83),

$$ds^2_{(T)} = -dt^2 + a^2\left(\delta_{ij} + h_{ij}\right) dx^i dx^j \,. \tag{4.54}$$

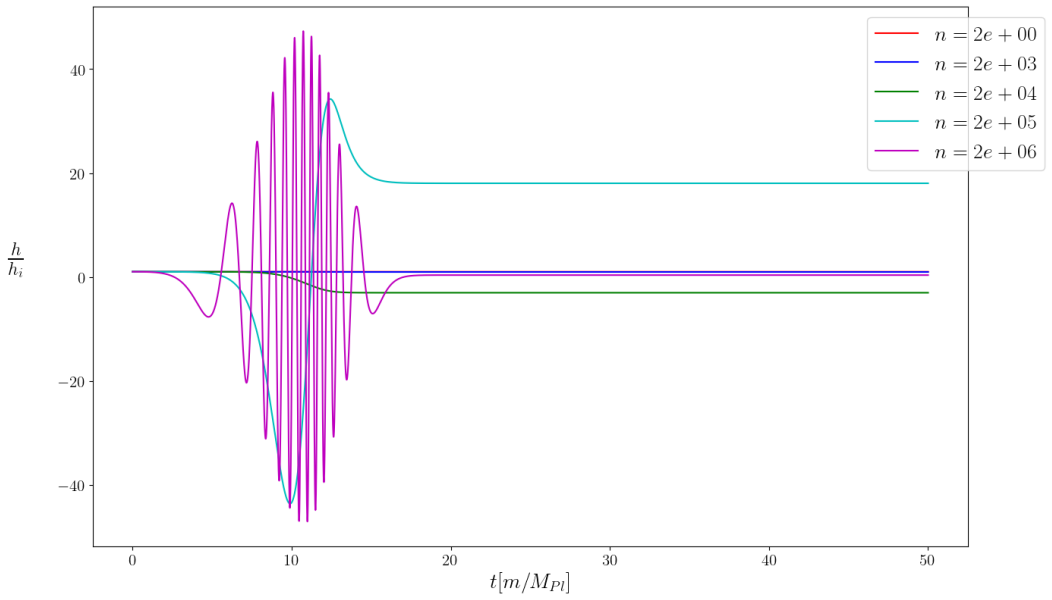

Figure 4.9: Here we see the amplitude growth of tensor perturbations governed by eq. (4.55) for a range of wavelengths. The parameters used are the same for fig. 4.8, with initial perturbation chosen to be $h_i = 10^{-5}$.

In the context of modified gravity and in a closed universe, the gravitational wave equation reads

$$\ddot{h} + \left(3H + \frac{\dot{\psi}}{\psi}\right)\dot{h} + \left(\frac{k^2 + 2K}{a^2}\right)h = 0, \tag{4.55}$$

where h is the amplitude of the two polarisation sates, $h_{ij} = he_{ij}^{(+,\times)}$. Provided the scale factor does not vanish and the background equations eq. (4.13) - (4.15) result in a bounce, we see that the amplitude will remain finite as illustrated in fig. 4.9, as it follows similar dynamics to the KG equation. Moreover, adding modified gravity reduces the growth of h during the collapse, as $\dot{\psi}/\psi$ counteracts the Hubble term. We, therefore, conclude that the tensor modes remain small and well-behaved throughout the bounce.

4.3 Discussion on classical bouncing cosmology

Bouncing cosmologies remove the singularity associated with the Big Bang theory. However, an issue of classical bouncing cosmologies is the divergent nature associated with a collapsing universe. We have studied how the normal damping effect, from the Universe's expansion, becomes a source term in a collapsing scenario, leading to a diverging solution and often resulting in a singularity. Assuming classical GR and a homogeneous and isotropic Universe, additional contributions are required in the Friedmann equations to satisfy the null energy conditions whilst simultaneously allowing for a bounce. Therefore finding a well-motivated additional degree of freedom that dominates the Friedmann equation and then vanishes, such that the model remains compatible with observations, often requires an unnatural amount of fine-tuning.

We studied a particular classical bouncing toy universe with a transition into an inflationary phase using a generalised Starobinsky $f(R)$ model. Our model assumes a spatially closed universe to achieve the bounce without violating the null energy condition. However, in the most straightforward picture of including a singular scalar field, inducing a bounce from a spatially closed universe, requires fine-tuning initial conditions. [211] investigated this scenario to address the initial conditions leading to a bounce. They argued that the pre-bounce universe was dominated by a false vacuum identified as dark energy that set the initial conditions. We built upon their work of an initially collapsing universe dominated by dark energy by extending the action to include a Starobinksy R^2 term, such that the bounce will be followed by a period of inflation.

The field responsible for dark energy, ϕ, sits in a false vacuum until the bounce happens. It then settles at the true minimum of the effective potential. The scalaron, ψ, obtains a kick from ϕ during the bounce, driving it up its effective potential but remains almost dormant before and during the bounce. Thus, the interaction between the dark energy field and the scalaron leads naturally to a single field Starobinksy inflationary epoch after the bounce. Moreover, the arbitrary initial conditions required for inflation, as discussed in section 4.2.3, are predetermined by the potential giving rise

to dark energy pre-bounce. We also investigated the perturbations involved during a bouncing epoch. Due to the collapse, the same divergent behaviour at the background level also exists in first order perturbations. However, an additional degree of freedom does not lead to divergent behaviour. Rather, we find evidence that the scalaron assists the stability of the perturbations of this model, as discussed in section 1.3.1.

Unfortunately, the model does not exhibit cyclic behaviour due to the fields settling in the global minimum away from the initial conditions. Extending the model to include a cyclic behaviour requires a new non-trivial mechanism to drive the field back to its initial conditions.

5 | Conclusion and Discussion

As discussed in the introduction to cosmology, section 1.3, the observed accelerated expansion of the Universe challenges the validity of standard General Relativity (GR), described by the Einstein-Hilbert action, at large scales. As a consequence to describe the acceleration, we look for approaches to extend GR by introducing additional degrees of freedom. This approach aims to identify whether minimal extensions to the theory can account for the observations and provide a satisfactory model of the Universe. However, modifying a theory is a delicate process that requires caution. It is easy to include an arbitrary number of additional degrees of freedom to fit the data, resulting in overfitting the data and losing predictability; therefore, we aim to implement Occam's razor into any models studied. Moreover, we expect modifications to resolve the shortcomings and provide new phenomenological insight into the fundamental theory, predicting new detectable phenomena. Consequently, many modifications are motivated by an external theory, such as a quantum description of gravity or a connection to the standard model of particle physics.

A simple modification was included to GR, a cosmological constant, Λ, and non-relativistic matter that does not interact with EM to address the observed dark sector of the Universe. This became our best-fitting cosmological model dubbed ΛCDM. While this model initially provided a good fit to observational data, significant fine-tuning was required to match observations, which led to many conceptual issues. Moreover, a fundamental embedding of this constant still imposes a challenge. With the recently increased precision of cosmological observations, tensions have arisen between different epochs that highlight issues with the current paradigm, which motivates more complex extensions to GR.

We have discussed the relation in section 1.2, between two commonly

modified theories of gravity, $f(R)$ and quintessence. We highlight that the $f(R)$ theories enable a more general framework of modifications, such as including multiple higher-order terms in the gravitational sector. A particularly interesting model examined throughout this thesis is Starobinsky's R^2 model: originally motivated from a quantum description of gravity intended to resolve the initial singularity of the Big Bang, it has proven to be a robust model in the context of inflation. This model exhibits an effective potential that naturally allows for slow-rolling inflation and the resulting inflationary parameters surprisingly fits exceptionally well with new precise cosmological observations from the CMB. However, extensions to the original model produce potentially interesting phenomenology that is expected to generate cosmological features that are detectable in the future.

In chapter 2, we studied the constraining power of gravitational wave experiments on dark energy models that aim to replace the role of Λ, which utilises the introduction of a scalar field. We generated mock data to forecast the results of gravitational waves from third-generation gravitational detectors, assuming ΛCDM as our fiducial model, creating a slight bias. Then using mock data, we analysed the constraining power of GW compared to local measurements of BAO and SNIa.

The analysis revealed that GWs are expected to provide improved accuracy in estimating the parameter H_0 compared to local measurements. However, due to the bias set by the input model, the estimated parameters were limited to the fiducial values. Furthermore, our findings indicated that the GW data sets did not yield better constraints on the model parameters than BAO+SNIa. However, combining the two data sets reduced the error bars, in some cases, by more than a factor of 2, providing strong constraints on the new model parameters.

Therefore, we can conclude that GWs will be critical in addressing cosmological tensions, particularly those about H_0. This will indicate the validity of current cosmological paradigms, most notably ΛCDM. In the context of modified gravity, GWs offer multiple features that can constrain cosmological models. Although they provide an additional probe to constrain cosmological model parameters, the accuracy in constraining these parameters from 3G detectors is expected to be lower than that given by local

measurement data sets.

In chapter 3, we analysed the theory of inflation in the context of modified gravity. Initially showing the success of Starobinksy's inflation, we studied a modification intending to embed the theory into a more fundamental theory of gravity by introducing a dynamically induced Planck mass. This involved the introduction of additional non-minimally coupled scalar fields, which generated the Planck mass through their vacuum expectation values. Although the cosmological parameters resulted in the same value as Starobinky inflation, the model naturally produced a non-zero minimum potential energy after inflation that can be identified as a cosmological constant. The model's parameters must be set to unnatural values to equate the resulting cosmological constant to current observations. Therefore to resolve the issue and allow the model to remain viable without fine-tuning the parameters, we introduced an additional field that forced the potential to vanish at the minimum. This additional field introduced non-trivial features into the model, such as the presence of a small local effective well in the potential, which delayed the slow-rolling mechanism. Additionally, the third–field induced an additional period of inflation.

We also investigated the behaviour of cosmological perturbations during inflation, using this model as an example. As argued in section 3.4, the resulting perturbations from inflation are the strongest success of the theory: It naturally produces a near-flat power spectrum and a small ratio of tensor to scale perturbations, r. Although the result is relatively generic for inflationary models, the increased precision of the CMB detection has led to many of the simplest models being excluded. Therefore a natural extension that has been exhaustively studied is multi-field inflation. However, this has primarily been limited to two fields. To analyse our model, the formalism, well established for two fields, was extended to incorporate a third field building upon the structure of spherical coordinates. Our three-field model's power spectrum displayed a power drop at specific wavelengths, thus preventing the production of primordial black holes through a mechanism that required a spike in the power spectrum at low wavelengths.

Due to the successes of Starobinsky inflation, we also analysed incorporating this modification to resolve a conceptual issue with inflation, primar-

ily the initial singularity. In chapter 4, we aimed to replace the singularity with a transition from collapsing to expanding called a bounce. Constructing a bounce transition within the framework of GR in a homogeneous and isotropic background requires specific initial conditions, as the collapsing epoch naturally leads to divergent behaviour and the formation of a singularity. To overcome this challenge, we developed a model that employed a potential with a false vacuum, representing the Universe's dark energy before the bounce and incorporated suitable initial conditions. This model required an additional non-minimally coupled field to generate the bounce.

The model is constructed in a way that allows for the dynamics of the bounce to be primarily governed by the behaviour of the additional field, which subsequently settled at the origin. Therefore after the bounce, the scalaron, produced by the R^2 term, dominates the Friedmann equation and successfully reproduces a period of single-field Starobinsky inflation, benefiting from the successes that arise with the inflationary model. Interestingly, the interaction between the two fields drives the scalaron up its effective potential. This feature naturally produces the initial conditions of Starobinsky inflation and ensures inflation lasts sufficiently long.

Similar to the background, perturbations in a collapsing epoch are divergent due to the amplifying $-|H|$ term, resulting in a breakdown of the model [215, 227]. Our analysis examined the evolution of perturbations in a general $f(R)$ theory before, during, and after the bounce. We observed that the presence of a scalaron in a generic $f(R)$ theory can contribute to the stability of the bounce. Although, this characteristic is model dependent. For our model, studied in section 4.2, we observed enhanced stability on the perturbations, resulting in large freedom in the choice of initial conditions.

As the Universe transitions from the bounce to an inflationary epoch, the perturbations induced during the bounce become frozen, as reviewed in chapter 3. Consequently, the specific bounce dynamics of the model determine the background field and perturbation initial conditions for inflation. Therefore in future work, constraints from cosmic microwave background (CMB) measurements can be utilised to study both the inflationary dynamics and the characteristics of the bounce transition.

In summary, we have looked at different modified gravity models in

separated epochs. However, if we expect modified gravity to highlight the fundamental theory governing cosmology, we expect a uniform model across all epochs that is consistent with observations. The current paradigm of ΛCDM distinctly separates the two epochs and generally relies on a new fundamental field called the inflaton with specific potential. Moreover, the cosmological constant is measured to have a value not motivated by any fundamental theory. Dark energy and inflation have similar dynamics, resulting in a quasi-de-Sitter universe, albeit with very different energy scales. Modified gravity offers a unique way to unify these two separate but similar epochs. A future task for modified gravity is to predict the nature of this large discrepancy of energy scales between the two epochs. There have already been many successful models in reproducing a modified gravity model that unifies inflation and dark energy [228, 229]. Although not statistically favourable due to the need for many new ingredients, it highlights the interesting phenomenology of modified gravity. Furthermore, assuming ΛCDM, new cosmological tensions have arisen from precision cosmology, identifying the breakdown of the model. A unifying modified gravity model between dark energy and inflation will also potentially address these issues.

An interesting aspect of modified gravity is the unification of a bouncing scenario that naturally exits into an inflationary epoch. Bouncing cosmologies are not part of the current cosmological paradigm, unlike inflation which still relies on a singularity. However, further complexities are required when considering bouncing cosmologies and, by extension, cyclic Universes. Many models of cyclic Universes in the literature describe a "cut and paste" universe, where the Universe is indeed cyclic but undergoes the same behaviour every iteration [204, 205]. However, with the inclusion of matter from reheating and the decay before the collapse, we expect a change in the dynamics of each cycle. This also provides a change in the total entropy in each universe, and thus an arrow of time [230, 231]. Therefore when considering a bounce, we aim to find a bouncing behaviour for a range of different initial conditions. This is a future task of modified gravity to provide a complete picture of cosmology, compatible with each epoch.

Throughout the thesis, we have presented an argument that modifications to gravity are a prominent and exciting area of research with meaning-

ful applications in different epochs. We have illustrated a range of non-trivial mechanisms that yield interesting predictions and characteristics in different epochs. Although a singular modified gravity theory does not exhibit a complete picture of cosmology, it can be used to develop EFT approaches in specific regimes that provide a greater understanding of the phenomenology of gravity.

A | Derivation of Modified Einstein Equation

We have discussed the Friedmann equations are determined from the EFE. For the given class of modified gravity models with the action,

$$\mathcal{S} = \int d^4x\sqrt{-g}f(R) \tag{A.1}$$

We can find the equations of motion and EFE by varying the action with respect to $g^{\mu\nu}$.

$$\begin{aligned}
\delta\mathcal{S} &= \int d^4x\{\delta(\sqrt{-g})f(R) + \sqrt{-g}\delta f(R)\} \\
&= \int d^4x\left(-\frac{1}{2}\sqrt{-g}g_{\mu\nu}\delta g^{\mu\nu}\right)f(R) + \int d^4x\sqrt{-g}f(R)_{,R}\,\delta(g^{\mu\nu}R_{\mu\nu}) \\
&= -\frac{1}{2}\int d^4x\sqrt{-g}g_{\mu\nu}f(R)\delta g^{\mu\nu} + \int d^4x\sqrt{-g}f(R)_{,R}\,R_{\mu\nu}\delta(g^{\mu\nu}) \\
&\qquad + \int d^4x\sqrt{-g}f(R)_{,R}\,g^{\mu\nu}\delta R_{\mu\nu}.
\end{aligned} \tag{A.2}$$

Now since only the last term is not in the desired form, we will focus on that one.

$$\begin{aligned}
\int d^4x\sqrt{-g}f_{,R}\,g^{\mu\nu}\delta R_{\mu\nu} &= \int d^4x\sqrt{-g}f_{,R}\,g^{\mu\nu}\delta R^{\lambda}_{\mu\lambda\nu} \\
&= \int d^4x\sqrt{-g}f_{,R}\,g^{\mu\nu}(\nabla_\lambda\delta\Gamma^{\lambda}_{\nu\mu} - \nabla_\nu\delta\Gamma^{\lambda}_{\lambda\mu}) \\
&= \int d^4x\sqrt{-g}f_{,R}\,\nabla_\lambda(g^{\mu\nu}\delta\Gamma^{\lambda}_{\nu\mu} - g^{\mu\lambda}\delta\Gamma^{\nu}_{\nu\mu}) \\
&= \int d^4x\sqrt{-g}f_{,R}\,\nabla_\lambda(g_{\mu\nu}\nabla^\lambda\delta g^{\nu\mu} - \nabla_\nu\delta g^{\lambda\nu}) \\
&= \int d^4x\sqrt{-g}f_{,R}\,(g_{\mu\nu}\Box\delta g^{\nu\mu} - \nabla_\lambda\nabla_\nu\delta g^{\lambda\nu})
\end{aligned} \tag{A.3}$$

Now we need to take out the $\delta g^{\mu\nu}$. To do this by taking advantage that we force the variation to vanish at infinity. Allowing us to freely integrate by

parts.

$$
\begin{aligned}
\int d^4x\sqrt{-g}f_{,R}\,g^{\mu\nu}\delta R_{\mu\nu} &= \int d^4x\sqrt{-g}f_{,R}\,g_{\mu\nu}\frac{1}{\sqrt{-g}}\partial_\rho(\sqrt{-g}g^{\rho\sigma}\partial_\sigma\delta g^{\nu\mu}) \\
&\quad - \int d^4x\sqrt{-g}f_{,R}\,\nabla_\lambda V^\lambda \\
&= -\int d^4x\partial_\rho(f_{,R}\,g_{\mu\nu})\sqrt{-g}g^{\rho\sigma}\partial_\sigma\delta g^{\nu\mu} - \int d^4x\sqrt{-g}f_{,R}\,(\partial_\lambda V^\lambda \\
&\quad + \Gamma^\lambda_{\lambda\gamma}V^\gamma) \\
&= \int d^4x\partial_\sigma[\partial_\rho(f_{,R}\,g_{\mu\nu})\sqrt{-g}g^{\rho\sigma}]\delta g^{\nu\mu} + \int d^4x\partial_\lambda(\sqrt{-g}f_{,R})V^\lambda \\
&\quad - \int d^4x\sqrt{-g}f_{,R}\,\Gamma^\lambda_{\lambda\gamma}V^\gamma) \\
&= \int d^4x\sqrt{-g}\delta g^{\nu\mu}\Box(f_{,R}\,g_{\mu\nu}) + \int d^4x\sqrt{-g}(\Gamma^\gamma_{\gamma\lambda}f_{,R} + \partial_\lambda f_{,R})V^\lambda \\
&\quad - \int d^4x\sqrt{-g}f_{,R}\,\Gamma^\lambda_{\lambda\gamma}V^\gamma) \\
&= \int d^4x\sqrt{-g}\delta g^{\nu\mu}\Box(f_{,R}\,g_{\mu\nu}) + \int d^4x\sqrt{-g}\partial_\lambda f_{,R}\,V^\lambda \\
&= \int d^4x\sqrt{-g}\delta g^{\nu\mu}\Box(f_{,R}\,g_{\mu\nu}) + \int d^4x\sqrt{-g}(\partial_\lambda f_{,R})(\nabla_\nu\delta g^{\lambda\nu}) \\
&= \int d^4x\sqrt{-g}\delta g^{\nu\mu}\Box(f_{,R}\,g_{\mu\nu}) \\
&\quad + \int d^4x\sqrt{-g}(\partial_\lambda f_{,R})(\partial_\nu\delta g^{\lambda\nu} + \Gamma^\lambda_{\nu\gamma}\delta g^{\gamma\nu} + \Gamma^\nu_{\nu\gamma}\delta g^{\lambda\gamma}) \\
&= \int d^4x\sqrt{-g}\delta g^{\nu\mu}\Box(f_{,R}\,g_{\mu\nu}) - \int d^4x\partial_\nu[\sqrt{-g}(\partial_\lambda f_{,R})]\delta g^{\lambda\nu} \\
&\quad + \int d^4x\sqrt{-g}(\partial_\lambda f_{,R})(\Gamma^\lambda_{\nu\gamma}\delta g^{\gamma\nu} + \Gamma^\nu_{\nu\gamma}\delta g^{\lambda\gamma}) \\
&= \int d^4x\sqrt{-g}\delta g^{\nu\mu}\Box(f_{,R}\,g_{\mu\nu}) - \int d^4x[\sqrt{-g}\Gamma^\gamma_{\gamma\nu}(\partial_\lambda f_{,R}) \\
&\quad + \sqrt{-g}\partial_\nu\partial_\lambda f_{,R}]\delta g^{\lambda\nu} + \int d^4x\sqrt{-g}(\partial_\lambda f_{,R})(\Gamma^\lambda_{\nu\gamma}\delta g^{\gamma\nu} + \Gamma^\nu_{\nu\gamma}\delta g^{\lambda\gamma}) \\
&= \int d^4x\sqrt{-g}\delta g^{\nu\mu}\Box(f_{,R}\,g_{\mu\nu}) \\
&\quad - \int d^4x\sqrt{-g}[\partial_\nu\partial_\lambda f_{,R} - (\partial_\mu f_{,R})\Gamma^\gamma_{\nu\mu}]\delta g^{\mu\nu}
\end{aligned}
\tag{A.4}
$$

Where we used a temporary vector to simplify, $V^\lambda = \nabla_\nu\delta g^{\lambda\nu}$. Also the fact $\partial_\gamma\sqrt{-g} = \Gamma^\lambda_{\lambda\gamma}$. In the last line, we cancelled out equivalent terms and relabelled the indices.

Putting this altogether, we can find Einstein's modified tensor,

$$\frac{\delta \mathcal{S}}{\delta g^{\mu\nu}} = \int d^4x\sqrt{-g}\left[-\frac{1}{2}g_{\mu\nu}f(R) + f(R)_{,R}\,R_{\mu\nu} + \Box(f_{,R}\,g_{\mu\nu}) - \nabla_\mu\nabla_\nu f_{,R}\right]$$
$$\tilde{G}_{\mu\nu} = f_{,R}\,R_{\mu\nu} - \frac{1}{2}g_{\mu\nu}f + g_{\mu\nu}\Box f_{,R} - \nabla_\mu\nabla_\nu f_{,R} \tag{A.5}$$

Normally in modified gravity theories, there will also be an additional scalar field and matter Lagrangian.

B | Conformal Transformation

Given a generic action, for an $f(R)$ theory with an additional scalar field, in the Jordan frame is given by

$$\mathcal{S} = \int d^4x\sqrt{-\tilde{g}}\left[f(\tilde{R}) - \frac{1}{2}\tilde{g}^{\mu\nu}\partial_\mu\chi\partial_\nu\chi\right]. \tag{B.1}$$

The tilde above the metric and curvature indicates a Jordan frame metric. We can transform this into the scalar-tensor representation by introducing an auxiliary field α. We are free to then rewrite the action to include the auxiliary field

$$\mathcal{S} = \int d^4x\sqrt{-g}\frac{M_{\rm Pl}}{2}\left[f(\alpha) + f'(\alpha)\,(R-\alpha) - \frac{1}{2}\tilde{g}^{\mu\nu}\partial_\mu\chi\partial_\nu\chi - U(\chi)\right], \tag{B.2}$$

where the prime indicates a derivative with respect to α. When the action is varied with respect to α we obtain the result $f''(\alpha)(R-\alpha) = 0$. Therefore provided $f''(\chi) \neq 0$, we recover our original action using the result that $R = \alpha$. We then identify the additional degree of freedom, the scalaron, as

$$\phi = f'(\chi),$$

Thus, to write the action as a scalar-tensor theory, similar to that of BD, eq. (3.78) we set the total effective potential to be $V(\phi) = \alpha\phi - f(\alpha) + V(\chi)$. Therefore the action therefore we can rewrite our action as,

$$\mathcal{S} = \int d^4x\sqrt{-\tilde{g}}\left[\phi\tilde{R} - \frac{1}{2}\tilde{g}^{\mu\nu}\partial_\mu\chi\partial_\nu\chi - V(\phi,\chi)\right]. \tag{B.3}$$

For a conformal transformation of the form $\tilde{g}_{\mu\nu} = \Omega^2 g_{\mu\nu}$, we identify how the metric will transform and how the Ricci scalar will transform:

$$\tilde{g}_{\mu\nu} = \Omega^2 g_{\mu\nu}, \qquad \tilde{g}^{\mu\nu} = \Omega^{-2}g^{\mu\nu}, \qquad \sqrt{-\tilde{g}} = \Omega^4\sqrt{-g}, \tag{B.4}$$

$$\tilde{R} = R\Omega^{-2} - 6\Omega^{-3}\Box\Omega. \tag{B.5}$$

Substituting these transformations into (B.3) produces the action,

$$\mathcal{S} = \int d^4x\sqrt{-g}\left[\phi(R\Omega^2 - 6\Omega\Box\Omega) - \frac{1}{2}\Omega^2 g^{\mu\nu}\partial_\mu\chi\partial_\nu\chi - \Omega^4 V(\alpha,\phi,\chi)\right]. \quad \text{(B.6)}$$

Here, it is clear to transform into the Einstein frame we need to define $\phi\Omega^2 = 1/2\kappa^2$. Focusing on the second term in (B.6), we expand the d'Alembert's operator and put everything in terms of Ω,

$$\int d^4x\sqrt{-g}\phi\Omega\Box\Omega = \frac{1}{2\kappa^2}\int d^4x\sqrt{-g}\frac{1}{\Omega}\frac{\partial_\mu\left(\sqrt{-g}g^{\mu\nu}\partial_\nu\Omega\right)}{\sqrt{-g}}. \quad \text{(B.7)}$$

This then allows us to perform an integration by parts to move the derivative. Ignoring the boundary terms,

$$\int d^4x\sqrt{-g}\phi\Omega\Box\Omega = -\frac{1}{2\kappa^2}\int d^4x\sqrt{-g}\partial_\mu\left(\frac{1}{\Omega}\right)g^{\mu\nu}\partial_\nu\Omega \quad \text{(B.8)}$$

$$= \frac{1}{2\kappa^2}\int d^4x\sqrt{-g}\frac{1}{\Omega^2}g^{\mu\nu}\partial_\mu\Omega\partial_\nu\Omega. \quad \text{(B.9)}$$

We can then rewrite this in terms of ϕ and substitute back into (B.6) to give the action in terms of ϕ

$$\mathcal{S} = \int d^4x\sqrt{-g}\left[\frac{R}{2\kappa^2} - \frac{3}{4\kappa^2\phi^2}g^{\mu\nu}\partial_\mu\phi\partial_\nu\phi - \frac{1}{4\kappa^2\phi}g^{\mu\nu}\partial_\mu\chi\partial_\nu\chi - \frac{1}{4\kappa^2\phi^2}V(\phi,\chi)\right]. \quad \text{(B.10)}$$

We can then perform a field redefinition to a canonically normalised field, $2\kappa^2\phi = \exp(\beta\kappa\psi)$, finally reducing our action to

$$\mathcal{S} = \int d^4x\sqrt{-g}\left[\frac{R}{2\kappa^2} - \frac{3}{4}\beta^2 g^{\mu\nu}\partial_\mu\psi\partial_\nu\psi - \frac{1}{2}e^{-\beta\kappa\psi}g^{\mu\nu}\partial_\mu\chi\partial_\nu\chi - e^{-2\beta\kappa\psi}V(\psi,\chi)\right]. \quad \text{(B.11)}$$

Therefore we set $\beta = \sqrt{2/3}$ to ensure a canonical kinetic term of ψ.

C | Additional LISA constraints: varied fiducial and smearing

Conformal Coupled Quintessence				
Data sets	Ω_m^0	H_0	α	λ
BAO+SNIa	$0.3019^{+0.0088}_{-0.0059}$	$73.2^{+4.7}_{-3.5}$	$0.085^{+0.055}_{-0.043}$	$0.42^{+0.20}_{-0.36}$
Double error				
LISA pop3	$0.295^{+0.014}_{-0.0053}$	$66.55^{+0.64}_{-0.42}$	$0.120^{+0.053}_{-0.095}$	$0.49^{+0.24}_{-0.45}$
LISA pop3+BAO+SNIa	$0.2999^{+0.0077}_{-0.0037}$	66.88 ± 0.39	$0.041^{+0.020}_{-0.034}$	$0.37^{+0.18}_{-0.32}$
$H_0 = 70$ prior				
LISA pop3	$0.307^{+0.016}_{-0.0056}$	$70.20^{+0.97}_{-0.62}$	$0.138^{+0.064}_{-0.10}$	$0.48^{+0.22}_{-0.45}$
LISA pop3+BAO+SNIa	$0.304^{+0.011}_{-0.0052}$	69.87 ± 0.60	$0.069^{+0.040}_{-0.047}$	$0.48^{+0.25}_{-0.37}$

Table C.1: Marginalized constraints on cosmological and model parameters for coupled quintessence at 68% C.L.

In the analysis presented in section 2.2.1, we analysed the results given a particular fiducial value, specifically H_0= 67[km s^{-1} Mpc^{-1}]. Consequently, we could not rely on the estimated values predicted for H_0 and Ω_m^0. Furthermore, to incorporate the deviations from the given ΛCDM model in the simulation of GWs, we applied a smear function on each merger. This ensured that the measurements were distributed away from the given ΛCDM model. This was determined by a Gaussian distribution, with a limit of 1σ, which was determined by the total measurement error.

The effects of changing the fiducial value to H_0 = 70 km s^{-1} Mpc^{-1} and increasing the smearing can be observed in Table C.1. As expected, changing the fiducial value of H_0= 70[km s^{-1} Mpc^{-1}] generates an estimated value that

is close to the fiducial value. Although interestingly this has resulted in a slightly worse accuracy compared to the fiducial value of H_0= 67[km s^{-1} Mpc^{-1}]. The effect of this change of value can be seen in as a shift in the distribution in fig. C.1b[1].

We also increased the smearing effect to 2σ, identified in as "double error" in fig. C.1 and table C.1. However, we notice a negligible effect, compared to table 2.1, in either the parameter estimation or the accuracy of the parameters. This can be further highlighted in fig. C.1a, where there is very little change in the distribution compared to that of fig. 2.3b.

[1]The table and figures presented here were created by Elsa Teixeira for the purposes of this collaborative work

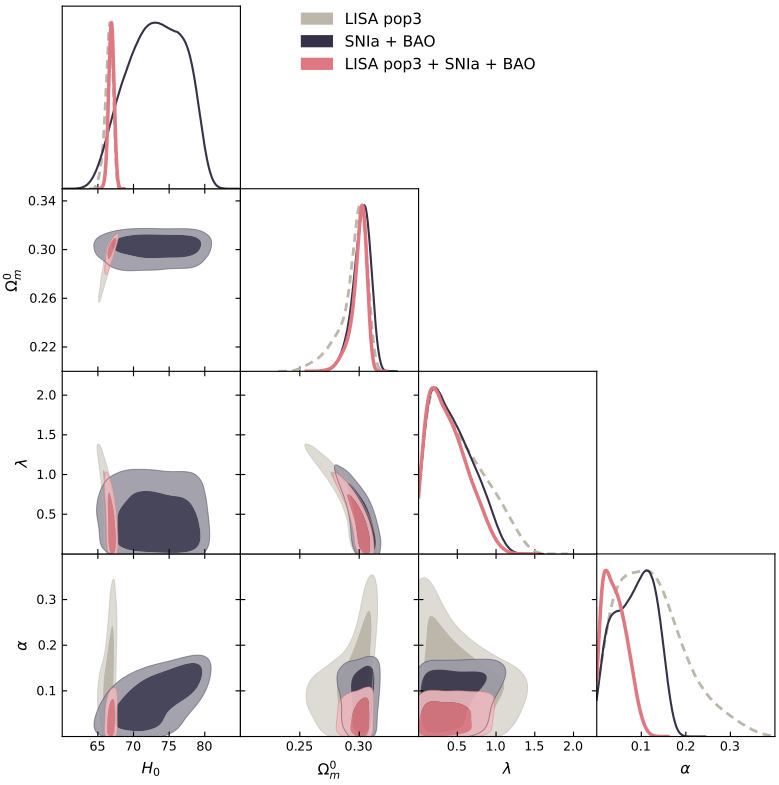

(a) Double error

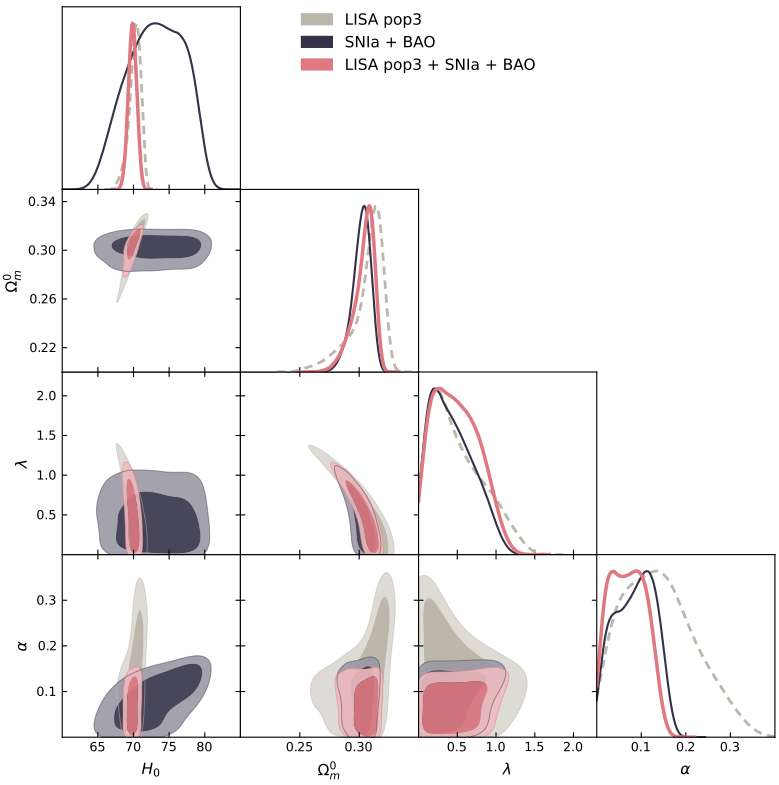

(b) $H_0 = 70[\mathrm{km\ s^{-1}\ Mpc^{-1}}]$

Figure C.1: Constraints for conformal coupled quintessence. The darker contour identifies the 1σ region, and the lighter 2σ.

References

[1] E. M. Teixeira, R. Daniel, N. Frusciante, and C. van de Bruck. Forecasts on interacting dark energy with standard sirens. *Phys. Rev. D*, 108(8): 084070, 2023. doi: 10.1103/PhysRevD.108.084070. arXiv: 2309.06544.

[2] C. van de Bruck and R. Daniel. Inflation and scale-invariant R^2 gravity. *Phys. Rev. D*, 103(12):123506, 2021. doi: 10.1103/PhysRevD.103.123506. arXiv: 2102.11719.

[3] R. Daniel, M. Campbell, C. van de Bruck, and P. Dunsby. Transitioning from a bounce to R^2 inflation. *JCAP*, 06:030, 2023. doi: 10.1088/1475-7516/2023/06/030. arXiv: 2212.01093.

[4] J.R. Primack. *The view from the center of the universe*. Riverhead, 2006.

[5] I. Newton, I. B. Cohen, A. Whitman, and J. Budenz. *The Principia: The Authoritative Translation and Guide: Mathematical Principles of Natural Philosophy*. University of California Press, 1999.

[6] U. Le Verrier. Lettre de m. le verrier à m.faye sur lathéorie de mercure et sur le mouvement du périhélie de cette planète, 1859. Comptes rendus hebdomadaires des séances de l'Académie des sciences (Paris), vol. 49 (1859), pp.379–383.

[7] A. Einstein. Explanation of the Perihelion Motion of Mercury from the General Theory of Relativity. *Sitzungsber. Preuss. Akad. Wiss. Berlin (Math. Phys.)*, 1915:831–839, 1915.

[8] A. Einstein. The Field Equations of Gravitation. *Sitzungsber. Preuss. Akad. Wiss. Berlin (Math. Phys.)*, 1915:844–847, 1915.

[9] A. Einstein. On the General Theory of Relativity. *Sitzungsber. Preuss. Akad. Wiss. Berlin (Math. Phys.)*, 1915:778–786, 1915.

[10] A. Einstein. The Foundation of the General Theory of Relativity. *Annalen Phys.*, 49(7):769–822, 1916. doi: 10.1002/andp.200590044.

[11] A. Einstein. Cosmological Considerations in the General Theory of Relativity. *Sitzungsber. Preuss. Akad. Wiss. Berlin (Math. Phys.)*, 1917: 142–152, 1917.

[12] R. S. Park, W. M. Folkner, A. S. Konopliv, J. G. Williams, D. E. Smith, and M.T. Zuber. Precession of mercury's perihelion from ranging to the messenger spacecraft. *The Astronomical Journal*, 153(3):121, feb 2017. doi: 10.3847/1538-3881/aa5be2.

[13] S.M. Carroll. *Spacetime and Geometry: An Introduction to General Relativity*. Cambridge University Press, 2019. doi: 10.1017/9781108770385.

[14] R.M. Wald. *General Relativity*. University of Chicago Press, 2010.

[15] J. B. Hartle. *Gravity: An Introduction to Einstein's General Relativity*. Cambridge University Press, 2021. doi: 10.1017/9781009042604.

[16] K. Schwarzschild. On the gravitational field of a mass point according to Einstein's theory. *Sitzungsber. Preuss. Akad. Wiss. Berlin (Math. Phys.)*, 1916:189–196, 1916.

[17] J. R. Oppenheimer and H. Snyder. On continued gravitational contraction. *Phys. Rev.*, 56:455–459, Sep 1939. doi: 10.1103/PhysRev.56.455.

[18] R. Penrose. Gravitational collapse and space-time singularities. *Phys. Rev. Lett.*, 14:57–59, Jan 1965. doi: 10.1103/PhysRevLett.14.57.

[19] A. Einstein and N. Rosen. On Gravitational waves. *J. Franklin Inst.*, 223:43–54, 1937. doi: 10.1016/S0016-0032(37)90583-0.

[20] B. P. Abbott et al. Observation of Gravitational Waves from a Binary Black Hole Merger. *Phys. Rev. Lett.*, 116(6):061102, 2016. doi: 10.1103/PhysRevLett.116.061102.

[21] J. Wheeler and K. Ford. Geons, black holes and quantum foam: A life in physics. *American Journal of Physics*, 68, 06 2000. doi: 10.1119/1.19497.

[22] A. Einstein. On the electrodynamics of moving bodies. *Annalen Phys.*, 17:891–921, 1905. doi: 10.1002/andp.200590006.

[23] D. Hilbert. Die Grundlagen der Physik. 1. *Gott. Nachr.*, 27:395–407, 1915.

[24] W. de Sitter. Einstein's theory of gravitation and its astronomical consequences, Third Paper. *Mon. Not. Roy. Astron. Soc.*, 78:3–28, 1917.

[25] S. M. Carroll. The Cosmological constant. *Living Rev. Rel.*, 4:1, 2001. doi: 10.12942/lrr-2001-1.

[26] T. Clifton, P. G. Ferreira, A. Padilla, and C. Skordis. Modified Gravity and Cosmology. *Phys. Rept.*, 513:1–189, 2012. doi: 10.1016/j.physrep.2012.01.001.

[27] B. Ryden. *Introduction to cosmology*. Cambridge University Press, 1970. doi: 10.1017/9781316651087.

[28] E. J. Copeland, M. Sami, and S. Tsujikawa. Dynamics of dark energy. *Int. J. Mod. Phys. D*, 15:1753–1936, 2006. doi: 10.1142/S021827180600942X.

[29] S. Weinberg. The Cosmological constant problems. In *4th International Symposium on Sources and Detection of Dark Matter in the Universe (DM 2000)*, pages 18–26, 2 2000.

[30] S. W. Hawking and R. Penrose. The Singularities of gravitational collapse and cosmology. *Proc. Roy. Soc. Lond. A*, 314:529–548, 1970. doi: 10.1098/rspa.1970.0021.

[31] Arvind Borde, Alan H. Guth, and Alexander Vilenkin. Inflationary space-times are incompletein past directions. *Phys. Rev. Lett.*, 90:151301, 2003. doi: 10.1103/PhysRevLett.90.151301. arXiv: gr-qc/0110012.

[32] J. M. M. Senovilla and D. Garfinkle. The 1965 Penrose singularity theorem. *Class. Quant. Grav.*, 32(12):124008, 2015. doi: 10.1088/0264-9381/32/12/124008.

[33] K. Akiyama et al. First M87 Event Horizon Telescope Results. I. The Shadow of the Supermassive Black Hole. *Astrophys. J. Lett.*, 875:L1, 2019. doi: 10.3847/2041-8213/ab0ec7.

[34] K. Akiyama et al. First Sagittarius A* Event Horizon Telescope Results. I. The Shadow of the Supermassive Black Hole in the Center of the Milky Way. *Astrophys. J. Lett.*, 930(2):L12, 2022. doi: 10.3847/2041-8213/ac6674.

[35] G. 't Hooft and M. J. G. Veltman. One loop divergencies in the theory of gravitation. *Ann. Inst. H. Poincare Phys. Theor. A*, 20:69–94, 1974.

[36] H. Sahlmann and T. Thiemann. Towards the QFT on curved space-time limit of QGR. 1. A General scheme. *Class. Quant. Grav.*, 23:867–908, 2006. doi: 10.1088/0264-9381/23/3/019.

[37] S. Tsujikawa. Quintessence: A Review. *Class. Quant. Grav.*, 30:214003, 2013. doi: 10.1088/0264-9381/30/21/214003.

[38] V. Sahni. The Cosmological constant problem and quintessence. *Class. Quant. Grav.*, 19:3435–3448, 2002. doi: 10.1088/0264-9381/19/13/304.

[39] J. Hwang. Cosmological perturbations in generalized gravity theories: Conformal transformation. *Class. Quant. Grav.*, 14:1981–1991, 1997. doi: 10.1088/0264-9381/14/7/029.

[40] D. C. Rodrigues, F. de O. Salles, I. L. Shapiro, and A. A. Starobinsky. Auxiliary fields representation for modified gravity models. *Phys. Rev. D*, 83:084028, 2011. doi: 10.1103/PhysRevD.83.084028.

[41] A. De Felice and S. Tsujikawa. f(R) theories. *Living Rev. Rel.*, 13:3, 2010. doi: 10.12942/lrr-2010-3.

[42] S. Nojiri, S. D. Odintsov, and V. K. Oikonomou. Modified Gravity Theories on a Nutshell: Inflation, Bounce and Late-time Evolution. *Phys. Rept.*, 692:1–104, 2017. doi: 10.1016/j.physrep.2017.06.001.

[43] T. P. Sotiriou and V. Faraoni. f(R) Theories Of Gravity. *Rev. Mod. Phys.*, 82:451–497, 2010. doi: 10.1103/RevModPhys.82.451.

[44] C. Brans and R. H. Dicke. Mach's principle and a relativistic theory of gravitation. *Phys. Rev.*, 124:925–935, 1961. doi: 10.1103/PhysRev.124.925.

[45] T. P. Sotiriou. f(R) gravity and scalar-tensor theory. *Class. Quant. Grav.*, 23:5117–5128, 2006. doi: 10.1088/0264-9381/23/17/003.

[46] G. J. Olmo. Palatini Approach to Modified Gravity: f(R) Theories and Beyond. *Int. J. Mod. Phys. D*, 20:413–462, 2011. doi: 10.1142/S0218271811018925.

[47] G. W. Horndeski. Second-order scalar-tensor field equations in a four-dimensional space. *Int. J. Theor. Phys.*, 10:363–384, 1974. doi: 10.1007/BF01807638.

[48] L. Amendola. Coupled quintessence. *Phys. Rev. D*, 62:043511, 2000. doi: 10.1103/PhysRevD.62.043511.

[49] N. Chow and J. Khoury. Galileon Cosmology. *Phys. Rev. D*, 80:024037, 2009. doi: 10.1103/PhysRevD.80.024037.

[50] A. De Felice and S. Tsujikawa. Generalized Galileon cosmology. *Phys. Rev. D*, 84:124029, 2011. doi: 10.1103/PhysRevD.84.124029.

[51] T. Kobayashi. Horndeski theory and beyond: a review. *Rept. Prog. Phys.*, 82(8):086901, 2019. doi: 10.1088/1361-6633/ab2429.

[52] R. Kase and S. Tsujikawa. Dark energy in Horndeski theories after GW170817: A review. *Int. J. Mod. Phys. D*, 28(05):1942005, 2019. doi: 10.1142/S0218271819420057.

[53] E. Hubble. A relation between distance and radial velocity among extra-galactic nebulae. *Proc. Nat. Acad. Sci.*, 15:168–173, 1929. doi: 10.1073/pnas.15.3.168.

[54] M. Trodden and S. M. Carroll. TASI lectures: Introduction to cosmology. In *Theoretical Advanced Study Institute in Elementary Particle Physics (TASI 2002): Particle Physics and Cosmology: The Quest for Physics Beyond the Standard Model(s)*, pages 703–793, 1 2004.

[55] H. P. Robertson. Kinematics and World-Structure. *Astrophys. J.*, 82: 284–301, 1935. doi: 10.1086/143681.

[56] A. Friedmann. On the Possibility of a world with constant negative curvature of space. *Z. Phys.*, 21:326–332, 1924. doi: 10.1007/BF01328280.

[57] G. Lemaitre. A Homogeneous Universe of Constant Mass and Growing Radius Accounting for the Radial Velocity of Extragalactic Nebulae. *Annales Soc. Sci. Bruxelles A*, 47:49–59, 1927. doi: 10.1007/s10714-013-1548-3.

[58] A. G. Walker. On milne's theory of world-structure*. *Proceedings of the London Mathematical Society*, s2-42(1):90–127, 1937. doi: 10.1112/plms/s2-42.1.90.

[59] Heinz A. and Fritz Z. English and spanish translation of zwicky's (1933) the redshift of extragalactic nebulae, 2017.

[60] Fritz Z. On the masses of nebulae and of clusters of nebulae. *The Astrophysical Journal*, 86:217–246, 1937.

[61] J. F. Navarro, C. S. Frenk, and S. D. M. White. The Structure of cold dark matter halos. *Astrophys. J.*, 462:563–575, 1996. doi: 10.1086/177173.

[62] E. Holmberg. A study of double and multiple galaxies together with inquiries into some general metagalactic problems. *Annals of the Observatory of Lund*, 6:1–173, 1937.

[63] G. Bertone and D. Hooper. History of dark matter. *Rev. Mod. Phys.*, 90 (4):045002, 2018. doi: 10.1103/RevModPhys.90.045002.

[64] J. Schaye et al. The EAGLE project: Simulating the evolution and assembly of galaxies and their environments. *Mon. Not. Roy. Astron. Soc.*, 446:521–554, 2015. doi: 10.1093/mnras/stu2058.

[65] L. A. L. Da Silva. The classification of supernovae. *Astrophysics and Space Science*, 202:215–236, 1993.

[66] S. Perlmutter et al. Measurements of Ω and Λ from 42 high redshift supernovae. *Astrophys. J.*, 517:565–586, 1999. doi: 10.1086/307221. arXiv: astro-ph/9812133.

[67] A. G. Riess et al. Observational evidence from supernovae for an accelerating universe and a cosmological constant. *Astron. J.*, 116: 1009–1038, 1998. doi: 10.1086/300499.

[68] N. Aghanim et al. Planck 2018 results. VI. Cosmological parameters. *Astron. Astrophys.*, 641:A6, 2020. doi: 10.1051/0004-6361/201833910. arXiv: 1807.06209.

[69] S. Weinberg. The Cosmological Constant Problem. *Rev. Mod. Phys.*, 61:1–23, 1989. doi: 10.1103/RevModPhys.61.1.

[70] J. Martin. Everything You Always Wanted To Know About The Cosmological Constant Problem (But Were Afraid To Ask). *Comptes Rendus Physique*, 13:566–665, 2012. doi: 10.1016/j.crhy.2012.04.008. arXiv: 1205.3365.

[71] L. Amendola. Scaling solutions in general nonminimal coupling theories. *Phys. Rev. D*, 60:043501, 1999. doi: 10.1103/PhysRevD.60.043501.

[72] R. Durrer. *The Cosmic Microwave Background*. Cambridge University Press, 2008. doi: 10.1017/CBO9780511817205.

[73] D. Baumann. Inflation. In *Theoretical Advanced Study Institute in Elementary Particle Physics: Physics of the Large and the Small*, pages 523–686, 2011. doi: 10.1142/9789814327183_0010.

[74] D. Baumann. *Cosmology*. Cambridge University Press, 2022. doi: 10.1017/9781108937092.

[75] B. A. Bassett, S. Tsujikawa, and D. Wands. Inflation dynamics and reheating. *Rev. Mod. Phys.*, 78:537–589, 2006. doi: 10.1103/RevModPhys.78.537. arXiv: astro-ph/0507632.

[76] A. Riotto. Particle cosmology. In *5th CERN - Latin American School of High-Energy Physics*, 10 2010.

[77] R. B. Partridge. *A measurement of excess antenna temperature at 4080 Mc/s*, page 355–356. Cambridge Astrophysics. Cambridge University Press, 1995. doi: 10.1017/CBO9780511525070.010.

[78] R. H. Brandenberger, R. Kahn, and W. H. Press. Cosmological Perturbations in the Early Universe. *Phys. Rev. D*, 28:1809, 1983. doi: 10.1103/PhysRevD.28.1809.

[79] C. Gordon, D. Wands, B. A. Bassett, and R. Maartens. Adiabatic and entropy perturbations from inflation. *Phys. Rev. D*, 63:023506, 2000. doi: 10.1103/PhysRevD.63.023506.

[80] Y. Akrami et al. Planck 2018 results. X. Constraints on inflation. *Astron. Astrophys.*, 641:A10, 2020. doi: 10.1051/0004-6361/201833887.

[81] D. Battefeld and P. Peter. A Critical Review of Classical Bouncing Cosmologies. *Phys. Rept.*, 571:1–66, 2015. doi: 10.1016/j.physrep.2014.12.004. arXiv: 1406.2790.

[82] A. G. Riess, S. Casertano, W. Yuan, L. M. Macri, and D. Scolnic. Large Magellanic Cloud Cepheid Standards Provide a 1% Foundation for the Determination of the Hubble Constant and Stronger Evidence for Physics beyond ΛCDM. *Astrophys. J.*, 876(1):85, 2019. doi: 10.3847/1538-4357/ab1422. arXiv: 1903.07603.

[83] E. Di Valentino, O. Mena, S. Pan, L. Visinelli, W. Yang, A.o Melchiorri, D. F. Mota, A. G. Riess, and J. Silk. In the realm of the Hubble tension—a review of solutions. *Class. Quant. Grav.*, 38(15):153001, 2021. doi: 10.1088/1361-6382/ac086d.

[84] E. Di Valentino et al. Snowmass2021 - Letter of interest cosmology intertwined II: The hubble constant tension. *Astropart. Phys.*, 131:102605, 2021. doi: 10.1016/j.astropartphys.2021.102605. arXiv: 2008.11284.

[85] M. M. Ivanov, M. Simonović, and M. Zaldarriaga. Cosmological Parameters from the BOSS Galaxy Power Spectrum. *JCAP*, 05:042, 2020. doi: 10.1088/1475-7516/2020/05/042. arXiv: 1909.05277.

[86] A. G. Riess, S. Casertano, W. Yuan, J. B. Bowers, L. Macri, J. C. Zinn, and D. Scolnic. Cosmic Distances Calibrated to 1% Precision with Gaia EDR3 Parallaxes and Hubble Space Telescope Photometry of 75 Milky Way Cepheids Confirm Tension with ΛCDM. *Astrophys. J. Lett.*, 908 (1):L6, 2021. doi: 10.3847/2041-8213/abdbaf.

[87] S. Dhawan, D. Brout, D. Scolnic, A. Goobar, A. G. Riess, and V. Miranda. Cosmological Model Insensitivity of Local H_0 from the Cepheid Distance Ladder. *Astrophys. J.*, 894(1):54, 2020. doi: 10.3847/1538-4357/ab7fb0. arXiv: 2001.09260.

[88] W. L. Freedman et al. The Carnegie-Chicago Hubble Program. VIII. An Independent Determination of the Hubble Constant Based on the Tip of the Red Giant Branch. *Astrophys. J.*, 882:34, 2019. doi: 10.3847/1538-4357/ab2f73. arXiv: 1907.05922.

[89] B. P. Abbott et al. Gravitational Waves and Gamma-rays from a Binary Neutron Star Merger: GW170817 and GRB 170817A. *Astrophys. J. Lett.*, 848(2):L13, 2017. doi: 10.3847/2041-8213/aa920c.

[90] P. Creminelli and F. Vernizzi. Dark Energy after GW170817 and GRB170817A. *Phys. Rev. Lett.*, 119(25):251302, 2017. doi: 10.1103/PhysRevLett.119.251302. arXiv: 1710.05877.

[91] Daniel E. Holz and Scott A. Hughes. Using gravitational-wave standard sirens. *Astrophys. J.*, 629:15–22, 2005. doi: 10.1086/431341. arXiv: astro-ph/0504616.

[92] F. Acernese et al. Advanced Virgo: a second-generation interferometric gravitational wave detector. *Class. Quant. Grav.*, 32(2):024001, 2015. doi: 10.1088/0264-9381/32/2/024001. arXiv: 1408.3978.

[93] J. Aasi et al. Advanced LIGO. *Class. Quant. Grav.*, 32:074001, 2015. doi: 10.1088/0264-9381/32/7/074001. arXiv: 1411.4547.

[94] K. Somiya. Detector configuration of KAGRA: The Japanese cryogenic gravitational-wave detector. *Class. Quant. Grav.*, 29:124007, 2012. doi: 10.1088/0264-9381/29/12/124007. arXiv:1111.7185.

[95] T. Baker, E. Bellini, P. G. Ferreira, M. Lagos, J. Noller, and I. Sawicki. Strong constraints on cosmological gravity from GW170817 and GRB 170817A. *Phys. Rev. Lett.*, 119(25):251301, 2017. doi: 10.1103/PhysRevLett.119.251301. arXiv: 1710.06394.

[96] D. Langlois, R. Saito, D. Yamauchi, and K. Noui. Scalar-tensor theories and modified gravity in the wake of GW170817. *Phys. Rev. D*, 97(6): 061501, 2018. doi: 10.1103/PhysRevD.97.061501. arXiv: 1711.07403.

[97] M. Punturo et al. The Einstein Telescope: A third-generation gravitational wave observatory. *Class. Quant. Grav.*, 27:194002, 2010. doi: 10.1088/0264-9381/27/19/194002.

[98] P. Amaro-Seoane et al. Laser Interferometer Space Antenna. 2 2017. arXiv: 1702.00786.

[99] R. Daniel. Gwss. https://github.com/RDaniel396/GWSS, 2022.

[100] J. Lesgourgues. The Cosmic Linear Anisotropy Solving System (CLASS) I: Overview. 4 2011. arXiv: 1104.2932.

[101] D. Blas, J. Lesgourgues, and T. Tram. The Cosmic Linear Anisotropy Solving System (CLASS) II: Approximation schemes. *JCAP*, 07:034, 2011. doi: 10.1088/1475-7516/2011/07/034. arXiv: 1104.2933.

[102] J. Abadie et al. Calibration of the LIGO Gravitational Wave Detectors in the Fifth Science Run. *Nucl. Instrum. Meth. A*, 624:223–240, 2010. doi: 10.1016/j.nima.2010.07.089. arXiv: 1007.3973.

[103] A. Nishizawa, A. Taruya, and S. Saito. Tracing the redshift evolution of Hubble parameter with gravitational-wave standard sirens. *Phys. Rev. D*, 83:084045, 2011. doi: 10.1103/PhysRevD.83.084045. arXiv: 1011.5000.

[104] J. R. Gair, S. Babak, A. Sesana, P. Amaro-Seoane, E. Barausse, C. P. L. Berry, E. Berti, and C. Sopuerta. Prospects for observing extreme-mass-ratio inspirals with LISA. *J. Phys. Conf. Ser.*, 840(1):012021, 2017. doi: 10.1088/1742-6596/840/1/012021.

[105] C. Caprini and N. Tamanini. Constraining early and interacting dark energy with gravitational wave standard sirens: the potential of the eLISA mission. *JCAP*, 1610(10):006, 2016. doi: 10.1088/1475-7516/2016/10/006.

[106] P. A. Seoane et al. The Gravitational Universe. 2013. arXiv: 1305.5720.

[107] R. C. Hilborn. Gravitational waves from orbiting binaries without general relativity. *Am. J. Phys.*, 86(3):186–197, 2018. doi: 10.1119/1.5020984.

[108] M. Mapelli, C. Huwyler, L. Mayer, P. Jetzer, and A. Vecchio. Gravitational waves from intermediate-mass black holes in young clusters. *Astrophys. J.*, 719:987–995, 2010. doi: 10.1088/0004-637X/719/2/987.

[109] A. Klein et al. Science with the space-based interferometer eLISA: Supermassive black hole binaries. *Phys. Rev.*, D93(2):024003, 2016. doi: 10.1103/PhysRevD.93.024003.

[110] R.G. Cai, T. Liu, X. Liu, S.J. Wang, and T. Yang. Probing cosmic anisotropy with gravitational waves as standard sirens. *Phys. Rev.*, D97(10):103005, 2018. doi: 10.1103/PhysRevD.97.103005.

[111] W. Zhao, C. Van Den Broeck, D. Baskaran, and T. G. F. Li. Determination of Dark Energy by the Einstein Telescope: Comparing with CMB, BAO and SNIa Observations. *Phys. Rev.*, D83:023005, 2011. doi: 10.1103/PhysRevD.83.023005.

[112] R. D'Agostino and R. C. Nunes. Probing observational bounds on scalar-tensor theories from standard sirens. *Phys. Rev. D*, 100(4): 044041, 2019. doi: 10.1103/PhysRevD.100.044041. arXiv: 1907.05516.

[113] T. G. F. Li. *Extracting Physics from Gravitational Waves: Testing the Strong-field Dynamics of General Relativity and Inferring the Large-scale Structure of the Universe*. PhD thesis, Vrije U., Amsterdam, 2013.

[114] N. Tamanini, C. Caprini, E. Barausse, A. Sesana, A. Klein, and A. Petiteau. Science with the space-based interferometer eLISA. III: Probing the expansion of the Universe using gravitational wave standard sirens. *JCAP*, 1604(04):002, 2016. doi: 10.1088/1475-7516/2016/04/002.

[115] W. Hou, J. Qi, T. Han, J. Zhang, S. Cao, and X. Zhang. Prospects for constraining interacting dark energy models from gravitational wave and gamma ray burst joint observation. 11 2022.

[116] M. P. Hobson, A. H. Jaffe, A. R. Liddle, P. Mukherjee, and D. Parkinson. *Bayesian Methods in Cosmology*. Cambridge University Press, 2009. doi: 10.1017/CBO9780511802461.

[117] R. Trotta. *Bayesian Methods in Cosmology*. 1 2017. arXiv: 1701.01467.

[118] F. Feroz, M. P. Hobson, and M. Bridges. MultiNest: an efficient and robust Bayesian inference tool for cosmology and particle physics. *Mon. Not. Roy. Astron. Soc.*, 398:1601–1614, 2009. doi: 10.1111/j.1365-2966.2009.14548.x. arXiv: 0809.343.

[119] F. Feroz, M. P. Hobson, E. Cameron, and A. N. Pettitt. Importance Nested Sampling and the MultiNest Algorithm. *Open J. Astrophys.*, 2 (1):10, 2019. doi: 10.21105/astro.1306.2144. arXiv: 1306.2144.

[120] J. Buchner, A. Georgakakis, K. Nandra, L. Hsu, C. Rangel, M. Brightman, A. Merloni, M. Salvato, J. Donley, and D. Kocevski. X-ray spectral modelling of the AGN obscuring region in the CDFS: Bayesian model selection and catalogue. *Astron. Astrophys.*, 564:A125, 2014. doi: 10.1051/0004-6361/201322971. arXiv: 1402.0004.

[121] R. Trotta. Bayes in the sky: Bayesian inference and model selection in cosmology. *Contemp. Phys.*, 49:71–104, 2008. doi: 10.1080/00107510802066753. arXiv: 0803.4089.

[122] A. Lewis. GetDist: a Python package for analysing Monte Carlo samples. 10 2019. arXiv: 1910.13970.

[123] A. J. Ross, L. Samushia, C. Howlett, W. J. Percival, A. Burden, and M. Manera. The clustering of the SDSS DR7 main Galaxy sample – I. A 4 per cent distance measure at $z = 0.15$. *Mon. Not. Roy. Astron. Soc.*, 449(1):835–847, 2015. doi: 10.1093/mnras/stv154. arXiv: 1409.3242.

[124] F. Beutler et al. The clustering of galaxies in the completed SDSS-III Baryon Oscillation Spectroscopic Survey: baryon acoustic oscillations in the Fourier space. *Mon. Not. Roy. Astron. Soc.*, 464(3):3409–3430, 2017. doi: 10.1093/mnras/stw2373. arXiv: 1607.03149.

[125] F. Beutler, C. Blake, M. Colless, D. H. Jones, L. Staveley-Smith, L. Campbell, Q. Parker, W. Saunders, and F. Watson. The 6dF Galaxy Survey: Baryon Acoustic Oscillations and the Local Hubble Constant. *Mon. Not. Roy. Astron. Soc.*, 416:3017–3032, 2011. doi: 10.1111/j.1365-2966.2011.19250.x. arXiv: 1106.3366.

[126] D. M. Scolnic et al. The Complete Light-curve Sample of Spectroscopically Confirmed SNe Ia from Pan-STARRS1 and Cosmological Constraints from the Combined Pantheon Sample. *Astrophys. J.*, 859 (2):101, 2018. doi: 10.3847/1538-4357/aab9bb. arXiv: 1710.00845.

[127] A. D. Linde. A New Inflationary Universe Scenario: A Possible Solution of the Horizon, Flatness, Homogeneity, Isotropy and Primordial Monopole Problems. *Phys. Lett. B*, 108:389–393, 1982. doi: 10.1016/0370-2693(82)91219-9.

[128] A. A. Starobinsky. A New Type of Isotropic Cosmological Models Without Singularity. *Adv. Ser. Astrophys. Cosmol.*, 3:130–133, 1987. doi: 10.1016/0370-2693(80)90670-X.

[129] A. H. Guth. Inflationary universe: A possible solution to the horizon and flatness problems. *Phys. Rev. D*, 23:347–356, Jan 1981. doi: 10.1103/PhysRevD.23.347.

[130] A. H. Guth. *The inflationary universe: The quest for a new theory of cosmic origins*. 1997. doi: 10.1063/1.881979.

[131] Alan H. Guth. Eternal inflation. *Annals N. Y. Acad. Sci.*, 950:66, 2001. doi: 10.1111/j.1749-6632.2001.tb02128.x. arXiv: astro-ph/0101507.

[132] John D. Barrow and S. Cotsakis. Inflation and the Conformal Structure of Higher Order Gravity Theories. *Phys. Lett. B*, 214:515–518, 1988. doi: 10.1016/0370-2693(88)90110-4.

[133] C. T. Byrnes, P. S. Cole, and S. P. Patil. Steepest growth of the power spectrum and primordial black holes. *JCAP*, 06:028, 2019. doi: 10.1088/1475-7516/2019/06/028. arXiv: 1811.11158.

[134] A. D. Linde. *Particle physics and inflationary cosmology*, volume 5. 1990. arXiv: hep-th/0503203.

[135] A. Albrecht and P. J. Steinhardt. Cosmology for Grand Unified Theories with Radiatively Induced Symmetry Breaking. *Phys. Rev. Lett.*, 48:1220–1223, 1982. doi: 10.1103/PhysRevLett.48.1220.

[136] J. Martin, C. Ringeval, and V. Vennin. Encyclopædia Inflationaris. *Phys. Dark Univ.*, 5-6:75–235, 2014. doi: 10.1016/j.dark.2014.01.003.

[137] A. Nishizawa and H. Motohashi. Constraint on reheating after $f(R)$ inflation from gravitational waves. *Phys. Rev. D*, 89(6):063541, 2014. doi: 10.1103/PhysRevD.89.063541. arXiv: 1401.1023.

[138] S. Tsujikawa. Observational signatures of $f(R)$ dark energy models that satisfy cosmological and local gravity constraints. *Phys. Rev. D*, 77:023507, 2008. doi: 10.1103/PhysRevD.77.023507. arXiv: 0709.1391.

[139] J. E. Lidsey, A. R. Liddle, E. W. Kolb, E. J. Copeland, T. Barreiro, and M. Abney. Reconstructing the inflation potential : An overview. *Rev. Mod. Phys.*, 69:373–410, 1997. doi: 10.1103/RevModPhys.69.373. arXiv: astro-ph/9508078.

[140] A. Edery and Y. Nakayama. Critical gravity from four dimensional scale invariant gravity. *JHEP*, 11:169, 2019. doi: 10.1007/JHEP11(2019)169.

[141] S. Gottlober, V. Muller, and A. A. Starobinsky. Analysis of inflation driven by a scalar field and a curvature squared term. *Phys. Rev. D*, 43:2510–2520, 1991. doi: 10.1103/PhysRevD.43.2510.

[142] M. Rinaldi and L. Vanzo. Inflation and reheating in theories with spontaneous scale invariance symmetry breaking. *Phys. Rev. D*, 94(2):024009, 2016. doi: 10.1103/PhysRevD.94.024009.

[143] G. Tambalo and M. Rinaldi. Inflation and reheating in scale-invariant scalar-tensor gravity. *Gen. Rel. Grav.*, 49(4):52, 2017. doi: 10.1007/s10714-017-2217-8.

[144] K. Bamba, S.D. Odintsov, and P. V. Tretyakov. Inflation in a conformally-invariant two-scalar-field theory with an extra R^2 term. *Eur. Phys. J. C*, 75(7):344, 2015. doi: 10.1140/epjc/s10052-015-3565-8.

[145] I. Antoniadis, A. Karam, A. Lykkas, T. Pappas, and K. Tamvakis. Single-field inflation in models with an R^2 term. *PoS*, CORFU2019:073, 2020. doi: 10.22323/1.376.0073.

[146] X. Calmet and I. Kuntz. Higgs starobinsky inflation. *Eur. Phys. J. C*, 76(5):289, 2016. doi: 10.1140/epjc/s10052-016-4136-3.

[147] S. Capozziello, S. Nojiri, S. D. Odintsov, and A. Troisi. Cosmological viability of f(R)-gravity as an ideal fluid and its compatibility with a matter dominated phase. *Phys. Lett. B*, 639. doi: 10.1016/j.physletb.2006.06.034.

[148] Y. Tang and Y.L. Wu. Weyl scaling invariant R^2 gravity for inflation and dark matter. *Phys. Lett. B*, 809:135716, 2020. doi: 10.1016/j.physletb.2020.135716.

[149] C. van de Bruck and L. E. Paduraru. Simplest extension of Starobinsky inflation. *Phys. Rev. D*, 92:083513, 2015. doi: 10.1103/PhysRevD.92.083513.

[150] P.G. Ferreira, C.T. Hill, J. Noller, and G. G. Ross. Scale-independent R^2 inflation. *Phys. Rev. D*, 100(12):123516, 2019. doi: 10.1103/PhysRevD.100.123516.

[151] F. Bernardeau and J.P. Uzan. NonGaussianity in multifield inflation. *Phys. Rev. D*, 66:103506, 2002. doi: 10.1103/PhysRevD.66.103506. arXiv: hep-ph/0207295.

[152] A. Achúcarro and G. A. Palma. The string swampland constraints require multi-field inflation. *JCAP*, 02:041, 2019. doi: 10.1088/1475-7516/2019/02/041. arXiv: 1807.0439.

[153] A. D. Linde. Inflation and string cosmology. *Prog. Theor. Phys. Suppl.*, 163:295–322, 2006. doi: 10.1143/PTPS.163.295. arXiv: hep-th/0503195.

[154] K. Choi, L. M. H. Hall, and C. van de Bruck. Spectral Running and Non-Gaussianity from Slow-Roll Inflation in Generalised Two-Field Models. *JCAP*, 02:029, 2007. doi: 10.1088/1475-7516/2007/02/029. arXiv: astro-ph/0701247.

[155] D. Wands, N. Bartolo, S. Matarrese, and A. Riotto. An Observational test of two-field inflation. *Phys. Rev. D*, 66:043520, 2002. doi: 10.1103/PhysRevD.66.043520. arXiv: astro-ph/0205253.

[156] J. Rubio. Higgs inflation. *Front. Astron. Space Sci.*, 5:50, 2019. doi: 10.3389/fspas.2018.00050. arXiv: 1807.02376.

[157] A. Gundhi and C. F. Steinwachs. Scalaron–Higgs inflation reloaded: Higgs-dependent scalaron mass and primordial black hole dark matter. *Eur. Phys. J. C*, 81(5):460, 2021. doi: 10.1140/epjc/s10052-021-09225-2. arXiv: 2011.09485.

[158] H. Weyl. Gravitation and electricity. *Sitzungsber. Preuss. Akad. Wiss. Berlin (Math. Phys.)*, 1918:465, 1918.

[159] P. G. Ferreira, C. T. Hill, and G. G. Ross. Scale-Independent Inflation and Hierarchy Generation. *Phys. Lett. B*, 763:174–178, 2016. doi: 10.1016/j.physletb.2016.10.036.

[160] C. Wetterich. Cosmology and the Fate of Dilatation Symmetry. *Nucl. Phys. B*, 302:668–696, 1988. doi: 10.1016/0550-3213(88)90193-9. arXiv: 1711.03844.

[161] J. Garcia-Bellido, J. Rubio, M. Shaposhnikov, and D. Zenhausern. Higgs-Dilaton Cosmology: From the Early to the Late Universe. *Phys. Rev. D*, 84:123504, 2011. doi: 10.1103/PhysRevD.84.123504.

[162] K. Kannike, M. Raidal, C. Spethmann, and H. Veermäe. The evolving Planck mass in classically scale-invariant theories, 2017. arXiv: 1610.06571.

[163] A. Ghoshal, D. Mukherjee, and M. Rinaldi. Inflation and primordial gravitational waves in scale-invariant quadratic gravity with Higgs. *JHEP*, 05:023, 2023. doi: 10.1007/JHEP05(2023)023. arXiv: 2205.06475.

[164] P. G. Ferreira, C. T. Hill, and G. G. Ross. No fifth force in a scale invariant universe. *Phys. Rev. D*, 95(6):064038, 2017. doi: 10.1103/PhysRevD.95.064038.

[165] J. Kubo, M. Lindner, K. Schmitz, and M. Yamada. Planck mass and inflation as consequences of dynamically broken scale invariance. *Phys. Rev. D*, 100(1):015037, 2019. doi: 10.1103/PhysRevD.100.015037.

[166] J. Kubo, J. Kuntz, M. Lindner, J. Rezacek, P. Saake, and A. Trautner. Unified Emergence of Energy Scales and Cosmic Inflation. 12 2020.

[167] E. Noether. Invariante variationsprobleme. *Nachrichten von der Gesellschaft der Wissenschaften zu Göttingen, Mathematisch-Physikalische Klasse*, 1918:235–257, 1918.

[168] M. Bañados and I. A. Reyes. A short review on Noether's theorems, gauge symmetries and boundary terms. *Int. J. Mod. Phys. D*, 25(10): 1630021, 2016. doi: 10.1142/S0218271816300214. arXiv: 1601.03616.

[169] P. Brax, P. Valageas, and P. Vanhove. R^2 dark energy in the laboratory. *Phys. Rev. D*, 97(10):103508, 2018. doi: 10.1103/PhysRevD.97.103508. arXiv: 1711.03356.

[170] C. Gordon, D. Wands, B. A. Bassett, and R. Maartens. Adiabatic and entropy perturbations from inflation. *Phys. Rev. D*, 63:023506, 2000. doi: 10.1103/PhysRevD.63.023506. arXiv: astro-ph/0009131.

[171] V.F. Mukhanov, H.A. Feldman, and R.H. Brandenberger. Theory of cosmological perturbations. *Physics Reports*, 215(5):203 – 333, 1992. ISSN 0370-1573. doi: https://doi.org/10.1016/0370-1573(92)90044-Z.

[172] T. S. Bunch and P. C. W. Davies. Quantum Field Theory in de Sitter Space: Renormalization by Point Splitting. *Proc. Roy. Soc. Lond. A*, 360: 117–134, 1978. doi: 10.1098/rspa.1978.0060.

[173] C. M. Peterson and M. Tegmark. Testing multifield inflation: A geometric approach. *Phys. Rev. D*, 87(10):103507, 2013. doi: 10.1103/PhysRevD.87.103507.

[174] Z. Lalak, D. Langlois, S. Pokorski, and K. Turzynski. Curvature and isocurvature perturbations in two-field inflation. *JCAP*, 07:014, 2007. doi: 10.1088/1475-7516/2007/07/014.

[175] F. Di Marco, F. Finelli, and R. Brandenberger. Adiabatic and isocurvature perturbations for multifield generalized Einstein models. *Phys. Rev. D*, 67:063512, 2003. doi: 10.1103/PhysRevD.67.063512.

[176] M. Braglia, D.K. Hazra, F. Finelli, G. F. Smoot, L. Sriramkumar, and A. A. Starobinsky. Generating PBHs and small-scale GWs in two-field models of inflation. *JCAP*, 08:001, 2020. doi: 10.1088/1475-7516/2020/08/001.

[177] D. I. Kaiser and E. I. Sfakianakis. Multifield Inflation after Planck: The Case for Nonminimal Couplings. *Phys. Rev. Lett.*, 112(1):011302, 2014. doi: 10.1103/PhysRevLett.112.011302. arXiv: 1304.0363.

[178] P. Carrilho, K. A. Malik, and D. J. Mulryne. Dissecting the growth of the power spectrum for primordial black holes. *Phys. Rev. D*, 100(10): 103529, 2019. doi: 10.1103/PhysRevD.100.103529. arXiv: 1907.05237.

[179] A. Gundhi and C. F. Steinwachs. Scalaron-Higgs inflation. *Nucl. Phys. B*, 954:114989, 2020. doi: 10.1016/j.nuclphysb.2020.114989.

[180] A. Gundhi, S. V. Ketov, and C. F. Steinwachs. Primordial black hole dark matter in dilaton-extended two-field Starobinsky inflation. 11 2020.

[181] I. D. Gialamas, A. Karam, and A. Racioppi. Dynamically induced Planck scale and inflation in the Palatini formulation. *JCAP*, 11:014, 2020. doi: 10.1088/1475-7516/2020/11/014.

[182] C. van de Bruck and C. Longden. Running of the Running and Entropy Perturbations During Inflation. *Phys. Rev. D*, 94(2):021301, 2016. doi: 10.1103/PhysRevD.94.021301.

[183] A. Lewis, A. Challinor, and A. Lasenby. Efficient computation of CMB anisotropies in closed FRW models. *Astrophys. J.*, 538:473–476, 2000. doi: 10.1086/309179.

[184] M. Gleiser. Phase transitions in the universe. *Contemp. Phys.*, 39:239–253, 1998. doi: 10.1080/001075198181937. arXiv: ep-ph/9803291.

[185] M. Kawasaki, K. Kohri, and N. Sugiyama. Cosmological constraints on late time entropy production. *Phys. Rev. Lett.*, 82:4168, 1999. doi: 10.1103/PhysRevLett.82.4168. arXiv: astro-ph/9811437.

[186] K. Ichikawa, M. Kawasaki, and F. Takahashi. The Oscillation effects on thermalization of the neutrinos in the Universe with low reheating temperature. *Phys. Rev. D*, 72:043522, 2005. doi: 10.1103/PhysRevD.72.043522. arXiv: astro-ph/0505395.

[187] R. Allahverdi, R. Brandenberger, F. Cyr-Racine, and A. Mazumdar. Reheating in Inflationary Cosmology: Theory and Applications. *Ann. Rev. Nucl. Part. Sci.*, 60:27–51, 2010. doi: 10.1146/annurev.nucl.012809.104511. arXiv: 1001.2600.

[188] L. Kofman, A.D. Linde, and A.A. Starobinsky. Reheating after inflation. *Phys. Rev. Lett.*, 73:3195–3198, 1994. doi: 10.1103/PhysRevLett.73.3195. arXiv: hep-th/9405187.

[189] L. Kofman, A. D. Linde, and A. A. Starobinsky. Towards the theory of reheating after inflation. *Phys. Rev. D*, 56:3258–3295, 1997. doi: 10.1103/PhysRevD.56.3258. arXiv: hep-ph/9704452.

[190] P. B. Greene, L. Kofman, A. D. Linde, and A. A. Starobinsky. Structure of resonance in preheating after inflation. *Phys. Rev. D*, 56:6175–6192, 1997. doi: 10.1103/PhysRevD.56.6175. arXiv: hep-ph/9705347.

[191] M. A. Amin, M. P. Hertzberg, D. I. Kaiser, and J. Karouby. Nonperturbative Dynamics Of Reheating After Inflation: A Review. *Int. J. Mod. Phys. D*, 24:1530003, 2014. doi: 10.1142/S0218271815300037. arXiv: 1410.3808.

[192] A. D. Linde. *Particle physics and inflationary cosmology*, volume 5. 1990. arXiv:hep-th/0503203.

[193] J. L. Cook, E. Dimastrogiovanni, D. A. Easson, and L. M. Krauss. Reheating predictions in single field inflation. *JCAP*, 04:047, 2015. doi: 10.1088/1475-7516/2015/04/047. arXiv: 1502.04673.

[194] A.y Ashtekar and J. Lewandowski. Background independent quantum gravity: A Status report. *Class. Quant. Grav.*, 21:R53, 2004. doi: 10.1088/0264-9381/21/15/R01. arXiv: gr-qc/0404018.

[195] C. Rovelli. Loop quantum gravity. *Living Rev. Rel.*, 1:1, 1998. doi: 10.12942/lrr-1998-1. arXiv: gr-qc/9710008.

[196] M. Novello and S. E. P. Bergliaffa. Bouncing Cosmologies. *Phys. Rept.*, 463:127–213, 2008. doi: 10.1016/j.physrep.2008.04.006. arXiv: 0802.1634.

[197] P. J. Steinhardt and N. Turok. The Cyclic universe: An Informal introduction. *Nucl. Phys. B Proc. Suppl.*, 124:38–49, 2003. doi: 10.1016/S0920-5632(03)02075-9. arXiv: astro-ph/0204479.

[198] R. Brandenberger. Initial conditions for inflation — A short review. *Int. J. Mod. Phys. D*, 26(01):1740002, 2016. doi: 10.1142/S0218271817400028. arXiv: 1601.01918.

[199] A. Linde. On the problem of initial conditions for inflation. *Found. Phys.*, 48(10):1246–1260, 2018. doi: 10.1007/s10701-018-0177-9. arXiv: 1710.04278.

[200] R. H. Brandenberger. The Matter Bounce Alternative to Inflationary Cosmology. 2012. arXiv: 1206.4196.

[201] Y. Cai, T. Qiu, R. Brandenberger, and X. Zhang. A Nonsingular Cosmology with a Scale-Invariant Spectrum of Cosmological Perturbations from Lee-Wick Theory. *Phys. Rev. D*, 80:023511, 2009. doi: 10.1103/PhysRevD.80.023511. arXiv: 0810.4677.

[202] P. Creminelli and L. Senatore. A Smooth bouncing cosmology with scale invariant spectrum. *JCAP*, 11:010, 2007. doi: 10.1088/1475-7516/2007/11/010. arXiv: hep-th/0702165.

[203] A. Ijjas and P. J. Steinhardt. Bouncing Cosmology made simple. *Class. Quant. Grav.*, 35(13):135004, 2018. doi: 10.1088/1361-6382/aac482. arXiv: 1803.01961.

[204] E. N. Saridakis, S. Banerjee, and R. Myrzakulov. Bounce and cyclic cosmology in new gravitational scalar-tensor theories. *Phys. Rev. D*, 98(6):063513, 2018. doi: 10.1103/PhysRevD.98.063513.

[205] P. Pavlović and M. Sossich. Dynamic properties of cyclic cosmologies. *Phys. Rev. D*, 103(2):023529, 2021. doi: 10.1103/PhysRevD.103.023529.

[206] T. Qiu, X. Gao, and E. N. Saridakis. Towards anisotropy-free and non-singular bounce cosmology with scale-invariant perturbations. *Phys. Rev. D*, 88(4):043525, 2013. doi: 10.1103/PhysRevD.88.043525. arXiv: 1303.2372.

[207] W. B. Bonnor. The Instability of the Einstein Universe. *Monthly Notices of the Royal Astronomical Society*, 115(3):310–322, 06 1955. doi: 10.1093/mnras/115.3.310.

[208] R. Brandenberger and P. Peter. Bouncing Cosmologies: Progress and Problems. *Found. Phys.*, 47(6):797–850, 2017. doi: 10.1007/s10701-016-0057-0. arXiv: 1603.05834.

[209] E. Di Valentino, A. Melchiorri, and J. Silk. Planck evidence for a closed Universe and a possible crisis for cosmology. *Nature Astron.*, 4(2): 196–203, 2019. doi: 10.1038/s41550-019-0906-9.

[210] W. Yang, W. Giarè, S. Pan, E. Di Valentino, A. Melchiorri, and J. Silk. Revealing the effects of curvature on the cosmological models. 10 2022.

[211] Ö. Güngör and G. D. Starkman. A classical, non-singular, bouncing universe. *JCAP*, 04:003, 2021. doi: 10.1088/1475-7516/2021/04/003.

[212] D. N. Page. Probability of R^2 inflation. *Phys. Rev. D*, 36:1607–1624, Sep 1987. doi: 10.1103/PhysRevD.36.1607.

[213] S. Carloni, P. K.S. Dunsby, and D. Solomons. Bounce conditions in f(R) cosmologies. *Classical and Quantum Gravity*, 23(6):1913–1922, March 2006. doi: 10.1088/0264-9381/23/6/006. arXiv: gr-qc/0510130.

[214] C. Molina-Paris and M. Visser. Minimal conditions for the creation of a Friedman-Robertson-Walker universe from a 'bounce'. *Phys. Lett. B*, 455:90–95, 1999. doi: 10.1016/S0370-2693(99)00469-4.

[215] C. Gordon and N. Turok. Cosmological perturbations through a general relativistic bounce. *Phys. Rev. D*, 67:123508, 2003. doi: 10.1103/PhysRevD.67.123508. arXiv: hep-th/0206138.

[216] F. T. Falciano, M. Lilley, and P. Peter. A Classical bounce: Constraints and consequences. *Phys. Rev. D*, 77:083513, 2008. doi: 10.1103/PhysRevD.77.083513. arXiv: 0802.1196.

[217] A. De Felice and S. Tsujikawa. f(R) theories. *Living Rev. Rel.*, 13:3, 2010. doi: 10.12942/lrr-2010-3. arXiv: 1002.4928.

[218] J. Hwang and H. Noh. Gauge ready formulation of the cosmological kinetic theory in generalized gravity theories. *Phys. Rev. D*, 65:023512, 2002. doi: 10.1103/PhysRevD.65.023512.

[219] J. M. Bardeen. Gauge Invariant Cosmological Perturbations. *Phys. Rev. D*, 22:1882–1905, 1980. doi: 10.1103/PhysRevD.22.1882.

[220] J. Hwang. Quantum fluctuations of cosmological perturbations in generalized gravity. *Class. Quant. Grav.*, 14:3327–3336, 1997. doi: 10.1088/0264-9381/14/12/016. arXiv: gr-qc/9607059.

[221] E. R. Harrison. Normal Modes of Vibrations of the Universe. *Rev. Mod. Phys.*, 39:862–882, 1967. doi: 10.1103/RevModPhys.39.862.

[222] J. Martin and P. Peter. Parametric amplification of metric fluctuations through a bouncing phase. *Phys. Rev. D*, 68:103517, 2003. doi: 10.1103/PhysRevD.68.103517.

[223] R. Lehoucq, J. Weeks, J.P. Uzan, E. Gausmann, and J.P. Luminet. Eigenmodes of three-dimensional spherical spaces and their application to cosmology. *Class. Quant. Grav.*, 19:4683–4708, 2002. doi: 10.1088/0264-9381/19/18/305. arXiv: gr-qc/0205009.

[224] G. Ellis, R. Maartens, and M. MacCallum. *Relativistic Cosmology*. Cambridge University Press, 4 2012. ISBN 978-0-521-38115-4. doi: 10.1017/CBO9781139014403.

[225] P. Bari and K. Bhattacharya. Evolution of scalar and vector cosmological perturbations through a bounce in metric $f(R)$ gravity in flat FLRW spacetime. *JCAP*, 11:019, 2019. doi: 10.1088/1475-7516/2019/11/019. arXiv: 1907.11607.

[226] K. A. Malik and D. Wands. Cosmological perturbations. *Phys. Rept.*, 475:1–51, 2009. doi: 10.1016/j.physrep.2009.03.001. arXiv: 0809.494.

[227] T. Biswas, R. Mayes, and C. Lattyak. Perturbations in bouncing and cyclic models. *Phys. Rev. D*, 93(6):063505, 2016. doi: 10.1103/PhysRevD.93.063505. arXiv: 1502.05875.

[228] P. J. E. Peebles and A. Vilenkin. Quintessential inflation. *Phys. Rev. D*, 59:063505, 1999. doi: 10.1103/PhysRevD.59.063505. arXiv: astro-ph/9810509.

[229] K. Dimopoulos and J. W. F. Valle. Modeling quintessential inflation. *Astropart. Phys.*, 18:287–306, 2002. doi: 10.1016/S0927-6505(02)00115-9. arXiv: astro-ph/0111417.

[230] A. Ijjas and P. J. Steinhardt. A new kind of cyclic universe. *Phys. Lett. B*, 795:666–672, 2019. doi: 10.1016/j.physletb.2019.06.056.

[231] J. D. Barrow and M. P. Dabrowski. Oscillating Universes. *Mon. Not. Roy. Astron. Soc.*, 275:850–862, 1995.